CHALMERS

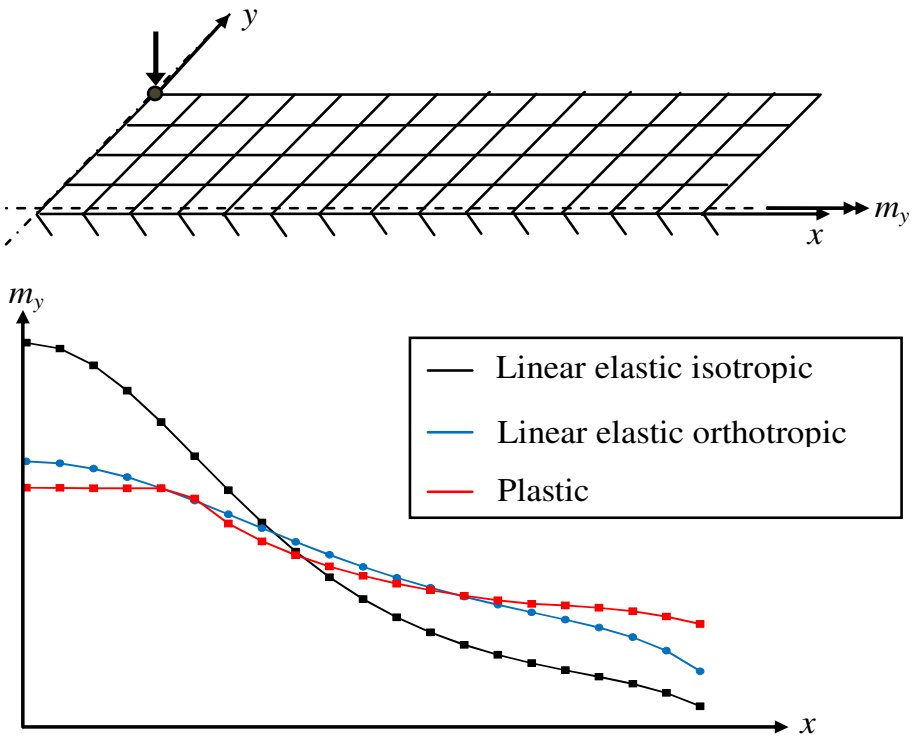

Redistribution of force concentrations in reinforced concrete cantilever slab using 3D non-linear FE analyses

Master of Science Thesis in the Master's Programme Structural Engineering and Building Technology

SONGLY LIM

Department of Civil and Environmental Engineering
Division of Structural Engineering
Concrete Structures
CHALMERS UNIVERSITY OF TECHNOLOGY
Göteborg, Sweden 2013
Master's Thesis 2013:100

MASTER'S THESIS 2013:100

Redistribution of force concentrations in reinforced concrete cantilever slab using 3D non-linear FE analyses

Master of Science Thesis in the Master's Programme Structural Engineering and Building Technology

SONGLY LIM

Department of Civil and Environmental Engineering
Division of Structural Engineering
Concrete Structures
CHALMERS UNIVERSITY OF TECHNOLOGY
Göteborg, Sweden 2013

Redistribution of force concentrations in reinforced concrete cantilever slab using 3D non-linear FE analyses

Master of Science Thesis in the Master's Programme Structural Engineering and Building Technology

SONGLY LIM

Examensarbete / Institutionen för bygg- och miljöteknik,
Chalmers tekniska högskola 2013:100

Department of Civil and Environmental Engineering
Division of Structural Engineering
Concrete Structures
Chalmers University of Technology
SE-412 96 Göteborg
Sweden
Telephone: + 46 (0)31-772 1000

Cover:
Cantilever slab subjected to a single point load and the resulting moment distribution along the support line for different types of structural response.

Chalmers Reproservice
Göteborg, Sweden 2013

Redistribution of force concentrations in reinforced concrete cantilever slab using 3D non-linear FE analyses

Master of Science Thesis in the Master's Programme Structural Engineering and Building Technology

SONGLY LIM
Department of Civil and Environmental Engineering
Division of Structural Engineering
Concrete Structures
Chalmers University of Technology

ABSTRACT

Finite element analyses (FE analyses) methods are nowadays commonly used for the analysis and design of civil engineering structures. When modeling reinforced concrete slabs, local force concentration arises when using 3D linear elastic FE analyses. These force concentrations will in reality be distributed due to concrete cracking and yielding of tensile reinforcement. This master thesis uses 3D non-linear FE analyses and simplified methods to describe the structural response of a reinforced concrete cantilever slab subjected to a single point load. The cantilever slab studied was modeled as a homogeneous material with different material models such as linear elastic isotropic and orthotropic material, and bilinear and multi-linear elasto-plastic model in order to investigate the structural response of the slab in different states.

For linear elastic isotropic and orthotropic analysis of the studied slab, a shell element model was used to validate the beam grillage model later used in the main investigation. The comparison of FE results shows that shell element is the most appropriate element to use and there is a divergence upon mesh refinement when using beam elements due to torsional effects. Nevertheless, the beam grillage model can be used in case that appropriate beam element mesh size is used.

For non-linear analysis, the studied cantilever slab was analyzed using the beam grillage model with non-linear moment-curvature relationship since shell element models previously have proven to give incorrect results when used with elasto-plastic material response, due to unwanted biaxial effects. Concerning non-linear analysis in service limit state (SLS), the orthotropic analysis is shown to provide a good approximation of maximum moment. In the ultimate limit state (ULS), there is a small need for plastic rotation of the slab before the slab fails in non-linear analysis. Hence, there is a possibility to redistribute the moment along the entire length of the studied slab due to yielding of tensile reinforcement. The comparison between a present guideline and the FE analyses shows that the recommendation provided in the former is conservative in terms of distribution width for moment in cantilever slabs. However, the user should be cautious with this conclusion since it is based on one particular load case. In order to provide a better understanding of the behaviour of the reinforced concrete cantilever slab and examine the recommendation further, further studies should be carried out.

Key words: Non-linear 3D FE analyses, redistribution of forces, reinforced concrete, cantilever slab, material model, moment-curvature, beam element, shell element

Contents

Preface

This master's thesis treats the redistribution of force concentrations in 3D finite element analyses. The work of the study has been carried out at Reinertsen's office from January 2013 to June 2013 in cooperation with the Division of Structural Engineering at Chalmers University of Technology and Reinertsen Sverige AB. Tools for this study are a combination of literature studies, linear and non-linear finite element analyses in which present guidelines are compared. The aim of this master's thesis is to determine the most appropriate strip width to distribute the force concentrations over. Examiner has been Mario Plos.

I would like to express my gratitude to my parents, Heng Leang Lim and Channy Sen, for their unconditional supports and encouragement throughout this academic journey.

Very special thanks to my supervisor, Morgan Johansson, PhD Reinertsen and also to my supervisor and examiner, Mario Plos, Associate Professor at Chalmers University of Technology for their valuable advice, support and guidance throughout the entire working period.

I would also like to thank M.Sc. Ginko Georgiev for his support and valuable thoughts along the project.

Finally, I would like to thank my opponents, Dimosthenis Floros and Ólafur Ágúst Ingason for having assisting me in my work and providing me with their thoughts.

SONGLY LIM

Göteborg, June 2013

Notations

Roman upper case letters

A	Area
A_I	Equivalent area state I
A_s	Area of reinforcement
D	Slab stiffness
E	Young's modulus
E_c	Young's modulus for concrete
E_I	Young's modulus for uncracked state
E_{II}	Equivalent Young's modulus for cracked reinforced concrete
E_s	Young's modulus for steel
F	External force
F_c	Force in concrete
F_s	Force in steel
G	Shear modulus
I	Moment of inertia
I_I	Moment of inertia state I
I_{II}	Moment of inertia state II
K_v	Torsional stiffness
L	Length
L_c	Characteristic span width
M	Moment
M_{cr}	Cracking moment
M_{Ed}	Design value of bending moment
M_{Rd}	Ultimate moment capacity
R	Reaction force
V	Shear force
V_{Ed}	Design value of shear

Roman lower case letters

b	Width of cross-section
c	Concrete cover
c_1	Factor depending on the height and width of the rectangular cross section
d	Effective depth of cross-section

f_c Concrete compressive strength

f_{cd} Design value of concrete compressive strength

f_{ct} Concrete tensile strength

f_{ctm} Mean value of concrete tensile strength

f_y Yield stress

f_{yd} Design value of yield stress

f_y^{mod} Fictitious yield stress

h Height of cross-section

h Slab thickness

k_λ Modification factor for rotation capacity

l Length

l_{pl} Development length of a plastic region

m Moment

m_{cr} Cracking moment

m_{rd} Ultimate moment capacity

m_{xy} Linear torsional moment

n_{hinges} Number of plastic hinges of the structure

r Radius of curvature

s Reinforcement bar spacing

t Height of a rectangular cross section

t Thickness of the surfacing

u_{el} Elastic displacement

u_{pl} Plastic displacement

u_{tot} Total displacement

u_z Vertical displacement

v_0 Principal shear force

w Width of the cross section

w Distribution width

w_{eff} Effective width

x Coordinate

x_u Height of compression zone

y Coordinate

y_{cs} Distance from the centre of the load to the critical cross section

z Coordinate

Greek lower case letters

α Angle that determine the direction of shear force vector

α Factor to transform f_y to f_y^{mod}

α Ratio between Young's Modulus for reinforcement and concrete

α_R Stress block factor

β_R Stress block factor

χ Curvature

χ_{el} Elastic curvature

χ_{pl} Plastic curvature

χ_y Yield curvature

δ Ratio of the distributed chosen moment to the elastic bending moment

ε Strain

ε_c Concrete compression strain

ε_{cu} Ultimate concrete strain

ε_s Steel strain

ε_y Yield strain

ε_{el} Elastic strain

ε_{pl} Plastic strain

ϕ Bar diameter

γ Different in percentage

λ Shear slenderness

μ Number of statically indeterminacy of the structure

θ_{pl} Plastic rotation

θ_{rd} Plastic rotation capacity

$\theta_{rd,\min}$ Minimum plastic rotation capacity

σ Stress

σ_c Concrete compressive stress

σ_{ct} Concrete tensile stress

τ Shear stress

υ Poisson's ratio

1 Introduction

1.1 Background

Finite element analyses based on linear elastic material response is often used to determine the force distribution in design of civil engineering structures. In the design of reinforced concrete slabs, different types and positions of loads may result in various force concentrations. The knowledge of how these linearly determined forces can be redistributed from one point to another is very crucial. The real force distribution of a structure may be difficult to explain and therefore simplified approaches are often used in design of the structure. Recently guidelines have been presented of how to design reinforced concrete slabs based on linear elastic analysis, including Pacoste *et al*. (2012). In the past, structural engineers used traditional design tools such as tables and 2D analyses to design concrete slabs. In this case the distribution of forces in the structure will be given by the choice of the structural model. However with the development of computer analysis capacity, there has been large increase in the use of three-dimensional (3D) finite element analyses (FE analyses) in analyses and design. For design of bridges, there has been a shift from traditional methods to 3D analyses in the last few years in Sweden.

3D FE analyses provide the possibility for a more accurate study of the structure than what is possible by using more traditional design tools. In liaison with the increased usage of such analyses, however, there have also appeared some problems that have not been known of when using simplified 2D analyses. One such problem is how to interpret local force concentrations that arise in linear elastic analysis, but that may be not so critical in reality.

Normally in concrete structure, such force concentrations lead to cracking and yielding of the reinforcement which result in the redistribution of forces. Hence, in a real structure, there will be a considerably more favourable force distribution than what is usually the case in a finite element analysis assuming linear elastic response. It would also be advantageous from an economic perspective to be able to distribute such force concentrations over a larger region of the structure in the design process in order to optimise material.

1.2 Purpose

The overall aim of this master's thesis was to provide a more comprehensive understanding about how concentrated forces in linear elastic FE analyses can be distributed over a larger region in the design of reinforced concrete slabs and to investigate technical and practical recommendations for such redistributions. The goal in this report was to determine a strip width in which concentrations of moments and shear forces acquired in a linear FE analysis may be distributed. Another objective of the study was to evaluate the recommendations given by Pacoste *et al*. (2012).

1.3 Method

A theoretical part was carried out through a literature study of both text books and research papers in order to get a good overall picture of how the distribution of moments and shear forces can be handled.

Investigations were carried out by performing linear and non-linear FE analyses of a cantilever slab in the student version of the finite element software ADINA, Adina (2011). To begin with, simplified 3D linear elastic isotropic and orthotropic analyses were performed. The orthotropic analyses were conducted to simulate different stiffness in two directions; this is what will happen in reality when concrete cracks. At a later stage, more complex 3D non-linear elastoplastic FE analyses, used to simulate the effect of cracking and yielding, were carried out with the same structure as the one used in the linear elastic analyses.

The result of the FE analyses were verified by checking the procedure, assumptions and modelling made. Several analyses were made in order to get reliable results and to check the influence of different parameters.

Finally, the results in term of moment and shear force distribution in the structure from 3D FE analyses were compared to those from the present guidelines found, Pacoste *et al*. (2012).

1.4 Limitations

The FE analyses carried out only treat reinforced concrete cantilever slabs subjected to point loads. As there is a limited time for the master thesis study, this project mainly focuses on bending response of a slab but also briefly treats the distribution of shear forces.

The thesis investigates the behaviour of the slabs in different states from cracking until the collapse of the structure. The studied slabs were subjected to out of plane load only. Other effects such as prestressing force, normal force, shrinkage, creep and thermal effects can be important, but were not taken into account in this master thesis study and these effects were not discussed in this report. Due to the complex material behaviour of reinforced concrete structures, the slabs studied were not modelled in detail with separate materials for concrete and reinforcement. Instead, the idealized behaviour of the slabs were modelled to be linear elastic isotropic, linear elastic orthotropic and to have a non-linear moment curvature response. As simplified properties of the slabs were used, there will be a difference between the response of the slabs obtained from FE analysis and the response of the real concrete slabs.

1.5 Outline of the report

Chapter 2 covers material response, structural response of reinforced concrete structures and design approaches for beams and slabs. This chapter also explains some recommendations on moment and shear force distribution in slabs based on Eurocode 2, CEN (2004), and other literature studied, including Pacoste *et al.* (2012).

Chapter 3 examines the behaviour of a reinforced concrete cantilever beam under a point load in elasto-plastic response. It also describes different approaches that are used to imitate the response of the beam in the elasto-plastic case including bilinear plastic material and elasto-plastic moment-curvature relationship. Comparisons between 2D beam and 3D beam using different material models were performed. This chapter also treats the plastic rotation of the cantilever beam studied.

Chapter 4 describes the responses of the cantilever slabs studied loaded by one point load in different states from cracked state until the collapse of the structure is formed.

Different types of modelling of the slab were investigated. The results in term of support reaction, moment distribution, shear force distribution and displacement received from FE analyses using beam grillage with beam elements and slab with shell elements were compared in order to see which is the most appropriate modelling in the design and in order to evaluate the accuracy of the modelling. This chapter also cover a method on how to determine the plastic rotation of the slab.studied. The recommendation on the distribution width of moments and shear forces from present guidelines were compared with the distribution width obtained from the FE analyses.

Chapter 5 summarises the discussion and conclusion of results of the projects. The suggestions to further studies and investigation are presented.

2 Theory

2.1 Finite element

The usage of finite element procedures has increased significantly over the last decades and these methods are nowadays commonly used for the analysis and design of engineering structures. In order to be able to rely on the solutions obtained from a FE analysis, it is necessary to choose an appropriate and effective model that will predict the response of the structures which are being analysed and to be able to assess the level of accuracy of the analysis. Some issues related to this method need to be mentioned and the combination of the knowledge of the structural behaviour of the structures studied and of FE method is needed.

For reinforced concrete slabs, linear finite analysis is normally used in the design in order to simplify its non-linear response. Using this method, we can superimpose different actions that act on the slab. This method is suitable as the design is based on moment and forces that fulfil equilibrium, i.e. and linear finite analysis is one of many possible solutions that fulfil equilibrium.

2.2 Structural response of reinforced concrete structures

2.2.1 Material response

2.2.1.1 Concrete

Concrete is a very variable material which has a wide range of strengths and stress-strain curve. Figure 2.1 shows a typical stress-strain for concrete in compression according to Molsey *et al.*(2007).

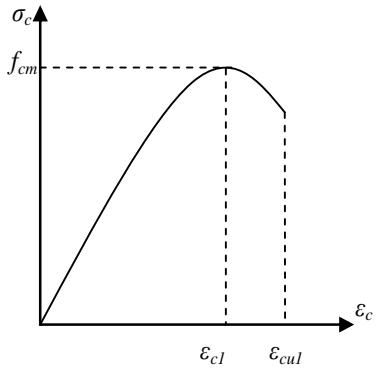

Figure 2.1. Typical stress-strain relationship for concrete in compression

According to Engström (2011a), for normal strength concrete, C12/16- C50/60, the ultimate strain is the same, i.e. $\varepsilon_{cu1} = 0.0035$, while the strain at the maximum stress ε_{c1} has different values for different concrete strength classes. For strength and deformation characteristics for concrete, reader can refer to Eurocode 2, CEN (2004).

The stress-strain relationship for concrete is in fact non-linear from the beginning, but this non-linearity is approximated to be linear when the compressive stress in concrete is smaller than the tensile strength of concrete, i.e. $\sigma_c < f_{ct}$. This means that the material response of reinforced concrete structure is non-linear even if the small load is applied. The behaviour of concrete is weak in tension. As a rule of thumb, the

tensile strength of concrete is 10 times smaller than its compressive strength, but the actual proportion depends on the strength of f_c though. If $\sigma_c > f_{ct}$, stress-strain relationship is no longer linear and the concrete behaves as a plastic material. A permanent deformation remains when the applied load is removed.

2.2.1.2 Reinforcing steel

Figure 2.2 shows a typical stress-strain relationship for hot rolled reinforcing steel and cold worked reinforcing steel.

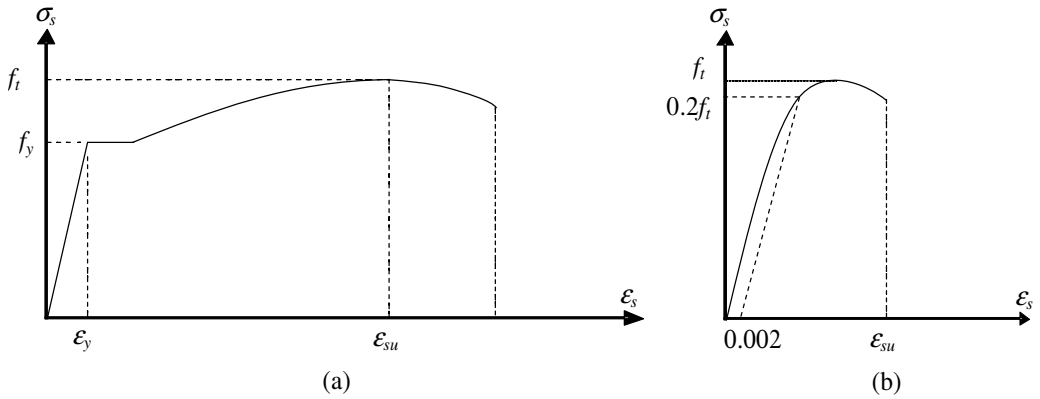

Figure 2.2. Typical stress-strain curve for reinforcing steel (a) hot rolled steel (Class B and Class C steel) (b) cold worked steel (Class A steel).

From Figure 2.2a, it is seen that hot rolled steel (Class B and Class C steel) has a pronounced yield stress, followed by a plastic plateau before strain hardening starts. After yield point, this becomes a plastic material and the strain increases rapidly up to the ultimate value. For cold worked steel (Class A steel) has no distinct yield stress and no plastic plateau, see Figure 2.2b.

Since the ductility of reinforcing steel depends mainly on its elongation at maximum stress, Eurocode 2, CEN (2004) defines the ductility classes with regard to both the ultimate strain and the ratio between tensile strength and yield strength.

Table 2.1. Properties of reinforcement from Eurocode 2, CEN (2004).

Product form	Bars and de-coiled rods		
Class	A	B	C
Characteristic yield strength f_{yk} *or* $f_{0.2k}$ (MPa)	400 to 600		
Minimum value of $k = (f_t/f_y)_k$	≥1.05	≥1.08	≥1.15 <1.35
Characteristic strain at maximum force, ε_{uk} (%)	≥2.5	≥5.0	≥7.5

From Table 2.1 and Figure 2.2, it is seen that Class B and Class C steel are more ductile than Class A steel since the ductility is characterized by the shape of $\sigma(\varepsilon)$, value of ε and ε_{su}.

Eurocode 2, CEN (2004), provides the possibility to analyse reinforced concrete structure with or without taking into account the strain hardening of reinforcement as depicted in Figure 2.3.

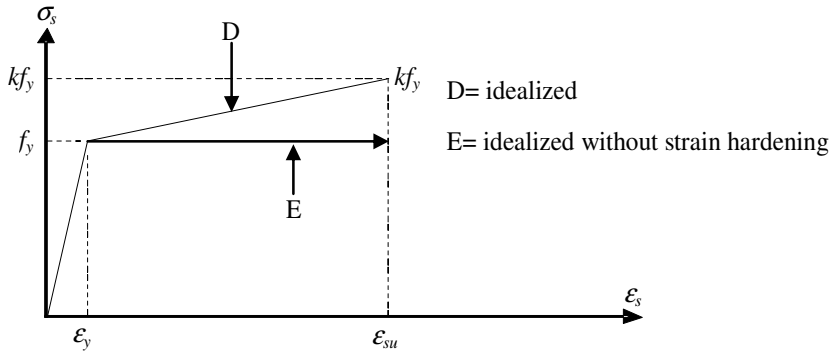

Figure 2.3. Idealised stress-strain diagrams for reinforcing steel (for tension and compression).

2.2.2 Structural response of reinforced concrete members

In concrete structures, the structural response depends on many parameters; e.g. the non-linear nature of the included materials, cracking of concrete and yielding of reinforcement.

When discussing the structural response of reinforced concrete beams it is very essential to understand two terms that are often used: local response and global response. The local response is the structural response of the cross-section determined by the relationship between the moment and the average curvature of the beam cross-section of a small region while the global response is the sum of all regional responses. The curvature χ of the cross-section corresponds to the inclination of deformation ε as shown in Figure 2.4. The relationship between the curvature χ and deformation ε is determined in equation (2-1):

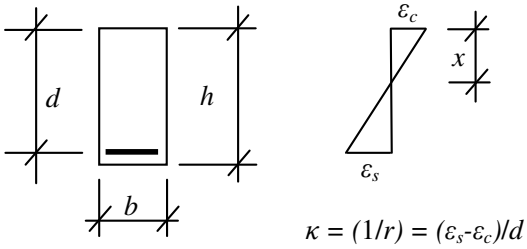

Figure 2.4. Curvature deformation relationship.

$$\chi = \frac{1}{r} = \frac{\varepsilon_s - \varepsilon_c}{d} \tag{2-1}$$

Where χ = curvature
r = radius of curvature
ε_c = concrete strain
ε_s = reinforcement strain
d = effective depth of the cross-section

The behaviour of a reinforced concrete beam can be described by moment-curvature relationship in three different states: state I (or uncracked state), state II (or cracked state) and state III as shown in Figure 2.5 and as described in Eurocode 2, CEN (2004).

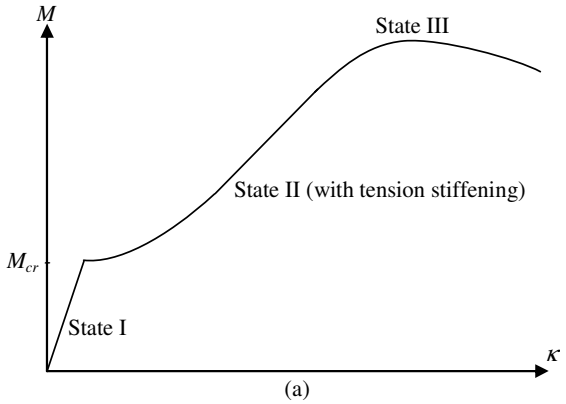

Figure 2.5. Different states of reinforced concrete structure with taking into account tension stiffening effect.

Stresses that varies over the cross-section of reinforced concrete develops when load is applied on the structure. As the load increases, the stress also increases. Theoretically, concrete will not crack when the stress is smaller than the tensile strength of concrete, but in reality there are micro cracks which are formed at local weak points in the material before the tensile strength of concrete is reached and these micro cracks are usually ignored in the design process.

In **State I** or **uncraked state,** the response of reinforced concrete beams is assumed to be linear elastic and the response increases linearly with the applied load. The deformed shape and curvature of the beam remain unchanged while only the magnitude increases proportional to the magnitude of the applied load. The influence of reinforcement is not so important in this state and can often be ignored in most cases, even though a large reinforcement ratio ρ will have non-negligible effect on the uncracked stiffness. The material stress-strain relations follows by the Hooke's law as shown in Figure 2.6 and in equation (2-2) in this state.

$$\sigma = E \cdot \varepsilon \tag{2-2}$$

Where σ = stress

E = Young's modulus
ε = strain.

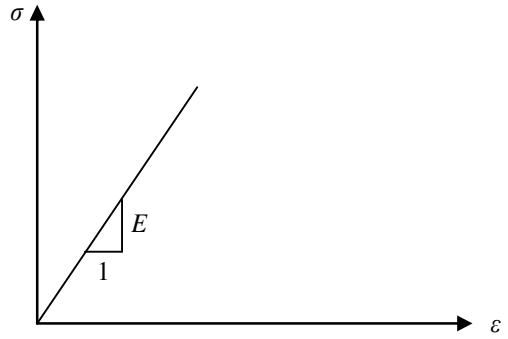

Figure 2.6. Linear stress-strain relationship.

In **state I**, the flexural behaviour of the beam is defined by a moment-curvature relationship shown in Figure 2.7 and in case of pure bending, the moment and curvature relationship is expressed in equation (2-3).

$$\chi = \frac{1}{r} = \frac{M}{EI} \tag{2-3}$$

Where EI = flexural rigidity which is the product of the Young's modulus E and the area moment of inertia I
χ = curvature
r = radius of curvature

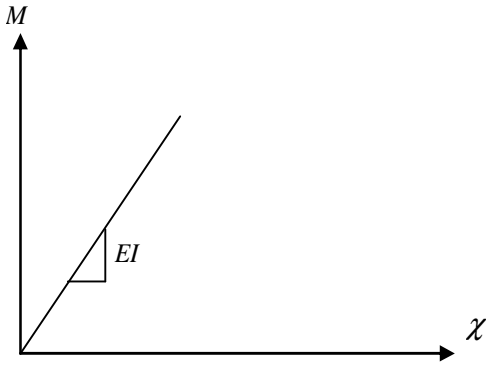

Figure 2.7. Linear moment-curvature relationship.

The behaviour of cracked concrete section is denoted by **state II** or **cracked state**. The load keeps increasing until the stress passes the tensile strength f_{ct} of the concrete. Then the concrete will crack, which will occur in a very early state as its behaviour is weak in tension. There is an abrupt change in stiffness when reinforced concrete section cracks due to bending. As the cracks develop, the stiffness in that region decreases dramatically comparing to the nearby region where the concrete remains uncracked. The uncracked parts in between the cracks will contribute to the stiffness of the reinforced concrete structure. This phenomenon is called the 'tension stiffening effect' When the concrete cracks, the tensile stresses start to develop in the reinforcement bar in the cracked region and are transferred to the surrounding concrete by bond stresses in the bar's interface. This means that the tension stiffening

effect greatly influence the stiffness of reinforced concrete when the concrete first cracks and this influence decreases gradually with regard to the cracks of concrete as shown in Figure 2.5. The stiffer region attracts more forces, which leads to a redistribution of forces and moment due to cracking. This redistribution will be discussed in more details in Chapter 4. In **State II**, the response of reinforced concrete structures is also assumed to be linear elastic when neglecting the effect of tension stiffening and Hooke's law relation in equation (2-2) still holds true in this state. The constant rigidity introduced in state I can be used for the moment which is lower than the cracking moment and constant rigidity introduced in state II can be used for the moment which is in between the cracking moment and the yielding moment where I_I and I_{II} is the moment of inertia of uncracked and cracked section, respectively. Further, E_cI_{II} corresponds to the flexural stiffness of a fully-cracked reinforced concrete section.

Based on Engström (2011a), this calculation model is just fairly true for the steel stress up to the yield point and the compressive strength of concrete is less than about 0.5 f_c. If the compressive stress is higher than this value, it is preferable to analyse the response of a reinforced concrete beam by using a state III model that allows non-linear material response of concrete even if the steel has a linear elastic response.

State III starts when the reinforcement start to yield or the concrete becomes nonlinear in compression in a section where the tensile stresses is larger than the yield stress when the beam is continued to be loaded. However the steel reaches yielding, there is also a possibility to increase the capacity of the section due to either the decreased compression zone as shown in Figure 2.8 or strain hardening of tensile reinforcement. The flexural capacity of the section is assumed to be reached when the reinforcement torn off or the concrete is crushed.

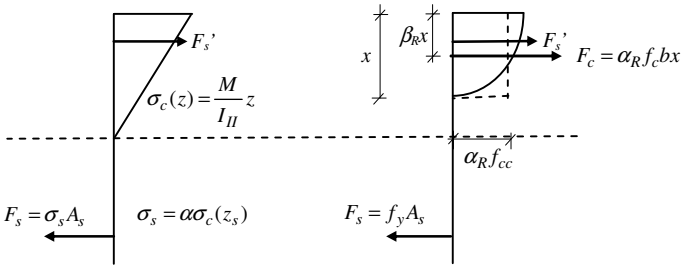

Figure 2.8. Moment capacity increases after the steel reaches yielding due to the decrease of the compression zone.

To summarize, the stress-strain relation and calculation procedures of reinforced concrete beam that correspond to each state mentioned above are described in Figure 2.9.

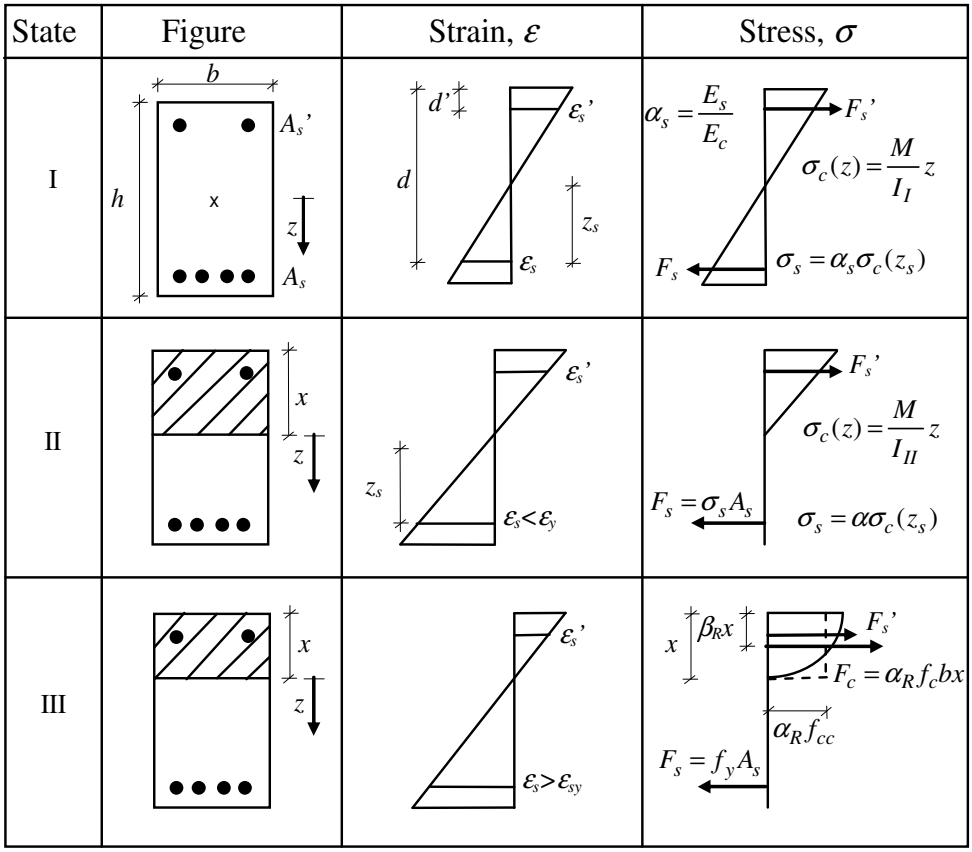

Figure 2.9. The different statges of a concrete section and internal forces.

2.2.3 Theory of plasticity and plastic hinges

After the reinforcement reach yielding, the cross-section is in plastic state and the maximum moment capacity is reached when the concrete crushes or reinforcement torn off. When the ultimate moment capacity is reached, the deformation increases rapidly in the most stressed region. Since this region is small, elements in this region yield and a plastic hinge is formed. For statically determinate structure as shown in Figure 2.10a, a formation of a plastic hinge will lead to collapse of the structure. If a structure is statically indeterminate as illustrated in Figure 2.10b, the yielding of the reinforcement can lead to a local failure if there is insufficient rotation capacity in that plastic region or lead to global failure which means the collapse of the whole structures if many plastic hinges are formed that transforms the structure into mechanism. This means that although the moment capacity of the section is reached in one part of the structure, more loads can be applied: This is due to a plastic redistribution which is the main study for this master thesis report. The number of plastic hinges in a structure can be determined as:

$$n_{hinges} = \mu + 1 \tag{2-4}$$

Where n_{hinges} = number of plastic hinges of the structure

μ = number of statically indeterminacy of the structure

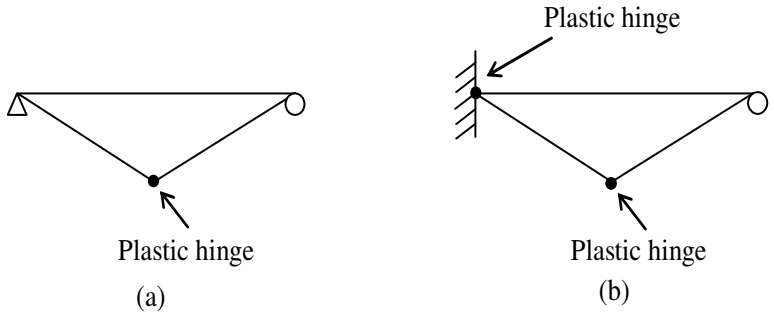

Figure 2.10. A collapse mechanism for (a) statically determinate structure (b) statically indeterminate structure.

2.2.4 Plastic rotation capacity

As described in Section 2.2.3, reinforced concrete members may fail due to local failure or global failure. In order to reach the intended global failure or mechanism, a structure needs to have sufficient plastic rotation capacity otherwise local failure due to the reinforcement being ripped off or the crushing of concrete will take place.

Plastic hinge is assumed to be formed in a section when its moment capacity is reached. Plastic deformation of the structures develop at a constant or higher plastic moment M_{pl} if sufficient rotation capacity of the section is allowed. This is illustrated in Figure 2.11. Such plastic deformation leads to redistribution in the structures, which leads to increased loading until a full mechanism is developed.

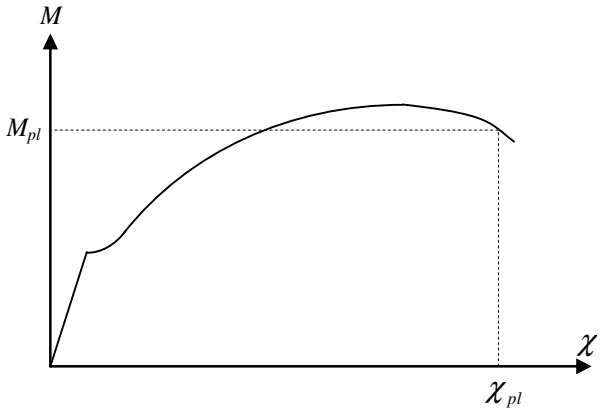

Figure 2.11. Development of plastic deformation after the formation of plastic hinge.

According to Engström (2011a) plastic hinges are assumed to be concentrated in a certain section with no extension along the members in the global structural analysis. In reality, those hinges develop along a certain length l_{pl} in the plastic region where the strain of tensile steel is greater than the yield strain as shown in Figure 2.12. The development of this length l_{pl} depends on reinforcement amount, reinforcement type and concrete strength. The plastic rotation can be found by integrating the plastic curvature over the length l_{pl}. Hence, the plastic rotation is the area below the plastic curvature over the length of plastic hinge. The plastic rotation can be determined using equation (2-5).

$$\theta_{pl} = \int_{x_1}^{x_2} \chi_{pl} dx \tag{2-5}$$

$$l_{pl} = x_1 - x_2 \tag{2-6}$$

$$\chi_{pl} = \chi - \chi_y \tag{2-7}$$

Where θ_{pl} = plastic rotation

χ_{pl} = plastic curvature

χ = curvature

χ_y = yield curvature

l_{pl} = development length of a plastic region

x_1 = section x_1

x_2 = section x_2

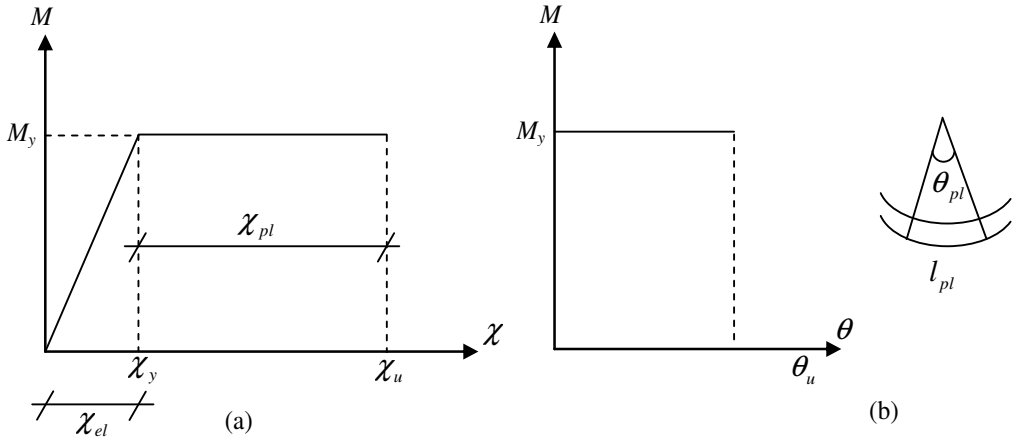

Figure 2.12. (a) moment-curvature relationship (b) plastic rotation develop over length l_{pl}.

Eurocode 2 provides a method to determine the plastic rotation capacity of a section by taking into account certain important parameters including concrete strength, reinforcement class and the ratio between the compressed zone x_u and the effective depth d. The diagram which determines allowable plastic rotation is shown in Figure 2.13 and provides a conservative plastic rotation value.

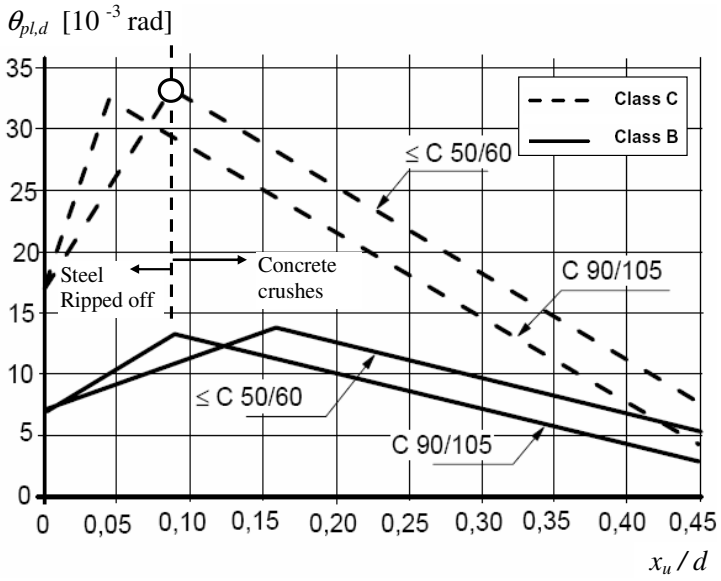

Figure 2.13. Diagram demonstrating the allowable rotation, $\theta_{pl,d}$,of reinforced concrete sections for Class B and C reinforcement from Eurocode 2, CEN (2004). The values apply for the shear slenderness $\lambda = 3$.

The diagram in Figure 2.13 show only the rotation capacity θ_{pl} for reinforcement steel Class B and Class C. Class A steel is not recommended for plastic analysis since it does not provide yielding possibility as shown in Figure 2.2 and Table 2.1 in Section 2.2.1.2. For concrete C55/67 to C90/105, the plastic rotation capacity may be interpolated accordingly. The value of plastic rotation capacity provided in Figure 2.13 is valid only for shear slenderness $\lambda = 3$. For other slenderness values, the plastic rotation capacity needs to modify by a modification factor that depends on the shear slenderness. According to Eurocode 2, CEN (2004), the plastic rotation capacity can be expressed as in equation (2-8).

$$\theta_{rd} = k_\lambda \theta_{pl,d} \tag{2-8}$$

$$k_\lambda = \sqrt{\frac{\lambda}{3}} \tag{2-9}$$

$$\lambda = \frac{l_0}{d} \tag{2-10}$$

Where θ_{rd} = rotation capacity

$\theta_{pl,d}$ = rotation capacity according to Figure 2.13

k_λ = modification factor for rotation capacity

λ = shear slenderness

l_0 = the distance between point of zero and maximum moment after redistribution.

d = effective depth of cross-section

As a simplification, Eurocode 2 provides an estimate L_0 values which is calculated based on design values of the bending moment and shear.

$$L_0 = \frac{M_{Ed}}{V_{Ed} d} \tag{2-11}$$

Where M_{Ed} = design value of bending moment

V_{Ed} = design value of shear

For the left part of the diagram shown in Figure 2.13, the plastic rotation capacity increase when x_u/d increases. It is governed by the ultimate steel strain and the failure of the structures is due to the rip off of the tensile reinforcement. For the right part of the same diagram, it is seen that the plastic rotation capacity decreases with increasing x_u/d value. The failure is due to the crushing of the concrete.

2.2.5 Non-linear response in service limit state, SLS

As mentioned in Section 2.2.1.1, the nature of reinforced concrete structures is non-linear. The structural response in the service limit state can be divided into state I and state II and described by moment-curvature relationship as depicted in Figure 2.14.

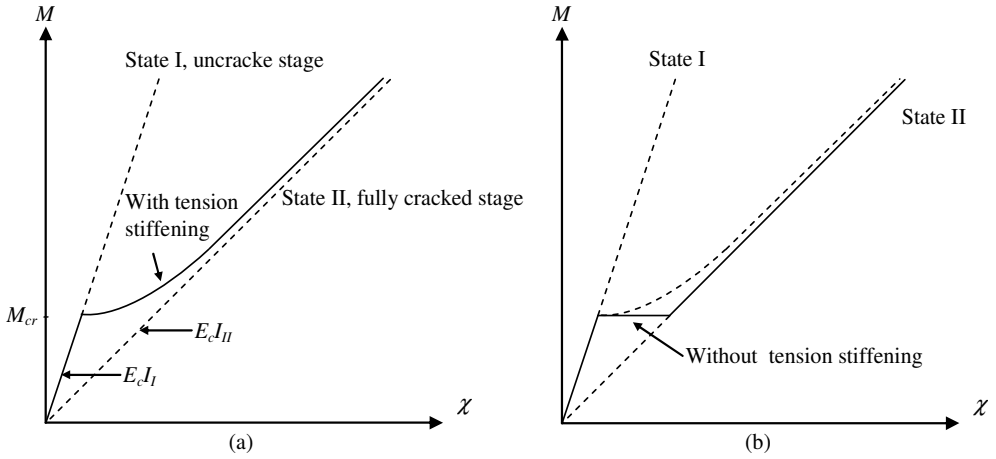

Figure 2.14. Non-linear response of concrete members under pure bending described using moment curvature diagram with the assumption of linear stress-strain relationship: (a) with tension stiffening (b) without tension stiffening.

When the design moment is smaller than the cracking moment, state I model can be used to predict the uncracked behaviour of reinforced concrete structure and state I stiffness is used.

When the cracks start to develop, a state II model can be used to simulate the response of a cracked section. As a simplification, this model uses stiffness of state II, fully cracked section, without taking into account the tension stiffening effect. This model describes the response of the cracked section well, but not the surrounding region as concrete between the cracks contributes to the stiffness of the structure. This means that the curvatures of the cracked section are larger than the curvature of the surrounding region. Hence, this model overestimates the overall deformation of reinforced concrete structure.

When the concrete cracks, the stiffness at those point changes rapidly, see Figure 2.14. The flexural stiffnesses of uncracked and cracked sections are denoted E_cI_I and E_cI_{II} respectively where E_c is the secant modulus of elasticity of concrete, and I_I and I_{II} are moment of inertia of uncracked section and cracked section, respectively.

2.2.6 Non-linear response in ultimate limit state ULS

The moment-curvature relationship described in this section is aimed for non-linear analysis in the ultimate state. As described in Section 2.2.2, in plastic state, the moment capacity has the possibility to slightly increase either due to the decreased compression zone or due to the ultimate strain in the tensile reinforcement until the failure of the Section takes place either by the crush of the concrete or the rip off of the reinforcement.

As non-linear analysis in ultimate limit state is performed in order to check the rotation capacity of the section, it is possible to simplify the non-linear moment-curvature relationship to a bilinear or multilinear moment curvature relationship with or without taking into account the tension stiffening effect as depicted in Figure 2.15. Since the tension stiffening effect help decrease the plastic rotation of the section, it is on the safe-side to ignore this effect.

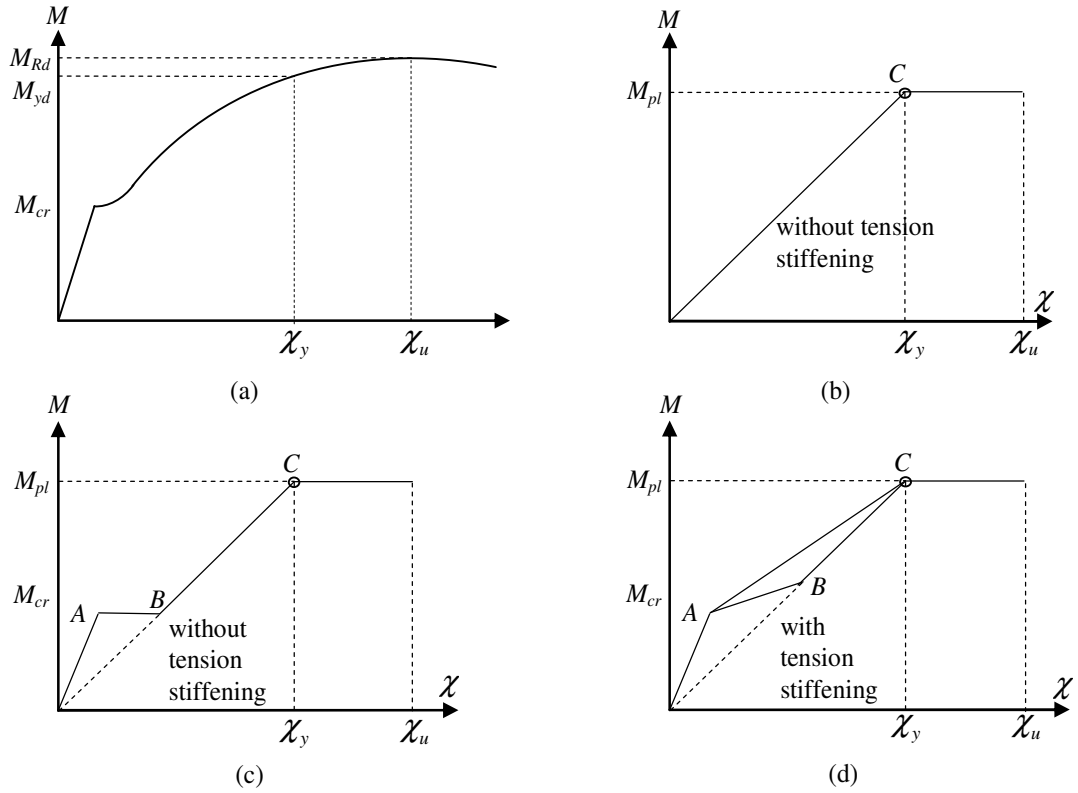

Figure 2.15. Moment-curvature relationship in ultimate limit state (a) true response (b) simplified bilinear without tension stiffening (c)simplified multilinear without tension stiffening (d) simplified multilinear with tension stiffening.

In Figure 2.15, the non-linear behaviour of the reinforced concrete structure before the reinforcement reaches yielding is modelled by a straight line. This straight line ends at a breakpoint where the yielding of the tensile reinforcement starts and its slope represent a simplified flexural rigidity of the cross-section in ultimate limit state before yielding. The yielding part of the tensile reinforcement is also modelled by a straight line. The slope of the latter indicates the flexural stiffness of the structures after yielding. There is a sharp loss of stiffness when the tensile reinforcement reaches yielding and the breakpoint between state II and state III can be seen clearly, see Figure 2.15. Concerning how to determine the values of specific points *A*, *B* and *C* in Figure 2.15, readers can refer to Chapter 4.

The simplified moment-curvature relationship of reinforced concrete structure subjected to pure bending is calculated from idealized stress-strain relation with the basis of design values of material properties, but with mean values of moduli of elasticity. In case of the design with regard to second order effect like slender column, the response of the structures is determined by using not only the design values of material strength but also the design values of moduli of elasticity according to Engström (2011a).

2.3 Beams

2.3.1 Introduction

A structural members is defined according to Eurocode 2, CEN (2004), as a beam if the span to depth ratio is greater than 3 and the width is less than 5 times the depth of the member. If the span is less, the member is considered as a 'deep beam'. According to Engström (2011a), beams are linear structural members that are predominantly loaded in flexure. Although the responses of the beams is mainly governed by flexural behaviour and the shear deformation can be ignored, the design of the reinforced concrete beam against both bending and shear is very essential and cannot be overlooked.

2.3.2 Global methods for the response of a reinforced concrete beam

There are four methods to design the reinforced concrete structures according to Eurocode 2, CEN (2004):

1) Linear elastic analysis which is based on the theory of elasticity and can be used for both service limit state (SLS) and ultimate limit state (ULS).
2) Linear elastic analysis with limited redistribution which is used to analyse the structural members for the verification of ULS. It is recommended to redistribute the elastic bending moment in such a way that the rotation capacity fulfils the condition as stated in Section 2.3.4.
3) Plastic analysis is aimed for ULS. It is based either on lower bound (static) method or on upper bound (kinematic) approach described in Section 2.3.5.
4) Non-linear analysis can be used for both ULS and SLS provided that equilibrium and compatibility condition are satisfied and appropriate non-

linear material is assumed. An effective modelling is to use non-linear moment curvature relationship that capture cracking of concrete, tension stiffening effect, yielding of reinforcement and strain hardening of steel. An even more detail and advanced approach is to use finite element method by considering the three dimensional behaviour of concrete in compression and fracture mechanics.

2.3.3 Simplified linear elastic analysis

Simplified linear elastic analysis is very common to be used for the design of reinforced concrete structures. In this method, the flexural rigidities of the Section are determined based on the gross concrete sections. This method predicts the behaviour of uncracked concrete neglecting the influence of reinforcement. Hence, it is not possible to describe the behaviour of reinforced concrete due to cracking and yielding. The response is linear elastic and the stress-strain relationship follows the Hooke's law as shown in Figure 2.6 and in equation (2-2). In case of pure bending, the flexural behaviour of the beam is defined by "moment-curvature relationship' depicted in Figure 2.7 and in equation (2-3).

Although the simplified linear elastic analysis assumes the linear elastic response of reinforced concrete structures, the nature of reinforced concrete structure is non-linear in reality. Hence, it is very important to be able to judge if the model used to describe the non-linear response of the structure is good enough to imitate its real behaviour. When the reinforcement reaches yielding and the load increases further, plastic hinges are formed and therefore, a plastic redistribution may form in the structures if enough rotation capacity is provided. Although there is a rotation of the section, there is no need to check the rotation capacity at that Section as the deformation will be small in this simplified linear elastic model. In a real structure even though the design is based on simplified linear elastic, plastic hinges will be formed under certain load level. However, in order to meet the requirement of the ductility needed, Eurocode 2, CEN (2004), provided the following conditions stated in equation (2-12) and (2-13) for the verification of the rotation capacity of the continuous reinforced concrete beams or slabs where plastic hinges are expected to be formed. It should be noted that the conditions in equation (2-12) and (2-13) do not apply for the cantilever slab studied in Chapter 4. According to Engström (2011a), the limitations in equation (2-12) and (2-13) should be given in the linear elastic analysis Section as a certain amount of plastic redistribution will take place in real structures even though the design is based on linear elastic analysis.

$$\frac{x_u}{d} \leq 0.45 \qquad \text{for concrete grades C12/15 to C50/60} \qquad (2\text{-}12)$$

$$\frac{x_u}{d} \leq 0.35 \qquad \text{for concrete grades C55/67 or greater} \qquad (2\text{-}13)$$

Where x_u = height of the compressive zone in ultimate limit state
d = effective depth of the section

2.3.4 Simplified linear elastic analysis with limited redistribution

In reality, there are various load combinations on the structures that will result in different moment distribution, which means that critical sections of the structures will vary depending on the different load combinations. This results in different needs of reinforcement along the structure. Moreover, linear elastic analysis produces peak moment values. In order to reduce the peak moment and simplify the reinforcement arrangement for practical use, it is possible to determine the amount of moment that can be reduced from linear elastic analysis in an efficient way and still meet the ductility requirement of the structure. This method is used for ultimate limit state (ULS) as it is based on the redistribution from a certain amount of moment computed from linear elastic analysis. This analysis is able to simulate the moment distribution due to yielding. Based on theory of plasticity in Section 2.2.3, it is possible to choose a moment distribution that fulfils the equilibrium as there is a plastic redistribution in the real reinforced concrete structures when the reinforcement yields. Although the chosen reduced moment distribution causes a certain plastic rotation of the cross-section of the structure, it is not necessary to check the plastic deformation of the structure if the requirements mentioned in Eurocode 2, CEN (2004), for this type of analysis are fulfilled. According to Eurocode 2, for continuous beams or slabs that are predominantly subjected to bending and have the ratio of the lengths of adjacent spans in the range 0.5 to 2, the redistribution of bending moments may be carried out without the check of the rotation capacity if the following conditions are fulfilled

$$\delta \geq k_1 + k_2 \frac{x_u}{d} \qquad \text{for concrete grades C12/15 to C50/60} \tag{2-14}$$

$$\delta \geq k_3 + k_4 \frac{x_u}{d} \qquad \text{for concrete grades C55/67 and greater} \tag{2-15}$$

$$\delta \geq k_5 \qquad \text{for Class B and Class C reinforcement} \tag{2-16}$$

$$\delta \geq k_6 \qquad \text{for Class A reinforcement} \tag{2-17}$$

The recommended value for k_1, k_2, k_3, k_4, k_5 and k_6 are:

$$k_1 = 0.44 \tag{2-18}$$

$$k_2 = 1.25 \cdot (0.6 + \frac{0.0014}{\varepsilon_{cu2}}) \tag{2-19}$$

$$k_3 = 0.54 \tag{2-20}$$

$$k_4 = 1.25(0.6 + \frac{0.0014}{\varepsilon_{cu2}}) \tag{2-21}$$

$$k_5 = 0.7 \tag{2-22}$$

$$k_6 = 0.8 \tag{2-23}$$

Where $\delta =$ ratio of the redistributed chosen moment to the elastic bending moment

$x_u =$ height of the compressive zone in ultimate limit state after redistribution

$\varepsilon_{cu2} =$ the ultimate strain according to Table 3.1 Eurocode 2, CEN (2004)

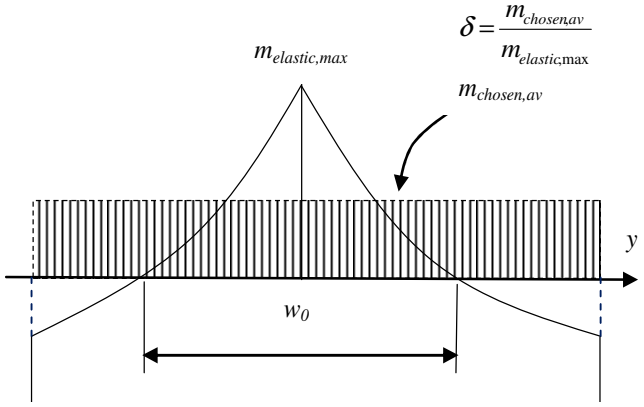

Figure 2.16. Ratio of the redistributed chosen moment to the linear elastic bending moment.

2.3.5 Plastic analysis

Plastic analysis can be used for the design in ultimate limit state and it is convenient for the preliminary design. This method is based on theory of plasticity as described in 2.2.3 with the assumption that the behaviour of a reinforced concrete beam is ideally plastic when the yield capacity is reached and there is no deformation limit as shown in Figure 2.17.

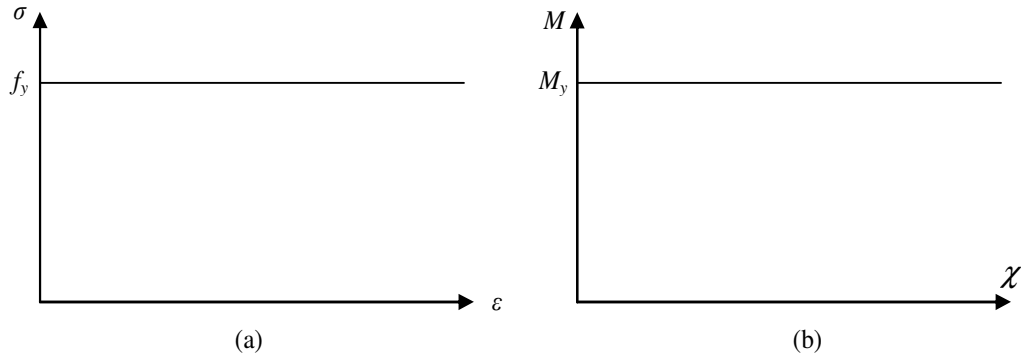

Figure 2.17. Idealized-plastic (a) material response, stress-strain relationship (b) structural response, moment-curvature relationship.

This method is either based on static method (lower bound approach) so-called strut-and-tie method or kinematic method (upper bound approach) so-called yield line method.

The static method provides a solution with a lower bound value. In this analysis, many possible moment redistributions that fulfil the equilibrium condition can be chosen. In the real structures though, there may be moment redistribution that is redistributed in a more efficient way than the one assumed in the design, but the latter at least made sure that it is possible to carry the load in one way. It means that the moment capacity of the structures is equal to or greater than the calculated values obtained from the assumption of the designers. Accordingly, the structures can probably resist higher loads than expected. That's also why the lower bound approach is on the safe-side and is preferred in the design.

The kinematic method gives an upper bound solution. It is necessary to assume many possible collapse mechanisms of the structures in order to find the most dangerous one. It means that expected plastic hinges are chosen in such a way that the selected plastic hinges are close to those that are formed in real structure and this will lead to the solution that converges to the real solution. In reality, it is not always easy to find the most critical mechanism; the calculated moment capacity based on the chosen plastic hinges will not be able to fully resist the design loads. That is why upper approach is a method in the unsafe-side that is not recommended in the design. The boundary between the static method and kinematic method is the real plastic solution.

The plastic analysis is used for very ductile members as it simulates the behaviour of reinforced concrete structures just before the collapse mechanisms are formed. This can be achieved if there is enough ductility of the critical sections. Based on Eurocode 2, CEN (2004), for continuous beams or slabs, the required ductility are satisfied without rotation capacity check if all the following conditions are fulfilled. It should be noted that the following conditions do not apply for the studied cantilever slab in Chapter 4.

1. The area of tensile reinforcement in critical section is limited so that

$$\frac{x_u}{d} \le 0.15 \qquad \text{for concrete grades C12/15 to C50/60} \qquad (2\text{-}24)$$

$$\frac{x_u}{d} \le 0.15 \qquad \text{for concrete grades C55/67 and greater} \qquad (2\text{-}25)$$

2. Reinforcing steel is either Class B or C
3. The ratio between moments at intermediate supports and spans should be

$$0.5 \le \frac{\left|M_{\sup port}\right|}{\left|M_{span}\right|} \le 2 \qquad (2\text{-}26)$$

2.3.6 Shear

Concrete structures subjected to loads will produce both bending moment and shear forces. The combination between bending moment and shear forces causes cracks in a

reinforced concrete beam if stresses resulting from these forces exceed the tensile strength of concrete at any points in the beam. Figure 2.18 shows a crack pattern of a simply supported beam subjected to uniformly distributed load. The crack at the mid-span of the beam is due to bending while the cracks at the support are due to shear and cracks which are located in between the mid-span and support are due to the combination between bending and shear forces. The shear failure is due to the shear sliding in the crack or the crushing of concrete and is often brittle

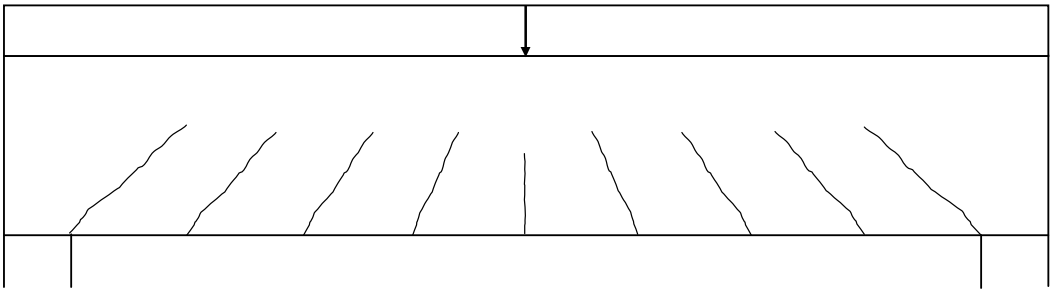

Figure 2.18. Cracking pattern of a simply supported reinforced concrete beam under uniformly distributed load.

The concrete can resist shear by a combination of the uncracked concrete in the compression zone, the dowelling action of the bending reinforcement and aggregate interlock across tension cracks according to Molsey *et al.*(2007). Reader can refer to Eurocode 2, CEN (2004) for the strength of sections without shear reinforcement.

If the shear capacity provided by the members without shear reinforcement is not sufficient to carry the design shear load, it is necessary to use shear reinforcement so called stirrups or transverse reinforcement. The shear reinforcement contributes significantly to the shear capacity as the stirrups need to yield before the shear sliding failure take places. In this case, the requirement of concrete strength to avoid the crushing of concrete needs to be fulfilled as the increase in shear capacity due to stirrups results in the risk of the crushing of concrete. The concrete is subjected to higher compression force in order to keep the equilibrium due to the vertical forces from the stirrups.

The most common type of shear reinforcement is stirrups that are normally placed vertically perpendicular to the main tensile reinforcement as illustrated in Figure 2.19a. The cracks due to the shear are inclined cracks. The most efficient way to deal with those cracks is to place shear reinforcement perpendicular to those cracks. This means that inclined shear reinforcement like in Figure 2.19b will be mounted. For practical reason, it is difficult to install the inclined reinforcement even though it contributes better to the shear capacity and vertical stirrups are normally used instead in reality.

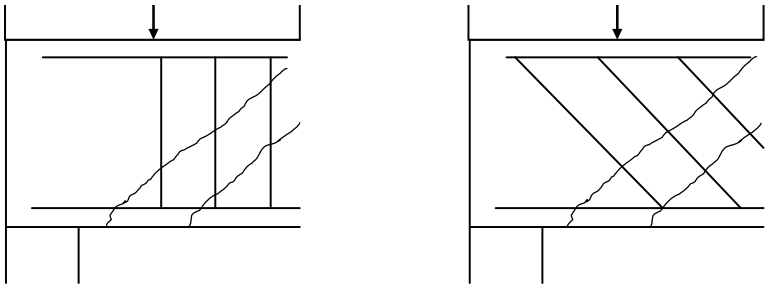

Figure 2.19. Alternative arrangements of shear reinforcement in reinforced concrete beam (a) vertical shear reinforcement mounted perpendicular to the main tensile reinforcement (b) inclined shear reinforcement placed perpendicular to the cracks.

Reader can refer to Eurocode 2, CEN (2004) for the shear resistance for members with vertical shear reinforcement and inclined shear reinforcement.

2.4 Slabs

2.4.1 Introduction

The slab is the main study of this thesis report. Slabs are different from beams since the transverse action is needed to be considered due to the larger width compare to the height.

Eurocode 2, CEN (2004), defines a slab as a structural member for which the minimum panel dimension is not less than 5 times the overall thickness. Slabs are classified into different categories by consideration of their functions and support conditions. Reinforced concrete slabs are in Eurocode 2 classified as either slabs or flat slabs. According to Engström (2011b) the slab is defined as flat slab if one of the supports is a column; otherwise it is classified as just a slab. Slabs are only supported by line supports or along its edges including beam-supported slab and wall-supported slab. It is not necessary for slab to be supported all along its edges. Figure 2.20 demonstrates flat slabs and slabs with various support conditions.

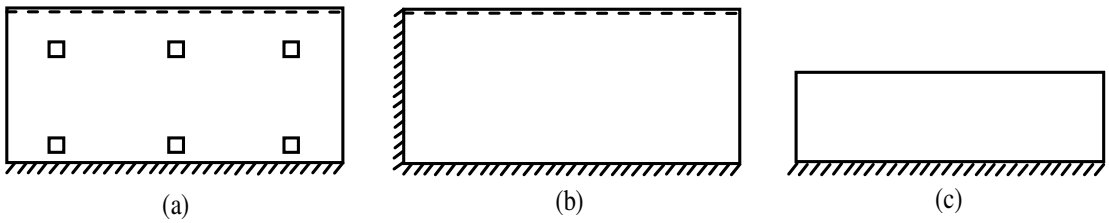

Figure 2.20. Slabs with various support conditions: (a) flat slabs supported by columns, wall and beam (b) slab supported along three edges (c) cantilever slab.

Slabs can carry the load in one or two directions. If the slab carries the load in one direction, it is called one way slab; otherwise it is called a two way slab, Engström (2011b). Eurocode 2, CEN (2004), distinguishes between one-way and two-way spanning slabs as following:

"A slab subjected to dominantly uniformly distributed loads may be considered to be one-way spanning if either:

- *It possesses two free (unsupported) and sensibly parallele edges or*
- *It is the cntral part of a sensibly rectangular slab supported on four edges with a ration of the longer to shorter span greater than 2".*

According to Pacoste *et al*. (2012), the definitions provided by Eurocode 2, CEN (2004), are not always directly applicable, especially for the case of slabs in bridges. Bridge slabs are normally supported by both line and point supports or by point supports that are arranged in rows that provide much larger spans in one direction compared to the other. Based on this, Pacoste *et al*. (2012), instead chose to classify slabs in three categories two-way, one-way and predominantly one-way spanning slabs as depicted in Figure 2.13. Figure 2.21a shows a slab supported by two rows of columns at support lines S_4 and S_5 and by bearings at support lines S_1, S_2 and S_3. As the distances between different supports in different directions have approximately the same magnitude, this slab is considered as a two-way spanning slab.

The slab in Figure 2.21b has line supports in lines S_1, S_2 and S_3 in the *y*-direction and two free edges E_1 and E_2 along the *x*-direction. This slab is treated as a one-way spanning slab. The geometry of the slab shown in Figure 2.21c is typical for many bridge slabs. It possesses point supports with a short distance (S_1, S_2, S_3) along the *y*-direction and point supports with a long distance (Edge *E1*, *E2*, *E3*) along the *x*-direction. The geometry of this type of slab is in between the extreme cases shown in Figure 2.21a and Figure 2.21b. For example, if a load is applied in between the columns along lines S_1, S_2 and S_3, the load will transfer to the nearest columns in the *y*-direction. However, if the load is applied in the field, the load will distribute in both in the *x*-direction and *y*-direction, but mainly in the *x*-direction. That's also why the slab illustrated in Figure 2.21c is denoted as a predominantly one-way spanning slab.

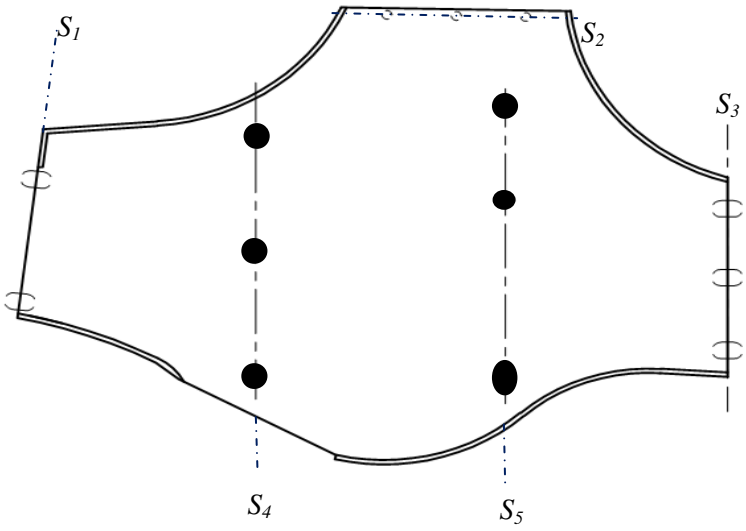

(a)

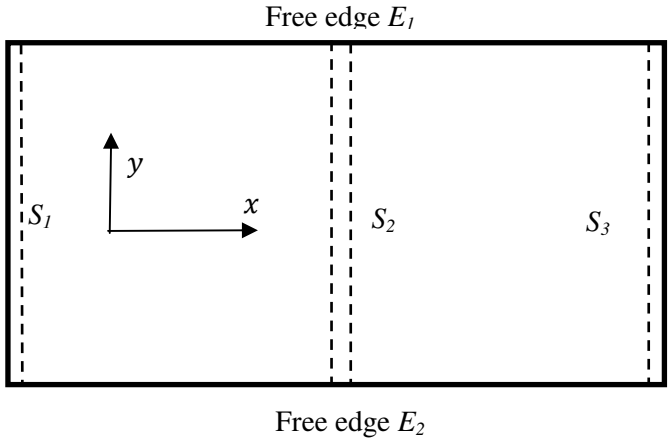

(b)

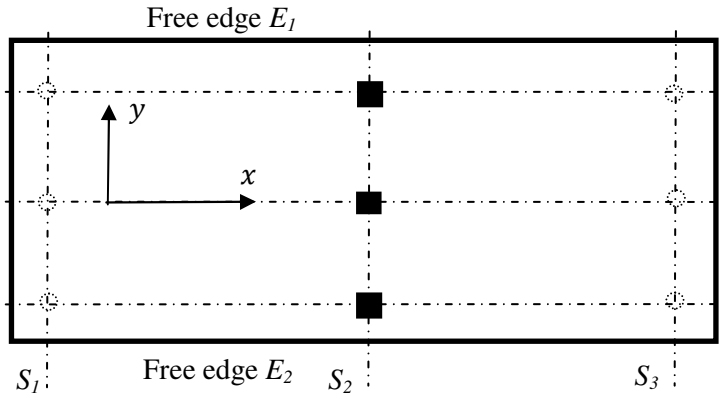

(c)

Figure 2.21. Different types of slabs due to load distribution: (a) two-way spanning slab (b) one-way spanning slab (c) predominantly one-way spanning slab. From Pacoste et al. (2012).

The analysis of a slab is normally a statically indeterminate problem. In some cases though, as illustrated in Figure 2.22, the problem is statically determinate. The structural response of one-way slabs shown in Figure 2.22 is similar to that of a beam

and can be conceptually designed as a beam per unit width. This argument is verified by the FE analysis using FE program ADINA.

However there are tables and diagrams that can be used for the design for typical two way slabs, a more complex two way slab require 3-D analysis in order to capture the load distribution in different direction and get a more accurate result.

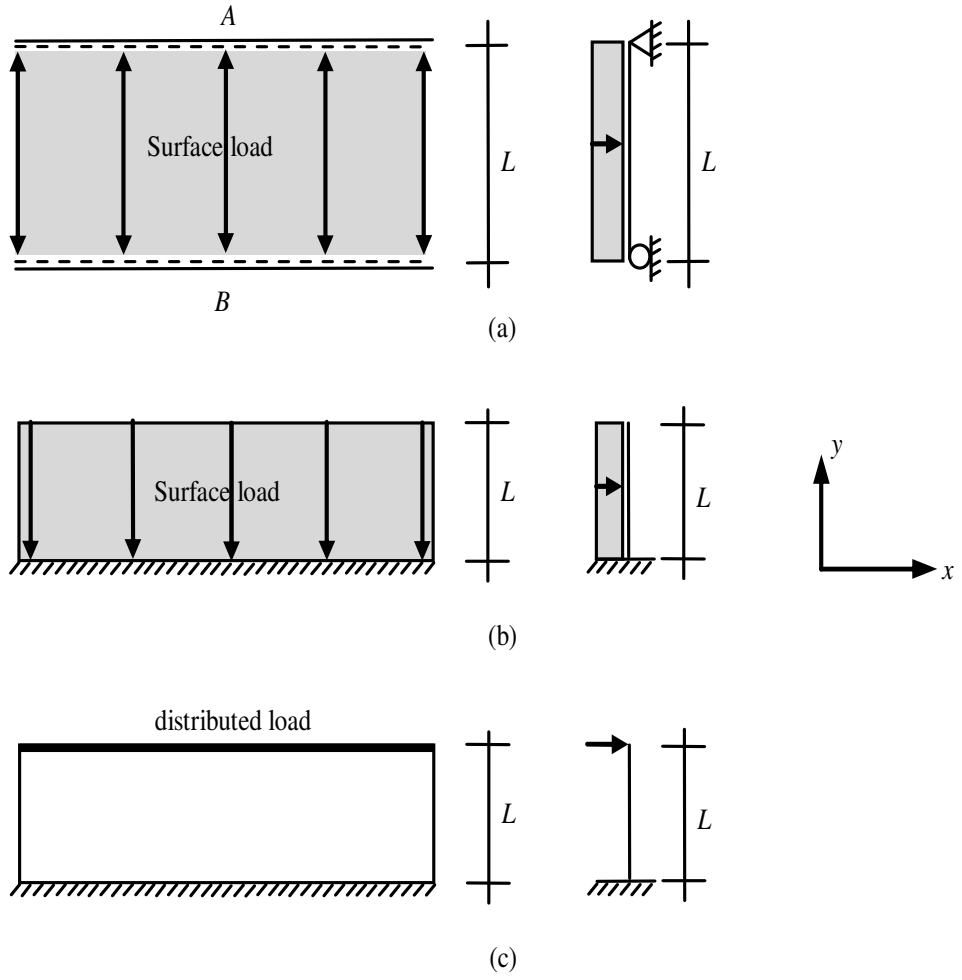

Figure 2.22. One-way slab action: (a) one-way simply supported slab under surface load (b) cantilever slab surface loads. (b) cantilever slab under distributed line loads.

Eventhough the slabs shown in Figure 2.22 can be designed as a beam per unit width, this approach cannot be applied if the same slab is subjected to a point load located in different positions of the slab. This means that various load types located in different positions on this cantilever slab will result in different load distributions. For instance, the point load applied in the middle of the one-way simply supported slab, as shown in Figure 2.23a, and the point load applied in the middle of free edge of the slab in Figure 2.23b is carried mainly in the transversal direction, but this load also distributes in the longitudinal direction. The response of the load distribution in different directions is very essential. The recommendation of cantilever slabs will be given separately from one-way and two-way spanning slabs and will be discussed in more detail in Section 2.4.10.1 and in Section 2.4.10.2, respectively.

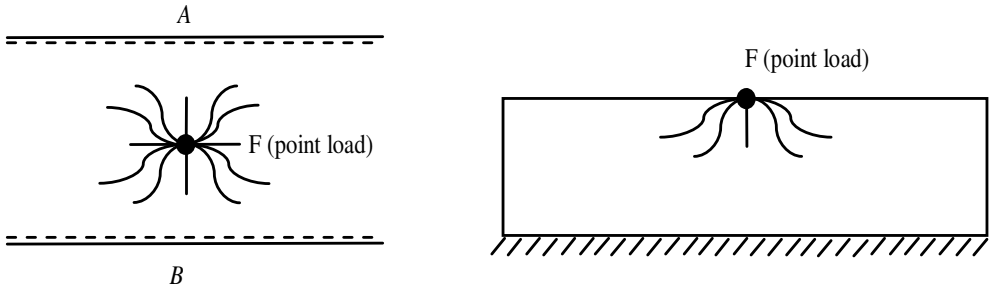

Figure 2.23. Load distribution of a slab (a) cantilever slab subjected to point load (b) one-way simply supported slab cantilever.

2.4.2 Definition

In a slab, the sectional forces are normally expressed per unit width of 1.0 m. In this report, a capital letter is used for concentrated forces while a small letter is used for forces per unit width. For example, the notation M [Nm] is used for concentrated moment whereas the notation m [Nm/m] is used for moment per unit width. When talking about slabs, it is very important to introduce coordinate system x,y and the moment per unit width of the slab in different directions. In this report, the bending moment that deflects strips in x-direction is denoted m_x and the bending moment that deflects strips in y-direction is denoted m_y. Figure 2.24 shows the notation of moment per unit width of a slab.

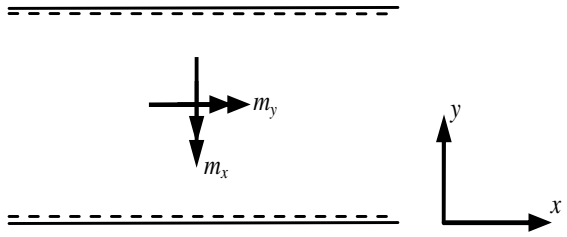

Figure 2.24. Definition of the bending moments m_x and m_y in a slab.

2.4.3 Alternative methods for slab analysis

The four methods described in Section 2.3.2 can be used to analyses a slab.

In linear elastic analysis, the slab is assumed to have a homogenous material which has a linear behaviour in sectional response and moment-curvature. In linear elastic analysis, the deformation shape and moment shape are constant and only their magnitudes are increased proportional to the increased load. It means that there is only one unique combination of m_x and m_y and torsional moment m_{xy} and m_{yx} that is found to resist a small element of load.

For linear elastic analysis with limited distribution, the moment is first calculated from linear elastic analysis and then the reduced moment is chosen due to the plastic redistribution capacity. The conditions provided by Eurocode 2, CEN (2004), about the check of rotation capacity of continuous beams or slabs in the longitudinal direction in equation (2-14) to equation (2-17) in Section 2.3.4 apply in this case also.

Concerning plastic analysis of a slab, two methods are usually adopted. The 'strip method', which assumes a moment distribution, is a lower bound approach and the 'yield line' method assuming a collapse mechanism of the structure provides an upper bound solution. The strip method and yield line method will be discussed in detail in Section 2.4.5 and Section 2.4.6 respectively.

Non-linear analysis can capture the non-linear response of reinforced concrete slabs from uncracked state to the failure of the structures. The non-linear response can be described by moment-curvature relationship depicted in Figure 2.14 and in Figure 2.15 in Section 2.2.5 by changing notation *M* (concentrated moment) to notation *m* (moment per unit width) in the diagram. This is valid for a slab with beam grillage model in Figure 4.7 but not necessarily for a slab with shell model in which m_{xy} will also be present.

2.4.4 Design based on linear elastic analysis

Linear elastic analysis of slabs can be based on Mindlin plate theory or Kirchhoff's plate theory. Kirchhoff's plate theory is often used and the assumptions used are that the material has a linear stress-strain relation and the middle plane of the slab remains plane; i.e. no stress develops perpendicular to the slab when loaded and the shear deformation is ignored. The stress-strain relationship and the moment and deflection relationship of a small slab element are expressed in equation (2-27) and (2-28) respectively.

$$\begin{bmatrix} \sigma_x \\ \sigma_y \\ \tau_{xy} \end{bmatrix} = \frac{E}{1-\upsilon^2} \begin{bmatrix} 1 & \upsilon & 0 \\ \upsilon & 1 & 0 \\ 0 & 0 & \frac{1-\upsilon}{2} \end{bmatrix} \begin{bmatrix} \varepsilon_x \\ \varepsilon_y \\ \gamma_{xy} \end{bmatrix} \tag{2-27}$$

$$\begin{bmatrix} m_x \\ m_y \\ m_{xy} \end{bmatrix} = -D \begin{bmatrix} \frac{\partial^2}{\partial x^2} + \upsilon \frac{\partial^2}{\partial y^2} \\ \upsilon \frac{\partial^2}{\partial x^2} + \frac{\partial^2}{\partial y^2} \\ (1-\upsilon) \frac{\partial^2}{\partial x \partial y} \end{bmatrix} u \tag{2-28}$$

Where $D = \frac{Eh^3}{12(1-\upsilon^2)}$ slab stiffness

υ = Poisson's ratio

u = deflection

h = slab thickness

The slab equation that relates the vertical displacement u_z to the applied distributed load q is given in equation (2-29).

$$\frac{\partial^4 u}{\partial x^4} + \frac{\partial^4 u}{\partial y^4} + 2\frac{\partial^4 u}{\partial_x^2 \partial_y^2} = \frac{q}{D} \tag{2-29}$$

Although the linear elastic analysis assumed linear material response, the nature of the reinforced concrete slab is non-linear and it possesses plastic parts in ultimate limit state. Based on the theory of plasticity, it is possible to find a different combination of m_x and m_y and torsional moment m_{xy} and m_{yx} and shear force v_x and v_y that can keep equilibrium in a small element of the slab subjected to the same applied load.

In the reinforced concrete slab, it is difficult to design and arrange reinforcement exactly according to the linear elastic solution and the torsional moments cannot be resisted effectively by reinforcement bars. Therefore, for a practical reason, the bars are instead arranged in two perpendicular directions x and y. In order to do so, it is necessary to transform the linear elastic solution to resisting bending moments m_{rx} and m_{ry} in these two perpendicular directions.

The reinforcement moment m_{rx} and m_{ry} for design of reinforcement in two perpendicular directions x and y are expressed in equation (2-30) and (2-31) respectively.

$$m_{rx,pos(neg)} = m_x \pm \mu \left| m_{xy} \right| \tag{2-30}$$

$$m_{ry,pos(neg)} = m_y \pm \mu \left| m_{xy} \right| \tag{2-31}$$

Where m_{rx} reinforcement moment for design of reinforcement in perpendicular direction x

m_{ry} reinforcement moment for design of reinforcement in perpendicular direction y

m_x linear bending moment in x-direction

m_y linear bending moment in y-direction

m_{xy} linear torsional moment

μ factor that can be chosen with respect to practical considerations, usually close to 1.0 or equal to 1.0

2.4.5 Strip method

Based on Engström (2011b), the strip method is a static method that provides lower bound solutions when performing plastic analysis of reinforced concrete slabs. A moment distribution is chosen so that the equilibrium condition in ultimate limit state (ULS) is fulfilled. According to Engström (2011b), the following steps are performed in the strip method:

- Torsional moment are chosen $m_{xy} = - m_{yx} = 0$
- Slab is divided in strips in the main x-and y-direction
- The load on an element is distributed between the two strips in x- and y-direction
- Each strip is designed for one-way action

It is important to note that the sum of the loads carried in two strips in *x*- and *y*-direction must be equal to the total load acting on the considered element.

As mentioned in Section 2.4.4, theory of plasticity provides the possibility for the designer to choose a set of m_x and m_y and torsional moment m_{xy} and m_{yx} that fulfil equilibrium in ultimate limit state. It means that strips can be chosen in various ways which will result in various load distribution. This can be examined by studying a rectangular slab supported along four edges with a uniformly distributed load q as shown in Figure 2.25.

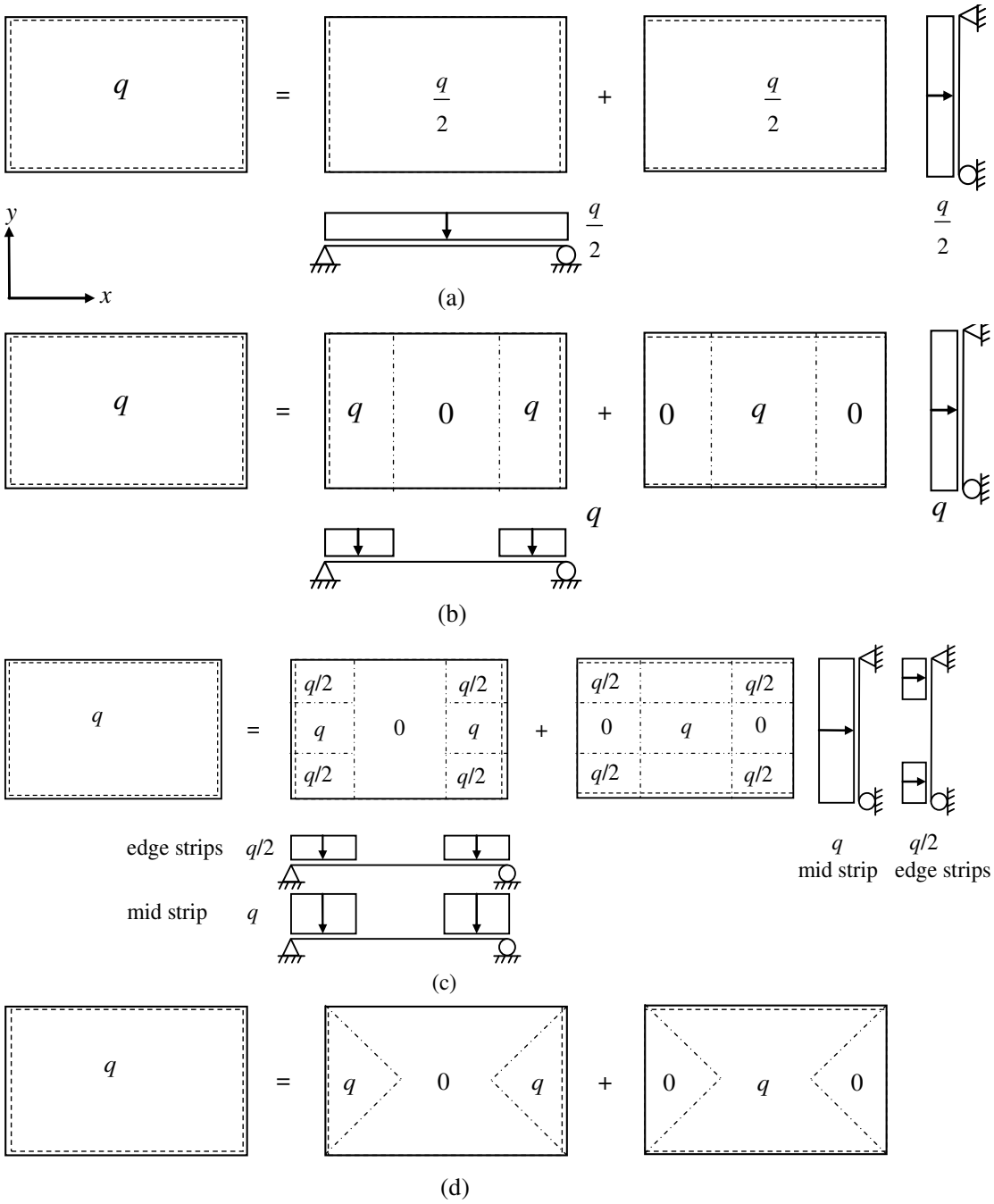

Figure 2.25. Load distribution: (a) half the load in each direction (b) load is carried shorter way to support (c) load distribution at corner region is improved (c) load distribution follows the natural load dividing lines. From Engström (2011b).

In Figure 2.25a, half of the load is taken in each direction. This load distribution is strange since the long direction carries much of the load. In Figure 2.25b, some loads are carried by support nearby while much of the load is carried in short direction. It is still strange since the load is carried only in $\underline{x}$-direction at the corner. The solution is improved as the load is distributed into equal amount in both $\underline{x}$-and y-direction at the corner region, see Figure 2.25c. From Figure 2.25d, it is seen that the load is distributed due to the load dividing lines which intersect the corner region. These load dividing lines separate parts of the slab and there is no shear forces acting along this cut. Since various load distribution can be chosen, this will result in different reinforcement arrangement as illustrated in Figure 2.26.

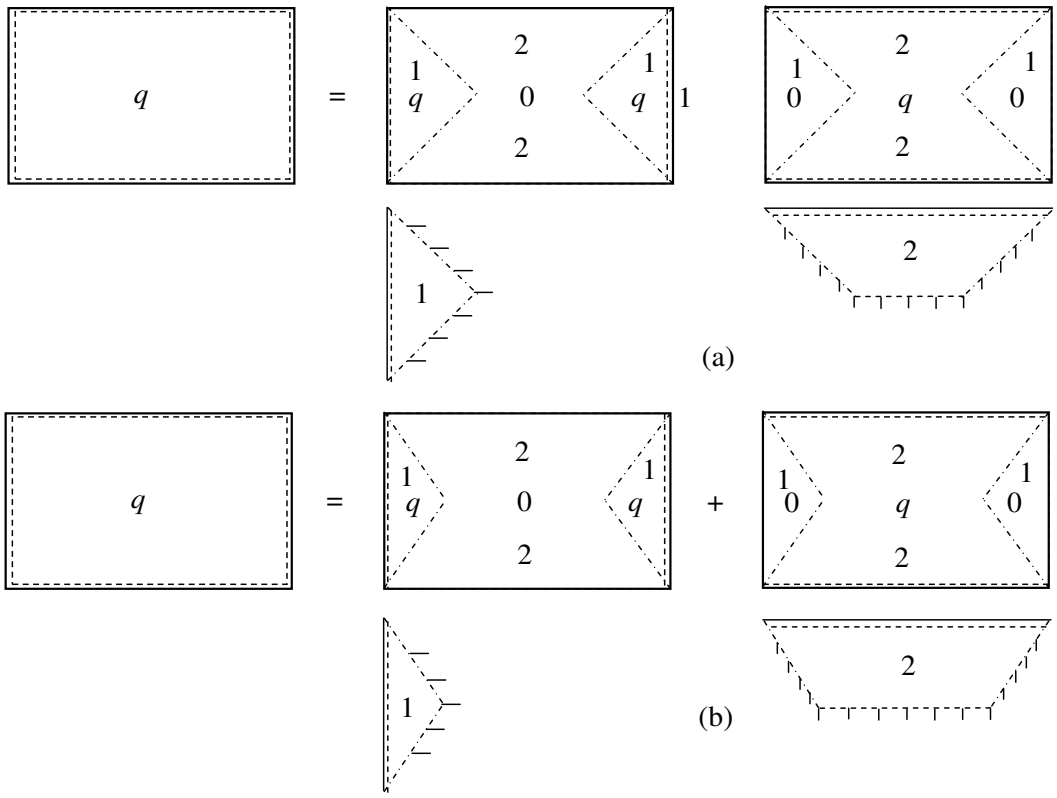

Figure 2.26. Load distribution follows load diving line: (a) longitudinal reinforcement increased (b) longitudinal reinforcement decreased.

In Figure 2.26a and Figure 2.26b, the total number of bars are the same. Figure 2.26a shows a more distributed bar in x-and y-direction while Figure 2.26b provides more bars in the centre regions (y-direction) and less bars along the edges (x-direction).

The more the chosen load distribution of the slab close to the real load distribution of the slab, the better the solution converge to the true plastic solution. Assuming that there is no limitation in the plastic redistribution capacity, the failure load obtained from strip method is always larger than the actual failure load. That is why this method is always on the safe side and preferred in the design.

2.4.6 Yield line method

A slab is assumed to collapse at a certain load in the pattern of fracture which is determined by a system of yield lines or fracture lines. The yield line method is a

kinematic method providing upper bounds to the ultimate load capacity so-called true collapse load of reinforced concrete slab. Therefore, it always provides a solution on the unsafe side since the slab will fail at the load that requires least energy. There are two possible methods in the yield line theory. The first approach is the study of equilibrium of the various parts of the slab which are divided by yield lines assuming the pattern of the collapse mechanism of the slab. The second method is an energy method in which the external work done by the applied loads are equal to the internal work. The development of the yield can be described by examining the collapse behaviour of a slab simply supported along four edges under surface load as shown in Figure 2.27.

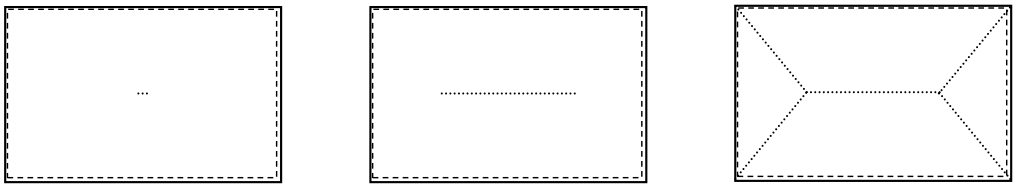

Figure 2.27. Yield line development: (a) hinge takes place in the middle of the slab (b) hinges develop along yield line (c) the collapse mechanism is formed when yield line spreads to the corner.

In Figure 2.27a a hinge is first formed in the middle of the slab which is the most stressed point of the slab when the yield limit is reached. Then the hinge spreads along a yield line as shown in Figure 2.27b. Eventually, the hinge spreads to the corner as illustrated in Figure 2.27c and the collapse mechanism is formed and then the slab fail. In the collapse mechanism behaviour, the portions of the slab rotate more or less as rigid bodies and the slab will deflect under constant load. The collapse mechanism must fulfil kinematic requirement which means the slab portions determined by yield line must fit together when the slab deflects in the failure mechanism as shown in Figure 2.28a. This requirement is fulfilled if the yield line between the two slab portions or it extensions passes through the intersection of the rotation axes of the two slab portions. From Figure 2.28b, it is seen that the yield between slab portion 1 and slab portion 2 passes through the intersection between the rotation axe AB and AC. The rotation axes AC and BD of the slab portion 2 and slab portion 3 respectively never intersects as the rotation axe AC parallel to the rotation axe BD. The kinematic requirement is fulfilled by extending the rotation axes AC and BD to infinity which creates the illusion that these two axes intersect in the infinity as shown in Figure 2.28c. By extending the centre intersection yield line between slab portion 2 and slab portion 3 to infinity, it also creates an imaginary intersection in the infinity as illustrated in Figure 2.28c.

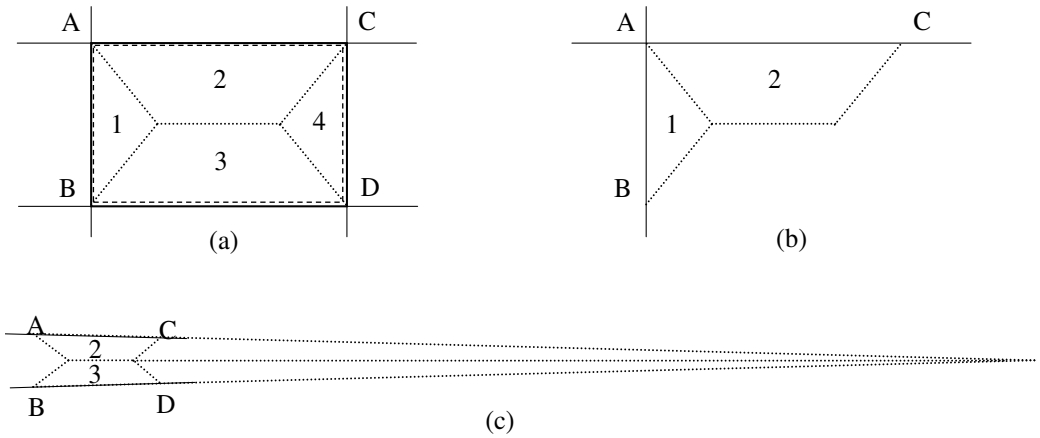

Figure 2.28. Kinematic requirement (a) fractures pattern in a slab (b) yield line passes through intersection of rotation axes at the corner (c) the illusion of the intersection of yield in the infinity.

2.4.7 Distribution width for moment in ultimate limit states

Pacoste *et al.* (2012), provides recommendation on how the moments and forces from linear elastic analysis can be redistributed. The recommendations are based on the assumption that the reinforced concrete slab has enough rotation capacity, but reinforcement need to be concentrated in support regions in order to provide good response in service limit state. The recommendations are applicable for slabs supported by concentrated supports such as columns or bearings and these recommendations should also be applicable for the field moment at a point load in a slab with line supports as shown in Figure 2.29.

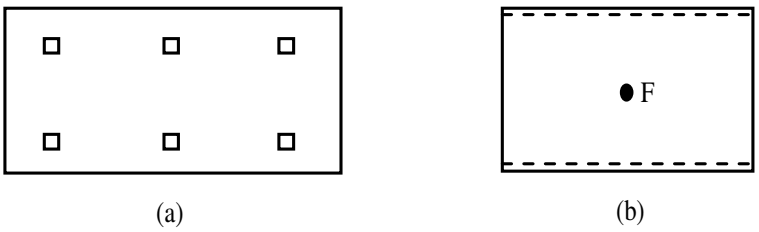

Figure 2.29. (a) slab supported by concentrated supports (b) slab with line supports subjected to point load F.

Wider distributed widths than the limitation of distributed width givens in the following recommendation can be used for slabs with distributed load and line supports. These recommendations are believed to be conservative and need a better knowledge to be improved according to Pacoste *et al.* (2012).

The following recommendation for a support like column and bearing are based on Pacoste *et al.* (2012):

$$w = \min(3h, \frac{L_c}{10}) \text{ for } \frac{x_u}{d} = 0.45 \text{ (0.35 for concrete grades} \geq \text{C55/67)} \quad (2\text{-}32)$$

$$w = \min(5h, \frac{L_c}{10}) \text{ for } \frac{x_u}{d} = 0.3 \text{ (0.23 for concrete grades} \geq \text{C55/67)} \quad (2\text{-}33)$$

$$w = \frac{L_c}{4} \text{ for } \frac{x_u}{d} = 0.25 \text{ (0.15 for concrete grades} \geq \text{C55/67)} \quad (2\text{-}34)$$

$$w = \frac{L_c}{2} \text{ for } \frac{x_u}{d} = 0.15 \text{ (0.1 for concrete grades} \geq \text{C55/67)} \quad (2\text{-}35)$$

$$w = \min\left(5h, \frac{L_c}{5}\right) \text{ for } \frac{x_u}{d} = 0.0 \quad (2\text{-}36)$$

Where $h =$ height of the cross-section
$x_u =$ depth of the neutral axis at the ultimate limit state after redistribution
$d =$ effective depth
$L_c =$ characteristic span width

The value of x_u/d in between the value of x_u/d given in equation (2-32) to equation (2-36) can be determined by linear interpolation. For the details of how to determine the value of L_c for the distribution width for moment in longitudinal and transversal direction, the reader can refer to Section 4.2.1.1 to Section 4.2.1.3 in Pacoste *et al.* (2012). For comments concerning the above limits and plastic rotation capacity requirements, the reader can also consult Appendix B in Pacoste *et al.* (2012).

According to Pacoste *et al.* (2012), the value of the distribution width should not be taken less than

$$w \geq w_{\min} = 2h + a \quad (2\text{-}37)$$

Where $a =$ dimension of the support or load width if it is a point load in the considered section.

In case of columns without drop panel, the ratio of the averaged and maximum reinforcement moments should be restricted to:

$$\delta = \frac{m_{rx,av}}{m_{rx,\max}} \geq 0.6 \quad (2\text{-}38)$$

Where $m_{rx,av}$ and $m_{rx,max}$ can be determined based on Figure 2.30a and equation (2-39) for distribution width exceeds w_o (the distance between points of zero moment) and Figure 2.30b and equation (2-40) for distribution width less than w_o.
The above moment distribution limitation applies for the distribution width calculated based on equation (2-32) to equation (2-36):

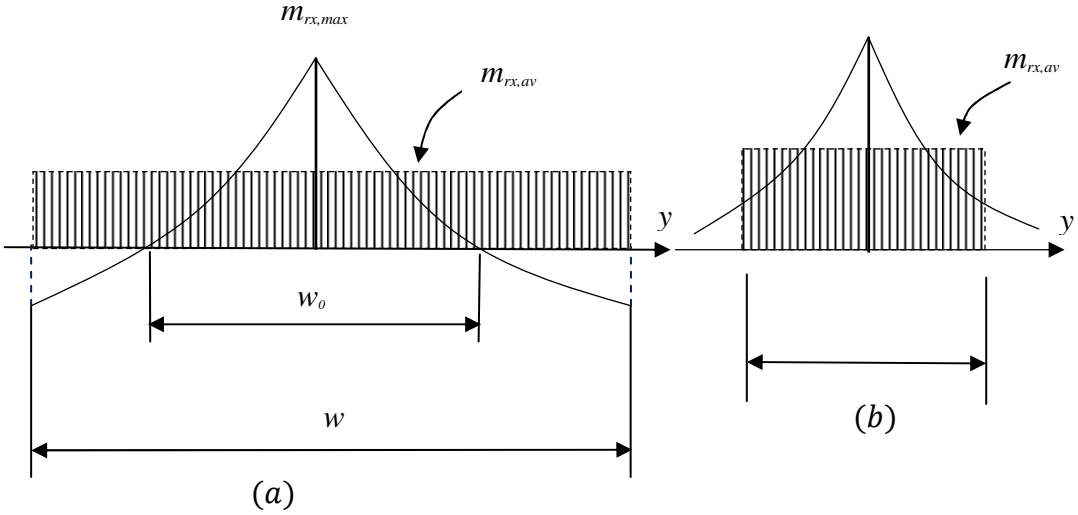

Figure 2.30. Definition of the average value of moment distribution (a) distribution width exceeds the distance between points of zero moment (b) distribution width is less than the distance between points of zero moment. From Pacoste et al. (2012).

The $m_{rx,av}$ in Figure 2.30a and Figure 2.30b can be calculated using equation (2-39) and equation (2-40) respectively.

$$m_{rx,av} = \frac{1}{w}\int_0^{w_0} m_{rx}\,dy \tag{2-39}$$

$$m_{rx,av} = \frac{1}{w}\int_0^{w} m_{rx}\,dy \tag{2-40}$$

Where $m_{rx,\max}$ = maximum moment from linear elastic analysis

$m_{rx,av}$ = average moment chosen to redistribute the maximum moment from linear elastic analysis

This principle is also applied for the reinforcement moment in the *y*-direction, i.e m_{ry}. For the distribution width in case of the columns has a capital or drop panel and in case of supports placed near the edge of the plate, reader can refer to Section 4.2.1 of Pacoste *et al.* (2012).

2.4.8 Distribution width for moment in serviceability limit states

In serviceability limit states, it is more complicated to choose an appropriate distribution width as it is difficult to determine the degree to which the force redistribution will take place. When a slab starts to crack, the moment will distribute from cracked regions to uncracked region. But when the whole slab is cracked, the region which contains high amount of reinforcement will be stiffer than the region that contains less reinforcement. According to Eurocode 2 (SS-EN 1992-1-1:2005), the reinforcement distribution should take into account the behaviour of slab in working condition where there is a concentration moment over the column. Unless

rigorous checks are made for serviceability, half of the total top reinforcement should be concentrated into a column strip with the width determined in equation (2-41).

$$w = \frac{L_1}{8} + \frac{L_2}{8} \tag{2-41}$$

Where L_1, L_2 = distances from the columns of the strip to the adjacent columns in the direction perpendicular to the reinforcement

Pacoste *et al.* (2012) stated that the large concentration of reinforcement over the column width results in moment that is larger than the moment from linear elastic analysis.) Based on this reason, Pacoste *et al.* (2012) provides a limitation for the distribution width for serviceability limit state as stated in equation (2-42) which is more conservative than in the ultimate limit state.

$$\min(3h, \frac{L_c}{10}) \leq w \leq \min(5h, \frac{L_c}{5}) \tag{2-42}$$

2.4.9 Distribution width for shear forces

There is a very limited knowledge on redistribution of shear forces from linear elastic analysis. There is no specific guideline concerning redistribution of shear forces provided in Eurocode 2, CEN (2004). Pacoste *et al.* (2012), though, provides the following recommendations on redistribution of shear forces. Like the recommendations given for moment distribution, these recommendations are based on the assumption that the reinforced concrete structures have sufficient plastic redistribution in the ultimate state. This recommendation is also believed to be conservative and needs further improvement based on increased knowledge on the response and distribution of shear forces on reinforced concrete slab and based on how the slabs behave with regard to linear elastic analysis. The recommendation is valid for the redistribution of the resultant shear force determined in equation (2-43) and the direction of this principal shear force is determined by an angle α in equation (2-44). The shear redistribution is made along the direction perpendicular to the direction of the principal shear as illustrated in Figure 2.31.

$$v_0 = \sqrt{v_x^2 + v_y^2} \tag{2-43}$$

$$\alpha = \arctan(\frac{v_x}{v_y}) \tag{2-44}$$

Where v_0 = the principal (or resultant) shear force

α = angle that determine the direction of the vector v_0

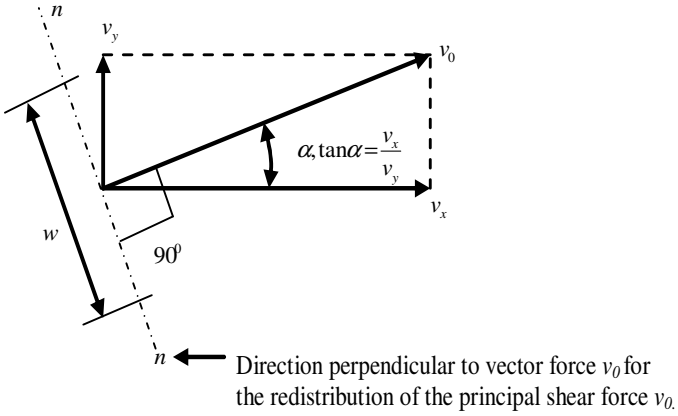

Figure 2.31. Redistribution of the resultant shear force in the direction perpendicular to the principal shear. From Pacoste et al. (2012).

The distribution width for shear forces can be chosen as equal to the distribution width for the reinforcement moments in equation (2-32) to equation (2-36). Apart from this, two more conditions need to be taken into account:

1. The distribution width for the shear force should not exceed 5*h* where *h* is the thickness of the slab at the considered section.
2. The distribution width for the shear force should be chosen in such a way that a variation of the angle α in Figure 2.32 is less than 45^o. It is mathematically expressed as $|\alpha_i - \alpha_0| \leq 45^0$. The distribution width in Figure 2.32 is restricted to w_{eff} as $|\alpha_5 - \alpha_0| \geq 45^0$ and $|\alpha_6 - \alpha_0| \geq 45^0$.

Along the direction *n*, perpendicular to v_0 at the chosen critical section shown in Figure 2.32a, it is possible to determine the distribution of principal shear force v_0 illustrated in Figure 2.32b along line *n* from the points that are situated along that line based on equation (2-43). Then it is possible to distribute the average value of $v_{0,av}$ $v_{0,av}$ within the effective w_{eff}.

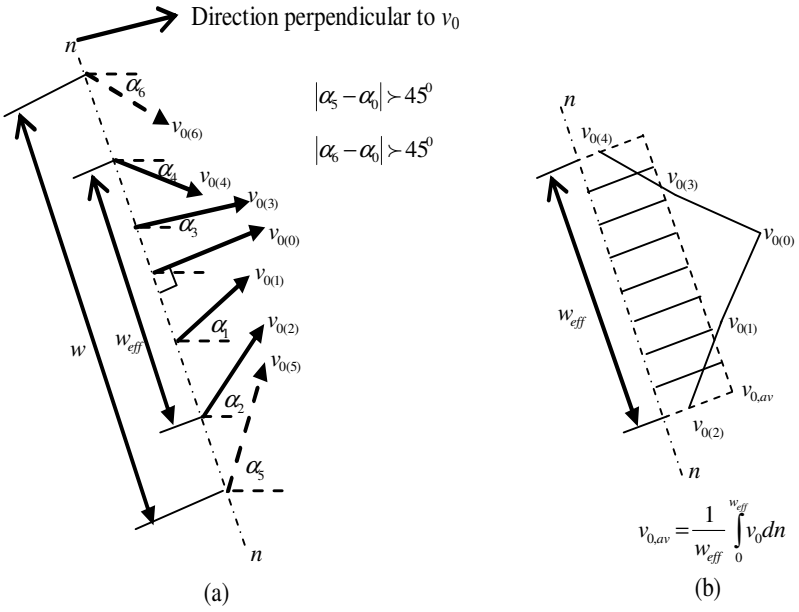

Figure 2.32. Variation of the direction of the resultant shear force within a distribution width. From Pacoste et al. (2012).

From a FE analysis it may be cumbersome to determine the shear force along a line perpendicular to an arbitrary section as the points situated along that line do not coincide with nodes of structures in the FE program. As a result, an alternative method to use the direction of resultant shear v_o based on the global coordinate is also proposed in Pacoste *et al.* (2012). The principal shear force $v_{0,i}$ and angle α_i at each Section in the global *x*-and *y*-coordinate can be computed as:

$$v_{0,i} = \sqrt{v_{x,i}^2 + v_{y,i}^2} \tag{2-45}$$

$$\alpha_i = \arctan(\frac{v_{x,i}}{v_{y,i}}) \tag{2-46}$$

The design shear force is made in the global *x*- and *y*-coordinate system. Design shear force v_{dx} and v_{dy} at each section point *i* in Figure 2.33a are determined based on Table 2.2. If the angle α_i is less than 45^0, the design shear force v_d is assumed to act in the *x*-direction and if α_i is greater than 45^0, v_d is assumed to act in the *y*-direction.

$$\alpha_i \le 45^0 \rightarrow \begin{cases} v_{dx,i} = v_{0,i} \\ 0 \end{cases} \tag{2-47}$$

$$\alpha_i \succ 45^0 \rightarrow \begin{cases} 0 \\ v_{dy,i} = v_{0,i} \end{cases} \tag{2-48}$$

Different load positions result in the envelope of the resultant shear force $v_{0,i}$. Therefore, two resultant shear forces $v_{01,i}$ and $v_{02,i}$ are used for a certain section point.

$$v_{01,i} = \sqrt{v_{x,\max,i}^2 + v_{y,cor,i}^2} \tag{2-49}$$

$$v_{02,i} = \sqrt{v_{x,cor,i}^2 + v_{y,\max,i}^2} \tag{2-50}$$

$$\alpha_{1,i} = \arctan(\frac{v_{y,cor,i}}{v_{x,\max,i}}) \tag{2-51}$$

$$\alpha_{2,i} = \arctan(\frac{v_{y,\max,i}}{v_{x,cor,i}}) \tag{2-52}$$

Here, the index *max* indicates the maximum value while index *cor* indicates it corresponding values in the global coordinate system.

Table 2.2 summaries the design shear values at a certain section point based on the limitation of the angle α_i and the shear envelope from different load positions and load combinations.

Table 2.2 Determination of design shear forces $v_{dx,i}$ and $v_{dy,i}$ in Section point i as a function of the resultant angles $\alpha_{1,i}$ and $\alpha_{2,i}$.

Case	$\alpha_{1,i}$	$\alpha_{2,i}$	$v_{dx,i}$	$v_{dy,i}$
1	$\leq 45^0$	$\leq 45^0$	$\max(v_{01,i}, v_{02,i})$	0
2	$\leq 45^0$	$\succ 45^0$	$v_{01,i}$	$v_{02,i}$
3	$\succ 45^0$	$\leq 45^0$	$v_{02,i}$	$v_{01,i}$
4	$\succ 45^0$	$\succ 45^0$	0	$\max(v_{01,i}, v_{02,i})$

The design shear force v_{dx} is distributed in the y-direction while v_{dy} is distributed in the x-direction as the distribution needs to be done in the direction perpendicular to the acting shear force. This is schematically illustrated in Figure 2.33, the distribution width in the y-direction for design shear force v_{dx} is limited by a section point where $v_{dx} = 0$.

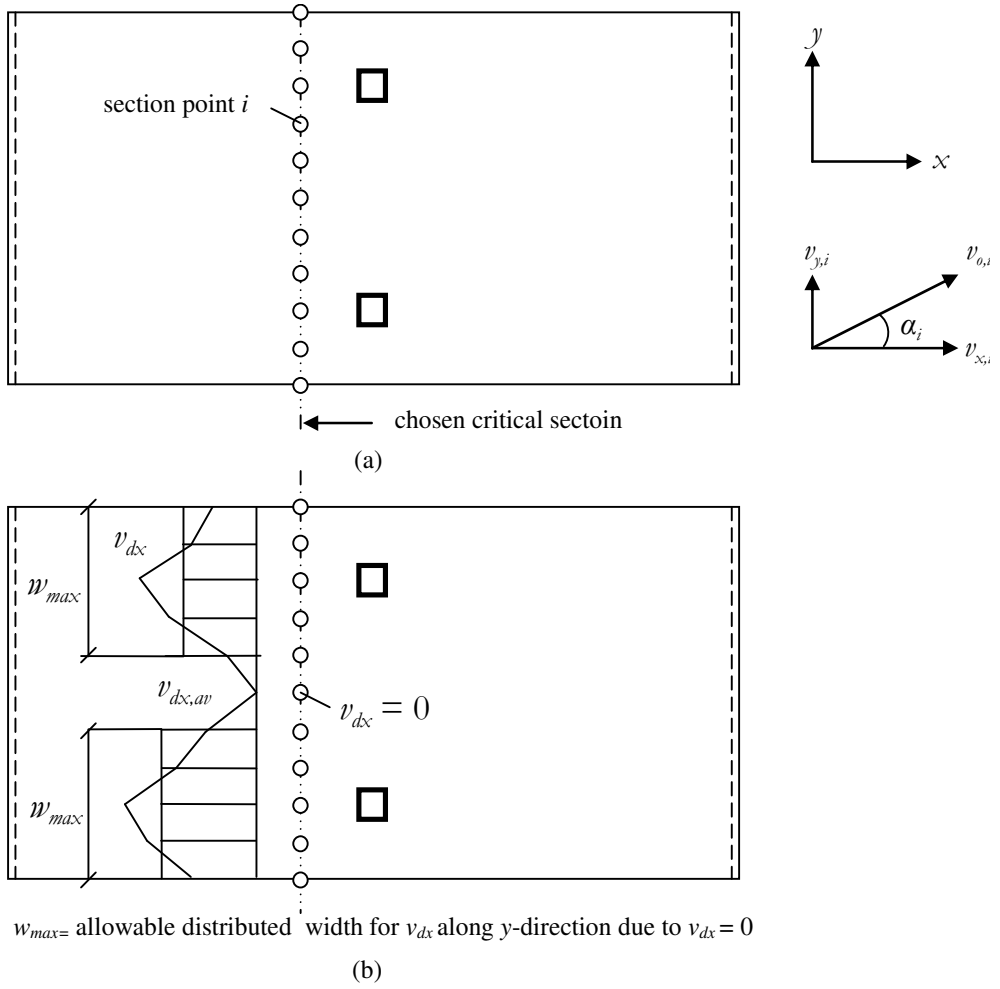

Figure 2.33. (a) variation of the direction of the resultant shear force within a distribution width.(b) distribution width limitation for v_{dx} along y-direction due to $v_{dx} = 0$. From Pacoste et al. (2012).

2.4.10 Cantilever slabs

Cantilever slabs can be found in different types of structures. For example, the most common reinforced concrete cantilever slab of a building is the balcony. The balcony is supported at the clamped edge and free at the other and is subjected to evenly distributed loads over the whole surface as shown in Figure 2.34. The cantilever slabs carry the load in the transversal direction, i.e. *y*-direction to the fixed support depicted in Figure 2.34b. This cantilever slab can be considered as a one way slab and can be designed like a beam per meter width. Such a cantilever slab under the distributed load is not so critical for the design and it is not of interest in this thesis report. However, if the same cantilever slab is subjected to a point load of high magnitude in different positions, it would be of more interest.

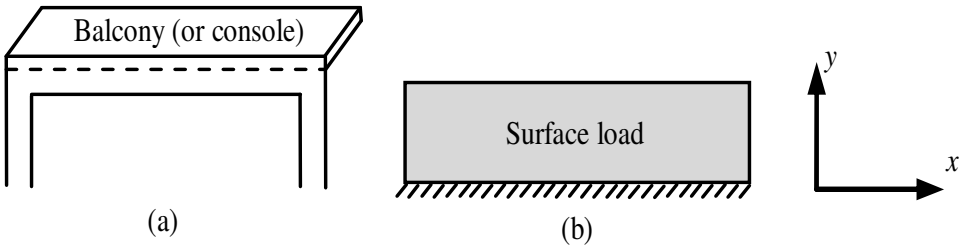

Figure 2.34. Cantilever slab in the building: (a) balcony supported by a clamped support and free at the other in 3D view (b) balcony subjected to distributed load on the whole surface in 2D view.

The knowledge on how to redistribute the moment and shear forces on the cantilever slab is limited. Further studies on the response of moment and shear forces on these cantilever slabs are being continued. Cantilever slabs which are found in the bridge design community such as composite bridges or concrete beam bridges are more or less the same as the balcony in Figure 2.34a, but the loads on a bridge is more complex. These cantilever slabs are subjected to concentrated traffic loads, like traffic point loads which are the movable loads. As a result, the redistribution of moments and shear forces are rather complex and difficult to determine. The traffic load acting on the cantilever slab of the reinforced concrete bridge deck can be modelled either as a concentrated load or distributed load as shown in Figure 2.35a. These two models of axle loads provide similar structural response, but it is recommended to use surface load in order to avoid numerical problem, i.e. singularity problem when analysing a slab under point load using shell element. The surface load gives somewhat lower sectional forces. These loads will transfer transversally along *y*-direction to the clamped support. If the cantilever slab includes the edge beam, the loads will be transfer to both the clamped edge and the edge beam, then the loads will be transferred to support of the clamped edge as shown in Figure 2.35b.

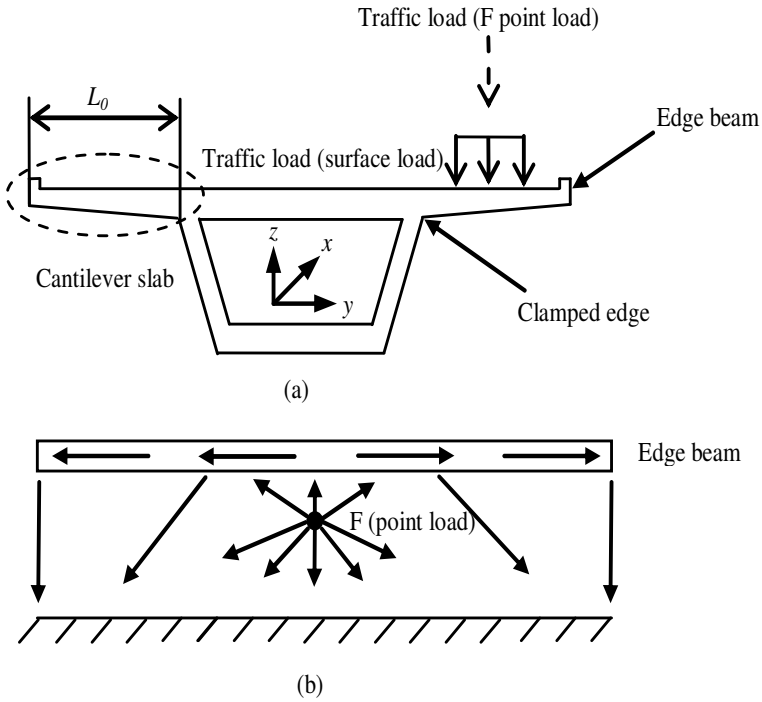

Figure 2.35. Cantilever slab of a reinforced concrete bridge: (a) axle loads modeled as concentrated loads (b) axle loads modeled as distributed loads

2.4.10.1 Distribution width for moment

The recommendations given in this Section are based on the work of Pacoste *et al.* (2012), and it applies only for the load transfer in the transversal *y*-direction of the cantilever slab These recommendations are believed to be less conservative than the recommendations on the distribution width for moment and shear forces for one-way spanning and two-way spanning slabs described in the Section 2.4.7 to Section 2.4.9.

The distribution width given below is for the reinforcement moment m_{ry} in the transversal direction as defined in equation (2-31) Section 2.4.4.

For a single load *F* modelled as a surface load in Figure 2.36a or a concentrated point load in Figure 2.36b, the distribution width w_x for the ultimate limit states is given by:

$$w_x = \min\begin{cases} 7d + b + t \\ 10d + y_{cs} \end{cases} \tag{2-53}$$

Where d = effective depth at the critical cross section
b = width of the load in case of surface load
t = thickness of the surfacing
y_{cs} = distance from the centre of the load (resultant force) to the critical cross section

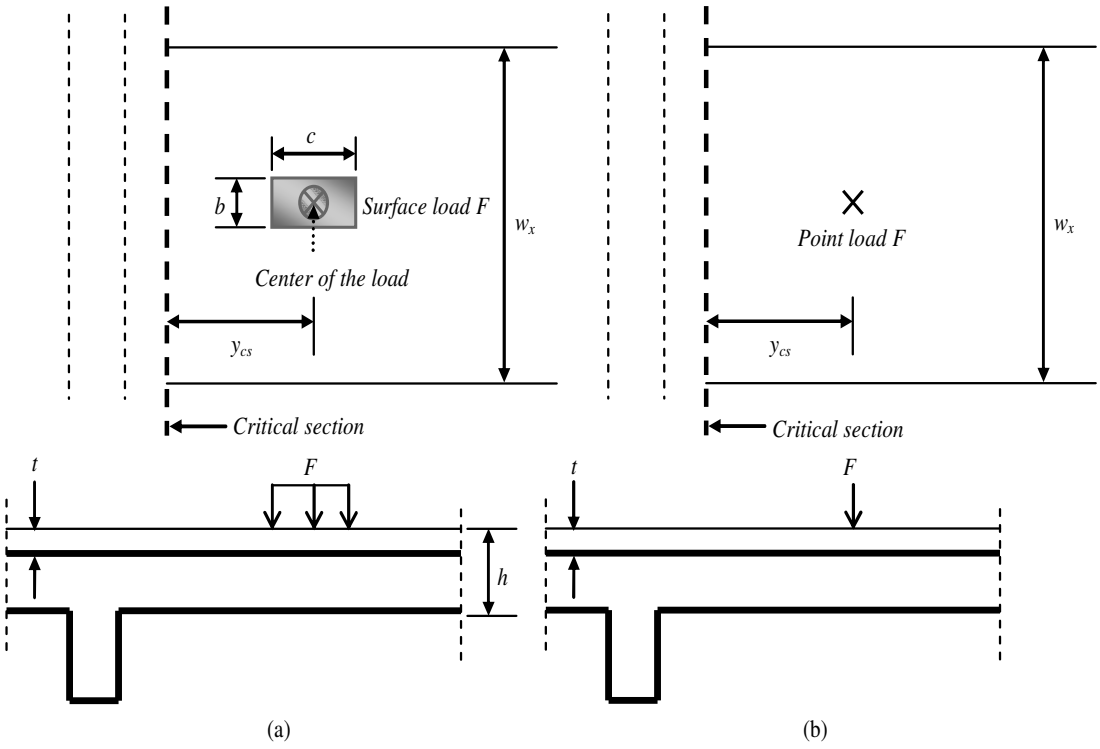

Figure 2.36. Distribution width w_x for the reinforcement moment m_{ry} in the transverse direction: (a) a single force modelled as surface load F (b) a single force modelled as concentrated load F. Based on Pacoste et al. (2012).

The distribution width in equation (2-53) is valid to use if the ratio between the height of the compression zone x_u and the effective depth d at the critical section fulfil:

$$0.15 \le \frac{x_u}{d} \le 0.25 \qquad \text{for concrete classes C12/15 to C50/60} \qquad (2\text{-}54)$$

$$0.10 \le \frac{x_u}{d} \le 0.15 \qquad \text{for concrete classes C55/67 and greater} \qquad (2\text{-}55)$$

If x_u/d does not fulfil these requirements, the distribution width w_x can instead be determined as:

$$w_{\min} = 2h + b + t \qquad (2\text{-}56)$$

Where h = height of the cantilever slab at the critical cross section.

The distribution width for serviceability limit states is also given by equation (2-56).
In case of many forces that are located close to each other so that the distribution width of each force overlaps each other, a distribution width can be computed based on Figure 2.37 and equation (2-57).

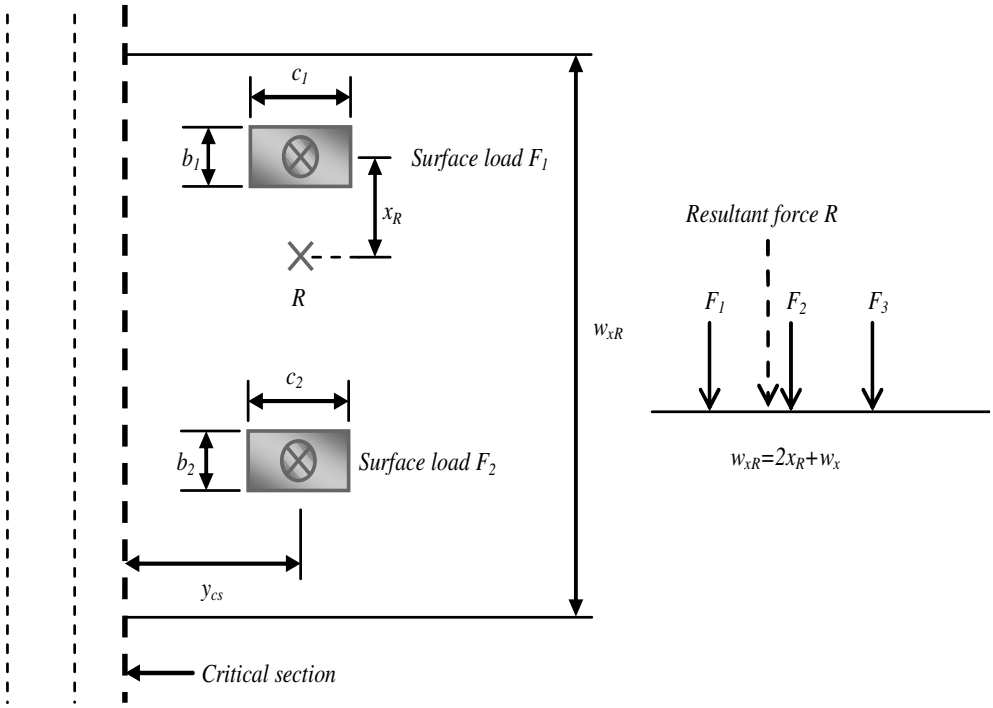

Figure 2.37. Distribution width w_{xR} for the reinforcement moment m_{ry} in the transverse direction for two or several forces located close to each other. Based on Pacoste et al. (2012).

$$w_{xR} = 2x_R + w_x \tag{2-57}$$

Where w_x = distribution width in case of a single force

2.4.10.2 Distribution width for shear force

The distribution of shear force in the cantilever slab in Figure 2.36 is performed based on the principal shear in equation (2-43). The distribution width is conducted along the longitudinal *x*-direction. The limitation of the distribution width, point 2 in Section 2.4.9, still applies in this case. The limitation of the distribution width for shear forces in case of the cantilever slab that consists of load and geometrical symmetry can be found in Figure 2.38. For a cantilever slab that provides unsymmetrical response, the principle illustrated in Figure 2.32a is applied.

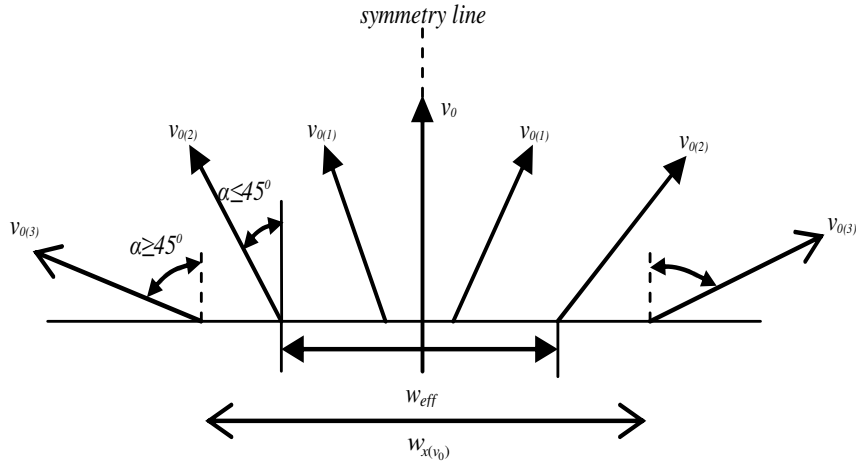

Figure 2.38. Limitation for the distribution width $w_{x(v_0)}$ in case of load and geometry symmetry. From Pacoste et al. (2012).

The critical cross-section for shear forces in case of a single force or a group of forces placed in the same row is the same and is always placed at a distance of $y_{cs} = (c+d)/2$ from the centre of the load as shown in Figure 2.39.

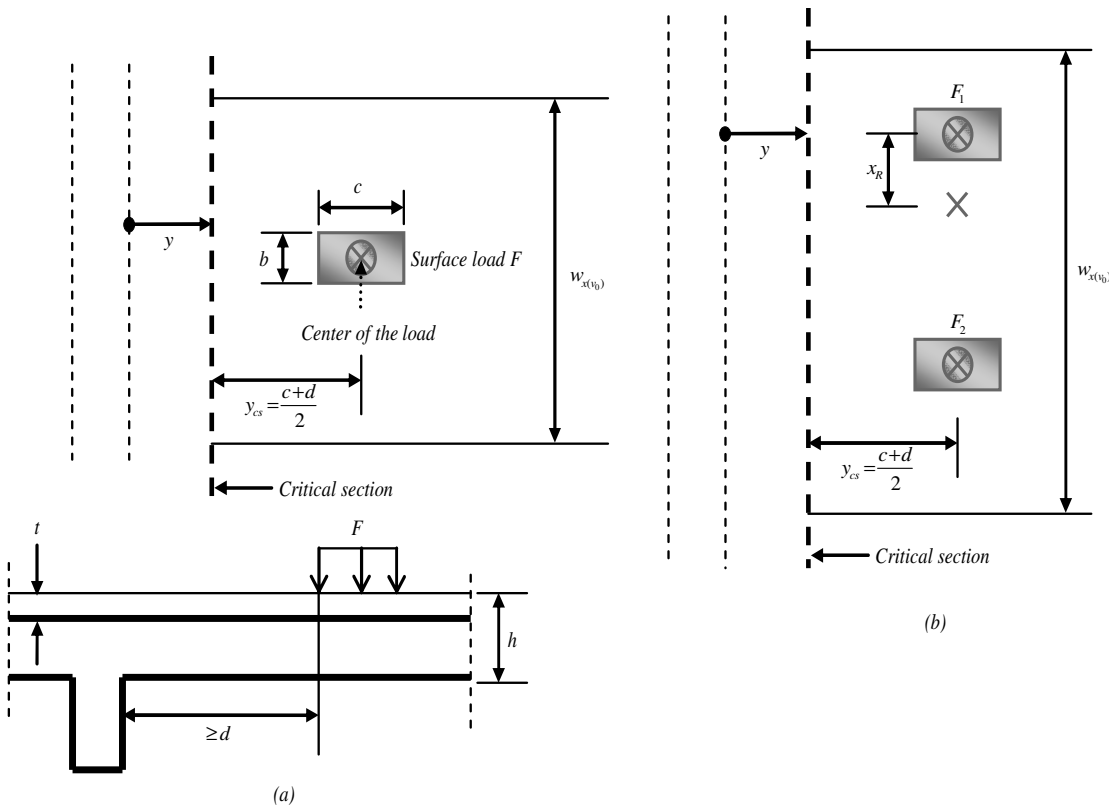

Figure 2.39. Critical cross Section for shear forces located at a distance y from console: (a) a single force modelled as surface load F (b) a group of forces in the same row modelled as surface load F. From Pacoste et al. (2012).

The rule for y_{cs} in Figure 2.39 is also applied for axle load modeled as concentrated force if the position of the center of that concentrated force is coincide with the center of the surface load shown in Figure 2.36.

Pacoste *et al.* (2012), provided a recommendation on the distribution width for the case shown in Figure 2.39 as following:

$$w_{\min} = \min\begin{cases} 7d + b + t \\ 10d + y_{cs} \end{cases} \qquad \text{for } y = y_{\max} \tag{2-58}$$

$$w_{\max} = \max\begin{cases} 7d + b + t \\ 10d + y_{cs} \end{cases} \qquad \text{for } y = 0 \tag{2-59}$$

Where y_{max} is defined in Figure 2.40 for single load. For the position of critical cross section y located in between $y = 0$ and $y = y_{max}$, linear interpolation can be used to determine the distribution width $w_{x(y_0)}$.

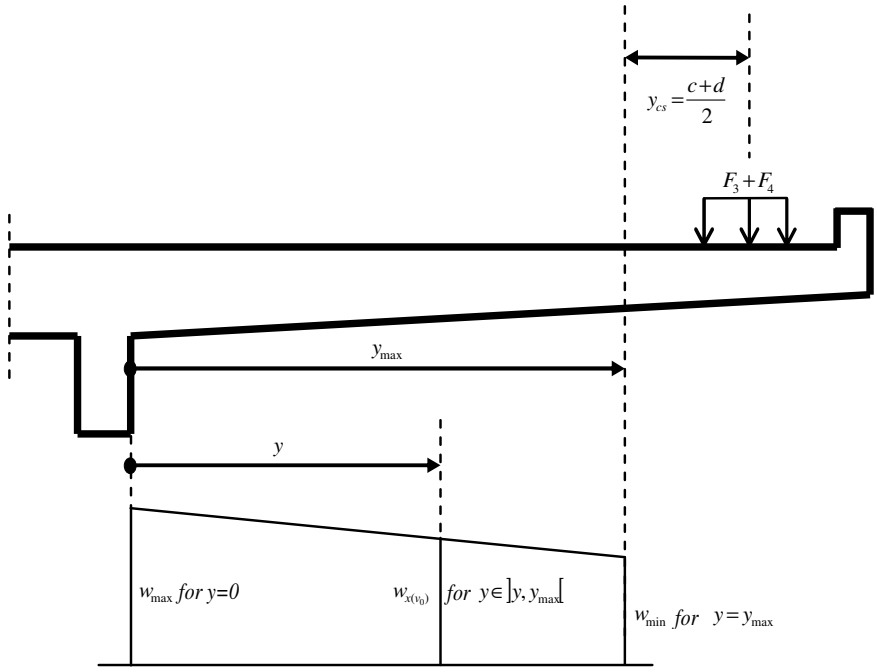

Figure 2.40. Distribution widths for shear forces -single load. From Pacoste et al. (2012).

For the loading situations in which several forces are situated in such a way that the distribution width from each force overlaps each other, the distribution width for the whole group of forces can be computed by equation (2-57) from Figure 2.37.

3 Reinforced concrete cantilever beam

3.1 Introduction

The understanding of the structural response of the cantilever beam in elastoplastic case is very essential since the slab in elastoplastic case in Chapter 4 was analysed using beam grillage of beam elements. In order to give a better understanding of the behaviour of the reinforced cantilever beam in elastoplastic case, examples were carried out. FE analysis of the cantilever beam was carried out using the student version of FE software ADINA, *ADINA* (2011) with a maximum of 900 nodes. For the analysis of the cantilever beam in elastoplastic case, the beam was modelled using beam elements and some modelling simplifications including equivalent Young's Modulus were made.

3.2 Equivalent Young's modulus

For beam elements, ADINA allows an elasto-plastic analysis of a structure using either a cross-section with rectangular shape and a plastic material model, or an elasto-plastic moment-curvature model. For bilinear plastic material model and moment-curvature model with multilinear plasticity, the reader can refer to APPENDIX A.

With bilinear plastic material response, it is not possible to capture the tension stiffening effect of reinforcement concrete structures. Hence, it is difficult to choose a correct Young's Modulus. ADINA does not recognize that the section is cracked as it assumes that the first part of the curve represent linear elastic response. It means that the behaviour of the structure is in uncracked state. ADINA considers the stiffness given by the user as stiffness of uncracked section. In a simplified bilinear model in state II, it is reasonable to model the section as a fully cracked section without taking into account the tension stiffening effect, which means that the state II stiffness (fully cracked section) is used. ADINA uses Young's modulus to capture the stiffness of cross-section for beam elements. In order to perform state II analysis and model a fully cracked section it is necessary to find an equivalent Young's modulus. This equivalent Young's modulus is determined based on the relationship between Young's modulus of uncracked concrete section, the moment of inertia in state I and the moment of inertia of cracked section in state II. Thereby, the equivalent Young's modulus can be expressed as following:

$$E_{II} = E_I \frac{I_{II}}{I_I} \tag{3-1}$$

Where E_I = Young's modulus of uncracked state, i.e. $E_I = E_c$

E_{II} = Equivalent Young's modulus in order to get the correct stiffness of fully cracked section state II.

I_I = moment inertia of uncracked state

I_{II} = moment inertia of cracked state

It should be noted that the equivalent Young's modulus is used in order to give an input in ADINA FE program so that it is possible to get the correct stiffness in cracked state. Accordingly, it is important to note that the equivalent Young's modulus has no physical meaning as the Young's modulus is constant in a real structure.

3.3 FE-elements

In ADINA FE program, beam elements can be modelled by a 2D beam element or a 3D beam element. The description of 2D beam action and 3D beam action is given in APPENDIX A.

In order to provide a better understanding of the response of the beam elements in elasto-plastic case, the analyses of 2D beam and 3D beam elements with different mesh sizes were carried out. Convergence study of 2D beam and 3D beam elements in elasto-plastic was also performed. The results received from FE analyses were compared with the analytical solutions.

3.4 Geometry and loading

A 1.6 m long, 0.2 m width and 0.2 m thickness cantilever beam subjected to a point load of 100 kN shown in Figure 3.1was examined.

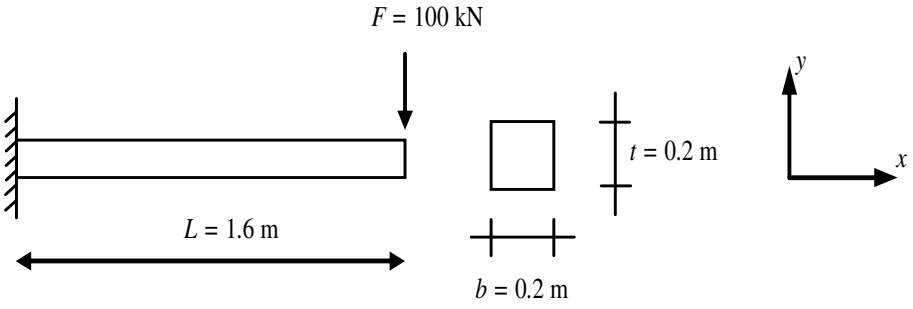

Figure 3.1. Cantilever beam subjected to a point load of 100 kN.

3.5 Elasto-plastic case

3.5.1 2D beam element-bilinear plastic material model

When analysing a cantilever beam in elasto-plastic case using 2D beam elements, ADINA provides the possibility to use 3-7 integration points over the cross-section, but the default value for this 2D action is 3. If 3 integration points over the cross-section height is chosen, the stress over the cross-section will vary linearly. The analysis of a cantilever beam using displacement control in Figure 3.2a was carried out so that the analysis can be performed until the moment capacity provided by ADINA reaches its maximum value, creating a plateau in the load-displacement relation. The stress distribution in Figure 3.2b is used to determine the input of fictitious yield stress depicted in Figure 3.3.

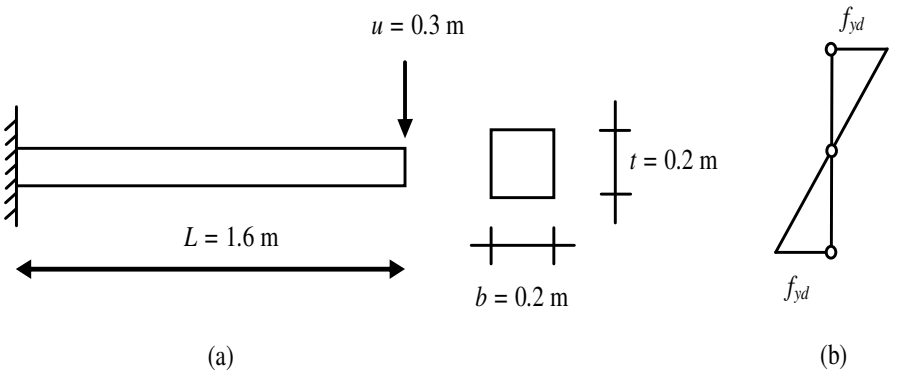

Figure 3.2. (a) Geometry of the cantilever beam studied under displacement control (b) stress distribution using 3 integration points over the cross-section height for 2D beam in ADINA.

The moment capacity of the cross section in elastic state can be computed in equation (3-2).

$$M_{Rd} = f_{yd} \cdot W_{el} \tag{3-2}$$

The moment capacity is chosen not be less than the exterior moment from the applied load in Figure 3.1. Therefore, the moment resistance of the cross-section can be expressed as:

$$M_{Rd} = M_{analy} = F \cdot L = 100 \cdot 1.6 = 160 \text{ kNm} \tag{3-3}$$

The elastic bending resistance w_{el} is computed in equation (3-4).

$$W_{el} = \frac{bh^2}{6} \tag{3-4}$$

Therefore, the fictitious yield stress can be derived in equation (3-5).

$$f_{yd} = \frac{6M_{Rd}}{bh^2} = \frac{6 \cdot 160 \cdot 10^3}{0.2 \cdot 0.2^2} = 120 \text{ MPa} \tag{3-5}$$

The stiffness $E_{c,II} = 6$ GPa is chosen for this analysis. The material data input for the analysis is illustrated in Figure 3.3.

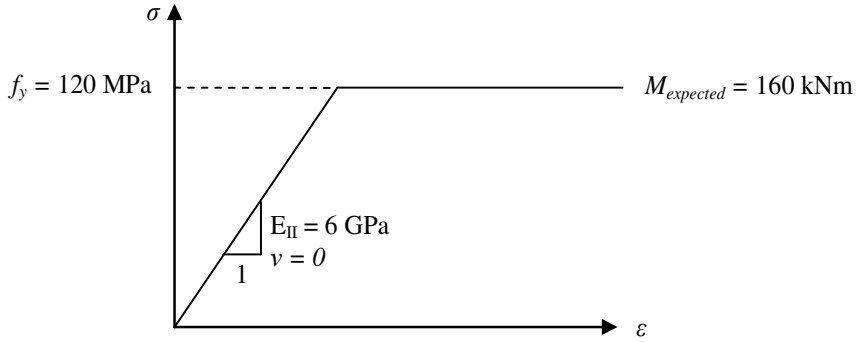

Figure 3.3. Material data used in ADINA for elasto-plastic analysis using 2D beam.

Three element mesh sizes including 0.2 m element size, 0.1 m element size and 0.025 m element size were computed in order to investigate the convergence problem. The results of the analysis are summarized in Table 3.1. The difference in percentage between analytical solution and those obtained from the FE analysis can be determined in equation (3-6) and (3-7).

$$\gamma_{elsto,M-2D} = 100 \cdot \frac{\left|M_{analytic}\right| - \left|M_{Adina}\right|}{\left|M_{analytic}\right|} \tag{3-6}$$

$$\gamma_{elsto,R-2D} = 100 \cdot \frac{\left|R_{analytic}\right| - \left|R_{Adina}\right|}{\left|R_{analytic}\right|} \tag{3-7}$$

Where $M_{analytic}$ = moment obtained from analytical solution

M_{Adina} = moment obtained from finite element program ADINA

$R_{analytic}$ = reaction force obtained from analytical solution

R_{Adina} = reaction force obtained from finite element program ADINA

$\gamma_{elsto,M-2D}$ = difference in percentage between $M_{analytic}$ and M_{Adina}

$\gamma_{elsto,R-2D}$ = difference in percentage between $R_{analytic}$ and R_{Adina}

Table 3.1. Bilinear plastic material model-2D beam elements

Element size (m)	M_{analy} (kNm)	R_{analy} (kN)	M_{Adina} (kNm)	R_{Adina} (kN)	$\gamma_{elasto,M-2D}$ $[\%]$	$\gamma_{elasto,R-2D}$ $[\%]$
0.2	-160	-100	-166.9	-104.3	-4.3	-4.3
0.1	-160	-100	-163.4	-102.1	-2.1	-2.1
0.025	-160	-100	-160.8	-100.5	-0.5	-0.5

From Table 3.1, it is seen that the solution converge to the analytical solutions if finer mesh is chosen. As a result, a conclusion can be drawn that for elasto-plastic analysis using 2D beam elements, a more accurate result can be achieved if sufficient fine mesh is provided.

3.5.2 3D beam element-bilinear plastic material model

Unlike the elasto-plastic case with 2D beam element in Section 3.5.1, ADINA provides no possibility to choose the number of integration points over the cross-section height when using 3D beam elements. Instead, ADINA uses 7 integrations points over the height by default regardless of input data for this problem. In this case, Newton-Cotes integration is used in all coordinate directions. Since 7 integration points are used, the analytical stress distribution in Figure 3.4a is expected. According

to Augustsson and HÄRENSTAM (2010), ADINA uses a polynomial equation of order six to compute the stress distribution over the cross-section height as shown in Figure 3.4b. Based on Figure 3.4b, it is seen that the expected stress distribution provided by ADINA is expected at the integration point. However, the stress distribution in between the integration points is determine by polynomial equation of order six and it generates a bending resistance that is about 4 % smaller than that expected, see Figure 3.4a. In order to get the expected moment capacity of the section by using the stress distribution provided by ADINA, a fictitious yield stress f_y^{mod} need to be used in bilinear plastic material input in ADINA instead of $f_y^{expected}$. The fictitious yield stress f_y^{mod} can be computed using equation (3-8). For the derivation of equation (3-8) and α factor, the reader can refer to APPENDIX B.

$$f_y^{\mathrm{mod}} = \frac{1}{\alpha}\frac{M_{Rd}}{b \cdot h^2} \tag{3-8}$$

Where f_y^{mod} = modified fictitious yield stress when using 7 integration points
α = 0.231 = factor to transform f_y to f_y^{mod} when using 7 integration points

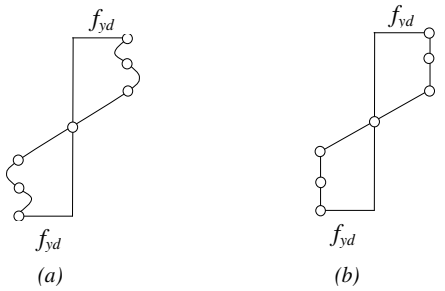

Figure 3.4. Stress distribution over the cross-Section height (a) analytical expected stress distribution (b) stress distribution in ADINA.

The same cantilever beam in Figure 3.2a was analysed with bilinear plastic material input in Figure 3.5. The modified fictitious yield stress of bilinear plastic material input in Figure 3.5 is calculated in equation (3-9).

$$f_y^{\mathrm{mod}} = \frac{1}{\alpha} \cdot \frac{M_{Rd}}{b \cdot h^2} = \frac{1}{0.23094} \cdot \frac{160 \cdot 10^3}{0.2 \cdot 0.2^2} = 86.6 \text{ MPa} \tag{3-9}$$

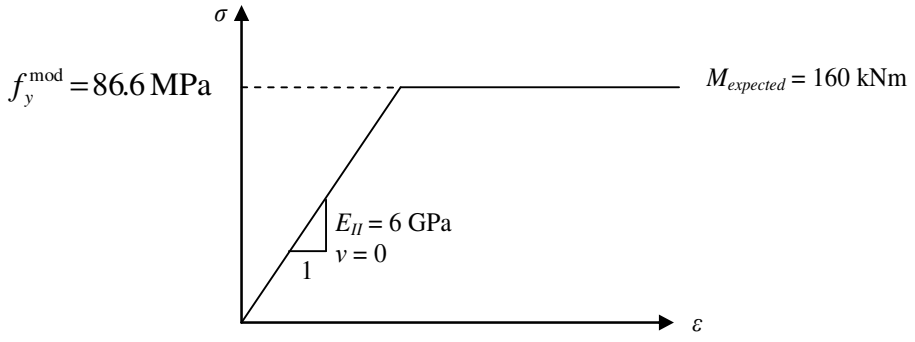

Figure 3.5. Material data used in ADINA for elasto-plastic analysis using 3D beam.

Six element mesh shown in Table 3.2 were chosen in order to perform the convergence study. The result of the analysis is summarized in Table 3.2 and Figure 3.6. The difference in percentage between analytical solutions and those obtained from FE analysis are computed using equation (3-10) and (3-11).

$$\gamma_{elsto,M-3D} = 100 \cdot \frac{\left|M_{analytic}\right| - \left|M_{Adina}\right|}{\left|M_{analytic}\right|} \tag{3-10}$$

$$\gamma_{elsto,R-3D} = 100 \cdot \frac{\left|R_{analytic}\right| - \left|R_{Adina}\right|}{\left|R_{analytic}\right|} \tag{3-11}$$

Table 3.2. Bilinear plastic material model-3D beam elements. Difference in percentage between expected moment capacity and the moment capacity provided by ADINA.

Element size (m)	M_{analy} (kNm)	R_{analy} (kN)	M_{Adina} (kNm)	R_{Adina} (kN)	$\gamma_{elasto,M-3D}$ $[\%]$	$\gamma_{elasto,R-3D}$ $[\%]$
0.2	-160	-100	-166.9	-104.3	-4.3	-4.3
0.1	-160	-100	-163.4	-102.1	-2.1	-2.1
0.05	-160	-100	-161.6	-101.1	-1.1	-1.1
0.025	-160	-100	-160.8	-100.5	-0.5	-0.5
0.01	-160	-100	-160.3	-100.2	-0.2	-0.2
0.005	-160	-100	-160.1	-100.1	-0.1	-0.1

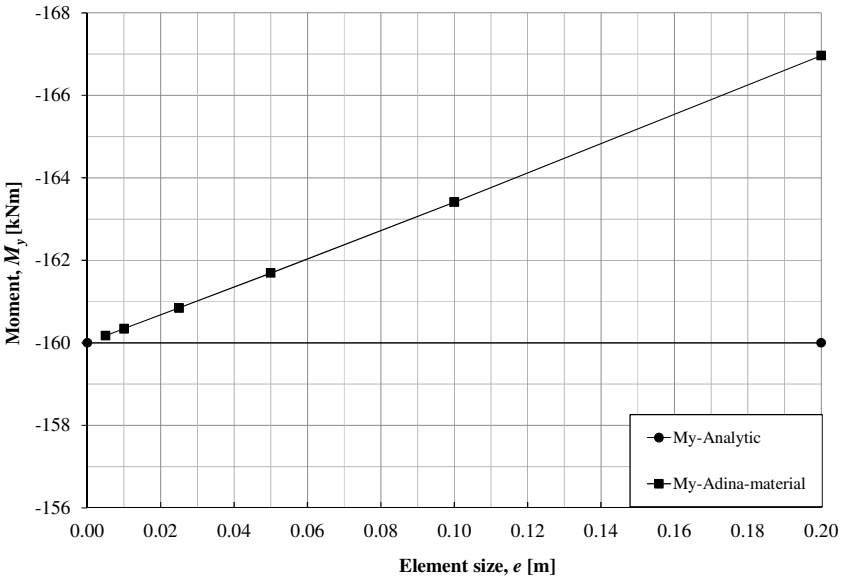

Figure 3.6. Moment capacity for 3D beam in term of element sizes.

From Figure 3.6, it is seen that the moment capacity provided by FE analysis ADINA is not exactly equal to the expected moment capacity, but it converges to the analytical solution when a very fine mesh is given. It is known that only the first element of the entire beam yield. Therefore, it is possible to determine a lever arm that is based on the moment capacity received from FE analysis. This lever arm is shown in Figure 3.7b. The equation (3-12) to equation (3-15) gives this modified lever arm.

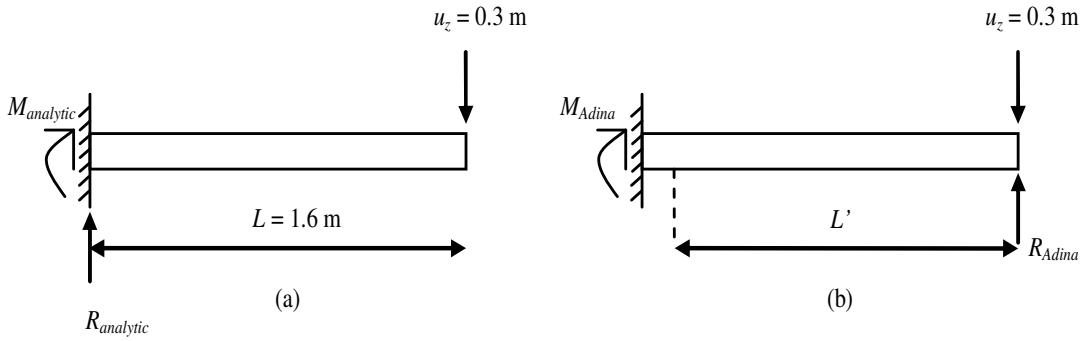

Figure 3.7. (a) Lever arm determined from $M_{analytic}$ (b) Lever arm computed from M_{Adina}.

The analytical moment from the load $F = 100\,\text{kN}$ in Figure 3.1 is determined in equation (3-12).

$$M_{analytic} = R_{analytic} \cdot L = 100 \cdot 1.6 = 160\ \text{kNm} \tag{3-12}$$

The moment received from the FE analysis for the same load is determined in equation (3-13).

$$M_{Adina} = R_{Adina} \cdot L' \tag{3-13}$$

Since the analytical moment is expected to be equal to the moment from the FE analysis, the equation (3-14) can be derived.

$$M_{analytic} = R_{Adina} \cdot L' \tag{3-14}$$

Therefore, the lever arm shown in Figure 3.7b can be computed using equation (3-15).

$$L' = \frac{M_{analytic}}{R_{Adina}} \tag{3-15}$$

As the first element yields, it is possible to find factor α that relates the lever arm computed from moment received from FE analysis to the element sizes used in the analysis. This factor α can be determined as:

$$\alpha = \frac{L - L'}{L_{el}} \tag{3-16}$$

Table 3.3. Bilinear plastic material model-3D beam elements. Lever arm computed from moment capacity received from ADINA.

Element size (m)	M_{analy} (kNm)	R_{analy} (kN)	L_{analy} (m)	M_{Adina} (kNm)	R_{Adina} (kN)	L'_{Adina} (m)	α [–]
0.2	-160	-100	1.6	-166.9	-104.3	1.533	0.334
0.1	-160	-100	1.6	-163.4	-102.1	1.567	0.334
0.05	-160	-100	1.6	-161.6	-101.1	1.583	0.335
0.025	-160	-100	1.6	-160.8	-100.5	1.592	0.336
0.01	-160	-100	1.6	-160.3	-100.2	1.597	0.340
0.005	-160	-100	1.6	-160.1	-100.1	1.598	0.348

From Table 3.3, it is observed that the lever arm computed from moment capacity received from ADINA is located about one third of the element length from the fixed support $L_\alpha = L_{ele}/3$ where L_α is this defined.

3.5.3 3D beam element-moment curvature model

As mentioned earlier, ADINA provides the possibility to compute the moment capacity using moment-curvature relationship. The input is based on the moment and corresponding curvature and it is not based on the yield stress any longer. The moment capacity is expected to be equal to maximum moment in the moment-curvature relationship in Figure 3.8. The same cantilever beam in Figure 3.2a is examined. The moment curvature input is calculated using equation (3-17) and (3-18) and are shown in Figure 3.8.

Since the influence of the element size on the ultimate moment capacity is interested in this case, the stiffness in state I and state II is not so important. The curvature of the first branch of the moment-curvature diagram in Figure 3.8 χ_I is determined from equation (3-17). Here, $M_{plastic} = 3\,M_{analy}/4$ is chosen.

$$\chi_I = \frac{M_{plastic}}{E_I I} = \frac{\frac{M_{analy}}{3.2}}{E_I I} = \frac{50\times10^3}{30\times10^9 \times \frac{0.2\times0.2^3}{12}} = 0.0125\,\mathrm{m}^{-1} \qquad (3\text{-}17)$$

The curvature of the second branch of the same moment-curvature diagram χ_{II} is determined from equation (3-18).

$$\chi_{II} = \frac{M_{analy}}{\frac{E_{II}}{2} I} = \frac{160 \times 10^3}{6 \times 10^9 \times \frac{0.2 \times 0.2^3}{12}} = 0.2 \text{ m}^{-1} \tag{3-18}$$

The curvature of the third branch χ_{III} is set to 10 so that FE analysis will not stop under certain load application. It means that under the applied vertical displacement-u_z, the curvature received from FE analysis will never pass $\chi_{III} = 10$.

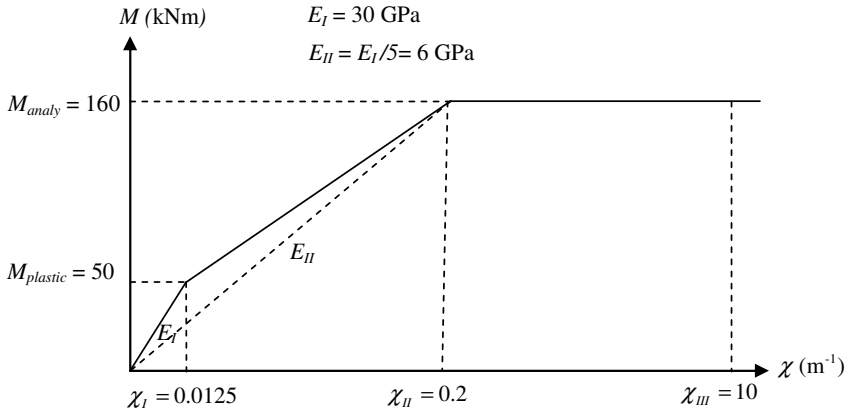

Figure 3.8. Moment curvature relationship input for 3-D beam in elastic-plastic case.

The same element mesh sizes as in Table 3.2 were chosen in order to perform the convergence study and compare with the results obtained from the analysis of 3D beam using bilinear plastic material. The results of the analysis are summarized in Table 3.4 and Figure 3.6. The difference in percentage between analytical solutions and those obtained from FE analysis can also be computed using equation (3-10) and equation (3-11) in Section 3.5.2.

Table 3.4. Moment-curvature model-3D beam elements. Difference in percentage between expected moment capacity and the moment capacity provided by ADINA.

Element size (m)	M_{analy} (kNm)	R_{analy} (kN)	M_{Adina} (kNm)	R_{Adina} (kN)	$\gamma_{elasto,M-3D}$ $[\%]$	$\gamma_{elasto,R-3D}$ $[\%]$
0.2	-160	-100	-166.957	-104.348	-4.35	-4.35
0.1	-160	-100	-163.404	-102.128	-2.13	-2.13
0.05	-160	-100	-161.684	-101.053	-1.05	-1.05
0.025	-160	-100	-160.838	-100.524	-0.52	-0.52
0.01	-160	-100	-160.334	-100.209	-0.21	-0.21

0.005	-160	-100	-160.167	-100.104	-0.10	-0.10

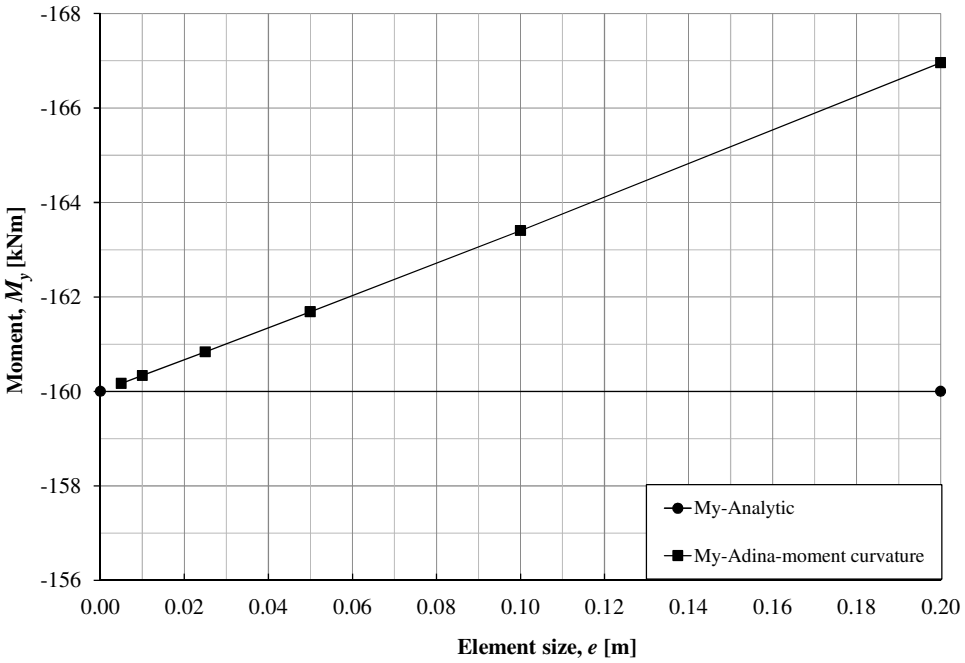

Figure 3.9. Moment capacity for 3D beam in term of element sizes-moment curvature input.

Figure 3.9 is similar to Figure 3.6. From Figure 3.9, it is seen that the moment capacity provided by FE analysis ADINA converges to the analytical solution when a very fine mesh is given.

The lever arm that is based on the moment capacity received from FE analysis in case of moment-curvature relationship in Figure 3.8 can also be determined using equation (3-15) and equation (3-16).

Table 3.5. Moment curvature model-3D beam elements. Lever arm computed from moment capacity received from ADINA.

Element size (m)	M_{analy} (kNm)	R_{analy} (kN)	L_{analy} (m)	M_{Adina} (kNm)	R_{Adina} (kN)	L'_{Adina} (m)	α [–]
0.2	-160	-100	1.6	-166.957	-104.348	1.533	0.333
0.1	-160	-100	1.6	-163.404	-102.128	1.567	0.333
0.05	-160	-100	1.6	-161.684	-101.053	1.583	0.333
0.025	-160	-100	1.6	-160.838	-100.524	1.592	0.334

0.01	-160	-100	1.6	-160.334	-100.209	1.597	0.334
0.005	-160	-100	1.6	-160.167	-100.104	1.598	0.332

From Table 3.5, it is observed that the lever arm computed from moment capacity obtained from FE analysis ADINA is also situated at about one third of the element length from the fixed support, i.e. $L_\alpha = L_{ele}/3$.

The comparison between plastic material and moment-curvature model using 3D beam has been made. The comparison showed that the same response was obtained.

3.5.4 Alternative methods for plastic rotation of cantilever beam

Since the main purpose of this thesis work is to determine the distribution width, it is also essential to determine the plastic rotation of the structure studied. Due to this, the plastic rotation of the cantilever beam in Figure 3.10 was examined. When subjected to an increasing deformation, a plastic rotation developed in the element next to the fixed support. However, since this cantilever beam is fixed at the support, it is not possible to determine the plastic rotation at that fixed point directly from the FE program ADINA. The reason is that when modeling the structure, the node at the fixed support of the beam was fixed. Therefore, the rotation at that point is zero. Although it is not possible to determine the plastic rotation of the cantilever beam studied directly from the FE program ADINA, there are three alternative methods that can be used to determine the plastic rotation of this cantilever beam. The first and the second method are based on plastic curvature while the third method depends on displacement and rotation relationship. For the description of these methods, see APPENDIX E.

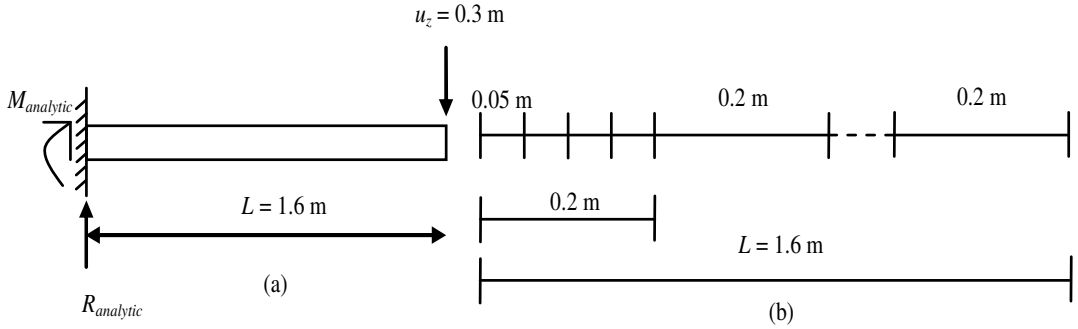

Figure 3.10. (a) Geometry of the cantilever beam (b) two different meshes.

The difference in percentage between method 1, method 2 and method 3 are calculated from equation (3-19), equation ((3-20) and equation (3-21), respectively.

$$\gamma_{12} = 100 \cdot \frac{\left|\theta_{pl,method1}\right| - \left|\theta_{pl,method2}\right|}{\left|\theta_{pl,method1}\right|} \tag{3-19}$$

$$\gamma_{13} = 100 \cdot \frac{\left|\theta_{pl,method1}\right| - \left|\theta_{pl,method3}\right|}{\left|\theta_{pl,method1}\right|} \tag{3-20}$$

$$\gamma_{23} = 100 \cdot \frac{\left|\theta_{pl,method2}\right| - \left|\theta_{pl,method3}\right|}{\left|\theta_{pl,method2}\right|} \tag{3-21}$$

In this Section, only the cantilever beam with two different meshes, as shown in Figure 3.10, was examined. For the cantilever beam with single mesh, see APPENDIX E.

Table 3.6 and Table 3.7 summarise the results of the plastic rotation of the studied cantilever beam in Figure 3.10 with bilinear moment curvature input in Figure E.5 and trilinear moment curvature input in Figure E.8 of APPENDIX E. The results in Table 3.6 and Table 3.7 are taken from the results in Table E.2 and Table E.3 of APPENDIX E.

Table 3.6. Comparisons of plastic rotation of the cantilever beam studied between the three methods using bilinear moment curvature relationship model.

Prescribed displacement u_{pre} (mm)	120	150	180	195	210	300
Reaction force R (kN)	70.3	87.9	101	101	101	101
$\theta_{pl,1} = \sum_{0}^{i} \chi_{pl,i} \cdot \Delta x_i$ (10^{-3} rad)	0	0	4.79	14.3	23.7	80.6
$\theta_{pl,2} = \frac{\chi_{pl,1} \cdot l_{el,1}}{2}$ (10^{-3} rad)	0	0	5.04	14.5	24	80.8
$\theta_{pl,3} = \frac{u}{L} - \frac{\chi_{ela} \cdot L}{3}$ (10^{-3} rad)	0	0	5.83	15.2	24.6	80.8
γ_{12} [%]	-	-	-5.3	-1.7	-1.1	-0.3
γ_{13} [%]	-	-	-21.7	-6.6	-3.5	-0.3
γ_{23} [%]	-	-	-15.6	-4.7	-2.4	0

From Table 3.6 it is seen that method 2 provides a larger plastic rotation than method 1 and method 3. The difference in percentage between method 1, method 2 and method 3 for plastic rotation of the cantilever beam converges when the prescribed displacement becomes larger and larger. As a result, it is concluded that method 2 is conservative method that is suitable to approximately determine the plastic rotation of the studied cantilever beam. Therefore method 2 will be used to determine a plastic rotation of the cantilever slab in Chapter 4.

Table 3.7. Comparisons of plastic rotation of the cantilever beam studied between the three methods using trilinear moment curvature relationship model.

Prescribed displacement u_{pre} (mm)	120	150	180	195	210	300
Reaction force R (kN)	90	101	101	101	101	101
$\theta_{pl,1} = \sum_{0}^{i} \chi_{pl,i} \cdot \Delta x_i$ (10^{-3} rad)	0	3.12	22.1	31.5	41	97.9
$\theta_{pl,2} = \frac{\chi_{pl,1} \cdot l_{el,1}}{2}$ (10^{-3} rad)	0	3.29	22.2	31.7	41.2	98
γ_{12} [%]	-	-5.38	-0.76	-0.53	-0.41	-0.17

Like bilinear moment-curvature results in Table 3.6, it is seen that difference for plastic rotation between method 1 and method 2 converges for large prescribed vertical displacement although method 2 still gives larger plastic rotation compared to method 1. Therefore method 2 will be used to determine a plastic rotation of the cantilever slab in Chapter 4.

It is also noted that method 3 is only valid for bilinear moment-curvature input. This method cannot be used with multi-linear moment curvature input for elasto-plastic case since it assumes a linear response prior to yielding.

4 Cantilever slab

4.1 Introduction

Since there is no analytical solution for cantilever slabs under point loads like in Figure 2.23, various analysis of cantilever slabs are performed using FE program ADINA in order to better understand its behaviour. The slab studied is first analysed with shell elements since the shell element is the most appropriate element type that are used for slab analysis. The reader can refer to APPENDIX A for further description of shell element. Since the aim of this thesis is to study the distribution of moments and shear forces, it is necessary to perform an analysis that can capture the behaviour of the slabs both in service limit state (load which is lower than the load that will cause yielding of the reinforcement) and in ultimate limit state (load that cause the yielding of reinforcement), i.e. to capture its response from uncracked state until the failure of the structure. In order to do so, different material models such as linear elastic isotropic and orthotropic material, and bilinear and multi-linear elasto-plastic models are used so that it is possible to investigate the response of the slab in different states.

4.2 Geometry and loading

An 8 m long and 1.6 m wide cantilever slab supported along one of the long edges and free at the other is subjected to a point load 200 kN, illustrated in Figure 4.1. In this report, the analysis was carried out using the student version of the FE software ADINA with a maximum of 900 nodes. As there is a restriction of the number of nodes used in the analysis, the symmetric cantilever slab with the dimensions shown in Figure 4.1c was studied instead.

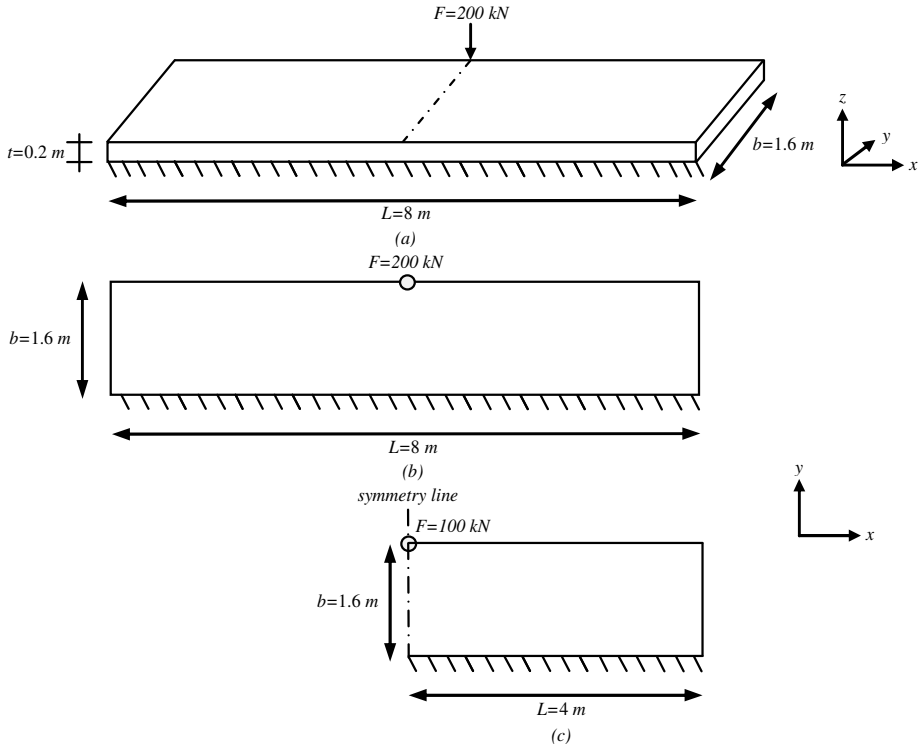

Figure 4.1. The dimension of the studied cantilever slab: (a) perspective view (b) 2D view (c) symmetrical geometry 2D view.

Five different result lines, L_1, L_2, L_3, L_4 and L_5, in plan as shown in Figure 4.2 were chosen in order to provide a better understanding of how different parts of the slab respond due to point load.

Where L_1 = result line along symmetry line.

L_2 = result line located 0.8 m away from symmetry line.

L_3 = result line along long free edge.

L_4 = result line 0.8 m away from fixed edge.

L_5 = result line along fixed edge.

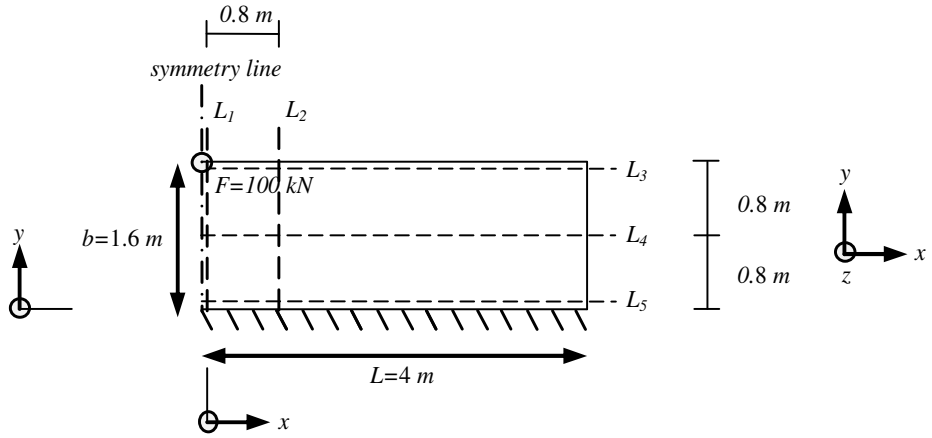

Figure 4.2. Result lines for moment and shear force distribution.

It is also noted that these five result lines were chosen as the interested lines from the very beginning of the study in order to understand structural response of the studied slab, but only L_1, L_2, L_4 *and* L_5 were used.

4.3 Isotropic case

4.3.1 Slab with shell elements

In this report, 4-nodes shell elements were used to analyses the slab in Figure 4.2. Since there is no analytical solution available for this type of slab, two different element sizes of shell elements, 0.1 m and 0.2 m element sizes for both *x*- and *y*-direction, were chosen to model the slab so that it was possible to perform a convergence study.

For an isotropic material model, Hooke's law in equation (2-2) applies. This model assumes linear elastic response of the slab. A Young's modulus $E_{c,I} = 30\ GPa$, corresponding to the stiffness of state I and a Poisson's ratio $\nu = 0$ shown in Figure 4.3 were used for this analysis.

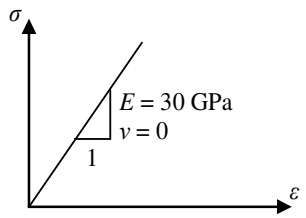

Figure 4.3. Material data used in ADINA for the isotropic case.

4.3.1.1 Moment

The moment distribution m_y along lines L_1 *and* L_5 for 0.1 m and 0.2 m element sizes of shell element are plotted in Figure 4.4a and Figure 4.4b, respectively. As can be seen, the moment distribution m_y along both lines L_1 *and* L_5 of 0.1 m shell element sizes coincided well with those of 0.2 m shell element sizes; the deviation of m_y were almost negligible.

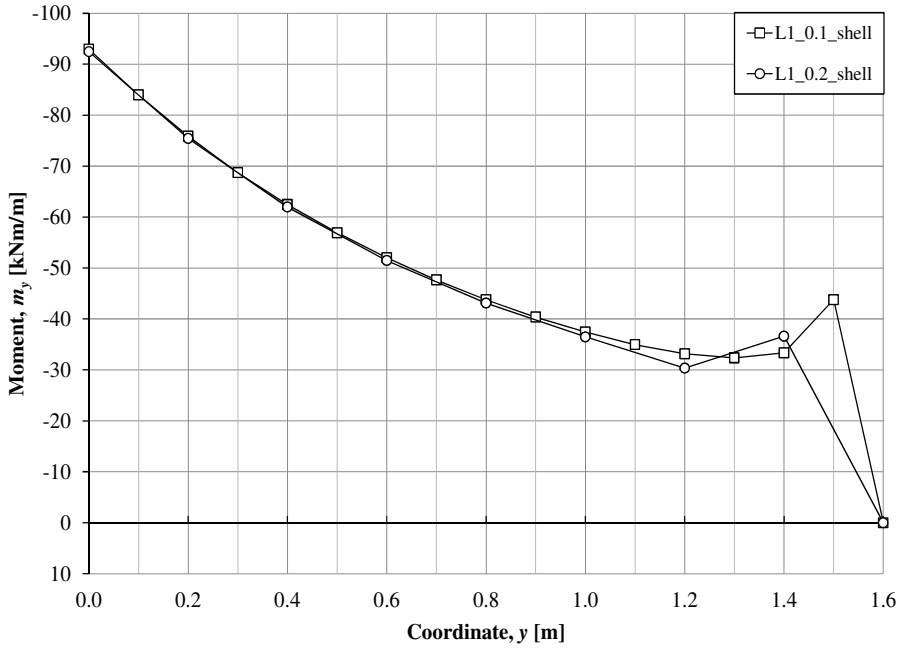

(a)

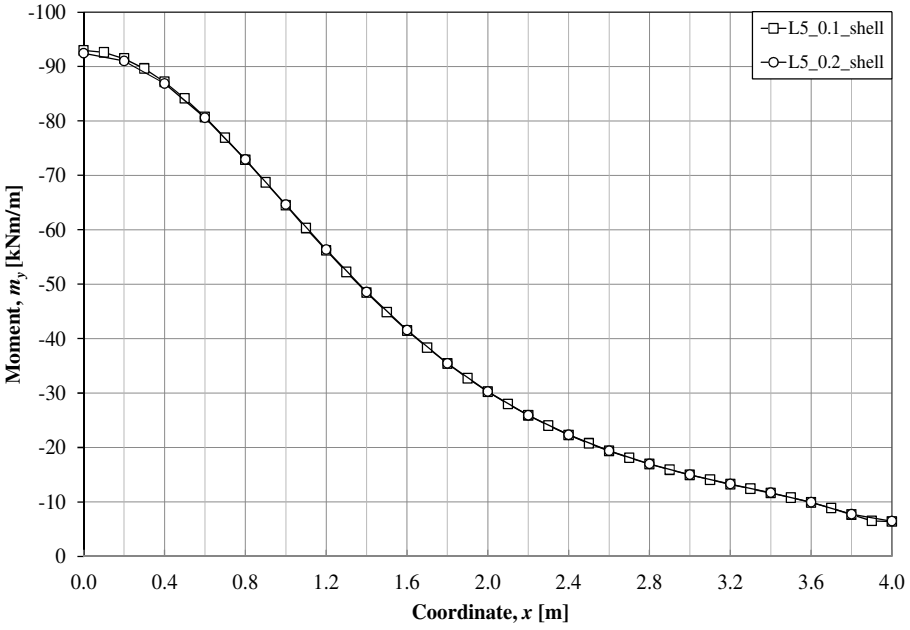

(b)

Figure 4.4. Moment distribution m_y from FE-linear elastic analysis, 0.1 m shell elements and 0.2 m shell elements with Poisson's ratio ν = 0: (a) m_y along L_1 (b) m_y along L_5.

The sum of the reaction moments along the fixed supports for both cases was equal to the expected results as shown in equation (4-1).

$$\begin{cases} \sum_{i=0}^{L_5} m_{y,FE} = 160\,\text{kNm} \\ M_{y,analy} = F \cdot b = 100 \cdot 1.6 = 160\,\text{kNm} \end{cases} \tag{4-1}$$

Therefore, the analysis of the cantilever slab using shell elements with linear elastic material model is believed to be correct. From Figure 4.4b, it is seen that the maximum moment $m_{y,max}$ obtained from the FE analysis is located next to the symmetry line as large portions of the applied load are transferred along the symmetry line toward the closet point of the fixed boundary along L_5. The remaining parts of the load will be distributed along their load paths to the fixed support and the magnitude of the moment m_y therefore gradually decreases as shown in Figure 4.4b. In Figure 4.4a, there is a jump at about x = 1.4 m to x = 1.6 m and x = 1.5 m to x = 1.6 m for 0.1 m and 0.2 m element sizes of shell element, respectively.

4.3.1.2 Shear

The distribution of shear force transferred in y direction, v_y, along lines L_5 for 0.1 m and 0.2 m element sizes of shell element is compared in Figure 4.5 and from this it can be concluded that the difference between the two models were small.

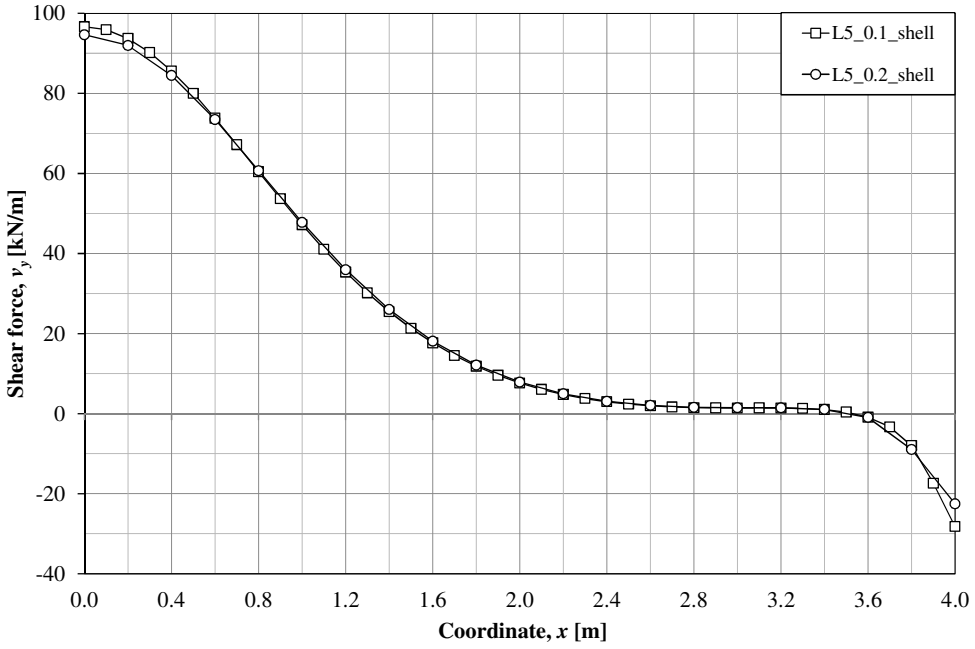

Figure 4.5. Shear force distribution v_y along L_5 from FE-linear elastic analysis, 0.1 m shell elements and 0.2 m shell elements with Poisson's ratio ν = 0.

The areas below both curves of the shear force distribution in Figure 4.5 were equal to the expected results as shown in equation (4-2).

$$\begin{cases} \sum v_{y,L_5,FE} = 100\ \text{kN} \\ F = 100\ \text{kN} \end{cases} \tag{4-2}$$

From Figure 4.5, it is seen that the part of the slab closet to the point load was subjected to the maximum shear $v_{y,max}$ and the magnitude of the shear force v_y gradually decreased along L_5 from the symmetry line to the free edge. In Figure 4.5, $v_y < 0$ at about $x = 3.6$ m to $x = 4$ m for both 0.1 m and 0.2 m element sizes of shell element. The reason for this disturbance is due to the torsional effect at the free edge of the slab. It might also indicate uplifting of the part of the slab in that region. In order to investigate this disturbance, a parametric study in term of the change of the length of the studied slab was performed. Two more analyses of slab using shell elements as shown in APPENDIX D were conducted for the shear forces distribution along L_5.

4.3.1.3 Vertical displacement

Like the moment distribution m_y and the shear forces distribution v_y illustrated in Figure 4.4 and Figure 4.5, respectively, the difference between the vertical displacement u_z along L_1 and L_2 in the two models studied is very small, see Figure 4.6. There is a large vertical displacement under the applied load. The vertical displacement gradually decreases toward the fixed support where $u_z = 0$.

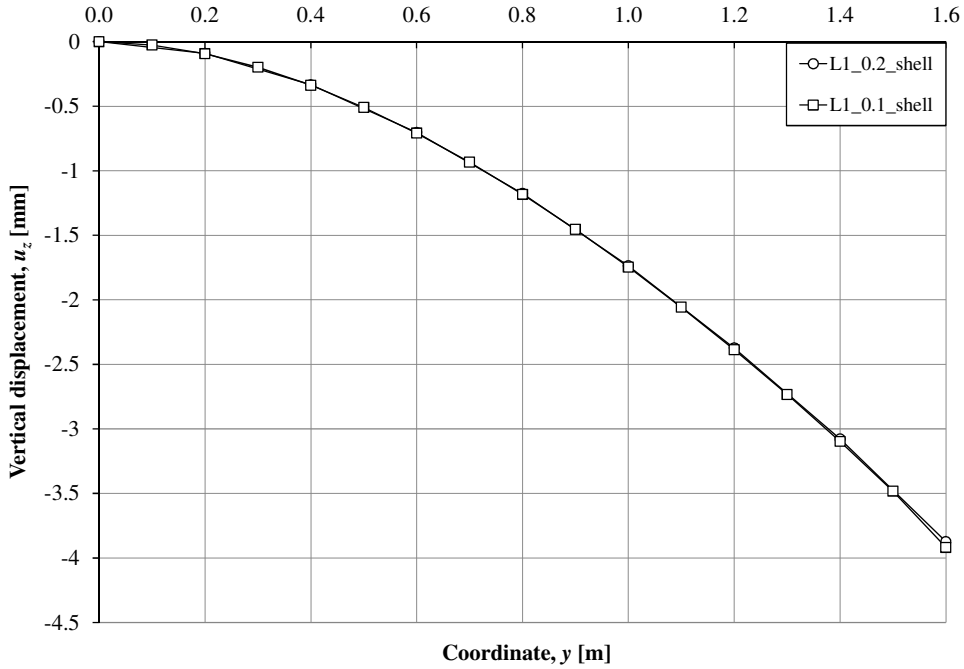

Figure 4.6. Vertical displacement u_z along L_1 from FE-linear elastic analysis, 0.1 m shell elements and 0.2 m shell elements with Poisson's ratio ν = 0

Based on the results received from linear FE analysis in Figure 4.4, to Figure 4.6, it is concluded that shell elements are the most appropriate elements for the analysis of the cantilever slab studied in linear elastic analysis. As the 0.1 m shell elements and 0.2 m shell elements sizes provide almost identical results, it is reasonable to consider these results comparable with analytical solutions. It is concluded that it is sufficient to use

only 0.2 m shell elements, and that these results can be used as a reference for comparison with beam grillage of beam elements in Section 4.3.2. For the moment distributions, shear forces and displacement of other result lines, reader can refer to APPENDIX C.

4.3.2 Slab with beam grillage model

A beam grillage model is composed of beam elements in both *x*- and *y*-direction which intersect each other at common intersection points, see Figure 4.7. The beam grillage model can be used to simulate the behaviour of a slab with the beams in *x*- and *y*-direction representing the strips in *x*- and *y*-direction of the slab, respectively.

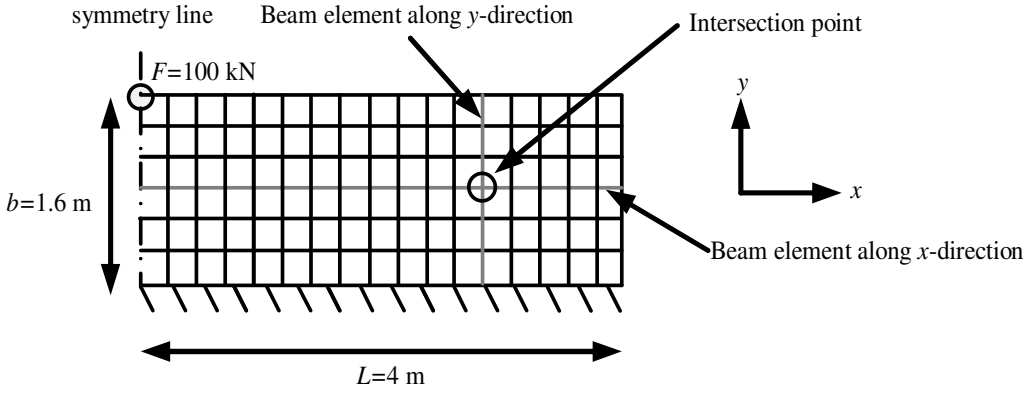

Figure 4.7. Arrangement of beam grillage elements in slab model

In order to make a comparison between the result from FE linear elastic analysis for shell elements and beam elements, the same cantilever slab in Figure 4.2 with the same material data as in Figure 4.3 are examined using beam grillage model. Three different element sizes of beam elements, 0.1 m, 0.2 m and 0.4 m element sizes for both *x*- and *y*-direction, are chosen to model the slab so that it is possible to perform a convergence study.

In ADINA FE program, beams can be modelled by 2D beam elements or 3D beam elements as described in Chapter 3 and APPENDIX A. Since the slab studied also will obtain torsional effects, torsional response needs to be included for the beam elements and, consequently, 3D beam element is the appropriate choice in this case.

4.3.2.1 Moment

Based on the results shown in Figure 4.8, it can be seen that moment distribution m_y along both L_1 and L_5 depends on the element sizes. It is seen that there is a large difference in m_y along both L_1 and L_5 when using beam grillage model with different element mesh sizes.

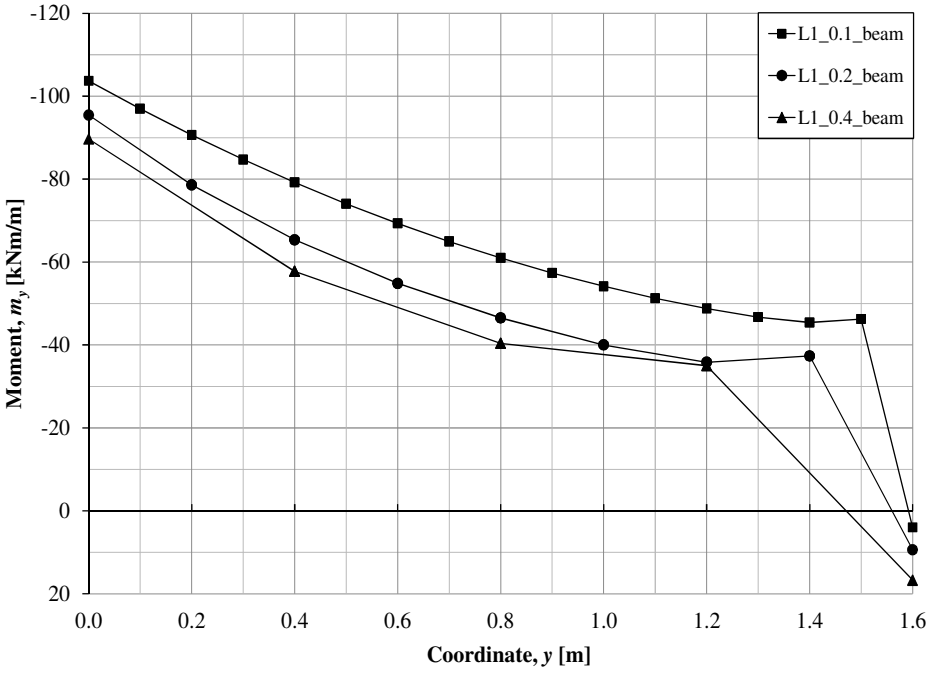

(a)

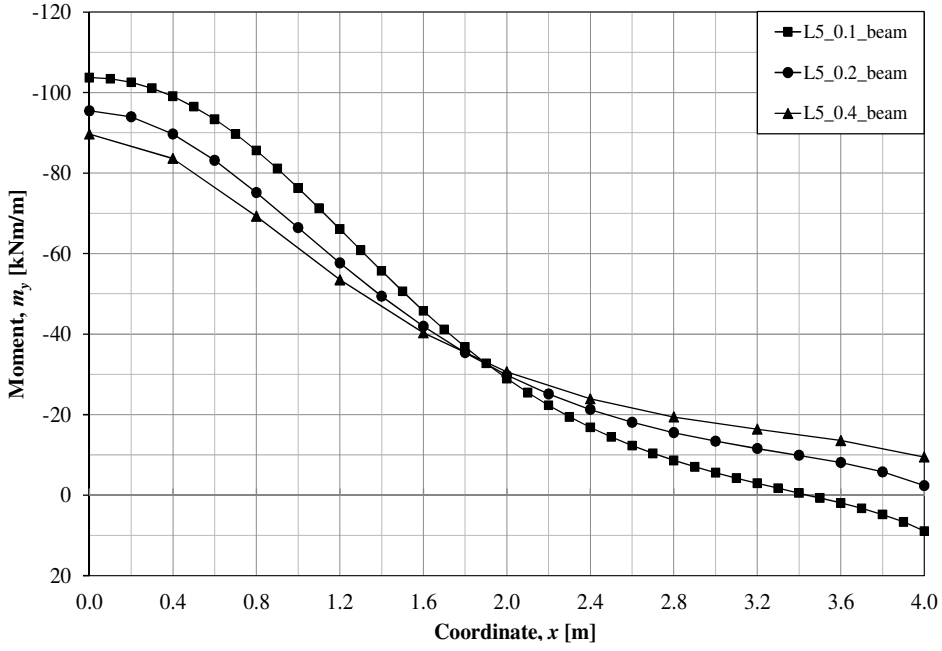

(b)

Figure 4.8. Moment distribution m_y from FE-linear elastic analysis, 0.1 m beam grids, 0.2 m beam grids and 0.4 m beam grids elements with Poisson's ratio ν = 0: (a) m_y along L_1 (b) m_y along L_5.

Since the beams are connected to each other, there is an additional stiffness added to the loaded beam from the crossing beams at the intersection points due to the torsional effect. A coarse mesh means that the beams will have a larger width, which will affect the size of their torsional difference. Thus, the torsional stiffness is mesh dependence. This can be further described by using equation (4-3) for the torsional stiffness of rectangular a cross section.

$$K_v = c_1 t b^3 \tag{4-3}$$

Where K_v = torsional stiffness of a rectangular cross-section.

c_1 = factor depending on the height and width of the rectangular cross-section determined from Table 4.1.

t = height of a rectangular cross-section

b = width of a rectangular cross-section

Table 4.1. The factor c_1 depends on the ratio between the height, t, and width, b, of the rectangular cross-section.

t/b	1	2	4	∞
c_1	0.141	0.229	0.281	0.333

For instance, if the width of the cross-section decreases with a factor of two, the torsional stiffness K_v decreases with a factor of eight.

$$K_v = c_1 t\left(\frac{b}{2}\right)^3 = \frac{c_1 t b^3}{8} \tag{4-4}$$

From Figure 4.8, it can be concluded that a decrease in grid mesh size does not lead to convergence with respect to the analysis results. Instead, it was found that when the mesh was made more dense, the deflection of the slab increased; this is a consequence of the reduced torsional stiffness of the narrower beam elements It is also observed that the load distribution on the studied slab, when using beam elements, is similar to those of the slab when using shell elements.

4.3.2.2 Shear

The shear distribution v_y along lines L_5 for 0.2 m and 0.4 m beam element sizes, see Figure 4.9 is close to each other. Along this line, the shear distribution v_y of 0.2 m and 0.4 m beam element deviate a lot from shear distribution v_y of 0.1 m beam element.

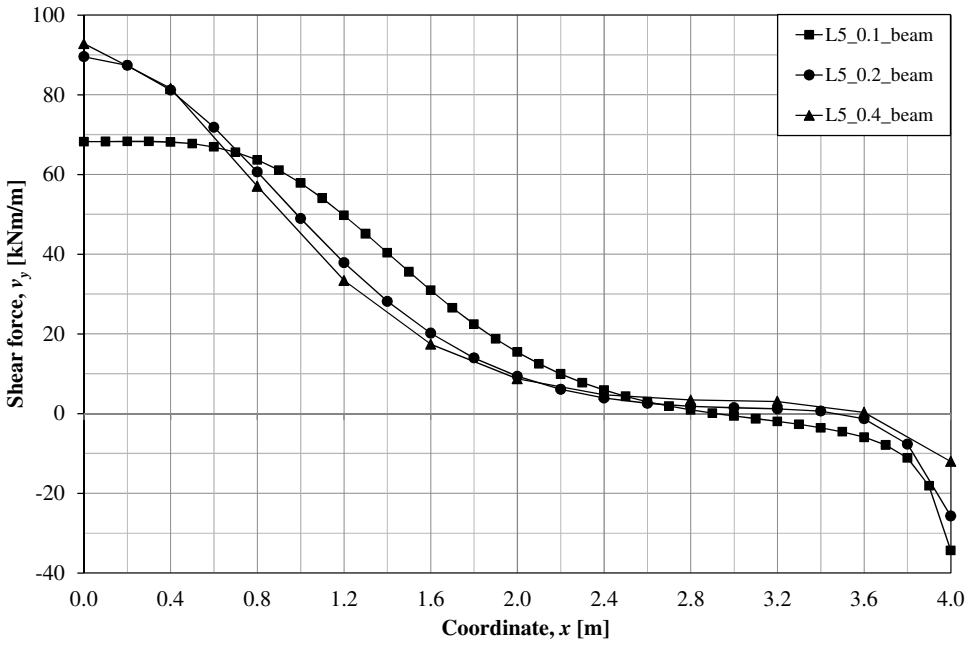

Figure 4.9. Shear force distribution v_y along L_5 from FE-linear elastic analysis 0.1 m beam elements, 0.2 m beam elements and 0.4 m beam elements with Poisson's ratio ν = 0.

Similarly to the shear distribution with shell elements in Figure 4.5, it can be seen from Figure 4.9 that $v_y < 0$ at about $x = 3.6$ m to $x = 4$ m for 0.2 m and 0.4 m element sizes of beam element and $v_y < 0$ at about $x = 2.8$ m to $x = 4$ m for 0.1 m beam element. The reason for this disturbance is believed to be the same as the one stated in Section 4.3.1.2.

4.3.2.3 Vertical displacement

Similar to the moment distribution m_y in Figure 4.8, vertical displacement u_z along L_1 in Figure 4.10 varies due to the change of element sizes. The maximum vertical displacement u_z occurs under the applied load. The vertical displacement-u_z decreases gradually toward the fixed support where $u_z = 0$.

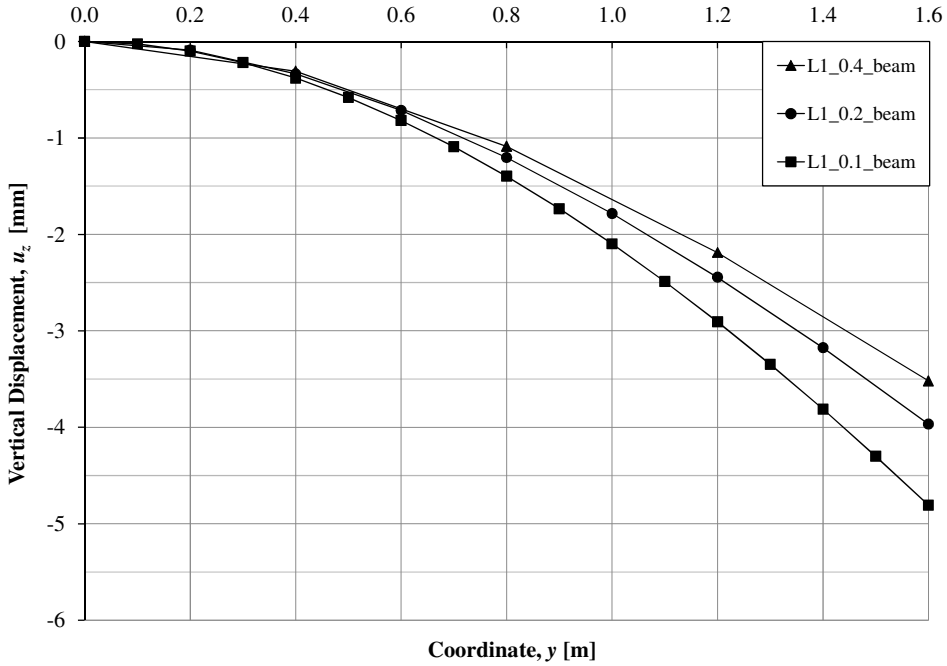

Figure 4.10. Vertical displacement u_z along L_1 from FE-linear elastic analysis, 0.1 m beam element, 0.2 m beam element and 0.4 m beam element with Poisson's ratio ν = 0.

Since the results received from beam grids model analyses greatly depend on the mesh sizes used, it is not possible to use the beam grids model directly for the analysis of the cantilever slab studied. One way to deal with such a problem is to compare the results of beam elements with different mesh sizes with the results from FE-analysis of the same slab with shell elements. The beam grillage model with a certain mesh size that provides the results most similar to those of the shell elements will be used for further analysis, i.e. orthotropic and elasto-plastic analysis.

To sum up, it is recommended to use shell elements for the analysis of the studied cantilever slab in linear elastic analysis. It is also possible to analyses the cantilever slab studied in linear elastic case using beam grid models if the appropriate element meshes size is chosen in such a way that the torsional stiffness provided by that beam element sizes is close to the torsion of the slab using the shell elements.

4.3.3 Comparisons between shell elements and beam elements

As mentioned in Section 4.3.2, beam elements cannot be used directly for the linear elastic analysis of the cantilever slab studied as the results obtained from FE analysis greatly depends on the element mesh sizes. From Figure 4.11a and Figure 4.12a, it can be seen that 0.2 m beam element sizes provides the results most similar to that of 0.2 m shell element. The different in percentage of moment distribution m_y between 0.2 m shell elements and 0.2 m beam elements are computed as:

$$\gamma = \frac{\left|m_{y,shell}\right| - \left|m_{y,beam}\right|}{\left|m_{y,shell}\right|} \times 100 \tag{4-5}$$

The difference in percentage between these two models along L_1 and L_5 is generally $|\gamma| < 10$ %, see Figure 4.11b and Figure 4.12b, respectively. These differences are believed to be acceptable. Therefore, the conclusion can be drawn that 0.2 m beam element sizes can be used for the analysis of the previous studied cantilever slab in orthotropic case and elasto-plastic case. It should be remarked that γ increases with increasing x and y due to the decrease of m_y along those lines. Therefore, a large value of γ is obtained when m_y is small. For instance, $\gamma = -8.10^{14}$ in Figure 4.11b at $x = 1.6$ m since $m_{y,shell} = 0$ in Figure 4.11a at $x = 1.6$ m.

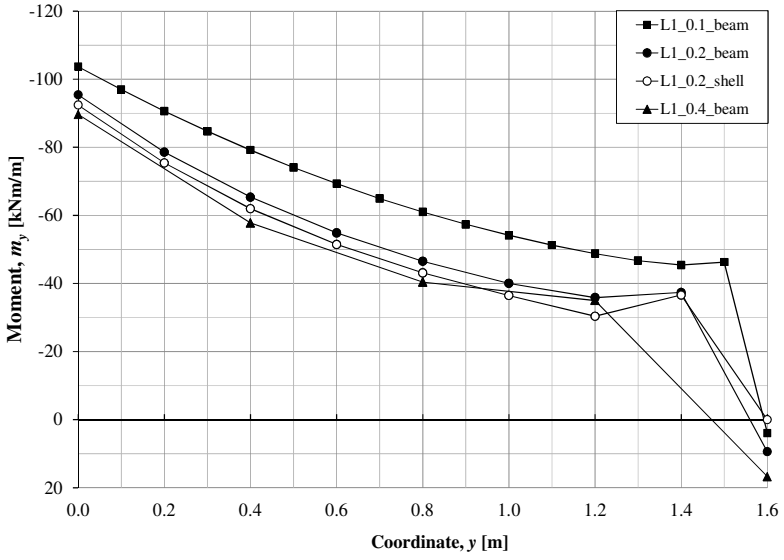

(a)

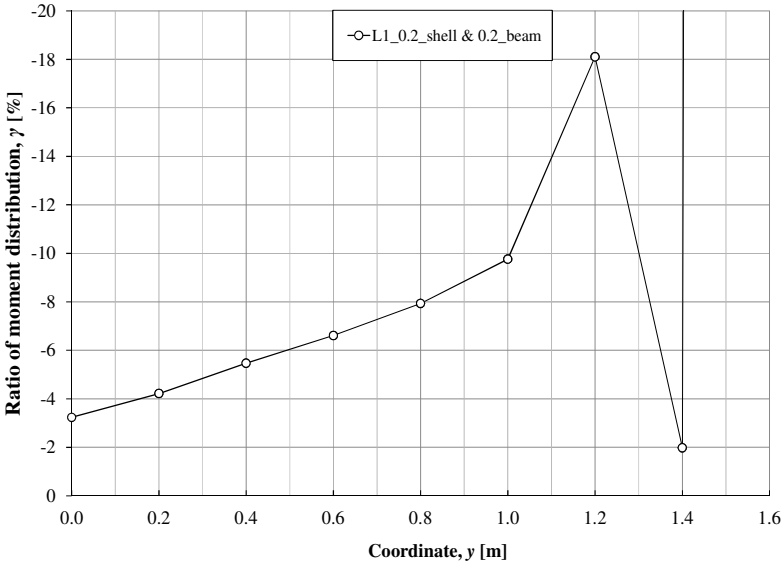

(b)

Figure 4.11. Moment distribution m_y from linear elastic FE-analysis with Poisson's ratio ν = 0: (a) comparisons between 0.1 m, 0.2 m, 0.4 m beam elements and 0.2 m shell elements along L_1 (b) difference in percentage between 0.2 m beam elements and 0.2 m shell element along L_1.

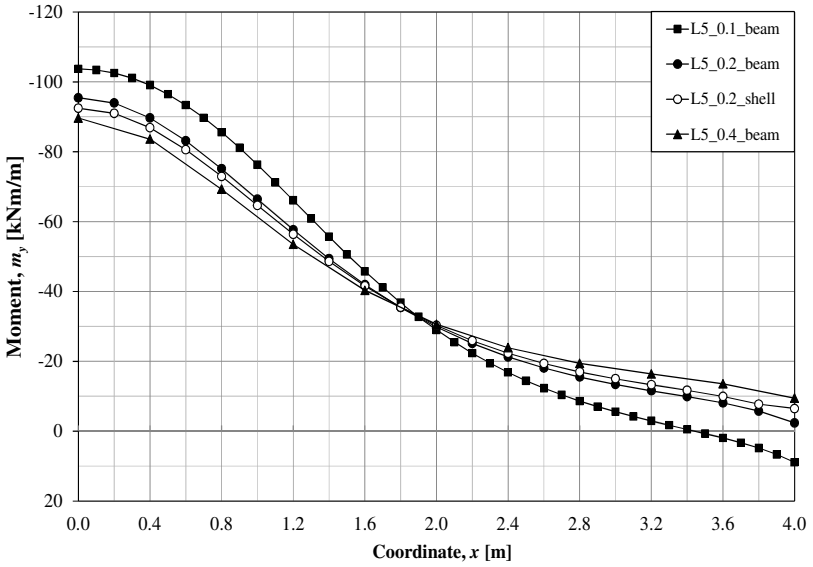

(a)

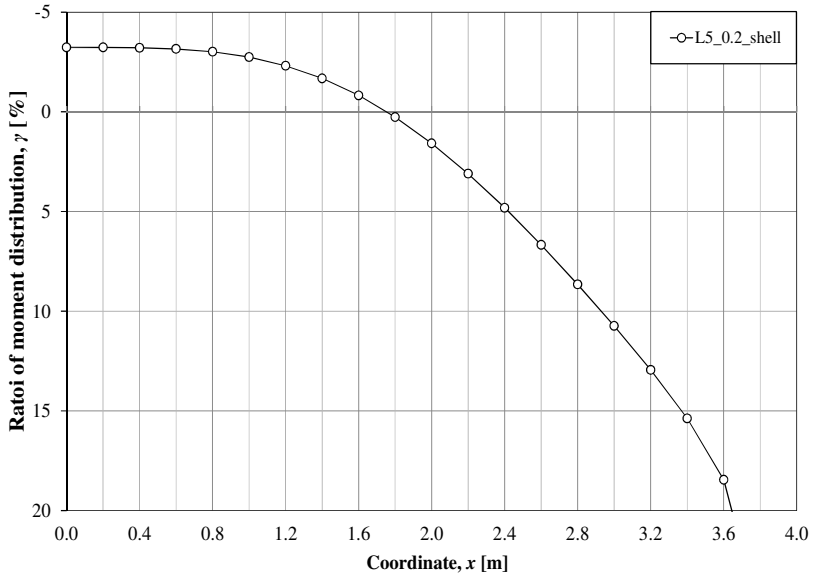

(b)

Figure 4.12. Moment distribution m_y from linear elastic FE-analysis with Poisson's ratio v = 0: (a) comparisons between 0.1 m, 0.2 m, 0.4 m beam elements and 0.2 m shell elements along L_5 (b) difference in percentage between 0.2 m beam elements and 0.2 m shell element along L_5.

4.4 Orthotropic case

4.4.1 Slab with shell elements

4.4.1.1 Convergence study

The aim of this thesis is also to examine the response of the slab due to the change of stiffness in different directions. Therefore, it is necessary to perform an orthropic analysis of the same slab studied in Figure 4.2, but using an orthotropic material input given, in Table 4.2. In order to be sure that reinforced concrete slab modelled with

orthotropic material using shell elements still provides a reliable result, 0.1 m and 0.2 m element sizes of shell element are examined. This way it is possible to compare the result of the slab with beam elements with those of shell elements received from the FE analysis.

For the analysis of orthotropic slab using shell elements, three stiffness values in *x*-direction is chosen while the stiffness in *y*-direction is kept constant, i.e. $E_x = 0.2,\ 1,\ 5E_y$.

In order to be able to run the analysis of shell element with orthotropic material in FE program ADINA, shear modulus, Young's modulus and Poisson's ratio in different directions are need. The shear modulus can be determined as:

$$G_{xy} = \frac{E_x E_y}{E_x + E_y + 2\nu_{xy} E_z} \tag{4-6}$$

$$G_{xz} = \frac{E_x E_z}{E_x + E_z + 2\nu_{xz} E_y} \tag{4-7}$$

$$G_{yz} = \frac{E_y E_z}{E_y + E_z + 2\nu_{yz} E_z} \tag{4-8}$$

The material data input when analyzing the studied elastic orthotropic slab with shell element in FE program ADINA is summarized in Table 4.2.

Table 4.2 Material data for orthotropic analysis with shell elements

	1 ($E_x = E_y$)	2 ($E_x = 0.2E_y$)	3 ($E_x = 5E_y$)
$E_x, (\text{GPa})$	30	6	150
$E_y, (\text{GPa})$	30	30	30
$E_z, (\text{GPa})$	30	30	30
$\nu_{xy}, \nu_{xz}, \nu_{yz}$	0	0	0
$G_{xy} = \frac{E_x E_y}{E_x + E_y + 2\nu_{xy} E_z}, (\text{GPa})$	15	5	25
$G_{xz} = \frac{E_x E_z}{E_x + E_z + 2\nu_{xz} E_y}, (\text{GPa})$	15	5	25
$G_{yz} = \frac{E_y E_z}{E_y + E_z + 2\nu_{yz} E_z}, (\text{GPa})$	15	15	15

The parameter E_z is not important in this case as the effect of this parameter is very small.

The results of vertical displacement u_z in Figure 4.13 and moment distribution m_y in Figure 4.14 show that there are almost no differences in value between these two element sizes when using shell elements. The difference between the maximum vertical displacement $u_{z,max}$ for $E_x = 0.2,\ 1,\ 5E_y$ are 1.1 %, 1.2 % and 1.2 % and the difference between the maximum value of $m_{y,max}$ for $E_x = 0.2,\ 1,\ 5E_y$ are 1.1 %, 0.6 % and 0.3 %, respectively. It is believed that shell element is an appropriate choice for the elastic orthotropic analysis of slab. As deviation between 0.1 m and 0.2 m shell element are considered negligible in this case, it is sufficient to use 0.2 m shell element in order to compare with the results obtained from orthotropic analysis of the same slab with beam element.

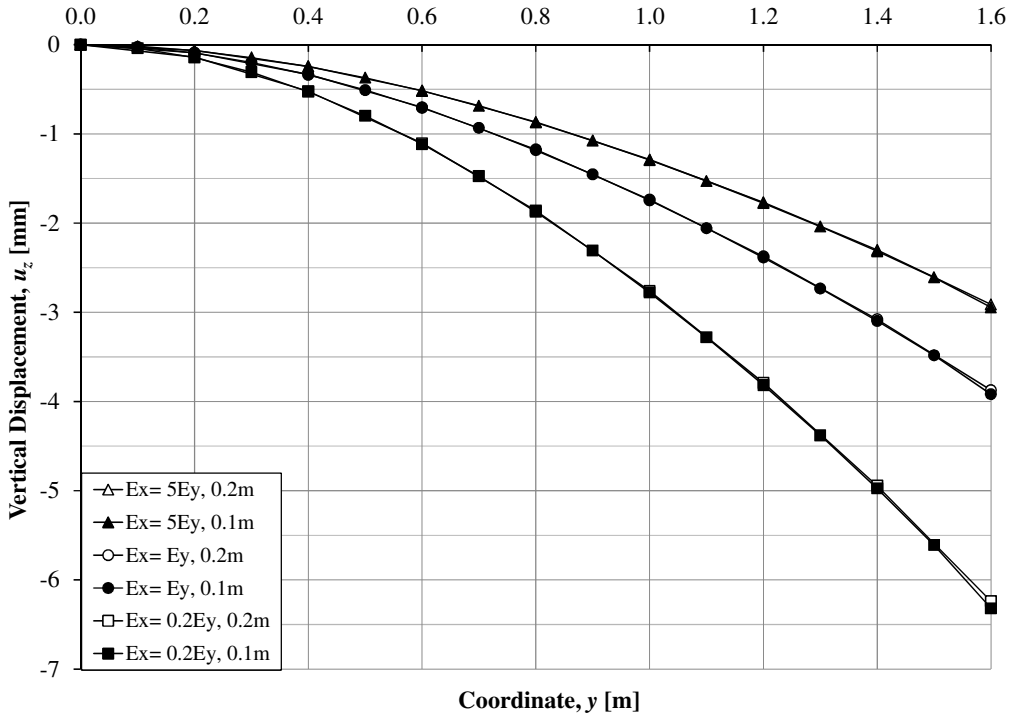

Figure 4.13. Comparisons of vertical displacement u_z from FE-elastic orthotropic with Poisson's ratio ν = 0 between 0.1 m and 0.2 m shell along L_1.

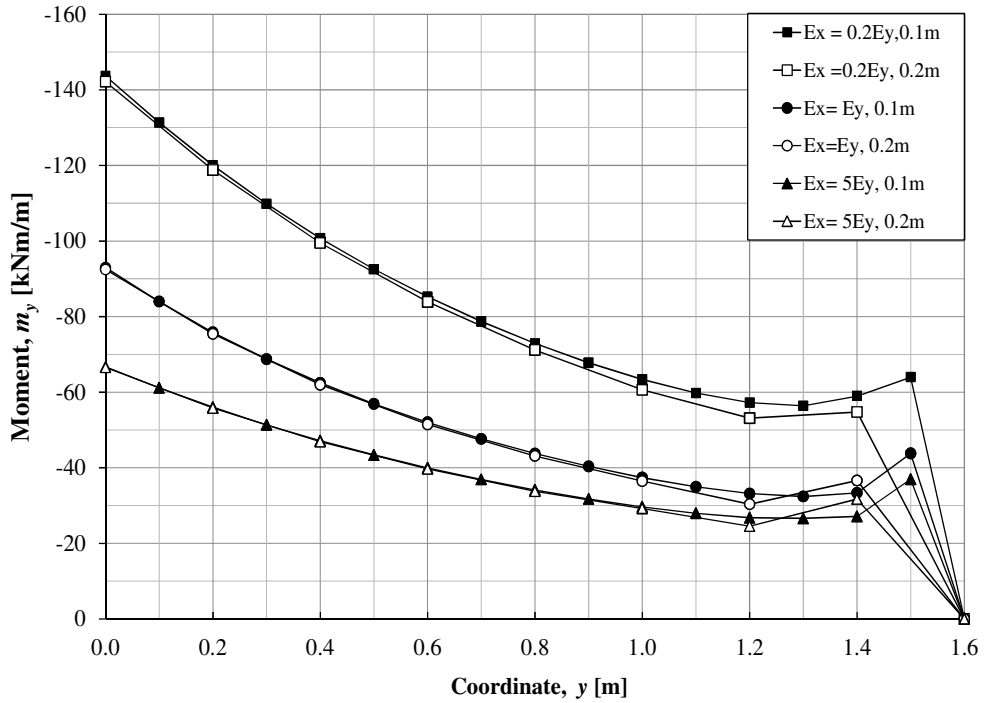

(a)

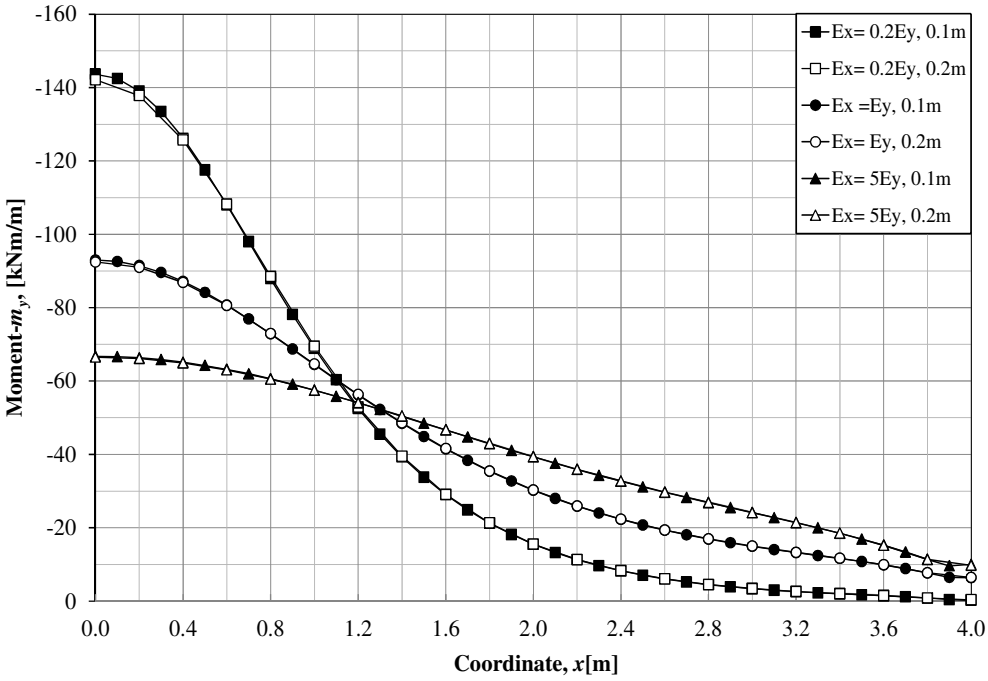

(b)

Figure 4.14. Comparisons of moment distribution m_y from FE-elastic orthotropic with Poisson's ratio ν = 0 between 0.1 m and 0.2 m shell: (a) m_y along L_1 (b) m_y along L_5.

4.4.2 Structural response of orthotropic slab

4.4.2.1 Moment

In order to investigate a structural response due to the change of stiffness of the studied cantilever slab with orthotropic material input in Table 4.2, the orthotropic slab with $E_x = 0.1,\ 0.2,\ 0.5,\ 1{,}2,\ 5,\ 10E_y$ are chosen to analyse with 0.2 m shell element.

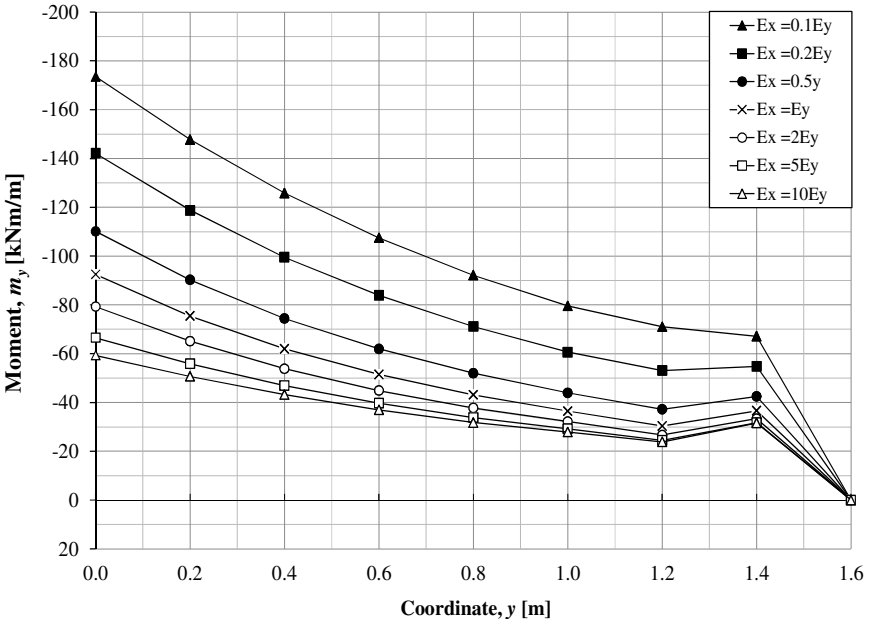

(a)

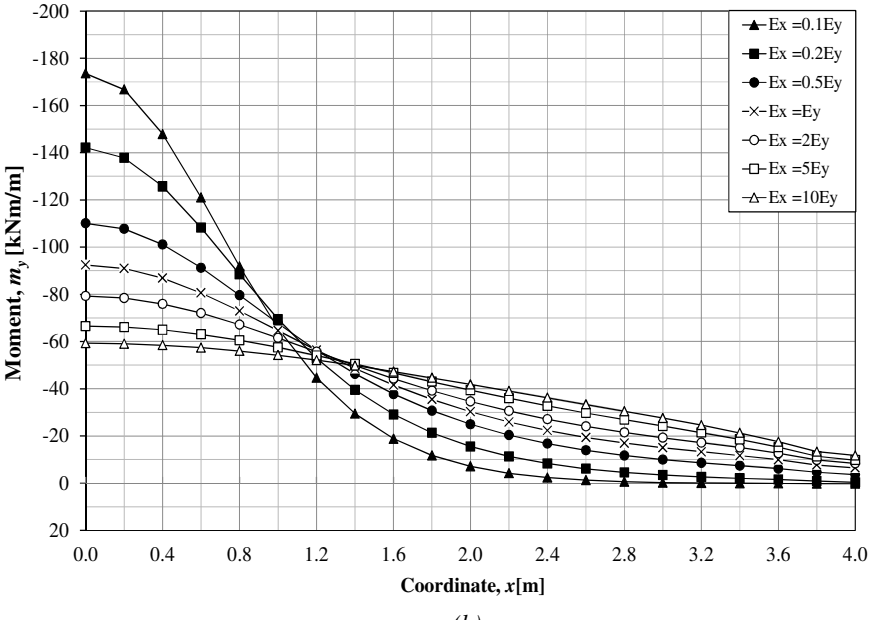

(b)

Figure 4.15. Moment distribution m_y from FE-elastic orthotropic with Poisson's ratio $\nu = 0$ using 0.2 m shell: (a) m_y along L_1 (b) m_y along L_5.

From Figure 4.15a, it can be seen that when E_y is greater than E_x, i.e. the elements along the *y*-direction are stiffer than the elements along *x*-direction, the m_y distribution along L_1 increases. Since the elements in *y*-direction become stiffer, a larger load portion tries to transfer through the stiff direction. The load distribution in the *y*-direction is stronger than the load distribution in the *x*-direction. From Figure 4.15b, it is clearly seen that in case of the elements in the *y*-direction is stiffer than the elements in the *x*-direction, a large portion of the load is carried by the elements close to the middle of the slab. Only a small part of the load is resisted by the elements located further away from the load as there is less load distribution in the *x*-direction. It can also be noticed that the moment distribution m_y decreases sharply and is not well distributed along the fixed boundary.

In case of the elements in the *x*-direction are stiffer than the elements along the *y*-direction, Figure 4.15a shows that the m_y distribution along L_1 decreases gradually. Further, Figure 4.15b illustrates that moment m_y along L_5 is more distributed along the fixed support. This smooth distribution is less severe. The elements located close to the middle of the slab still resist larger loads than the elements located further away, but the difference is much smaller than the case when the *y*-direction is stiffer than the *x*-direction.

The ratio of moment distribution γ in equation (4-9) is compared in Figure 4.16.

$$\gamma = 100 \times \frac{\left|M_{Ex=Ey}\right| - \left|M_{Ex=\alpha Ey}\right|}{\left|M_{Ex=Ey}\right|} \tag{4-9}$$

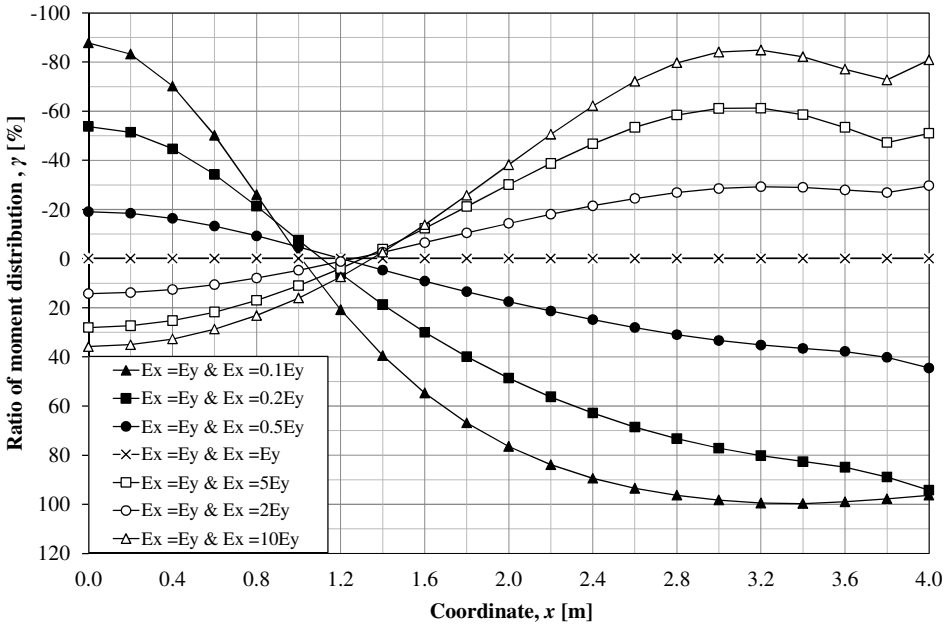

Figure 4.16. Ratio of moment distribution along L_5.

Based on Figure 4.16, it is observed that the change of moment distribution m_y is not linear. Figure 4.16 shows that the ratio of moment distribution γ increases slower when *x*-direction is stiffer than the *y*-direction and vice versa.

It is also noted that if the stiffness in *y*-direction is much larger than the stiffness in *x*-direction, the cantilever slab will present a structural behaviour similar to that of a cantilever beam. The distribution curve of m_y along L_5 in case of the elements in *y*-

direction are much stiffer than the elements in x-direction, i.e. $E_x = 0.01E_y$, is shown in Figure 4.17.

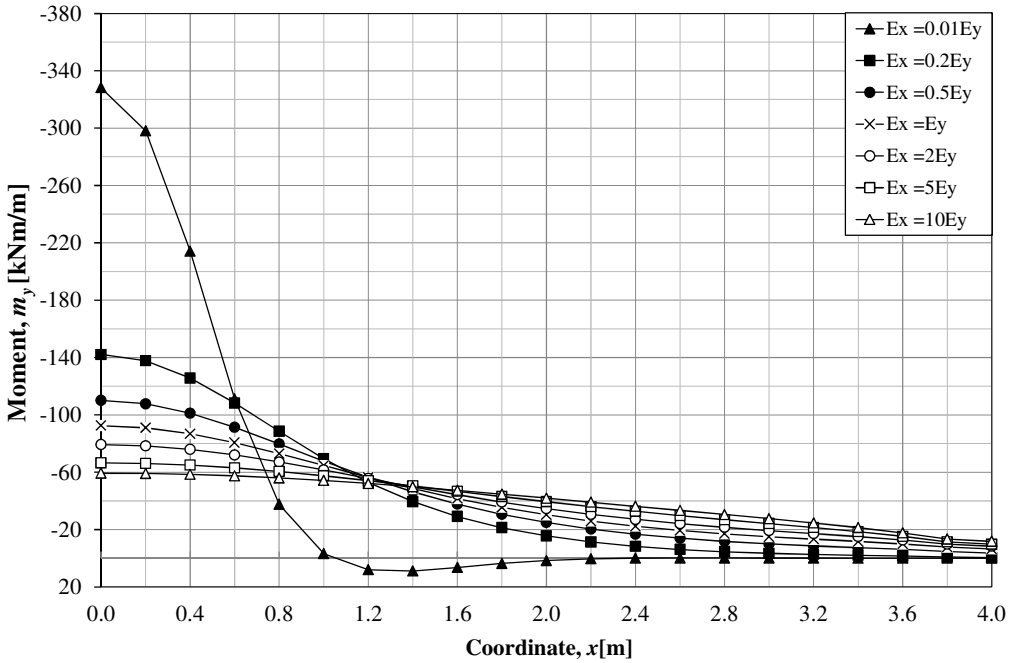

Figure 4.17. Moment distribution m_y from FE-elastic orthotropic with Poisson's ratio $v = 0$ using 0.2 m shellm_y along L_5 when $E_x = 0.01\ E_y$.

4.4.2.2 Shear

Figure 4.18 shows that the shear v_y along L_5 is more distributed when the elements along the x-direction is stiffer than the elements along the y-direction, i.e. $E_x > E_y$ and vice versa. There is a fluctuation of shear distribution at about $x = 1.6$ m to $x = 3.6$ m when $E_x = 0.1\ E_y$. For all the cases, i.e. $E_x = 0.2, 0.5, 1,2, 5, 10E_y$ in Figure 4.18, $v_y < 0$ at about $x = 3.6$ m to $x = 4$ m. This behaviour is the same as that observed in Figure 4.5. This negative value of shear $v_y < 0$ is due to the same reasons explained in Section 4.3.1.2.

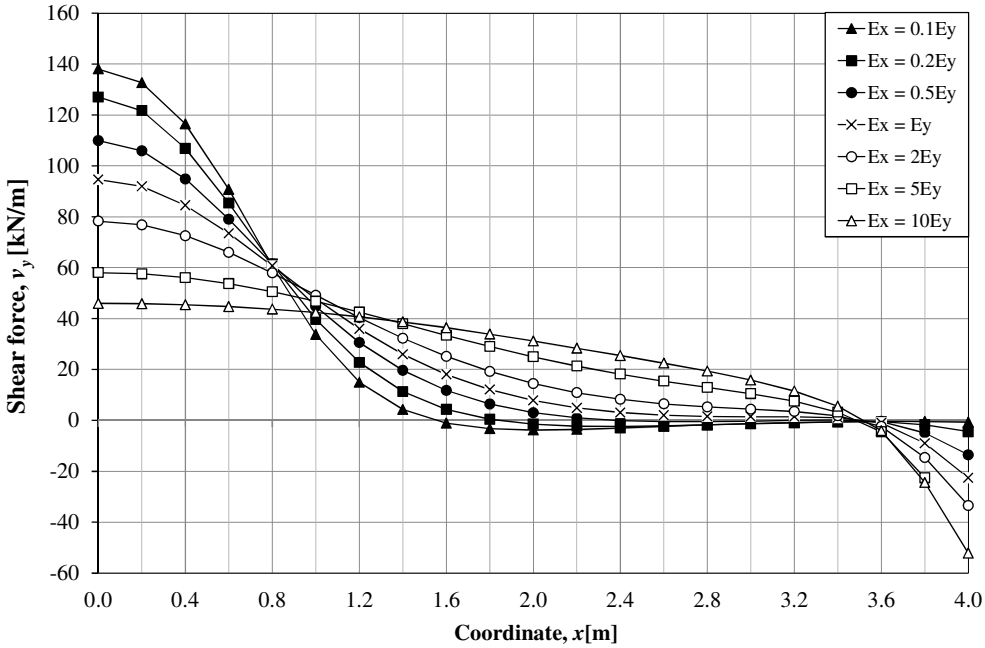

Figure 4.18. Shear force distribution v_y along L_5 from FE-linear elastic orthotropic analysis using 0.2 m shell elements with Poisson's ratio ν = 0.

4.4.2.3 Vertical displacement

The relationship between the stiffness and load distribution can also be explained by the vertical displacement u_z in Figure 4.19. When $E_x = 0.1E_y$ much load is transferred toward the element in *y*-direction which means that the transversal element along L_1 will resist much load. Therefore, along this line the deflection when $E_x = 0.1E_y$ is much larger than the deflection when $E_x = 10E_y$ where the load tries to distribute along the longitudinal direction.

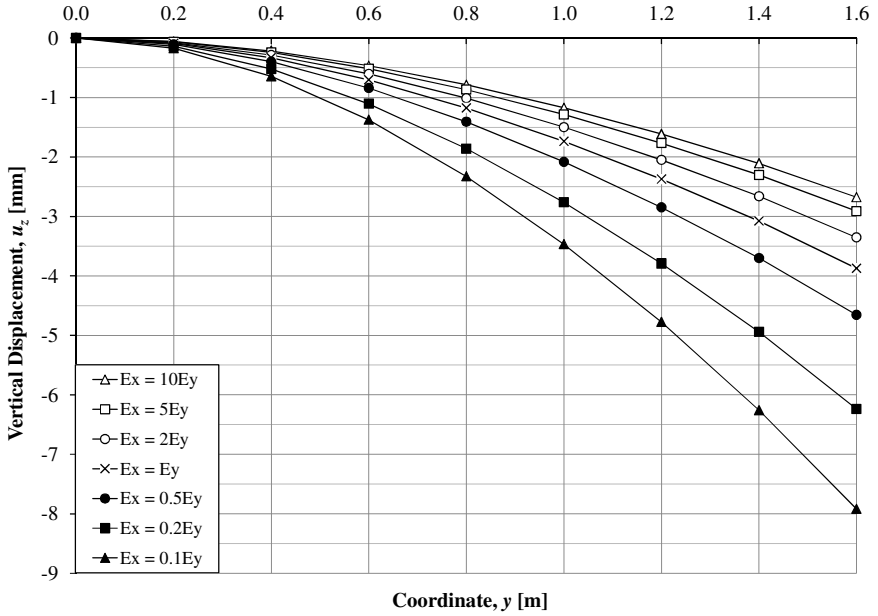

Figure 4.19. Vertical displacement u_z from FE-elastic orthotropic with Poisson's ratio ν = 0 using 0.2 m shell along L_1.

4.4.3 Distribution width of orthotropic slab

Due to the change of stiffness, moment and shear forces will distribute over a certain width denoted w_{eff} under a certain load level. In order to investigate the effect of the effective width in term of change of stiffness depending on factor $\alpha = E_x / E_y$, it is necessary to determine the effective width for moments $w_{eff,m}$ and the effective width for shear forces $w_{eff,v}$.

The effective width for moments $w_{eff,m}$ is computed as:

$$w_{eff,m} = \frac{\sum_{i=0}^{L_5} m_y}{m_{y,\max}} \tag{4-10}$$

$$\sum_{i=0}^{L_5} m_y = (x_{i+1} - x_i) \cdot \frac{m_{y,i+1} - m_{y,i}}{2} \tag{4-11}$$

Where $w_{eff,m}$ = effective width for moment

m_y = moment distribution m_y along L_5

$m_{y,\max}$ = maximum moment m_y along L_5

The effective width for shear forces $w_{eff,v}$ is computed as:

$$w_{eff,v} = \frac{\sum_{i=0}^{L_5} v_y}{v_{y,\max}} \tag{4-12}$$

$$\sum_{i=0}^{L_5} v_y = (x_{i+1} - x_i) \cdot \frac{v_{y,i+1} - v_{y,i}}{2} \tag{4-13}$$

Where $w_{eff,v}$ = effective width for shear

v_y = shear force distribution v_y along L_5

$v_{y,\max}$ = maximum shear force v_y along L_5

The maximum moment and moment distribution in equation (4-10) are determined from Figure 4.15 and the maximum shear and shear forces distribution in equation (4-12) are determined from Figure 4.18.

The difference between the effective width in case of $\alpha \neq 1$ and in case of $\alpha = 1$ for moment $\gamma_{differnce,m}$ and shear forces $\gamma_{difference,v}$ are computed in equation (4-14) and equation (4-15), respectively.

$$\gamma_{difference,m} = 100 \times \frac{\left|w_{eff,m,Ex=Ey}\right| - \left|w_{eff,m,Ex=\alpha Ey}\right|}{\left|w_{eff,m,Ex=Ey}\right|} \tag{4-14}$$

$$\gamma_{difference,v} = 100 \times \frac{\left|w_{eff,v,Ex=Ey}\right| - \left|w_{eff,v,Ex=\alpha Ey}\right|}{\left|w_{eff,v,Ex=Ey}\right|} \quad (4\text{-}15)$$

The ratio between the effective width in case of $\alpha \neq 1$ and in case of $\alpha = 1$ for moment $\gamma_{ratio,m}$ and shear forces $\gamma_{ratio,v}$ are determined in equation (4-16) and equation (4-17).

$$\gamma_{ratio,m} = \frac{\left|w_{eff,m,Ex=\alpha Ey}\right|}{\left|w_{eff,m,Ex=Ey}\right|} \quad (4\text{-}16)$$

$$\gamma_{ratio,v} = \frac{\left|w_{eff,v,Ex=\alpha Ey}\right|}{\left|w_{eff,v,Ex=Ey}\right|} \quad (4\text{-}17)$$

The results of effective width w_{eff} of moments and shear forces are summarized in Table 4.3 and Table 4.4.

Table 4.3. Effective width $w_{eff,m}$, difference $\gamma_{difference,m}$ and ratio $\gamma_{ratio,m}$ between the effective width in case of $\alpha \neq 1$ and in case of $\alpha = 1$ for moment.

α	$\sum_{i=0}^{L_5} m_y$	$m_{y,\max}$	$w_{eff,m}$	$\gamma_{difference,m}$	$\gamma_{ratio,m}$
0.1	-160	-173.5	0.9	46.7	1.8
0.2	-160	-142.1	1.1	34.9	1.5
0.5	-160	-110.1	1.4	16.1	1.1
1	-160	-92.4	1.7	0.0	1.0
2	-160	-79.2	2.1	-16.6	0.8
5	-160	-66.5	2.4	-38.9	0.7
10	-160	-59.3	2.7	-55.8	0.6

Table 4.4. Effective width $w_{eff,v}$, difference $\gamma_{difference,v}$ and ratio $\gamma_{ratio,v}$, between the effective width in case of $\alpha \neq 1$ and in case of $\alpha = 1$ for shear.

α	$\sum_{i=0}^{L_5} v_y$	$v_{y,\max}$	$w_{eff,v}$	$\gamma_{difference,v}$	$\gamma_{ratio,v}$
0.1	100	138.1	0.7	31.4	1.4
0.2	100	127.1	0.8	25.5	1.3
0.5	100	109.9	0.9	13.9	1.1

1	100	94.6	1.1	0.0	1.0
2	100	78.2	1.2	-20.8	0.8
5	100	58.1	1.7	-62.9	0.6
10	100	45.9	2.1	-105.8	0.4

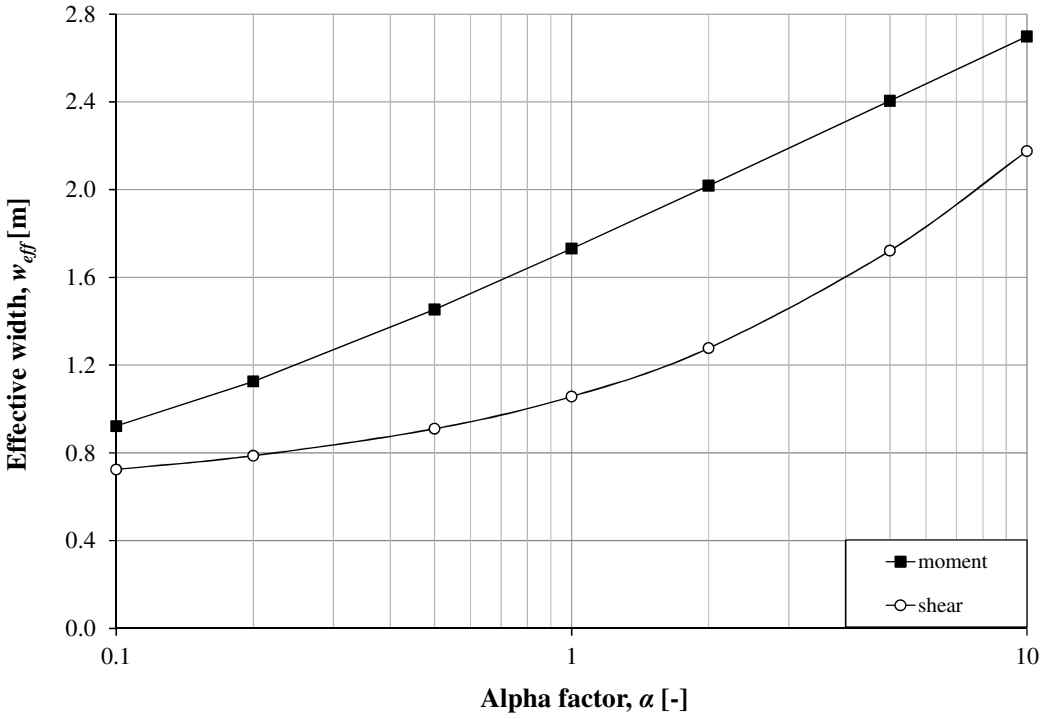

Figure 4.20. Effective width in term of $\alpha = E_x / E_y$ from FE-elastic orthotropic with Poisson's ratio $\nu = 0$ using 0.2 m shell element for moment and shear.

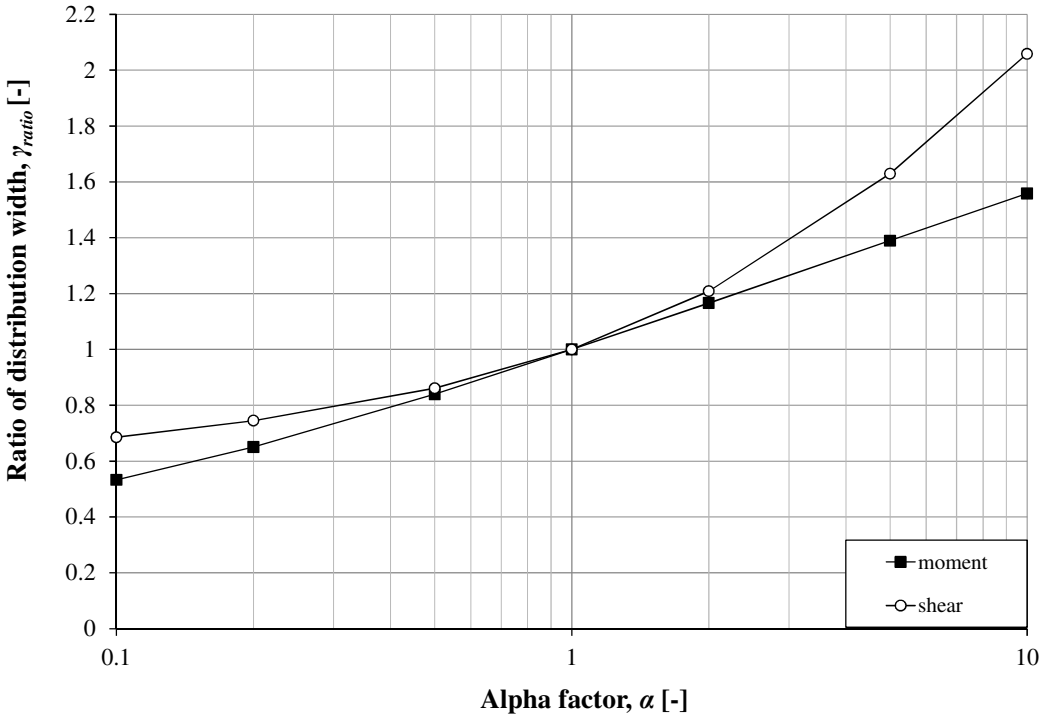

Figure 4.21. Ratio between effective width orthotropic and isotropic in term of $\alpha = E_x / E_y$ from FE-elastic orthotropic with Poisson's ratio $\nu = 0$ using 0.2 m shell elements for moment and shear.

From Figure 4.20, it is seen that the effective width for moment $w_{eff,m}$ increases with increasing α factor. Figure 4.20 also shows that when E_y is greater than E_x, i.e. $\alpha < 1$, the effective width for moment $w_{eff,m}$ is small since the elements in y-direction are stiffer than the elements in x-direction and a large portion of the load is carried by the elements close to the middle of the slab. When E_x is greater than E_y, i.e. $\alpha > 1$, the distribution width for moment $w_{eff,m}$ in Figure 4.20 is large as the x-direction are stiffer than the elements along the y-direction which leads to a more evenly distributed moment m_y along L_5 as shown in Figure 4.15b.

Like the effective width for moment $w_{eff,m,}$ the effective width for shear forces $w_{eff,y}$ in Figure 4.20 also increases with regard to increasing of α factor. Figure 4.20 also shows that the distribution width for shear force $w_{eff,v}$ is also small when $\alpha < 1$.

Based on Figure 4.21, it is observed that the change of effective width for shear $\gamma_{ratio,v}$ is not linear whereas the variation of the effective width for moment $\gamma_{ratio,m}$ increases more linearly when α increases comparing to $\gamma_{ratio,v}$.

4.4.4 Comparisons between shell elements and beam elements

It is not possible to combine orthotropic material with beam elements in ADINA. For orthotropic analysis, stiffness and shear modulus in different directions are required. For beam elements, only one stiffness is needed. Therefore, this combination is not available in FE program ADINA. As the beam grillage model consists of the beams in x- and y-directions, one way to deal with such a problem is to model the cantilever slab studied using beam elements with isotropic material, but the beam elements will have different stiffness for the beam located in x- and y-directions. It means that it is necessary to introduce the stiffness E_x for the beams located in x-direction and

introduce the stiffness E_y for the beam located in y-direction so that it simulates the orthotropic behaviour of the slab.

In order to evaluate this simplified model, four different stiffness in x-direction is chosen while the stiffness in y-direction is kept constant, i.e. $E_x = 0.2, 0.5, 1, 5E_y$.The geometry and orthotropic properties of the slab in Figure 4.2 using simplified model is depicted in Figure 4.22 and the result lines in Figure 4.2 are still valid in Figure 4.22.

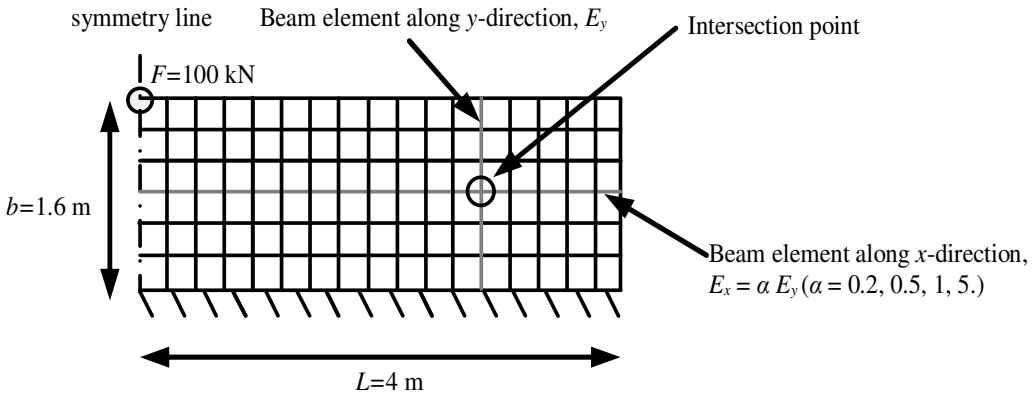

Figure 4.22. Simplified orthotropic slab model using beam elements

From the comparisons between shell elements and beam elements for isotropic case in Section 4.3.3, it is clearly shown that 0.2 m beam elements provide the results most similar to those of the shell elements. Therefore, it is sufficient to use only 0.2 m beam elements to compare with the results of 0.2 m shell elements in orthotropic case. The different in percentage of moment distribution m_y, shear forces distribution v_y and vertical displacement u_z between 0.2 m shell elements and 0.2 m beam elements are computed using equation(4-18), equation (4-19) and equation (4-20) respectively.

$$\gamma_{ortho,m} = 100 \times \frac{\left|m_{Ex=\alpha Ey,beam}\right| - \left|m_{Ex=\alpha Ey,shell}\right|}{\left|m_{Ex=\alpha Ey,beam}\right|} \tag{4-18}$$

$$\gamma_{ortho,v} = 100 \times \frac{\left|v_{Ex=\alpha Ey,beam}\right| - \left|v_{Ex=\alpha Ey,shell}\right|}{\left|v_{Ex=\alpha Ey,beam}\right|} \tag{4-19}$$

$$\gamma_{ortho,u_z} = 100 \times \frac{\left|u_{z,Ex=\alpha Ey,beam}\right| - \left|u_{z,Ex=\alpha Ey,shell}\right|}{\left|u_{z,Ex=\alpha Ey,beam}\right|} \tag{4-20}$$

For the comparisons of shear forces distribution v_y and vertical displacement u_z, readers can refer to APPENDIX C.

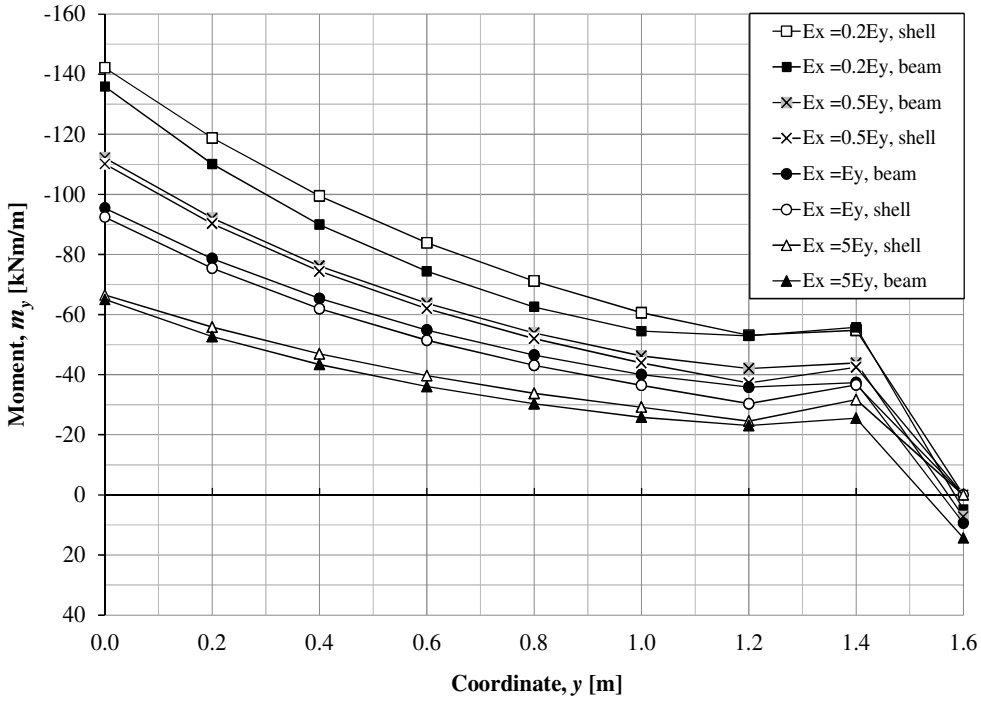

(a)

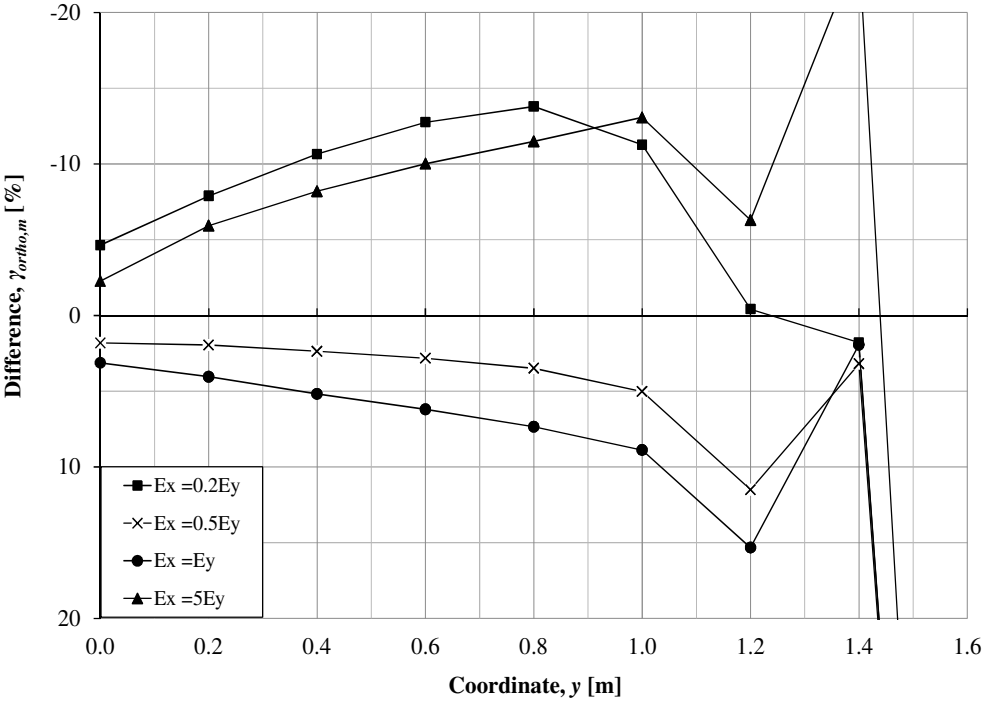

(b)

Figure 4.23. Comparisons between 0.2 m beam elements and 0.2 m shell elements from linear elastic orthotropic FE-analysis with Poisson's ratio ν = 0: (a) moment distribution m_y along L_1 (b) difference in percentage m_y along L_1.

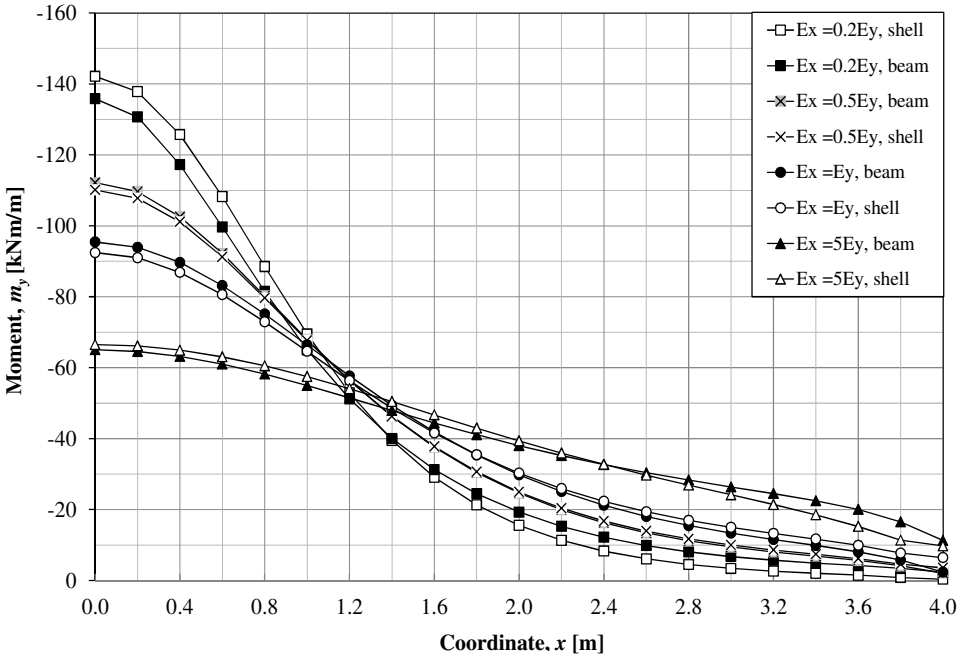

(a)

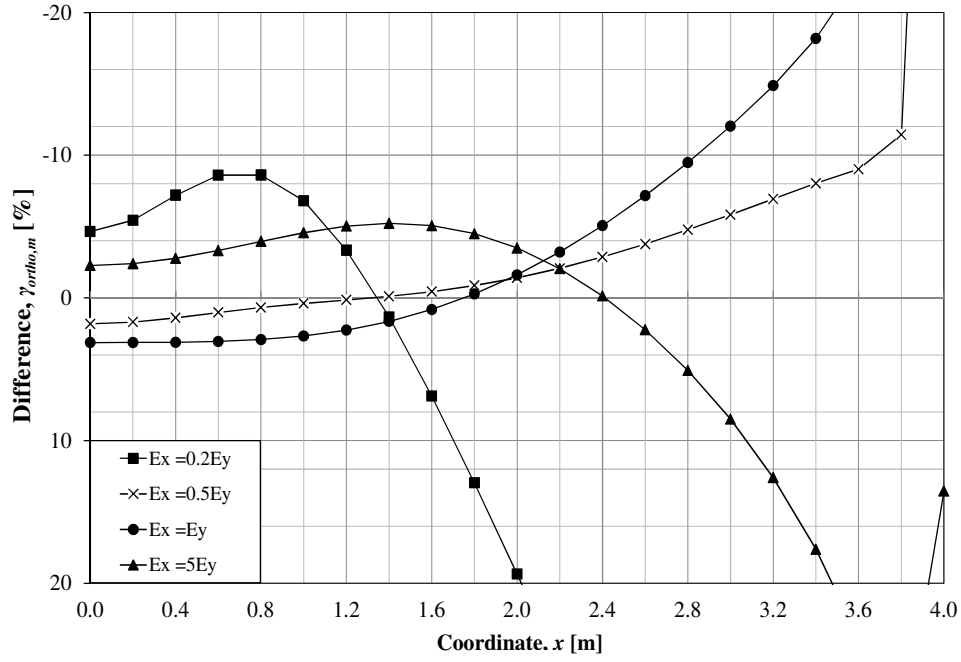

(b)

Figure 4.24. Comparisons between 0.2 m beam elements and 0.2 m shell elements from linear elastic orthotropic FE-analysis with Poisson's ratio ν = 0: (a) moment distribution m_y along L_1 (b) difference in percentage of m_y along L_5.

When observing the convergence and divergence of the 0.2 m beam grillage model and 0.2 m shell element model, it can be seen in Figure 4.23 and Figure 4.24 that there is the best convergence in case $E_x = 0.5E_y$ while $E_x = 0.2E_y$ shows the worst convergence among the four different cases that have been made. $E_x = E_y$ and $E_x = 5E_y$ cases give a rather good convergence comparing to $E_x = 0.5E_y$. The reason for the fluctuation in these differences due to the change of stiffness is not clearly known and explained but it is believed to be due to the simplification that has been made in beam

grillage model when analysing of slab in orthotropic case. As can be seen in Figure 4.23, the difference in m_y along L_1 is $|\gamma| < 10$ % for the elements situated at about $y < 0.8$ m in the transversal direction from the fixed supports. For the elements situated at about $y > 0.8$ m, the difference is larger. These differences are considered acceptable in the study since the large moment that is used for the design gives a small γ while a small absolute moment value give a large γ. This is not so critical in the design process. Similar to the difference in m_y along L_1, the difference in m_y along L_5 also shows a large γ where there is a small absolute moment value, i.e. in Figure 4.24, there is a huge divergence between 0.2 m beam elements and 0.2 m shell elements where the moment is close to zero. For m_y along L_5, there is a small difference around $|\gamma| = 10$ % for a large moment value that is used for the design in the critical section. In actual design, the minimum reinforcement will be able to resist this moment value. Moreover for the moment at around $x = 2$ m, $|\gamma| < 5$ %. This difference is acceptable since in elasto-plastic analysis, the distribution of moment due to yielding will take place only at the location where there is a huge moment which is larger than yielding capacity of the section. To sum up, the beam elements can be used for elasto-plastic analysis of the previous examined cantilever slab in Figure 4.2.

Based on the analysis of the cantilever slab both in linear elastic isotropic case in Section 4.3.3 and orthotropic case in Section 4.4.4, it is convinced that shell element is the most suitable and appropriate finite element choice to examine the cantilever slab studied in Figure 4.2. Therefore, it is recommended to use shell elements when analysing a cantilever slab under point load in linear elastic isotropic and orthotropic case.

4.5 Elastoplastic case-beam grillage model

4.5.1 Choice of model used for the analysis

There is a biaxial effect that increases the moment capacity of the slab when analysing a slab using shell elements with a combination of plastic material according to Augustsson and Härenstam (2010). Augustsson and Härenstam (2010) explained this effect by studying a one-way simply supported slab subjected to distributed loads over the whole surface as shown in Figure 4.25. The material model used is a bilinear-plastic material model depicted in Figure 4.26.

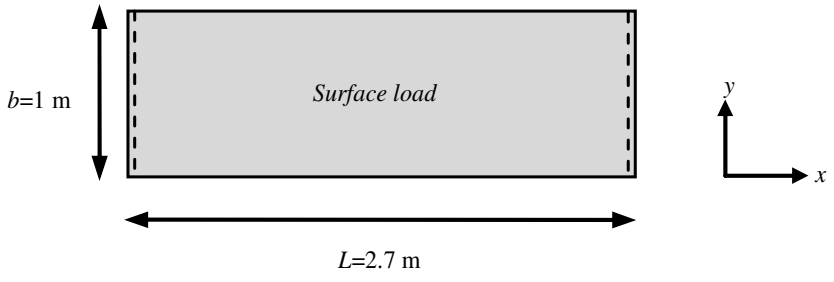

Figure 4.25. One-way simply supported slab subjected to surface loads.

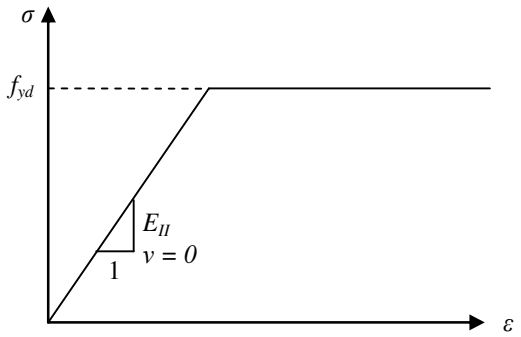

Figure 4.26. Bilinear plastic material data for simply supported slab analysis using shell elements.

The plastic moment capacity of the slab is determine by the yield stress provided in the material model.

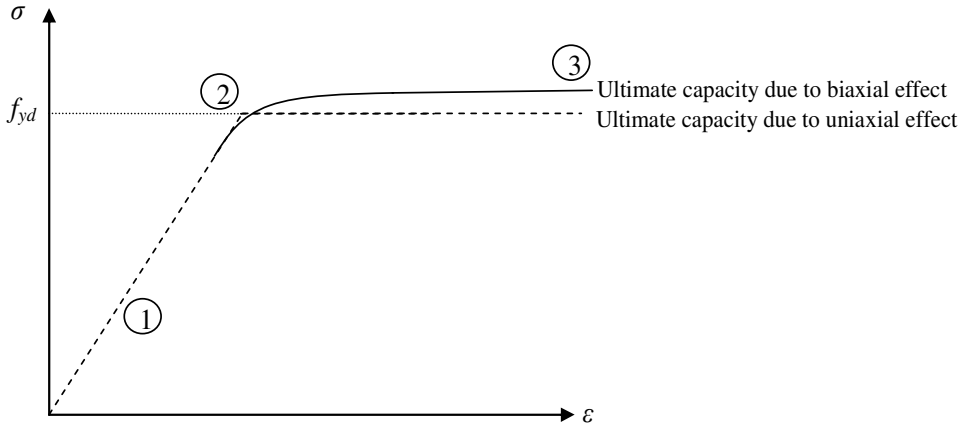

Figure 4.27. Ultimate capacity of the simply supported one-way slab: dot line represent expected capacity (uniaxial effect), solid line represent increased capacity from FE analysis (biaxial effect).

In Figure 4.27, point 1 corresponds to the elastic state where the Poisson's ratio $\upsilon = 0$. The stresses are developed only in *x*-direction and the result obtained from the FE analysis is equal to the expected solution. When continuing loading the slab, the stress reaches the yield stress which is denoted by point 2 in Figure 4.27. Point 2 corresponds to the expected capacity of the section with regard to the input in Figure 4.26. Continuing loading the slabs further, it is observed that the stress keeps increasing and passes the yield stress of the section. According to Augustsson and Härenstam (2010), this increase is due to the biaxial effect of plastic material used in ADINA. The plastic material used in ADINA is based on the Von Mises yield condition described, see Bathe (1996). When the material reaches plasticity, ADINA will set Poisson's ratio $\upsilon = 0.5$ no matter what Poisson's ratio input defined by the user. Consequently, the stress in the *y*-direction is developed due to restrain caused by the elements next to the element that yields when the stress in the *x*-direction reaches the yield stress defined in the material input. Due to the development of the stresses in the *y*-direction, a biaxial stress state is formed, which increases the yield stress in the *x*-direction.

In order to avoid this effect, beam elements described in Section 4.3 and 4.4 are used instead. Further, since the response of the slab in different states is of interest, it is necessary to model the slab in elasto-plastic case using 3D beam elements with multilinear moment-curvature relationship model.

As shown in Section 4.3 and Section 4.4, when analysing the slab using beam elements in isotropic and orthotropic case, 0.2 m beam elements provides a similar result to those when using shell elements. Therefore, 0.2 m beam element size was used in this case as well. From Section 3.5.3, it is seen that element mesh sizes have a large influence on the results when analysing the beam in elasto-plastic case using 3D beam elements. It is necessary to have sufficiently fine mesh in order to get acceptable results for the analysis of the slab. Hence based on Section 3.5.3, smaller element size than 0.2 m beam elements should be used.

In order to assure the accuracy of the analysis of the slab in elasto-plastic case when using beam elements, the torsional stiffness of the slab received from 0.2 m beam elements need to be kept constant. It is known that in order to keep the torsional stiffness of the slab constant when using beam elements, the element mesh sizes at the intersection points need to be unchanged. It means that the element mesh sizes for both *x* and *y*-direction have to have 0.2 m length at the intersection point.

One way to deal with such a problem is to subdivide the first element of the longitudinal beam (beam in *y*-direction) into 4 smaller elements. It means that 0.2 m element mesh size (first element of the beam in *y*-direction) is divided into four smaller element mesh sizes equal to 0.05 m element size as depicted in Figure 4.28. It is enough to just sub-divide the first element and not the other elements along the *y*-direction since it is known that only the first element yields and other elements will not yield. Therefore, a 0.05 m element mesh size is chosen as it provides an acceptable result according to Section 3.5.3. It is also noted that if the element is in elastic state, 0.2 m element size provides a good result.

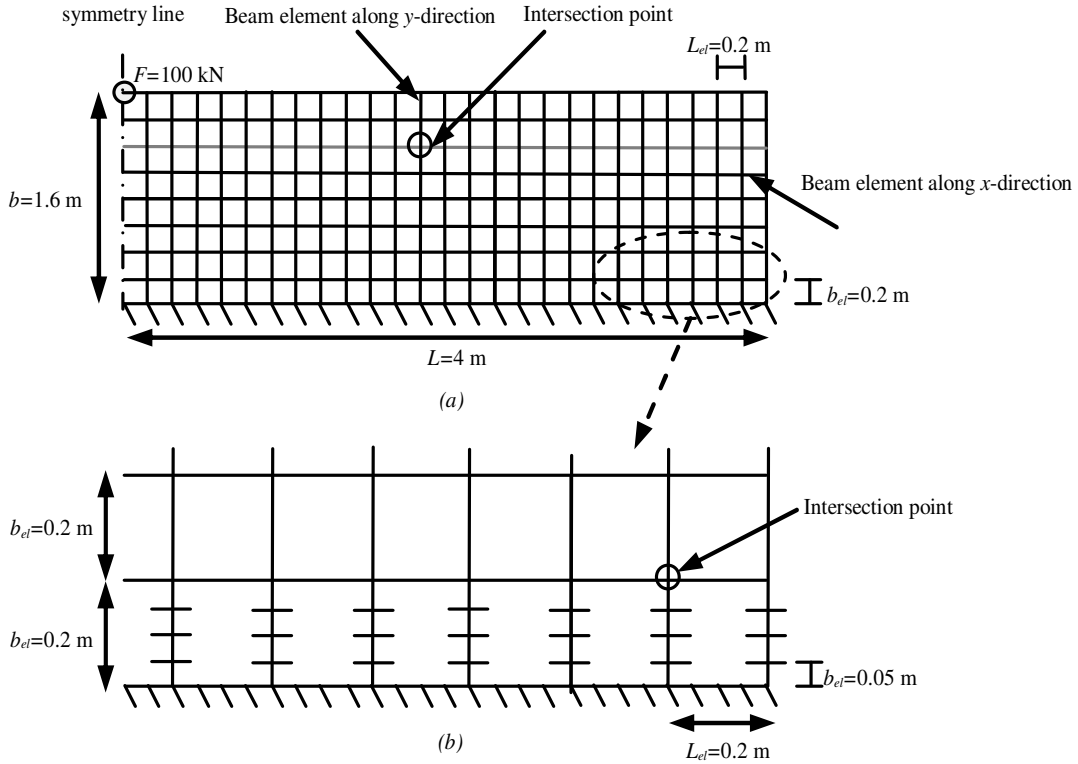

Figure 4.28. Element mesh sizes for cantilever slab (a) single mesh 0.2 m element size (b) 2 different meshes 0.05 m element size for the first element of beam in y-direction and 0.2 m element sizes for the rest of the beam elements.

4.5.2 Influence of mesh-isotropic case

Since the cantilever slab in Figure 4.2 is now modelled with two different meshes, it is important to check if the slab in Figure 4.28b gives the same results as the slab in Figure 4.28a in elastic isotropic case. The material input shown in Figure 4.3 that is used for the cantilever slab studied with single mesh size 0.2 m is also used for the cantilever slab studied with two different mesh sizes so that it is possible to compare the results.

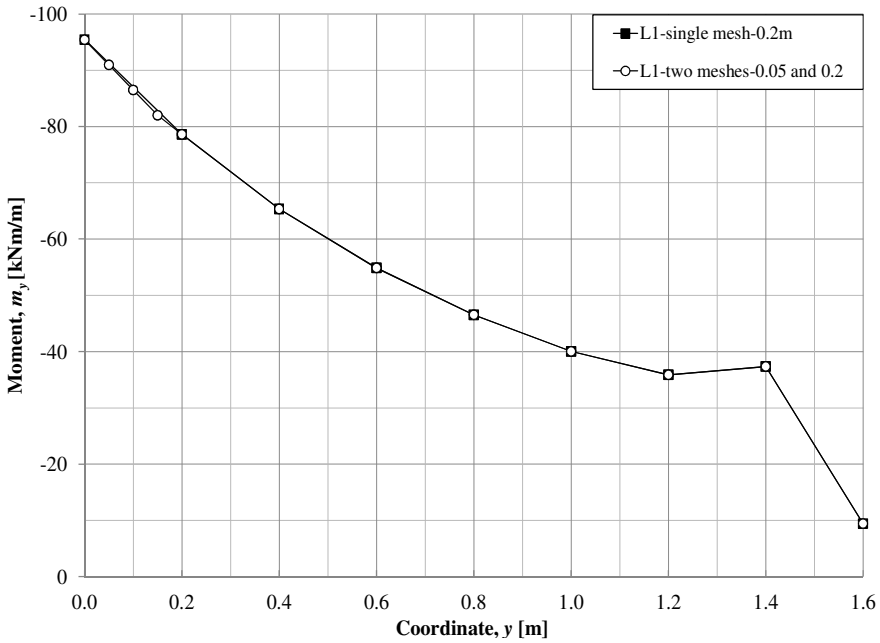

(a)

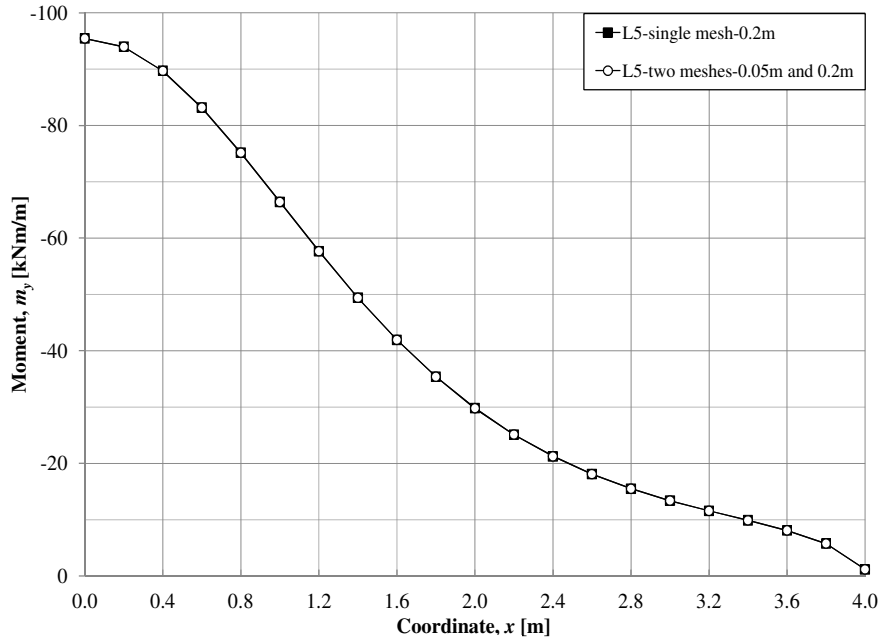

(b)

Figure 4.29. Comparisons between slab with single mesh size and slab with two different mesh sizes (a) m_y along L_1 (b) m_y along L_5.

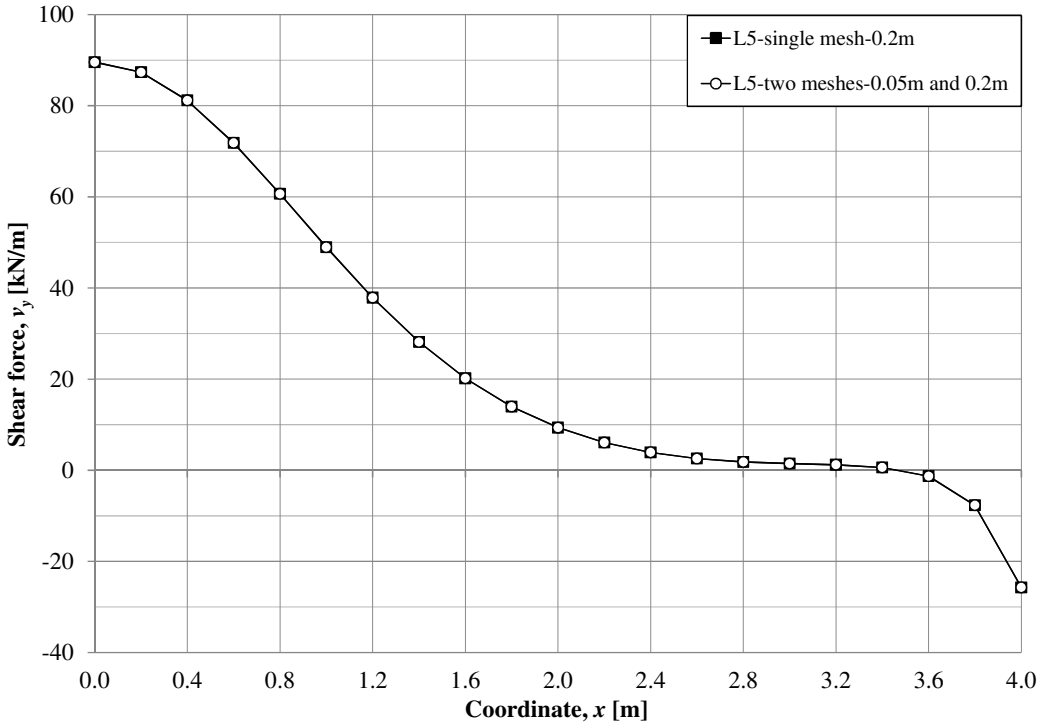

Figure 4.30. Comparisons of shear forces distribution v_y between slab with single mesh size and slab with two different mesh sizes.

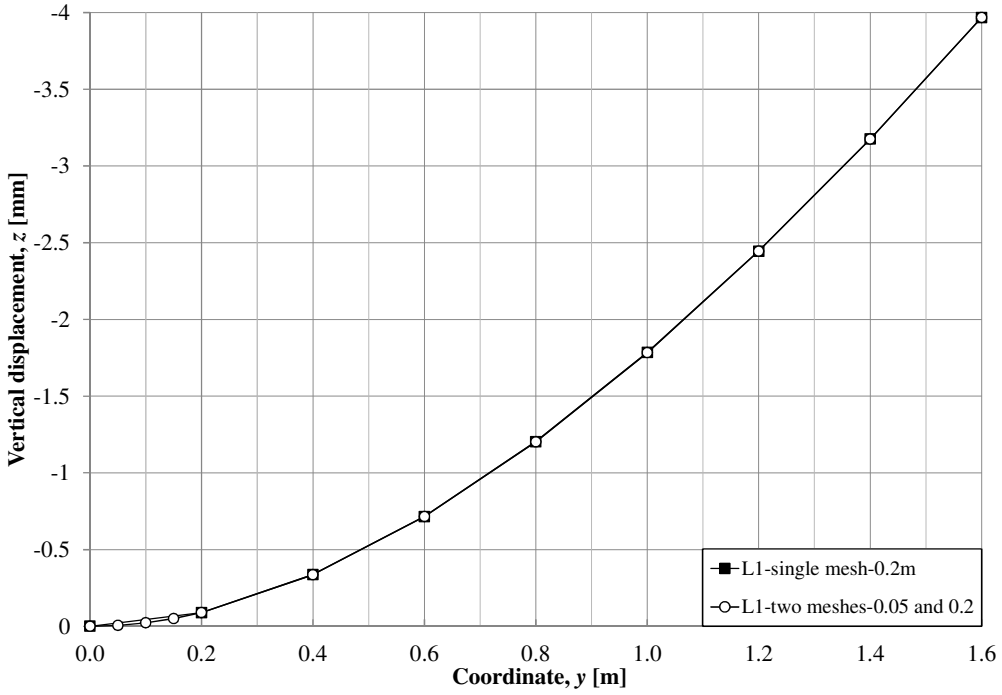

Figure 4.31. Comparisons of vertical displacement u_z between slab with single mesh size and slab with two different mesh sizes.

From Figure 4.29a to Figure 4.31, it is observed that the results of the two models at the intersection points between the elements in x and y-direction coincides well. The results of the first element of two different meshes model located at $y = 0.05$ m, $y = 0.1$ m and $y = 0.15$ m away from the fixed support provides more accurate results

as the result of single mesh model is computed based on linear interpolation between $y = 0$ m and $y = 2$ m. From Figure 4.29b and Figure 4.30, it is seen that the results of moment and shear forces along line L_5 are identical as the elements along x-direction are not subdivided. It is concluded that the cantilever slab in Figure 4.2 can be modeled with beam elements using two different meshes for the analysis in elasto-plastic case.

4.5.3 Quadlinear M(χ) - $M_{pl} = 0.6M_{el}$, $E_{II} = E_{II}/5$

4.5.3.1 Moment

A cantilever slab in Figure 4.32a with the same geometry and boundary condition as the cantilever slab in Figure 4.2 is subjected to a point load until failure. Thereby, it is possible to see how far plastic hinges along the clamped boundary of the studied slab can be formed if the plastic rotation capacity of the slab is sufficient.

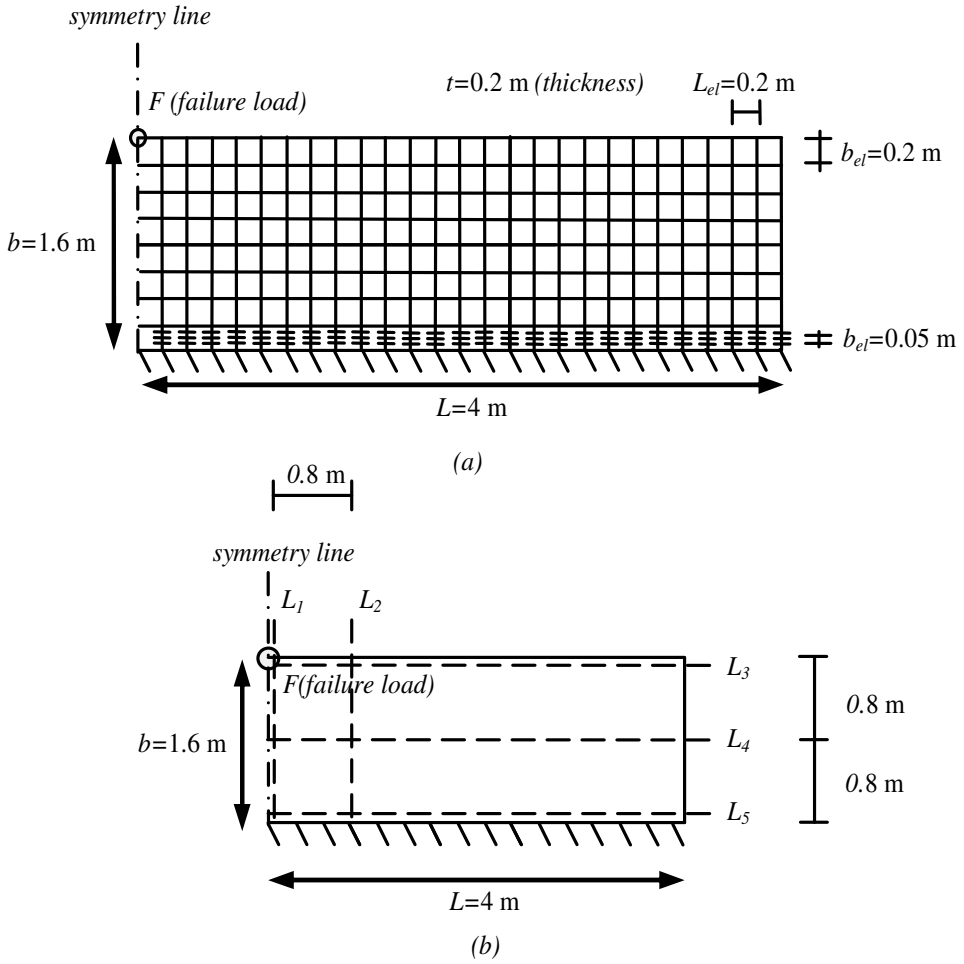

Figure 4.32. (a) Geometry and load of a cantilever slab with two different element mesh sizes (b) result lines for moment and shear force distribution.

The cantilever slab in Figure 4.32b was analyzed using a quadlinear moment curvature input illustrated in Figure 4.33. As the analysis does not model the real reinforced concrete slab, moment plastic and cracking moment is chosen based on practical experience so that they are close to value of a certain type of real reinforced

concrete slab, see APPENDIX F. According to Pacoste *et al.* (2012), moment plastic $M_{plastic}$ can be chosen $0.6M_{elastic} \leq M_{plastic} \leq M_{elastic}$ to redistribute the reinforcement moment. Here $M_{plastic} = 0.6M_{elastic}$ is chosen where $M_{elastic}$ is taken from the linear elastic isotropic analysis of the cantilever slab in Section 4.3.2. Further, the cracked moment $M_{cr1} = M_{plastic}/3$ and $M_{cr2} = M_{plastic}/2$ is chosen as input for the analysis carried out here. The stiffness in state I is kept the same as the stiffness in linear elastic isotropic case $E_I = 30$ GPa while the stiffness in state II is chosen equal to $E_{II} = E_I/5 = 6$ GPa. These input data are chosen close to a reinforced concrete slab of 1 m width with B500B 5ϕ16 and concrete strength C30/37 as shown in Figure F.1 in APPENDIX F.

It is important to note that 0.2 m beam element size is used to model the slab. The moment-curvature relationship input for beam element in FE program ADINA is in Nm unit. In order to make it easy to compare the result of moment in the slab, the moment in Nm is distributed per unit width in order to have intensity in Nm/m.

The cantilever slab studied in Figure 4.32 was analyzed using the following moment-curvature input:

$$M_{plastic} = 0.6 \cdot M_{elastic} = 0.6 \cdot 19 = 11.4 \text{ kNm} \tag{4-21}$$

$$m_{plastic} = \frac{11.4}{0.2} = 57 \text{ kNm/m} \tag{4-22}$$

$$M_{cr2} = \frac{M_{plastic}}{2} = \frac{11.4}{2} = 5.7 \text{ kNm} \tag{4-23}$$

$$m_{cr2} = \frac{5.7}{0.2} = 28.5 \text{ kNm/m} \tag{4-24}$$

$$M_{cr1} = \frac{M_{plastic}}{3} = \frac{11.4}{3} = 3.8 \text{ kNm} \tag{4-25}$$

$$m_{cr1} = \frac{3.8}{0.2} = 19 \text{ kNm/m} \tag{4-26}$$

The curvature χ_I , χ_{II} , χ_{III} and χ_{IV} ,of the moment-curvature diagram in Figure 4.33 is determined from equation (4-27) to equation (4-30).

$$\chi_I = \frac{M_{cr1}}{E_I I} = \frac{3.8 \cdot 10^3}{30 \cdot 10^9 \cdot \frac{0.2 \cdot 0.2^3}{12}} = 0.00095 \left[1/\text{m}\right] \tag{4-27}$$

$$\chi_{II} = \frac{M_{cr2}}{E_{II} I} = \frac{5.7 \cdot 10^3}{6 \cdot 10^9 \cdot \frac{0.2 \cdot 0.2^3}{12}} = 0.007125 \left[1/\text{m}\right] \tag{4-28}$$

$$\chi_{III} = \frac{M_{plastic}}{E_{II} I} = \frac{11.4 \cdot 10^3}{6 \cdot 10^9 \cdot \frac{0.2 \cdot 0.2^3}{12}} = 0.01425 \left[1/\mathrm{m}\right] \tag{4-29}$$

$$\chi_{IV} = 10 \left[1/\mathrm{m}\right] \tag{4-30}$$

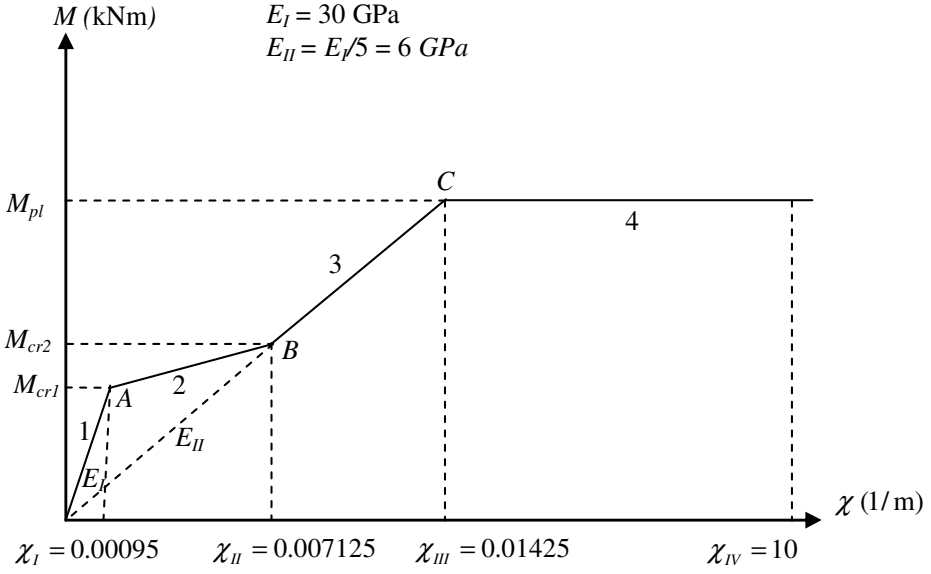

Figure 4.33. Quadlinear moment-curvature relationship for the analysis of the studied cantilever slab in elasto-plastic case, $E_{II} = E_I/5$.

There are four zones in Figure 4.33 that were used to simulate the behaviour of the cantilever slab studied. Zone 1 determined from 0 to point A represents uncracked state (state I). Zone 2 from point A to point B and zone 3 from point B to point C were used to simulate the tension stiffening effect in cracked state (state II). Zone 4 represents yielding part of the tensile reinforcement (state III). For more detail of structural response of reinforced concrete structure in serviceability limit state and ultimate limit state, reader can refer to Section 2.2.5 and 2.2.6.

The ratio of the maximum moment $m_{y,max}$ received from the FE analysis to moment distribution $m_{y,(x)}$ along x-direction is determined in equation (4-31).

$$\delta_{quad} = \frac{m_{y,\max}}{m_{y,x}} \tag{4-31}$$

From Figure 4.34a, it is seen that when $F = 20$ kN, the maximum moment intensity at the middle of the slab is $m_{y.max} = 19.2$ kNm/m. The remaining part along the fixed boundary is less than 19 kNm/m which means that they are in elastic state. When $F = 40$ kN, there is an abrupt change in stiffness at $x = 2$ m. This indicates that parts of the slab along fixed boundary, $0 \leq x \leq 2$ m, are cracked while the remaining parts located further away at $x > 2$ m is uncracked. For a load $F = 60$ kN, the cracks spread along L_5 and there is a change in stiffness at $x = 3$ m. It means that the slab cracks at $0 \leq x \leq 3$ m and is uncracked at $x > 3$ m. When the load keeps increasing, the cracks

develop even further until the slab yields at a length L_{yield} = 0.6 m from the symmetry line when F = 100 kN. This shows that there is a plastic redistribution of moment due to yielding where the yielding part is equal to L_{yield} = 0.6 m.

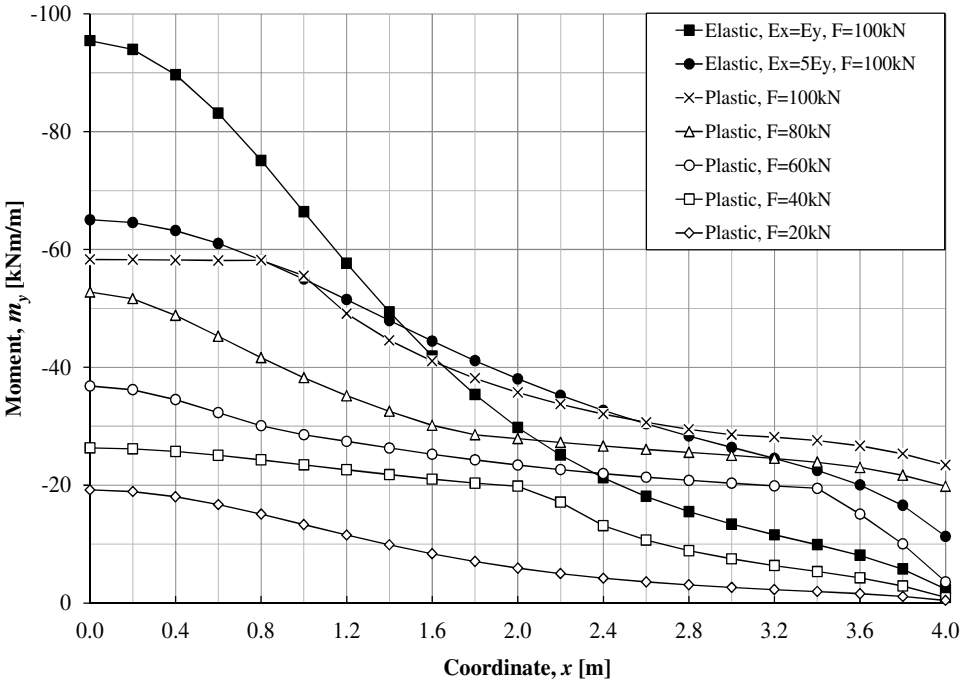

(a)

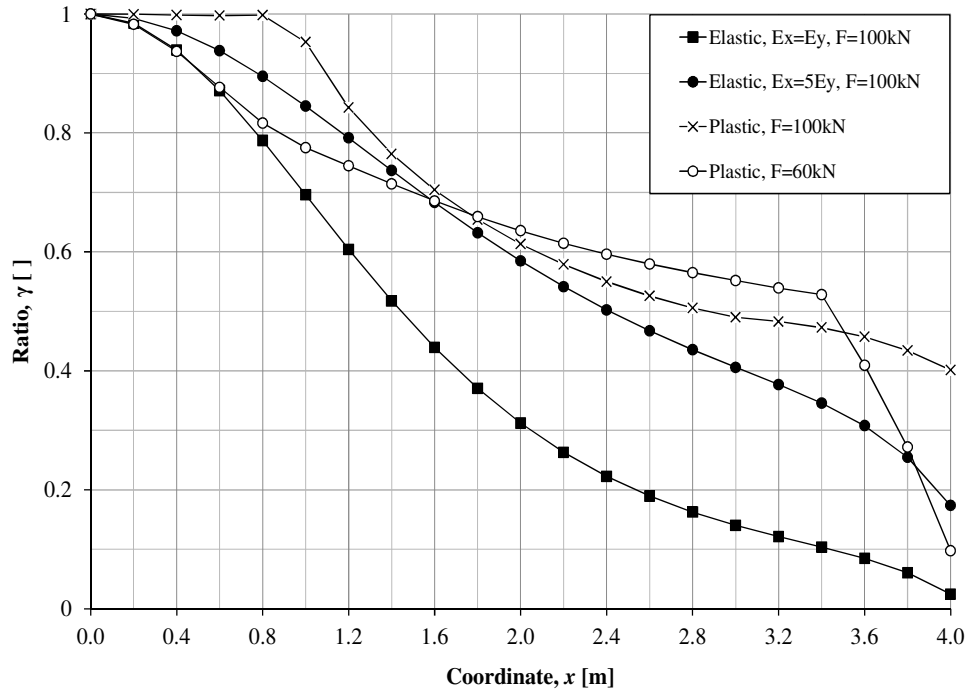

(b)

Figure 4.34. Moment distribution m_y along L_5 at different load level up to 100 kN (a) moment distribution m_y (b) ratio of maximum moment $m_{y,max}$ to $m_{y,x}$ moment along L_5.

From Figure 4.34b, it is observed that the moment distribution shape after plastic redistribution is smoother than the moment distribution shape after redistribution due

to the change of stiffness. Compared to the other curves in the same illustration, the distribution shape of moment from linear elastic FE analysis is very sharp.

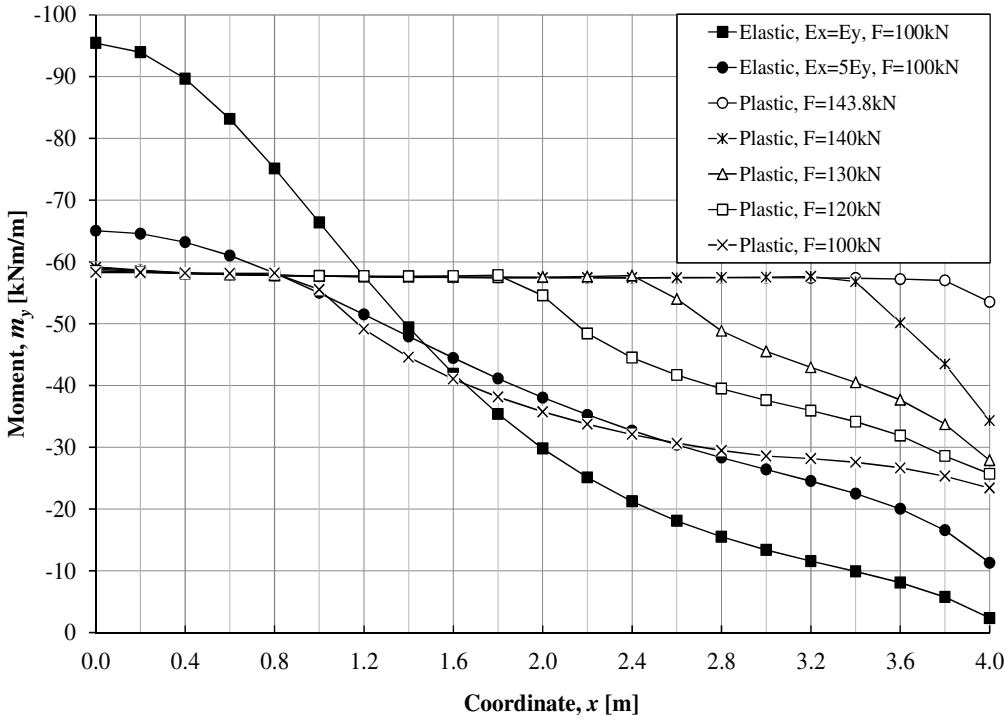

(a)

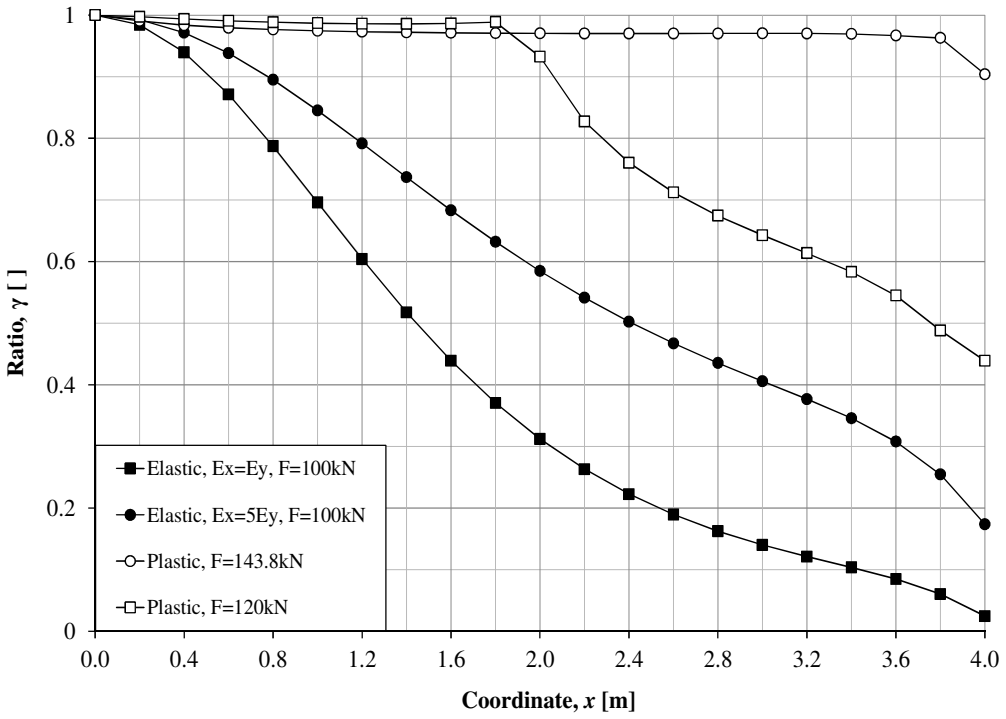

(b)

Figure 4.35. Moment distribution m_y along L_5 at different load level up to 143.8 kN (a) moment distribution m_y (b) ratio of maximum moment $m_{y,max}$ to $m_{y,x}$ moment along L_5.

Figure 4.35a shows that part of the slab that yields along the fixed boundary increases with increasing load F. If the load is increased until failure, a failure load of $F = 143.8$ kN is obtained as shown in Figure 4.35a and the whole part of the slab along L_5 yields. In Figure 4.35b, it is seen that the moment redistribution shape of the studied cantilever after yielding becomes more even with increasing applied load F and the moment distribution shape for $F = 143.8$ kN is constant, i.e. full redistribution.

4.5.3.2 Curvature contour plot

In order to investigate the structural response of the whole cantilever slab studied with regard to increasing of applied load F, the contour plot of m_y in Figure 4.36 and Figure 4.37 are plotted. In Figure 4.33, there are four different zones that represent the structural response of the cantilever slab studied from uncracked state until failure. Therefore, the contour plots in Figure 4.36 and Figure 4.37 of the same slab also have four different colours in which each colour corresponds to the zones in Figure 4.33. Green colour represent zone 1(uncracked state), orange colour represents zone 2 (first cracked state), yellow colour represents zone 3 (second cracked state) and red colour represents zone 4 (yielding of tensile reinforcement) of the quadlinear moment-curvature input in Figure 4.33.

From Figure 4.36, it is seen that when $F = 20$ kN, only the part of the slab located at $x = 0.2$ m and $y = 0.2$ m is in zone 2 since the maximum moment intensity at that position $m_{y.max} = 19.2$ kNm/m is higher than $M_{cr1} = 19$ kNm/m. However, the remaining parts of the slab is in zone 1 as the moment intensity of those parts is less than $M_{cr1} = 19$ kNm/m. When $F = 40$ kN, zone 2 propagates further, but there is a disturbance in part of the slab at $x = 0.2$ m and $y = 1.4$ m. This disturbance is believed to be due to the torsional effect at that position. Similar disturbances can also be seen in Figure 4.4a for 0.2 m shell element and Figure 4.8a for 0.2 m beam element. When $F = 60$ kN, cracks develop further until some parts of the studied slab along L_5 at about $0 \leq x \leq 1$ m are in zone 3 and along L_1 at about $0 \leq y \leq 1.4$ m are in zone 2. When $F = 80$ kN, zone 3 along L_5 develops further at about $0 \leq x \leq 1.8$ m and it extends along L_1 until $0 \leq y \leq 0.4$ m. When the load increases up to $F = 100$ kN, some parts of the slab along fixed boundary yields at about $0 \leq x \leq 0.8$ m and they are in zone 4 while the parts located at about $0.8 \leq x \leq 3$ m are in zone 3 and at about $3 \leq x \leq 4$ m are in zone 2.

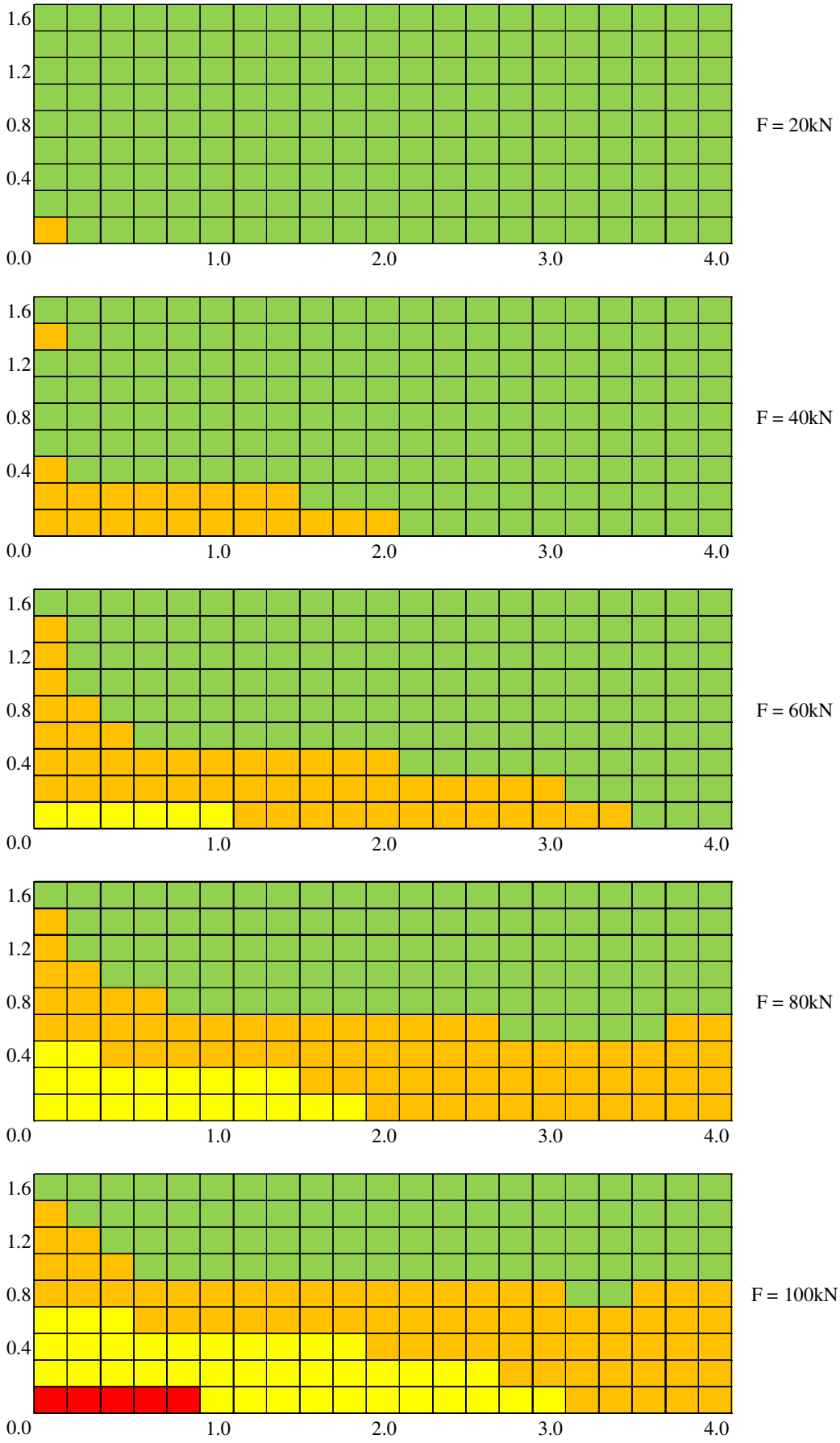

Figure 4.36. Contour plot at different load level up to 80 kN.

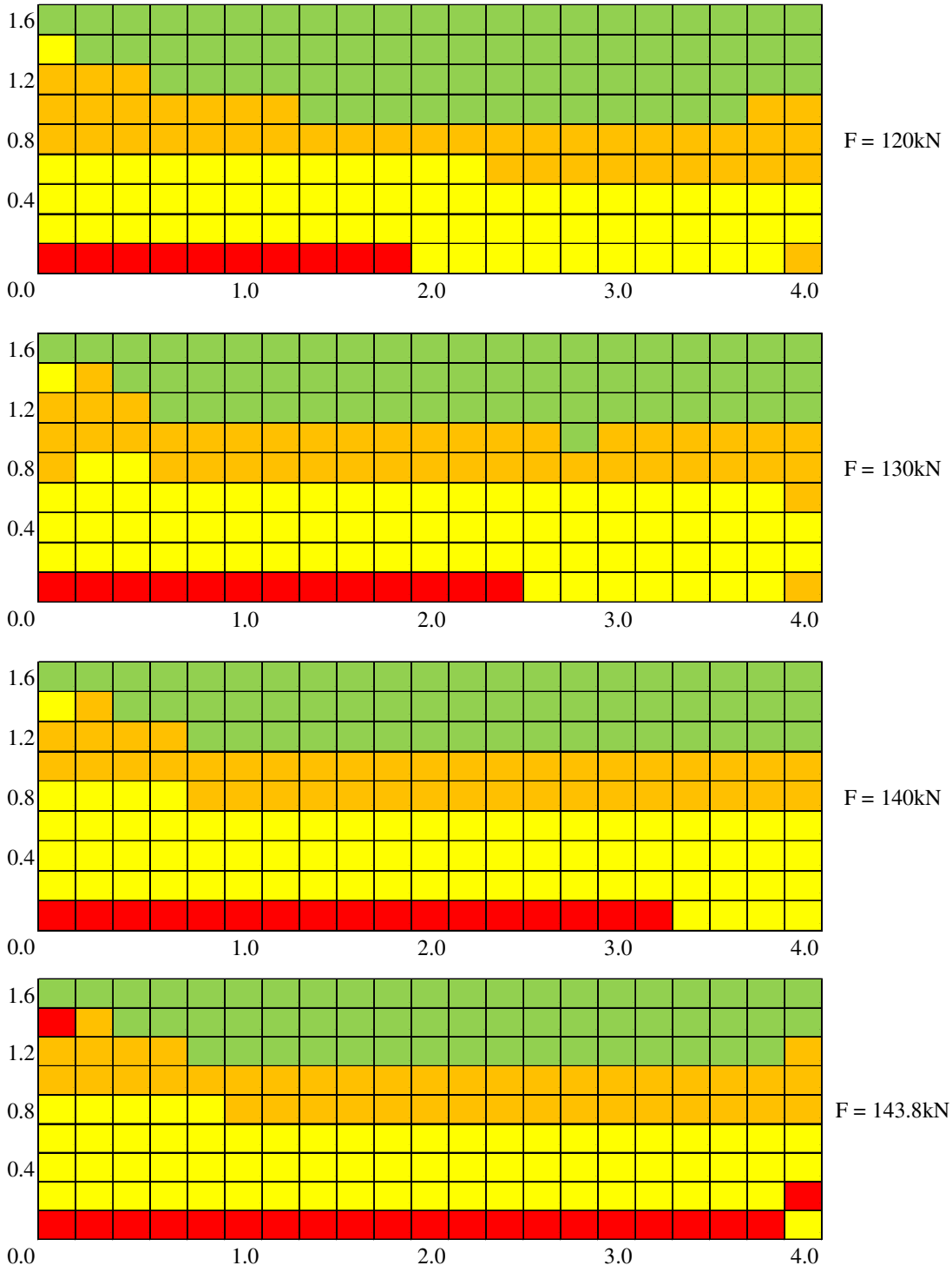

Figure 4.37. Contour plot at different load level up to 143.8 kN.

In Figure 4.37, when $F = 120$ kN, yielding parts of the slab propagates further at about $0 \leq x \leq 1.8$ m and it is clearly seen that there are disturbances at position ($x = 0.2$ m, $y = 1.4$ m) and position ($x = 4$ m, $y = 0.2$ m) of the slab. The development of yielding along L_5 and cracking in other parts continues until the collapse mechanism is formed when $F = 143.8$ kN. When $F = 143.8$ kN, parts of the slab along L_5 at about $0 \leq x \leq 3.8$ m are in zone 4. There are disturbances at position ($x = 0.2$ m, $y = 1.4$ m) and position ($x = 4$ m, $y = 0.2$ m).

It is noted that there are always disturbances at position ($x = 0.2$ m, $y = 1.4$ m) and position ($x = 4$ m, $y = 0.2$ m) of the slab in each load level. These disturbances cannot be seen when these parts and their surrounding regions are located in the same zone, for example when $F = 100$ kN. However, these disturbances can be seen clearly when these positions and the regions next to them situated in different zones, for instance when $F = 143.8$ kN.

4.5.3.3 Plastic rotation

From APPENDIX F, the cantilever slab studied in Figure 4.32 with input data in Figure 4.33 is similar to the real reinforced concrete cantilever slab in Figure F.1. Therefore, from APPENDIX F, it is concluded that the studied cantilever slab in Figure 4.32 has a plastic rotation capacity of about $\theta_{rd} = 24.5 \cdot 10^{-3}$ rad with $x_u/d = 0.179$ and has a minimum plastic rotation capacity of $\theta_{rd,min} = 10.6 \cdot 10^{-3}$ rad.

As shown in Section 3.5.4, method 2 presented in APPENDIX E is valid to determine the plastic rotation of the cantilever slab examined in Figure 4.32 in elastoplastic case. Therefore, method 2 was used to calculate the plastic rotation of the studied cantilever slab with quadlinear moment curvature relationship input depicted in Figure 4.33.

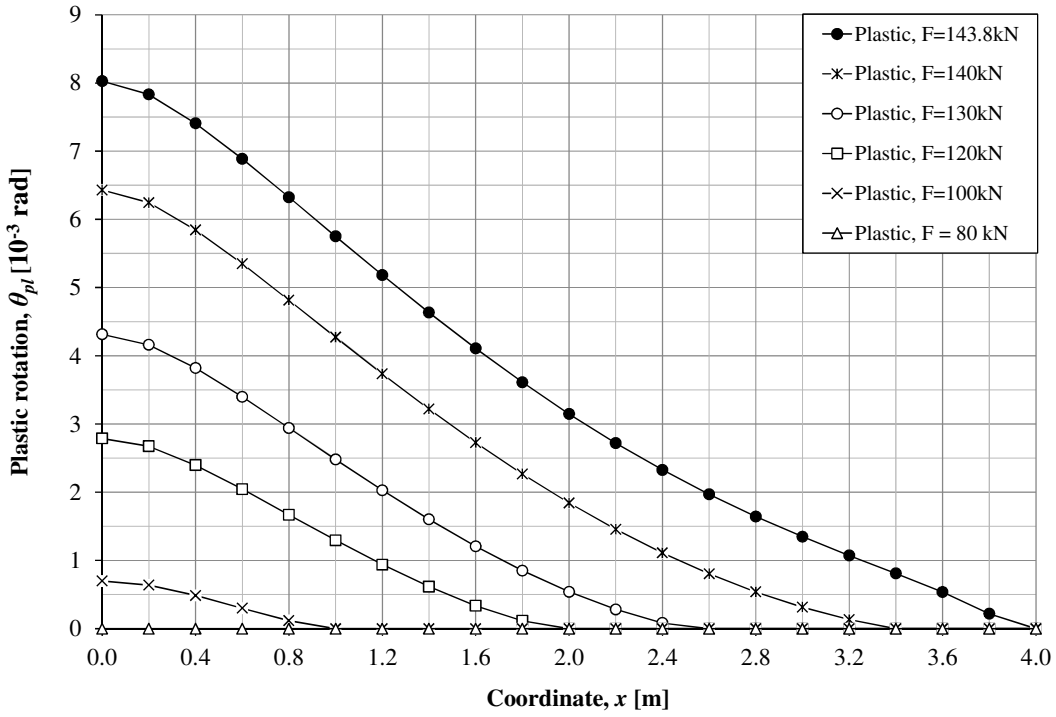

Figure 4.38. Plastic rotation distribution θ_{pl} along L_5 at different load level up to $F = 143.8$ kN.

$F = 100$ kN results in the maximum plastic rotation $\theta_{pl,max} = 7.0 \cdot 10^{-4}$ rad, see Figure 4.38. Since $\theta_{pl,max} = 7.0 \cdot 10^{-4}$ rad is smaller than the minimum plastic rotation capacity of the cantilever slab studied $\theta_{rd,min} = 10.6 \cdot 10^{-3}$ rad, it means that it is possible to increase the load further. When continue loading the slab until a failure load of $F = 143.8$ kN, all elements along L_5 yields and the cantilever slab studied fails due to the global failure when the mechanism is formed. A load $F = 143.8$ kN gives $\theta_{pl,max} = 8.0 \cdot 10^{-3}$ rad. It is seen that even when the collapse of the structure takes place,

$\theta_{pl,max}$ remains smaller than the minimum plastic rotation capacity of the cantilever slab studied $\theta_{pl,max} = 8.0 \cdot 10^{-3}$ rad $< \theta_{rd,min} = 10.6 \cdot 10^{-3}$ rad. This indicates that if $M_{plastic} = 0.6 M_{elastic}$, it is possible to redistribute the moment with a distribution width $w_x = 4$ m. This also indicates that a larger moment can be reduced from the moment received from FE analysis, i.e. $M_{plastic} < 0.6 M_{elastic}$ can be chosen to redistribute the reinforcement moment in this case.

4.5.3.4 Comparison with existing guideline

As mentioned in Section 4.5.3.3 and APPENDIX F, the cantilever slab studied in Figure 4.32 has a plastic rotation capacity of around $\theta_{rd} = 24.5 \cdot 10^{-3}$ rad with $x_u/\mathrm{d} = 0.179$ and has a minimum plastic rotation capacity of $\theta_{rd,min} = 10.6 \cdot 10^{-3}$ rad.

From Section 2.4.10.1, when $0.15 \leq x_u/\mathrm{d} = 0.179 \leq 0.25$, w_x can be determined as:

$$w_x = \min \begin{cases} 7d + b + t = 7 \cdot 0.15 + 0.2 + 0.05 = 1.3 \text{ m} \\ 10d + y_{cs} = 10 \cdot 0.15 + 1.6 = 3.1 \text{ m} \end{cases} = 1.3 \text{ m} \tag{4-32}$$

For a symmetry case, $w_x = 1.3 \text{ m}/2 = 0.65$ m. Therefore, a moment that can be redistributed from linear elastic FE analysis with $w = 0.65$ m can be determined as:

$$m_{y,mean} = \frac{\sum_{i=0}^{w} m_{y,FE}}{w} = \frac{58.68}{0.65} = 90.3 \text{ kNm} \tag{4-33}$$

Ratio between the maximum moment from the FE analysis and the mean moment that is distributed within $w = 0.65$ m is calculated as:

$$\gamma = \frac{m_{y,mean}}{m_{y,\max}} = 100 \cdot \frac{90.3}{95.4} = 95\,\% \tag{4-34}$$

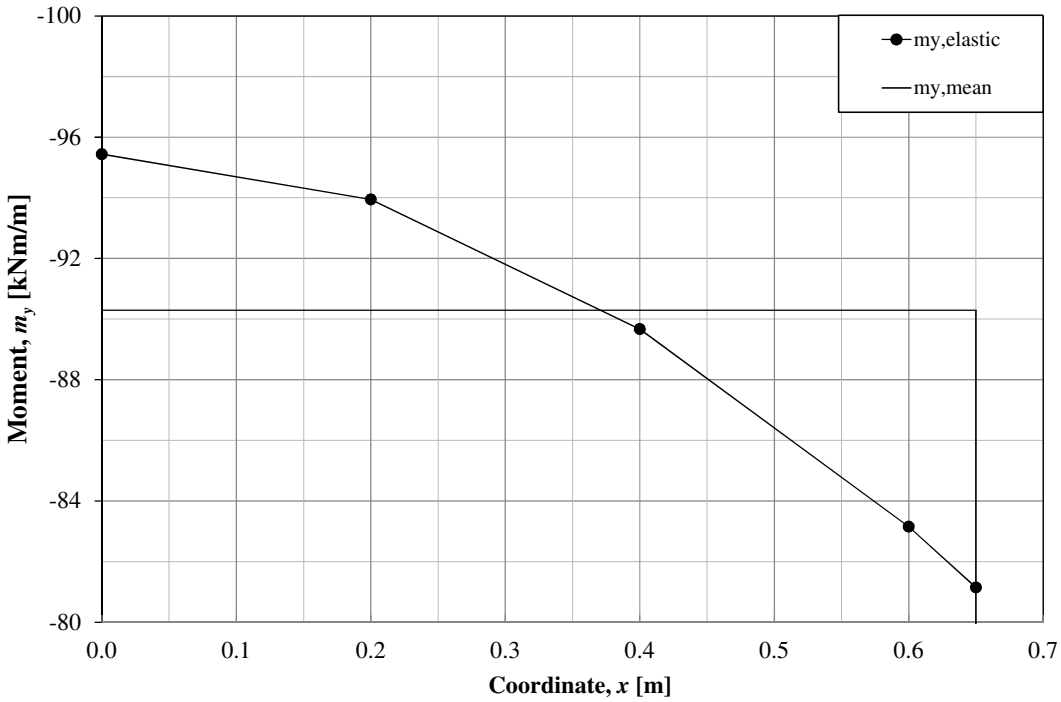

Figure 4.39. Redistributed moment from linear elastic FE analysis with w = 0.65 m.

From Figure 4.39 and equation (4-34), it is seen that it is possible to redistribute $m_{y,mean} = 0.95\ m_{y,max}$ within $w = 0.65$ m.

From Section 4.5.3.3, it is known that for this particular case, it is possible to reduce $m_{y,mean} = 0.6\ m_{y,max}$ within a distribution width $w_x = 4$ m. Therefore, it is concluded that the recommendation given by Pacoste *et al.* (2012) in equation (2-53) is conservative.

4.5.3.5 Shear

Figure 4.40 and Figure 4.41show that, $v_y < 0$ at about $x = 3.6$ m to $x = 4$ m for all load level $0 < F \leq 143.8$ kN. The reason is the same as the one explained in Section 4.3.1.2.

It is observed in Figure 4.40 and Figure 4.41 that there is shear force fluctuations taking place in certain load levels. For instance, there is a fluctuation of shear forces when $F = 60$ kN at 2.8 m $\leq x \leq$ 3.2 m, but there is no fluctuation when $F = 80$ kN and $F = 143.8$ kN. The reasons for this have not yet been understood and will not be further discussed in this master thesis.

Figure 4.40b and Figure 4.41b, it is seen that the shear forces redistribution shape of the cantilever slab studied after the tensile reinforcement yields looks smoother than the shear forces distribution shape in the linear elastic state. Hence, the shear forces distribution after the tensile reinforcement yields is not as critical as in the linear elastic FE analysis.

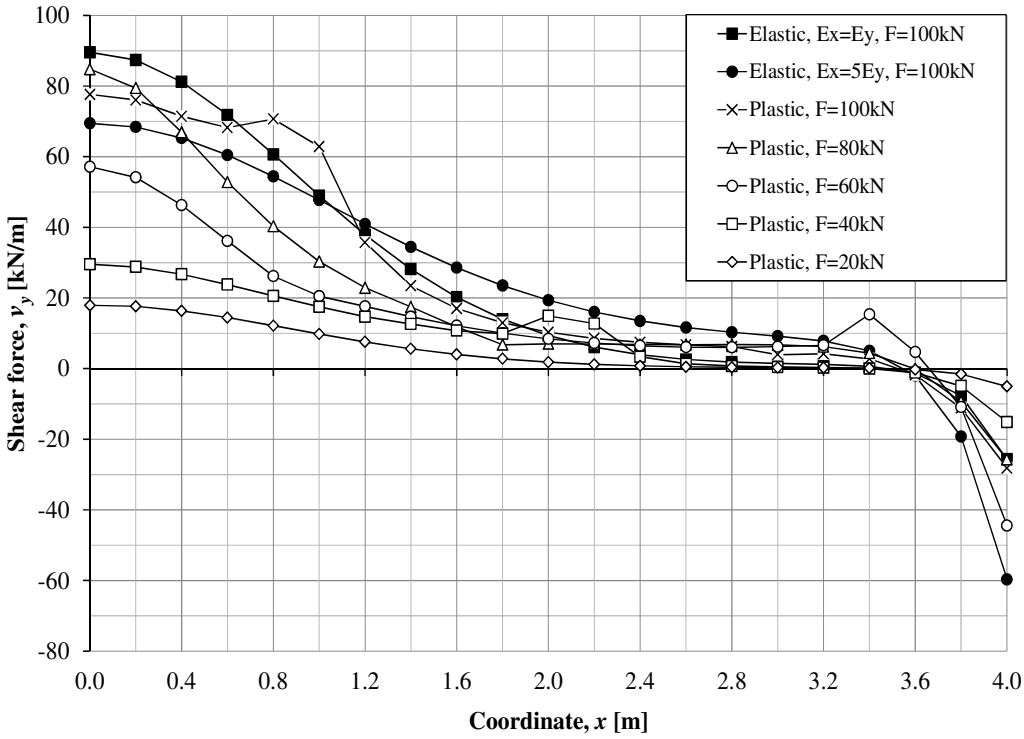

(a)

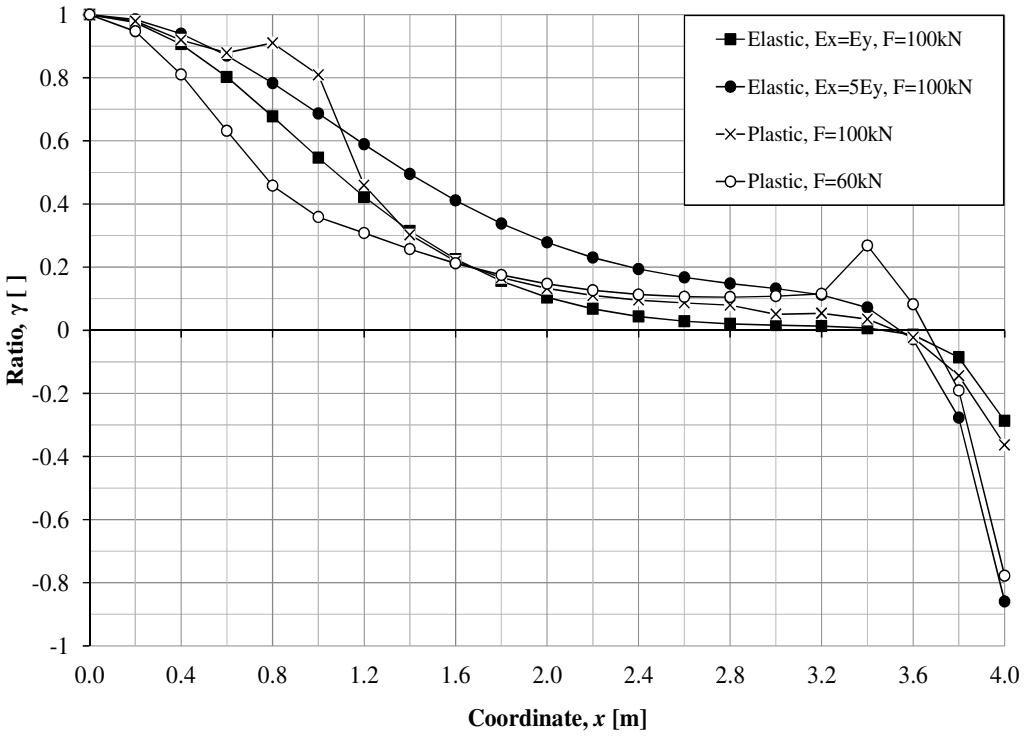

(b)

Figure 4.40. Shear force distribution v_y along L_5 at different load level up to 100 kN (a) shear force distribution v_y (b) ratio of maximum shear force $v_{y,max}$ to $v_{y,x}$ moment along L_5.

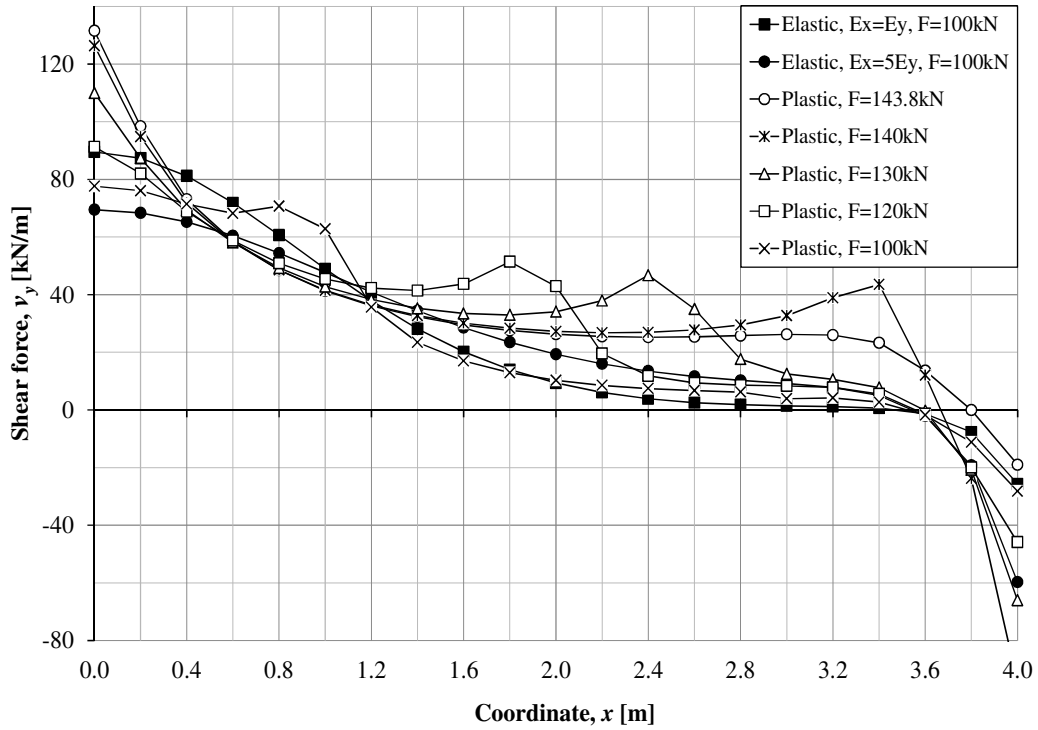

(a)

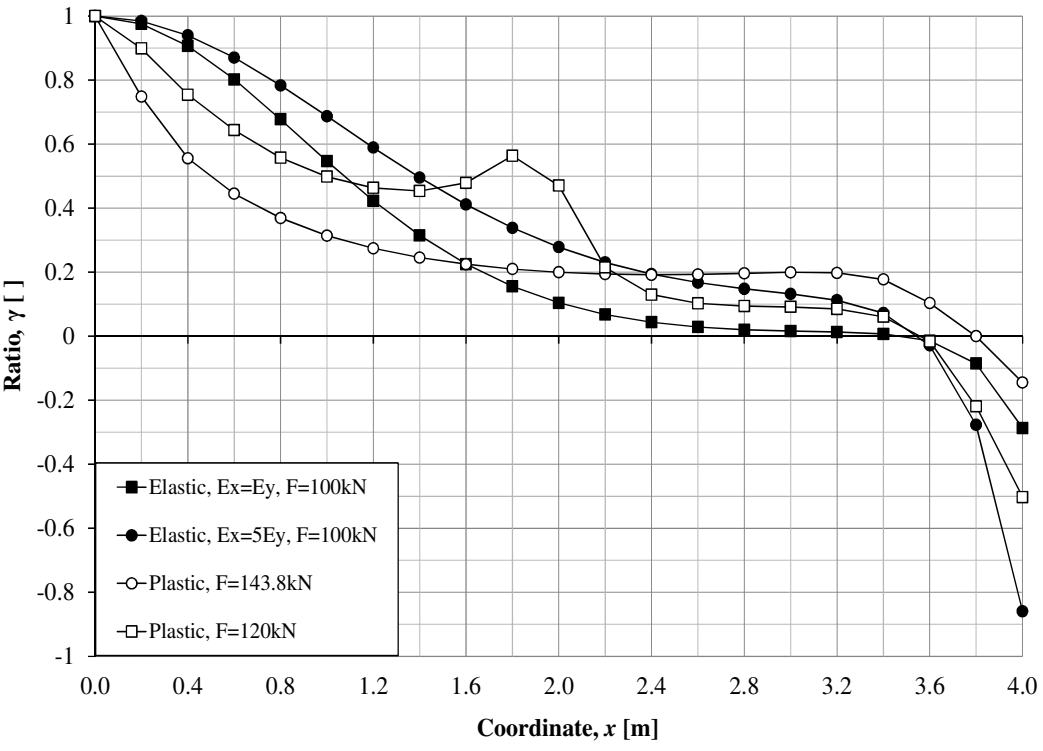

(b)

Figure 4.41. Shear force distribution v_y along L_5 at different load level up to 143.8 kN (a) shear force distribution v_y (b) ratio of maximum shear force $v_{y,max}$ to $v_{y,x}$ moment along L_5.

4.5.4 Influence of different state II stiffness in quadlinear M(χ)

4.5.4.1 Orientation

In order to investigate a structural response of the cantilever slab studied in Figure 4.32 in elasto-plastic case using quadlinear moment curvature relationship, a parametric study of the state II stiffness, i.e. $E_{II} = E_I/2$ =15 GPa, and $E_{II} = E_I/10$ =3 GPa were performed. This cantilever slab was analyzed using quadlinear moment curvature input when $E_{II} = E_I/2$ = 15 GPa and when $E_{II} = E_I/10$ = 3 GPa, see APPENDIX C. Reader can refer to APPENDIX C for the moment distribution, shear forces distribution and plastic rotation for these two cases.

4.5.4.2 Load-displacement relation

Figure 4.42 shows a load-displacement relation between the different cases. Before the studied slab cracks, the slab has a stiffness E_I = 30 GPa for all three cases and there is a linear relation between the applied load and vertical displacement u_z. The vertical displacement u_z for these three cases are identical, see Figure 4.42. After the slab cracks, the slab has a stiffness that corresponds to each case. Figure 4.42 shows that the slab with $E_{II} = E_I/10$ produces the largest vertical displacement while the slab with $E_{II} = E_I/2$ gives the smallest vertical displacement. For instance when $E_{II} = E_I/2$ = 15 GPa, the vertical displacement u_z = 17.4 mm and the failure load F = 143.4 kN while $E_{II} = E_I/5$ = 5 GPa gives u_z = 25.3 mm and F = 143.8 kN and $E_{II} = E_I/10$ = 3 GPa provides u_z = 37.9 mm and F = 144 kN. This gives a very good agreement since a stiffer slab produces smaller vertical displacement.

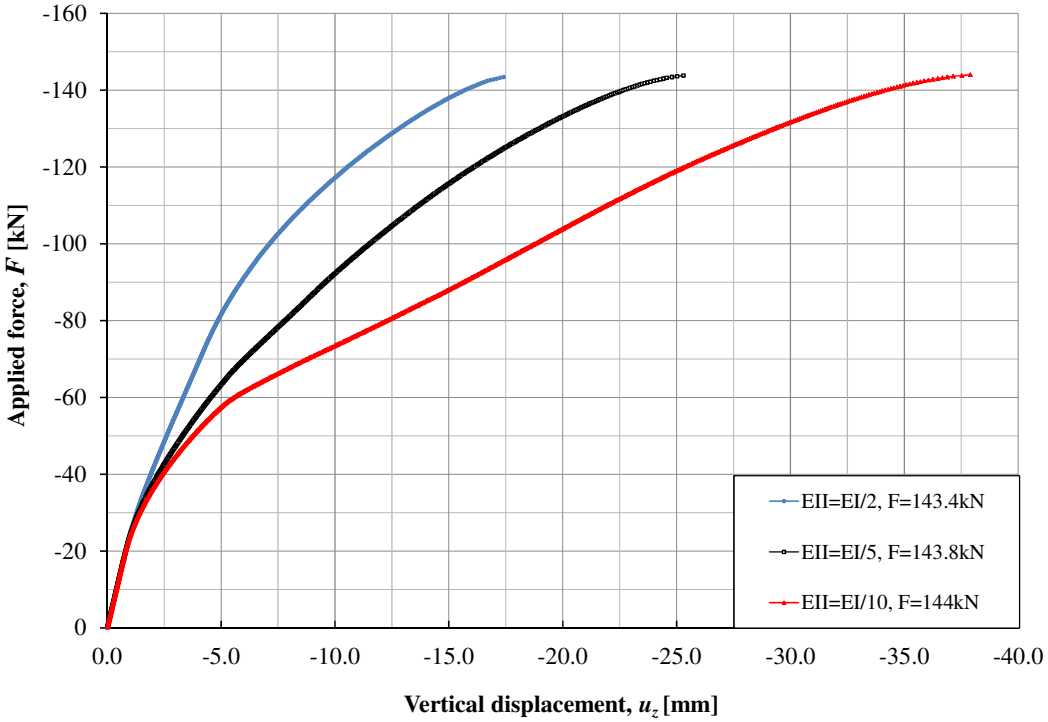

Figure 4.42. Vertical displacement u_z at different load level up to collapse load for $E_{II} = E_I/2$, $E_{II} = E_I/5$, $E_{II} = E_I/10$.

4.5.4.3 Plastic rotation

For the case $E_{II} = E_I/2 = 15$ GPa, the slab studied is stiffer, the amount of cracks is less and the tensile reinforcement starts to yield at a smaller curvature compared to the case when with $E_{II} = E_I/5 = 5$ GPa or $E_{II} = E_I/10 = 3$ GPa.

From Figure 4.43, it is seen that when $F = 120$ kN, $\theta_{pl,max,E_{II}=E_I/10} = 2.4\ 10^{-3}$ rad $< \theta_{pl,max,E_{II}=E_I/5} = 2.8\ 10^{-3}$ rad $< \theta_{pl,max,E_{II}=E_I/2} = 3.2\ 10^{-3}$ rad and $F = 130$ kN gives $\theta_{pl,max,E_{II}=E_I/10} = 4.2\ 10^{-3}$ rad $< \theta_{pl,max,E_{II}=E_I/5} = 4.3\ 10^{-3}$ rad $< \theta_{pl,max,E_{II}=E_I/2} = 4.5\ 10^{-3}$ rad. Therefore, $F = 120$ kN and $F = 130$ kN gives a larger $\theta_{pl,max}$ in case $E_{II} = E_I/2 = 15$ GPa and smaller $\theta_{pl,max}$ in case of $E_{II} = E_I/10 = 3$ GPa. However, when the load keep increasing until $F = 140$ kN, $\theta_{pl,max,E_{II}=E_I/10} = 6.7\ 10^{-3}$ rad $> \theta_{pl,max,E_{II}=E_I/5} = 6.4\ 10^{-3}$ rad $> \theta_{pl,max,E_{II}=E_I/2} = 6.3\ 10^{-3}$ rad. When the cantilever slab studied reaches its collapse load for each cases, it is seen that $\theta_{pl,max,E_{II}=E_I/10} = 8.8\ 10^{-3}$ rad $> \theta_{pl,max,E_{II}=E_I/5} = 8.0\ 10^{-3}$ rad $> \theta_{pl,max,E_{II}=E_I/2} = 7.3\ 10^{-3}$ rad. It is noticed that the maximum plastic rotation $\theta_{pl,max}$ of the studied cantilever slab in case $E_{II} = E_I/2 = 15$ GPa becomes smaller than $\theta_{pl,max}$ in both case $E_{II} = E_I/5 = 5$ GPa and $E_{II} = E_I/10 = 3$ GPa from $F = 130$ kN to $F = 140$ kN. The fluctuation of the maximum plastic rotation that took place between $F = 130$ kN and $F = 140$ kN has not yet been understood. Further investigations are needed so that reasons for this disturbance might be provided.

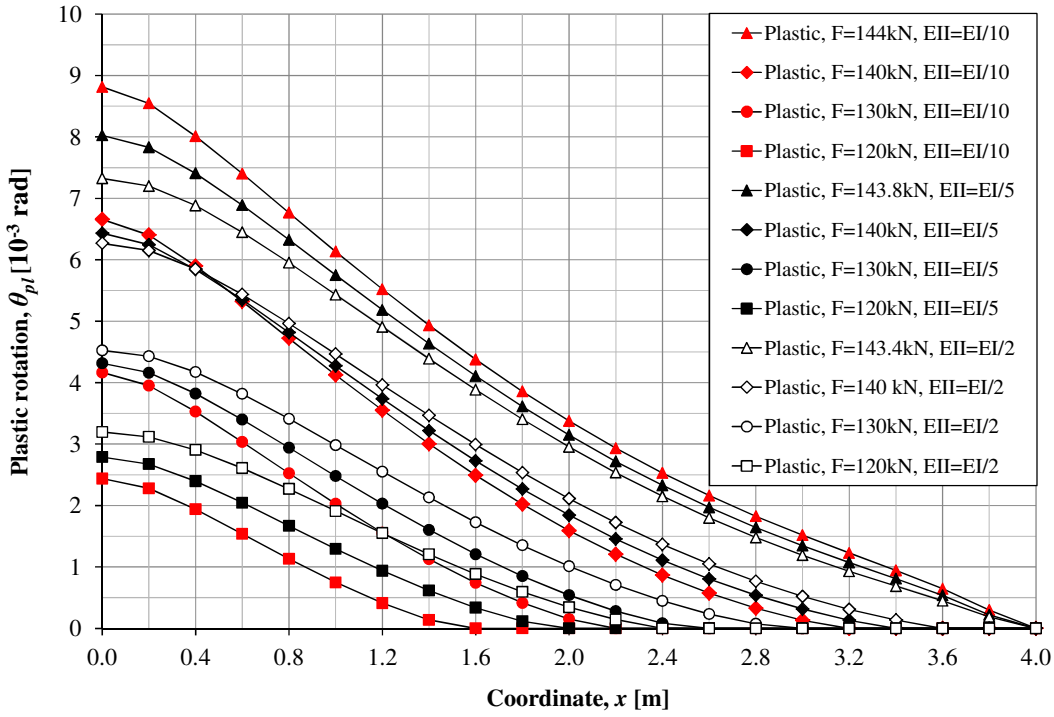

Figure 4.43. Plastic rotation distribution θ_{pl} along L_5 at different load level up to failure load for $E_{II} = E_I/2$, $E_{II} = E_I/5$, $E_{II} = E_I/10$.

From Figure 4.43, it is seen that for these three cases when the cantilever slab studied reached its collapse load, the yielding parts of the slab along L_5 is $L_{yield} = 4$ m from the symmetry line. From Figure 4.43, it is also seen that the maximum plastic rotation for each case when the collapse mechanism was formed is less than the minimum plastic rotation capacity of the studied cantilever slab $\theta_{rd,min} = 10.6 \cdot 10^{-3}$ rad. This indicates that it is possible to redistribute $m_y = 0.6\ m_{y,elastic}$ within $w = 4$ m. Therefore, it is concluded that the recommendation given by Pacoste *et al.* (2012) in equation (2-53)

is conservative with regardless of the changed stiffness from $E_{II} = E_I/2 < E_{II} < E_{II} = E_I/10$ when analysing the cantilever slab studied in Figure 4.32 with elasto-plastic moment curvature input in Figure 4.33, Figure C.30 and Figure C.36.

4.5.5 Comparisons between trilinear and quadlinear M(χ)

In order to investigate of how trilinear moment curvature relationship in Figure 4.44 affects the structural response of the cantilever slab studied in Figure 4.32, a comparison of slab in Figure 4.32 with moment curvature input in Figure 4.44 and in Figure 4.33 was made. $M_{plastic} = 0.6M_{elastic,}$ and $M_{cr1} = M_{plastic}/3$ in equation (4-21) and equation (4-25) in Section 4.5.3.1 were chosen for curvature χ_I and χ_{II} of the moment-curvature diagram in Figure 4.44 and χ_I, χ_{II} and χ_{III} are determined as:

$$\chi_I = \frac{M_{cr1}}{E_I I} = \frac{3.8 \cdot 10^3}{30 \cdot 10^9 \cdot \frac{0.2 \cdot 0.2^3}{12}} = 0.00095 \ [1/\mathrm{m}] \tag{4-35}$$

$$\chi_{II} = \frac{M_{plastic}}{E_{II} I} = \frac{11.4 \cdot 10^3}{6 \cdot 10^9 \cdot \frac{0.2 \cdot 0.2^3}{12}} = 0.01425 \ [1/\mathrm{m}] \tag{4-36}$$

$$\chi_{III} = 10 \ [1/\mathrm{m}] \tag{4-37}$$

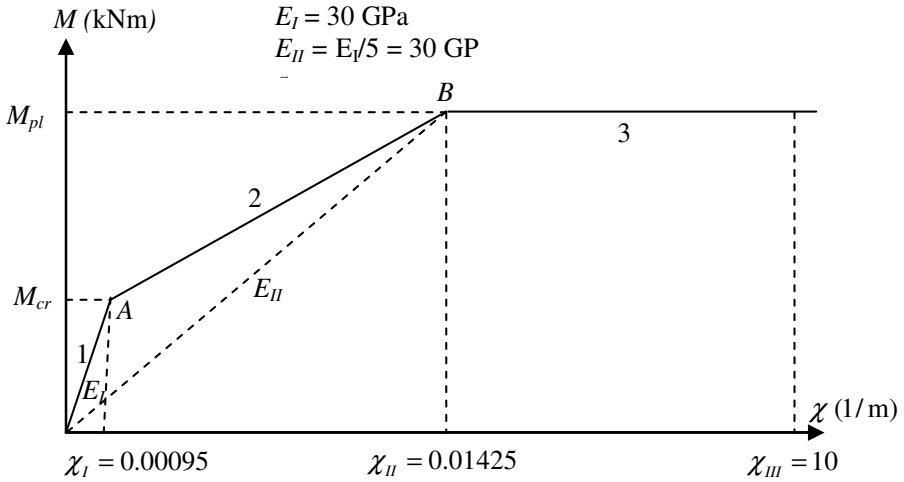

Figure 4.44. Trilinear moment-curvature relationship for the analysis of the slab in elasto-plastic case, $E_{II} = E_I/5$.

Line number 1 in Figure 4.44 represents elastic part (state I). Point *A* is the boundary between the uncracked and cracked part of the section. Line number 2 in Figure 4.44 is used to simulate the effect of tension stiffening after the concrete cracks. Line number 2 ends at a break point *B* where the yielding of the tensile reinforcement starts. Line number 3 is used to simplify a yielding part of the tensile reinforcement. The ratio of the maximum moment $m_{y,max}$ received from FE analysis to moment distribution $m_{y,(x)}$ along *x*-direction is determined in equation (4-38).

$$\delta_{tri} = \frac{m_{y,\max}}{m_{y,x}} \tag{4-38}$$

For the results of moment distribution, shear forces distribution and plastic rotation of the cantilever slab studied with the trilinear moment curvature input in Figure 4.44, Reader can refer to APPENDIX C.

4.5.5.1 Load-displacement relation

From Figure 4.45, it is seen that when F < 20 kN, the displacement due to trilinear and quadlinear moment curvature relationship are identical since the slab studied has the same stiffness before the slab starts to crack. When F > 20 kN, the slab studied starts to crack for both cases. The trilinear produce a smaller vertical displacement u_z = 23.7 mm while a quadlinear produce a larger vertical displacement u_z = 25.3 mm for the same collapsed load F = 143.8 kN. The reason is that the slab with trilinear moment curvature relationship in Figure 4.44 simulates a crack development which is slower than a crack development assumed by a quadlinear moment curvature input in Figure 4.33. The results shown in Figure 4.45 are reasonable as the stiffer slab produce a smaller vertical displacement. Since these two modelling gives the same failure load F = 143.8 kN, it is concluded that the assumption about the tension stiffening effect of the slab does not affect the failure load of the slab.

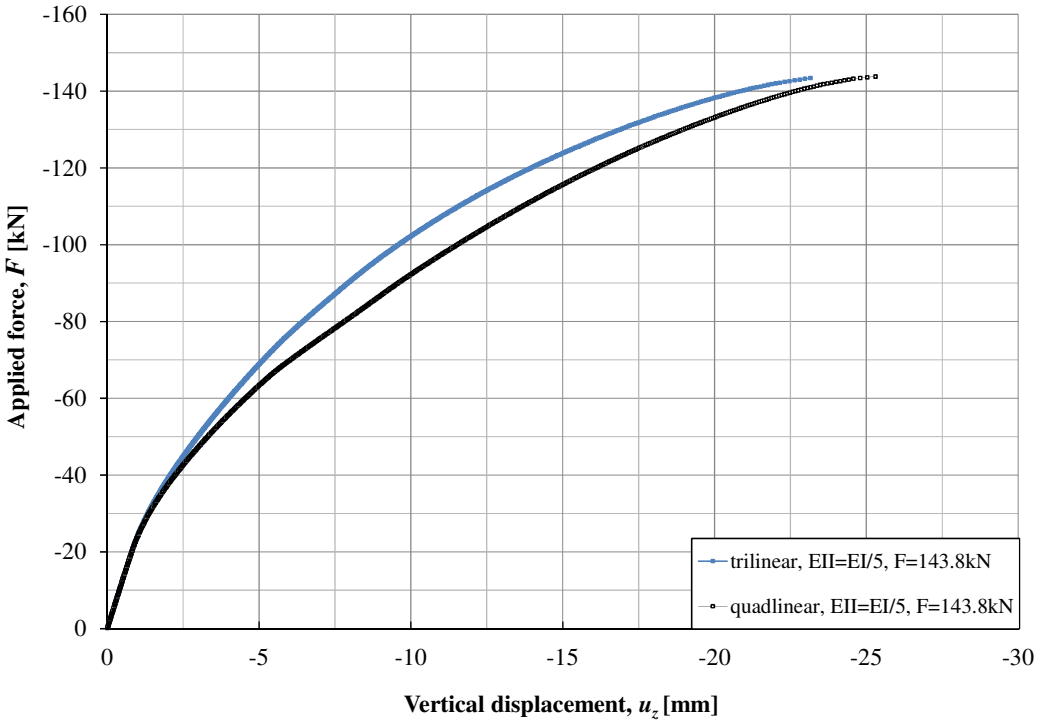

Figure 4.45. Comparisons of vertical displacement u_z at different load level up to collapse load between trilinear moment curvature relationship and quadlinear moment curvature relationship, $E_{II} = E_I/5$.

4.5.5.2 Moment

The moment m_y distribution along L_5 for both cases for different load level from F = 60 kN to F = 143.8 kN are illustrated in Figure 4.46.

From Figure 4.46a, it is seen that when F = 60 kN the slab with trilinear moment curvature input gives larger moment than slab with quadlinear moment curvature input, i.e. $m_{y,tri,}$ = 38.9 kNm/m $> m_{y,quad}$ = 36.8 kNm/m while F = 80 kN gives $m_{y,tri,}$ = 51.2 kNm/m $< m_{y,quad}$ = 52.8 kNm/m and when F = 100 kN, $m_{y,tri,}$ = 58.3 kNm/m > $m_{y,quad}$ = 58.29 kNm/m.

From Figure 4.46b, it is seen that $m_{y,tri,} < m_{y,quad}$ from F = 120 kN to F = 143.8 kN.

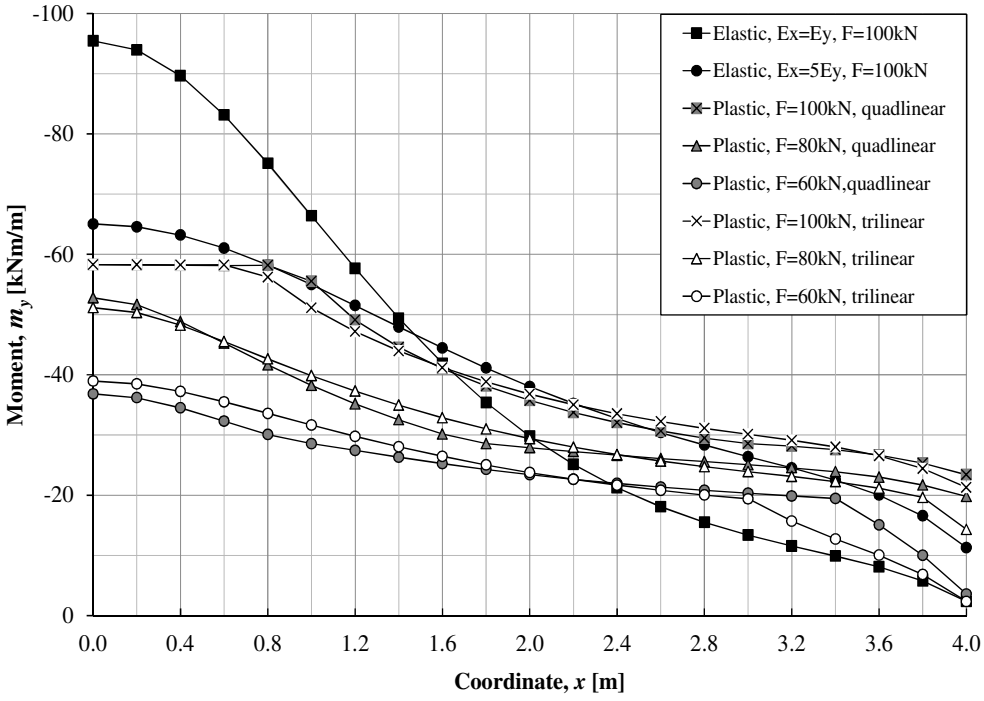

(a)

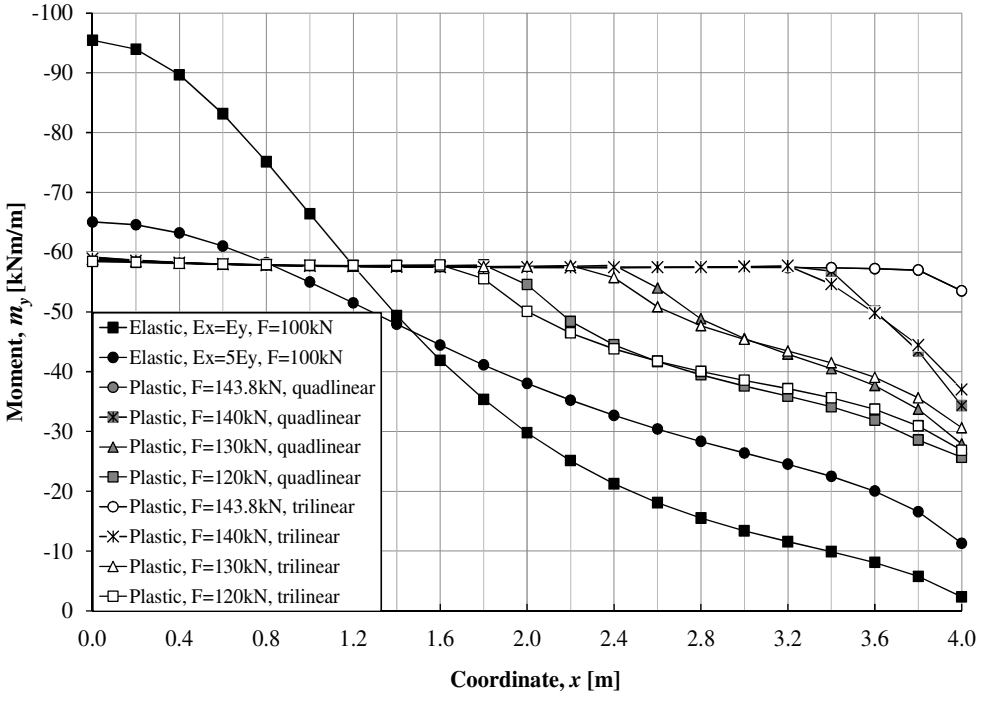

(b)

Figure 4.46. Moment distribution m_y along L_5 at different load level (a) moment distribution m_y up to 100 kN (b) moment distribution m_y up to 143.8 kN, $E_{II} = E_I/5$.

4.5.5.3 Plastic rotation

The comparisons in Figure 4.47 between the cantilever slab studied with trilinear and quadlinear moment curvature input shows that plastic rotation due to trilinear moment curvature input is smaller than plastic rotation with quadlinear moment curvature input,i.e. $\theta_{pl,max,tri} < \theta_{pl,max,quad}$ for $F = 120$ kN $< F < F = 143.8$ kN. Based on the comparisons of plastic rotation between slab with trilinear moment curvature input and slab with quadlinear moment curvature input, it is concluded that the stiffer the stiffer the slab is, the smaller the plastic rotation is received.

For the failure load $F = 143.8$ kN, $\theta_{pl,max,tri} = 7.99\ 10^{-3}$ rad and $\theta_{pl,max,quad} = 8.03\ 10^{-3}$ rad . This collapse load leads to yielding all over fixed boundary condition of the slabs, i.e. $L_{yield} = 4$ m. Since $\theta_{pl,max,tri} = 7.99\ 10^{-3}$ rad $< \theta_{pl,max,quad} = 8.03\ 10^{-3}$ rad $< \theta_{rd,min} = 10.6 \cdot 10^{-3}$ rad, it means that it is possible to redistribute $m_y = 0.6\, m_{y,elastic}$ within $w_x = 4$ m. Therefore, it is concluded the recommendation given by Pacoste *et al.* (2012) in equation (2-53) is conservative for these particular cases.

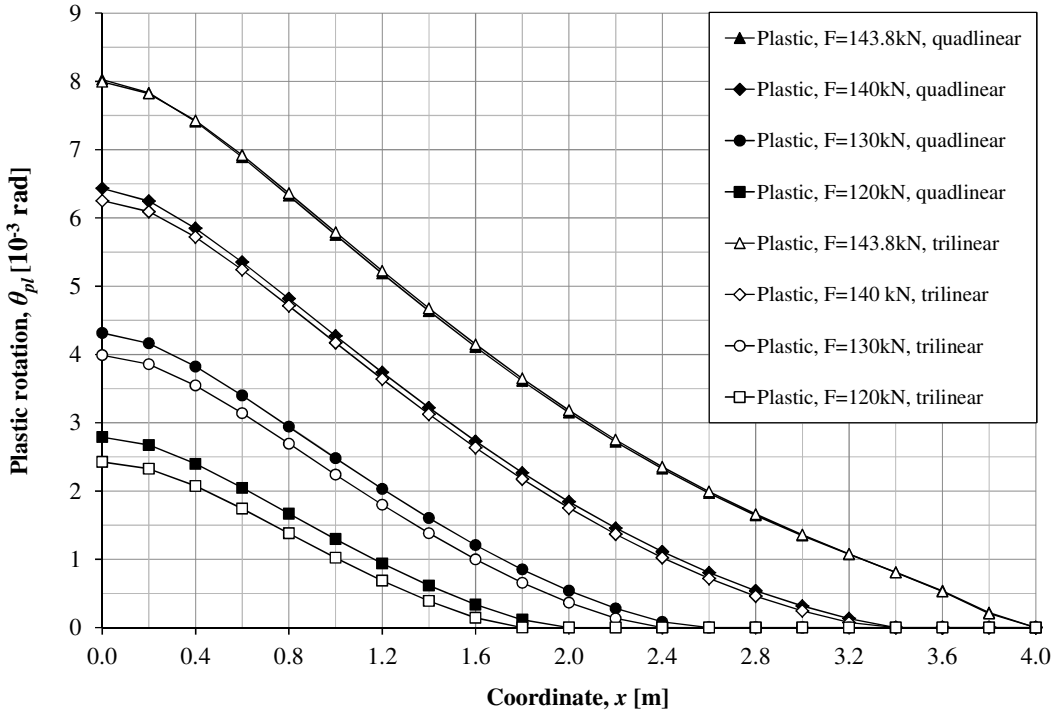

Figure 4.47. Comparisons between trilinear and quadlinear moment curvature input for plastic rotation distribution θ_{pl} along L_5 at different load level up to failure load for $E_{II} = E_I/5$.

4.5.6 Quadlinear M(χ)-$M_{pl} = 0.4M_{el}$, $E_{II} = E_{II}/5$

4.5.6.1 Moment

As mentioned in Section 4.5.3.3, there is a possibility to choose $M_{plastic} < 0.6M_{elastic}$ to redistribute the reinforcement moment for the cantilever slab studied in Figure 4.32. This cantilever slab was in this case analysed with the moment-curvature relationship input in Figure 4.48. Here $M_{plastic} = 0.4M_{elastic}$ was chosen while M_{cr1} and M_{cr2} input in equation (4-23) to (4-26) were kept unchanged.

$$M_{plastic} = 0.4 \cdot M_{elastic} = 0.6 \cdot 19 = 7.6\,\text{kNm} \tag{4-39}$$

$$m_{plastic} = \frac{7.6}{0.2} = 38\,\text{kNm/m} \tag{4-40}$$

The curvature χ_I, χ_{II} , and χ_{IV} in equation (4-27), equation (4-28) and equation (4-30) were also kept unchanged while χ_{III} is determined as:

$$\chi_{III} = \frac{M_{plastic}}{E_{II} I} = \frac{7.6 \cdot 10^3}{6 \cdot 10^9 \cdot \frac{0.2 \cdot 0.2^3}{12}} = 0.0095\ [1/\text{m}] \tag{4-41}$$

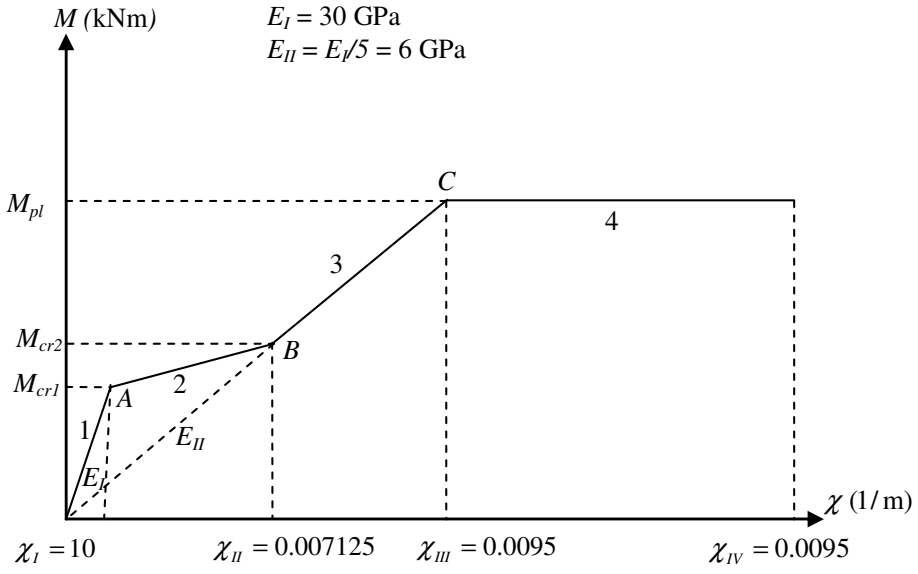

Figure 4.48. Quadlinear moment-curvature relationship for the analysis of the slab in elasto-plastic case, $M_{pl} = 0.4M_{el}$, $E_{II} = E_I/5$.

Figure 4.48 consists of four zones that were used to simulate the structural response of the slab studied in Figure 4.32. The only difference between quadlinear moment curvature input in Figure 4.33 and Figure 4.48 is that $M_{pl} = 0.4M_{el}$ was used instead of $M_{pl} = 0.6M_{el}$.

The ratio of the maximum moment $m_{y,max}$ received from FE analysis to moment distribution $m_{y,(x)}$ along x-direction can also be determined in equation (4-31).

From Figure 4.49, it is seen that from $F = 20$ kN to $F = 60$ kN, the structural response of the slab studied in this Section is the same as the behavior of the slab studied described in Section 4.5.3.1 since their geometry and moment-curvature input are the same for this load level.

When $F = 80$ kN, the maximum moment intensity at the middle of the slab is $m_{y,max} = 38.9$ kNm/m which is larger than the yielding moment intensity $m_{y,yield} = 38$ kNm/m. The slab studied yields at a length $L_{yield} = 1.6$ m from the symmetry line. When continuing loading the slab until collapse load $F = 95.8$ kN, it is

seen that the yielding occurs all along fixed boundary, $L_{yield} = 4$ m and the slab failed when the mechanism was formed.

From Figure 4.49, it is observed that the slab studied yields and collapse earlier compared to Figure 4.35. When $M_{pl} = 0.4M_{el}$ was chosen, it requires less reinforcement and it gives lower moment resistance than the case of $M_{pl} = 0.6M_{el}$. Therefore, the slab studied in case of $M_{pl} = 0.4M_{el}$ collapsed before the slab with $M_{pl} = 0.6M_{el}$.

The distribution shape of moment in Figure 4.49b after cracking and plastic redistribution is smoother than distribution shape of moment from linear elastic FE analysis. This indicates that the moment distribution from linear elastic FE analysis is critical in the design.

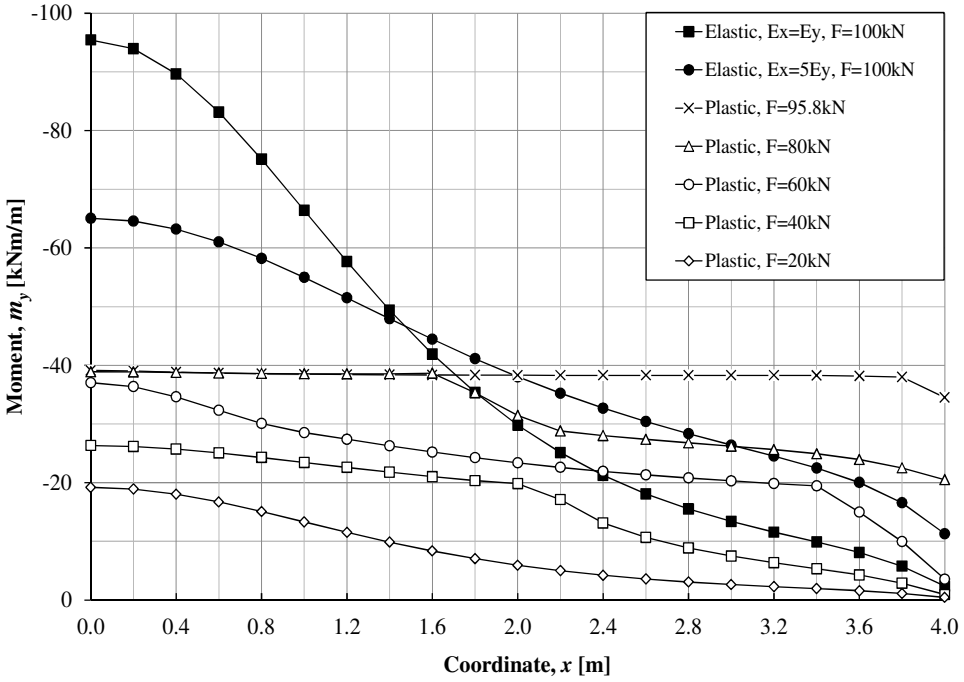

(a)

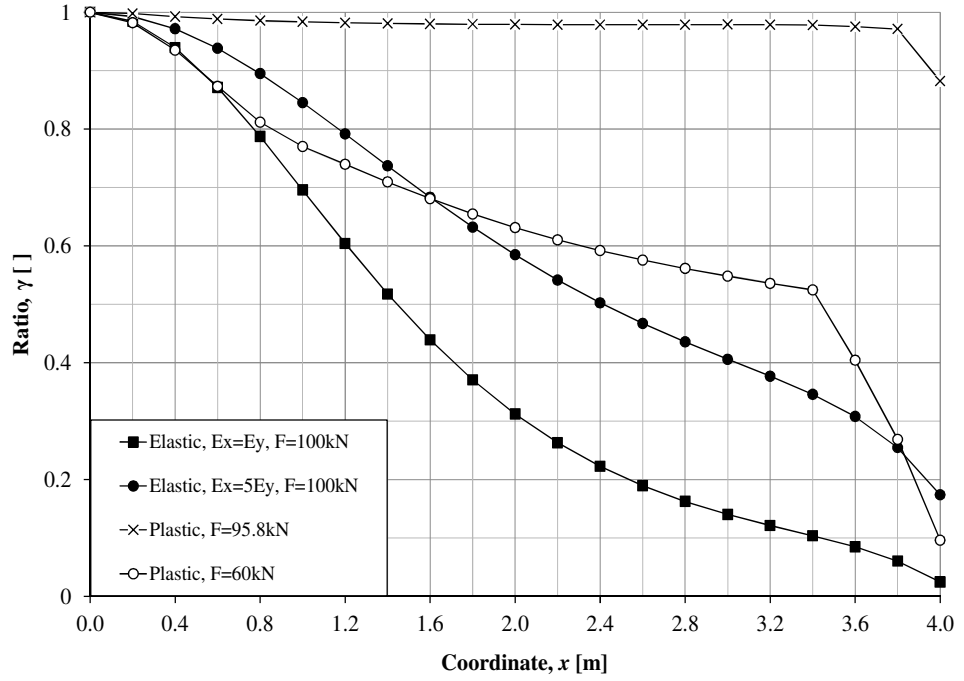

(b)

Figure 4.49. Moment distribution m_y along L_5 at different load level up to 95.8 kN (a) moment distribution m_y (b) ratio of maximum moment $m_{y,max}$ to $m_{y,x}$ moment along L_5, $M_{pl} = 0.4\ M_{el}$, $E_{II} = E_I/5$.

4.5.6.2 Contour plot

In Figure 4.50, there are four different colors that represent the structural response of the cantilever slab from uncracked state until failure. These colours have the same meaning as those described in Section 4.5.3.2.

From $F = 20$ kN to $F = 60$ kN, the contour plots in Figure 4.50 are identical to the contour plots in Figure 4.36.

When the load increases up to $F = 80$ kN, the slab examined starts to yield along fixed boundary at about $L_{yield} = 1.6$ m from the symmetry line while the remaining parts located at about $1.6\text{m} \leq x \leq 2.4\text{m}$ m are in zone 3 and at about $2.4\text{m} \leq x \leq 4$ m are in zone 2. When $F = 90$ kN, yielding parts of the slab propagates further at about $L_{yield} = 3$ m. When $F = 95.8$ kN, $L_{yield} = 4$ m along L_5 and the cracking parts of the studied slab develop further. The disturbances at position ($x = 0.2$ m, $y = 1.4$ m) and position ($x = 4$ m, $y = 0.2$ m) can be seen clearly.

Like Figure 4.36 and Figure 4.37, it is also noted that there are always disturbances at position ($x = 0.2$ m, $y = 1.4$ m) and position ($x = 4$ m, $y = 0.2$ m), but these disturbances cannot be seen when their surrounding regions located in the same zone.

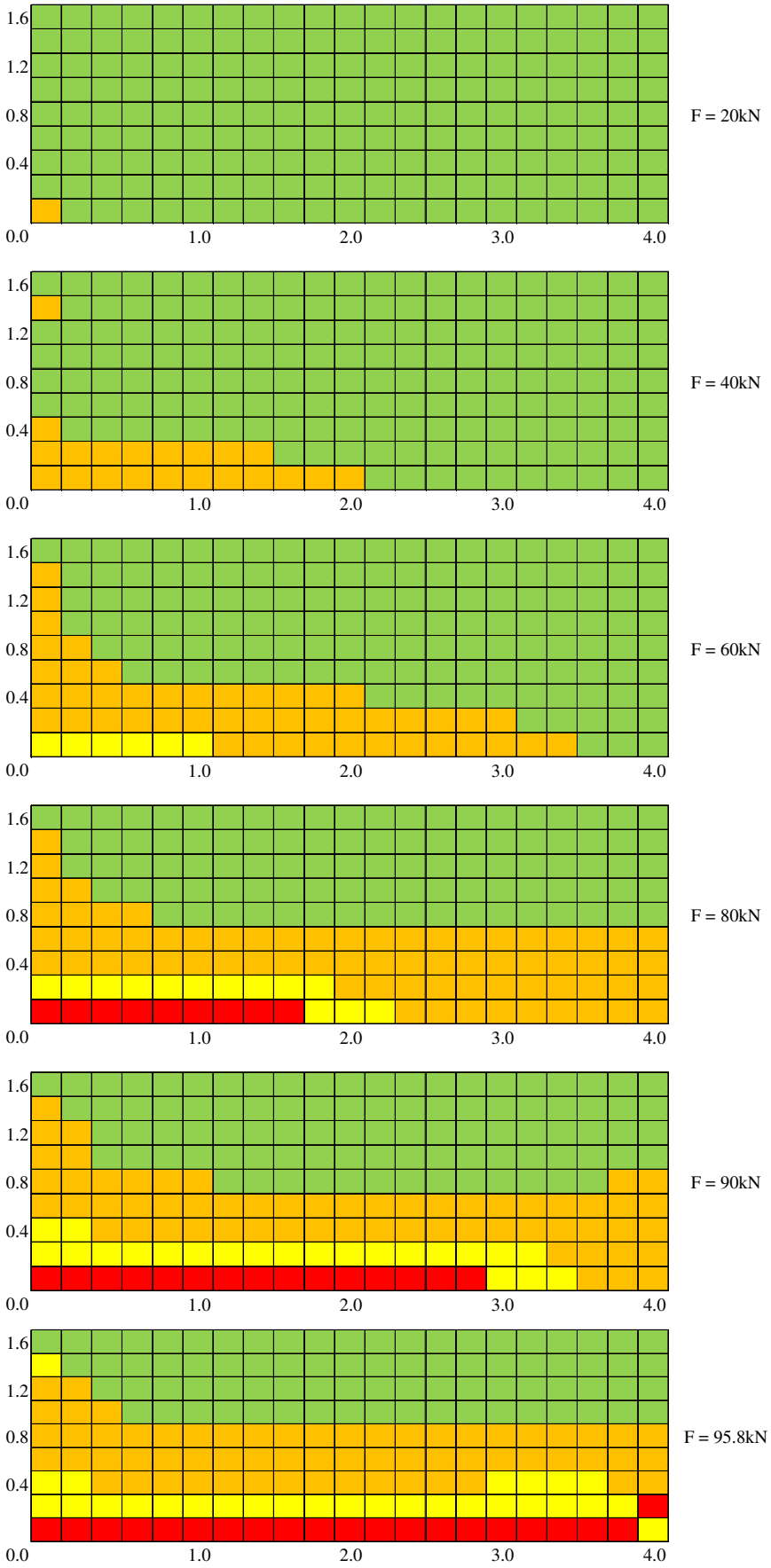

Figure 4.50. Contour plot at different load level up to failure load F = 95.8 kN, M_{pl} = 0.4 M_{el}, E_{II} = E_I/5.

4.5.6.3 Plastic rotation

Figure 4.38 shows that when the slab collapsed at $F = 95.8$ kN, the maximum plastic rotation is $\theta_{pl,max} = 5.2 \cdot 10^{-3}$ rad. Hence, this rotation is smaller than the minimum plastic rotation capacity of the cantilever slab examined $\theta_{rd,min} = 10.6 \cdot 10^{-3}$ rad as shown in APPENDIX F. It means that plastic rotation is not a problem in this case. Therefore, it is possible to redistribute the moment $M_{plastic} = 0.4 M_{elastic}$ with a distribution width $w = 4$ m (symmetrical case) if the applied load is not greater than $F = 95.8$ kN.

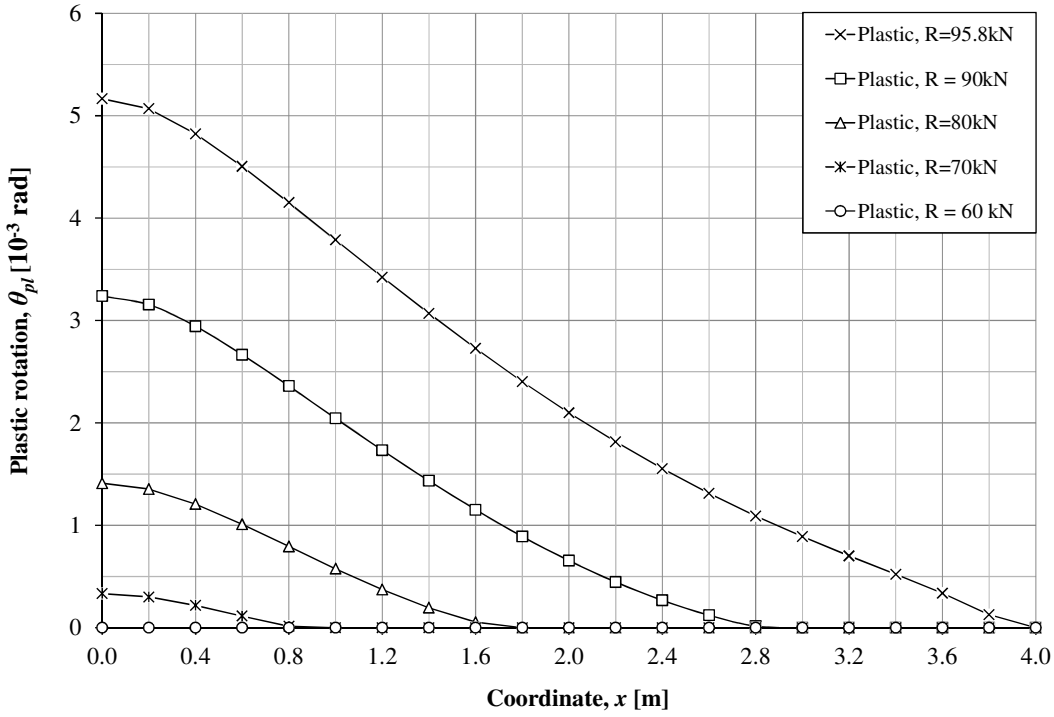

Figure 4.51. Plastic rotation distribution θ_{pl} along L_5 at different load level up to $F = 143.8$ kN, $M_{pl} = 0.4\ M_{el}$, $E_{II} = E_I/5$.

4.5.6.4 Comparison with existing guideline

From Section 4.5.3.4, the mean moment distribution $m_{y,mean} = 90.3$ kNm/m, determined from the recommendation given by Pacoste *et al.* (2012), can be distribute within $w_x = 0.65$ m for $F = 100$ kN.

When choosing $M_{plastic} = 0.6 M_{elastic}$ and $M_{plastic} = 0.4 M_{elastic}$, a failure load of $F = 143.8$ kN and $F = 95.8$ kN respectively, was obtained. In order to determine $M_{plastic}$ for a failure load $F = 100$ kN, linear interpolation between $M_{plastic} = 0.4 M_{elastic}$ and $M_{plastic} = 0.6 M_{elastic}$ were performed as following:

$$x = 0.4 + \frac{100 - 95.8}{143.8 - 95.8}(0.6 - 0.4) = 0.42 \tag{4-42}$$

$$M_{plastic} = 0.4175 \cdot M_{elastic} = 0.4175 \cdot 19 = 7.9 \text{ kNm} \tag{4-43}$$

$$m_{plastic} = \frac{7.93}{0.2} = 39.7 \text{ kNm/m} \tag{4-44}$$

Hence, in order to achieve a collapse load F = 100 kN, $m_{plastic}$ = 39.7 kNm/m needs to be provided. $m_{plastic}$ = 39.7 kNm/m resulted a plastic rotation as following:

$$\theta_{pl,F=100} = 5.2 \cdot 10^{-3} + \frac{100-95.8}{143.8-95.8}\left(8.0 \cdot 10^{-3} - 5.2 \cdot 10^{-3}\right) = 5.4 \cdot 10^{-3} \tag{4-45}$$

From Section 4.5.3.4, $m_{y,mean} = 0.6 m_{y,max}$ = 57 kNm/m results in $\theta_{pl,max} = 8.0 \cdot 10^{-3}$ rad and it is redistributed within w_x = 4 m. Therefore, it is concluded that for a collapse load F = 100 kN, $m_{y,mean}$ =$0.42 m_{y,max}$ = 39.7 kNm/m with $\theta_{pl,max} = 5.42 \cdot 10^{-3}$ rad can also be distributed within w_x = 4 m.

For load F = 100 kN, the ratio γ between the mean moment distribution in equation (4-33) determined from the recommendation given by Pacoste *et al.* (2012) and the mean moment distribution in equation (4-44) received from elasto-plastic FE analysis is calculated as:

$$\gamma = 100 \cdot \frac{m_{y,mean,recommendation}}{m_{y,mean,FE}} = 100 \cdot \frac{39.65}{90.3} = 44\,\% \tag{4-46}$$

γ = 44 % indicates that it is possible to reduce 44 % from mean moment obtained from the recommendation provided by Pacoste *et al.* (2012).

For shear forces distribution, reader can refer to APPENDIX C.

4.5.7 Trilinear M(χ) with no yielding - $E_{II} = E_{II}/5$

4.5.7.1 Moment

This case corresponds to a case where the yield capacity is high enough not to be reached. Thus, it can be used to compare with the response in service limit state. To give a better understanding of the structural behavior of the studied cantilever slab in this case, three more parametric studies were performed. The cantilever slab in Figure 4.52 was examined with a trilinear moment curvature relationship with no yielding input illustrated in Figure 4.53. This cantilever slab has the same geometry and boundary condition as the slab in Figure 4.32, but was subject to the applied load F = 200 kN. A very large value was given for ultimate moment capacity and the corresponding curvature so that yielding was not reached. For the input value in Figure 4.53, readers can refer to equation (4-21) to (4-29) in Section 4.5.3.1 where M_{cr1} = 19 kNm/m, M_{cr2} = 28.5 kNm/m, M_{pl} = 57 kNm/m.

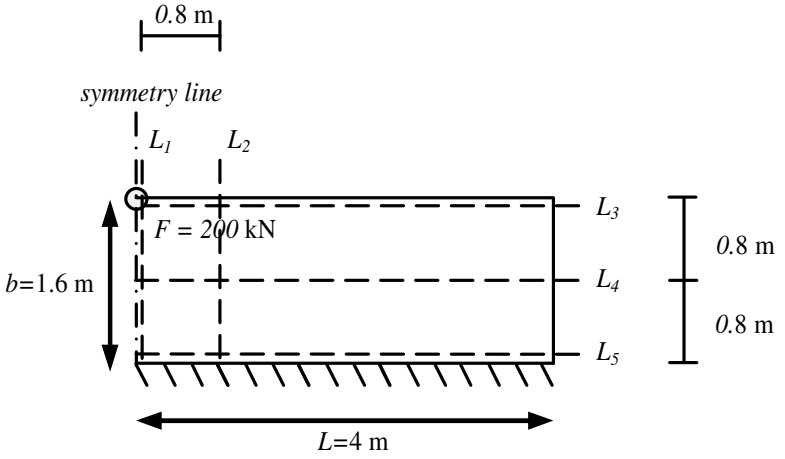

Figure 4.52. Geometry and result lines of the studied slab using trilinear moment-curvature relationship with no yielding.

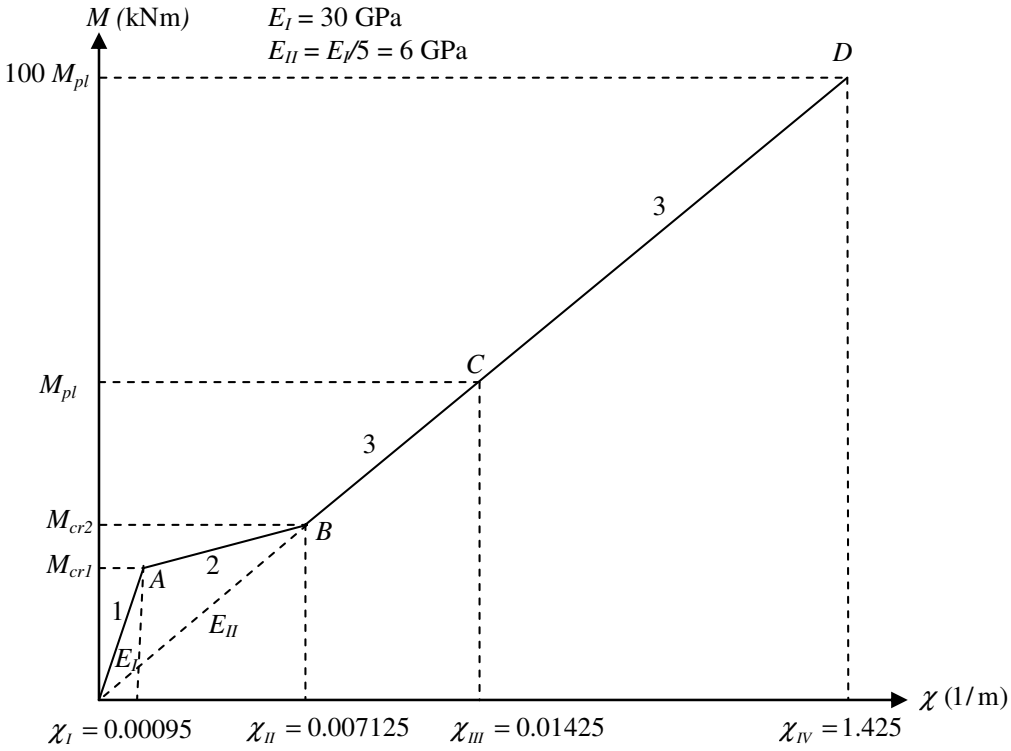

Figure 4.53. Trilinear moment-curvature relationship without yielding for the analysis of the slab, $E_{II} = E_I/5$.

In Figure 4.54a, $F = 20$ kN, $F = 40$ kN, $F = 60$ kN and $F = 80$ kN gives identical structural response to those in Figure 4.34a since these two cases have the same moment curvature input for $m_{y,max} = 52.5$ kNm/m $< m_{pl} = 57$ kNm/m. When $F = 100$ kN, it is seen that $m_{y,max} = 69$ kNm/m $> m_{pl} = 57$ kNm/m since there is no yielding in the moment curvature input in Figure 4.53 and the moment keeps increasing with increasing applied load. When $F = 100$ kN, $m_{y,max} = 69$ kNm/m is close to the maximum moment in elastic orthotropic case $m_{y,max,ortho} = 65.1$ kNm/m and deviates a lot from the maximum moment in the elastic isotropic case where $m_{y,max,iso} = 95$ kNm/m, see Figure 4.54a. The moment distribution shape for $F = 100$ kN is close to the distribution shape of the elastic isotropic case at about

$0 < x < 1$ m and these two curves deviate rather much from each other at around 1 m$< x < 4$ m, see Figure 4.54b.

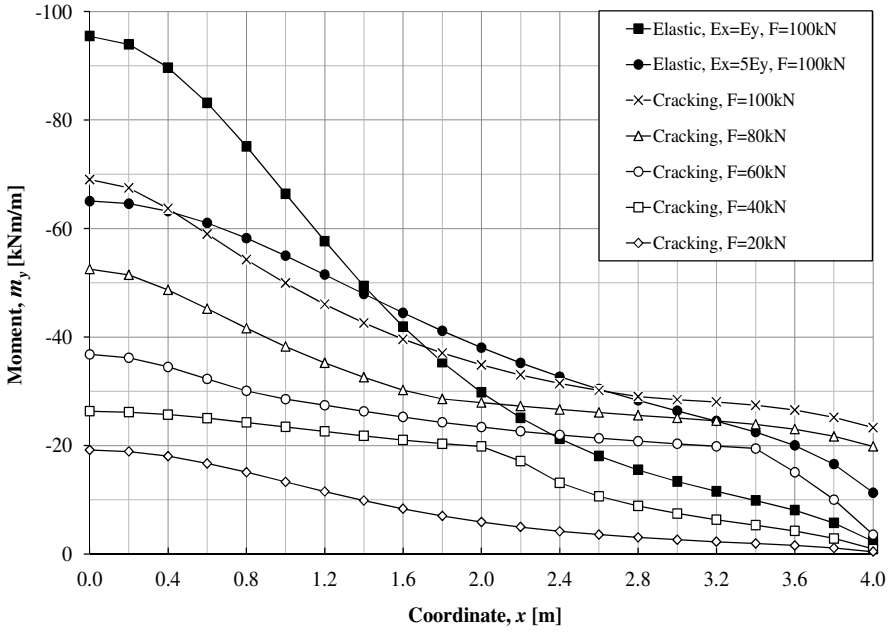

(a)

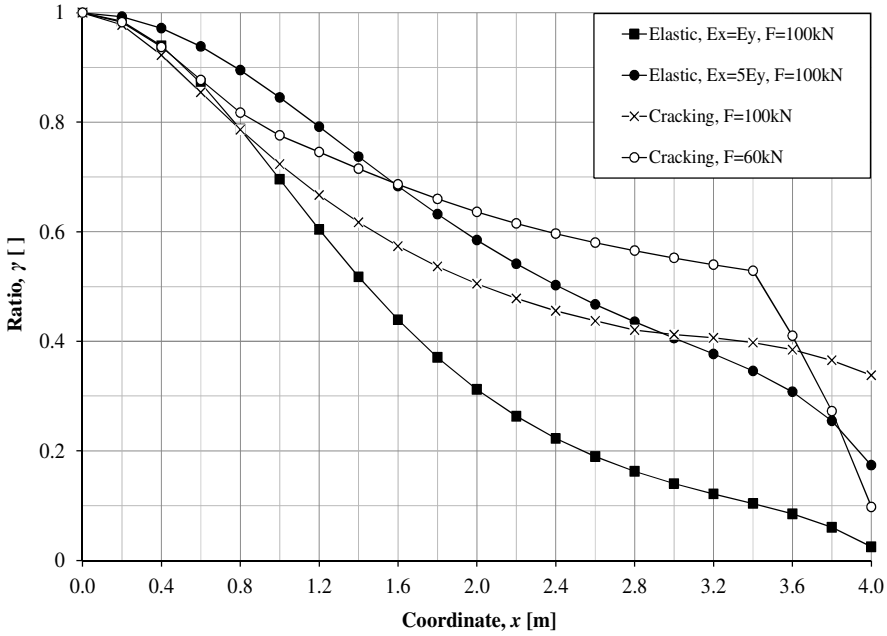

(b)

Figure 4.54. Moment distribution m_y along L_5 at different load level up to 100 kN (a) moment distribution m_y (b) ratio of maximum moment $m_{y,max}$ to $m_{y,x}$ moment along L_5, $E_{II} = E_I/5$.

From Figure 4.55a, it can be seen that the moment increases with increasing applied load F. The moment distribution shape when F = 140 kN and F = 200 kN is similar to each other. The similarity in the response is because the stiffness in the cracked parts in the slab are similar for these high loads.

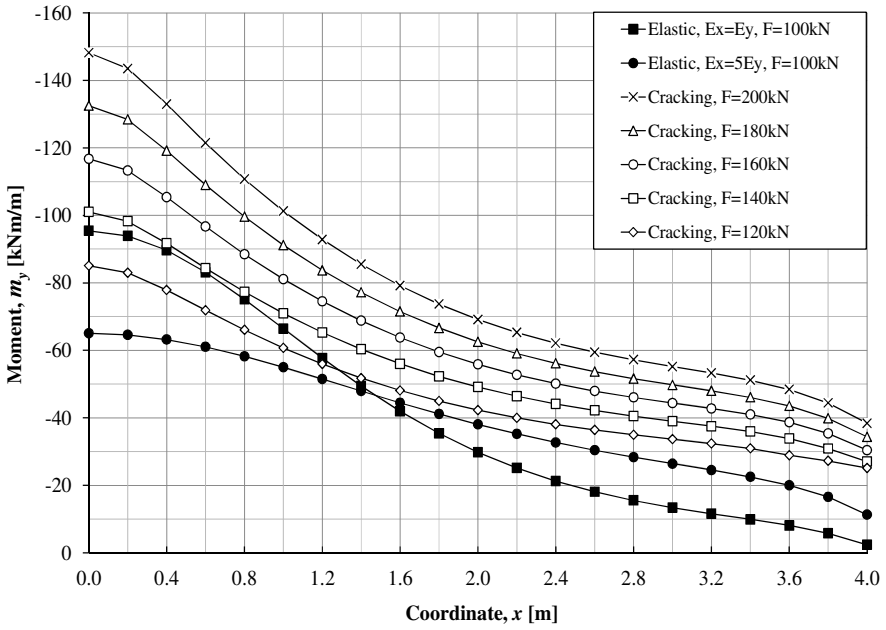

(a)

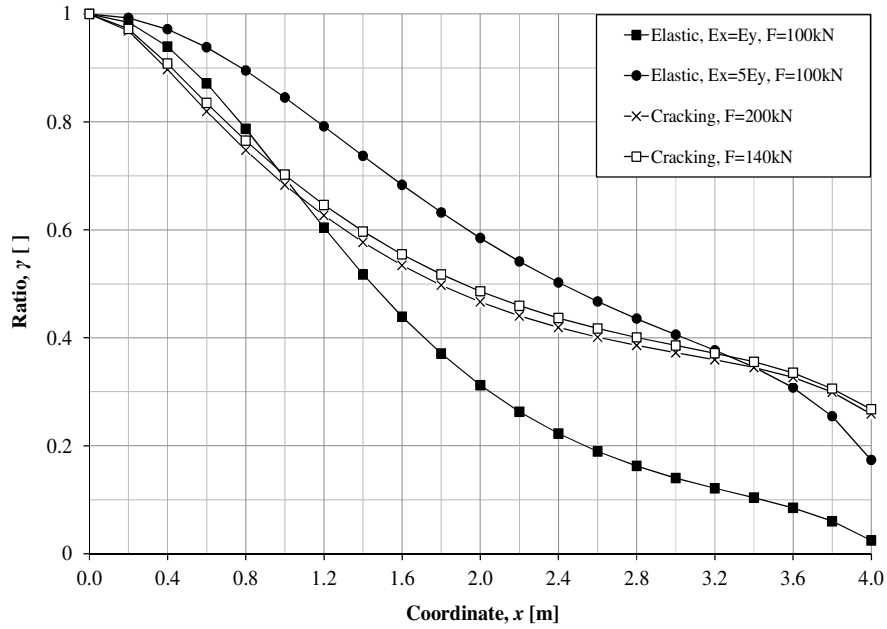

(b)

Figure 4.55. Moment distribution m_y along L_5 at different load level up to 200 kN (a) moment distribution m_y (b) ratio of maximum moment $m_{y,max}$ to $m_{y,x}$ moment along L_5, $E_{II} = E_I/5$.

Since $F = 100$ kN, $m_{y,max} = 69$ kNm/m is close to the maximum moment in elastic orthotropic case $m_{y,max,ortho} = 65.1$ kNm/m, it is concluded that orthotropic analysis can be used to rather well predict the maximum moment for design of the cantilever slab studied in Figure 4.52. Consequently, the maximum moment received from orthotropic analysis can be used directly for the design and do not need to reduce it like in the case of isotropic elastic analysis. For shear forces distribution, the reader can refer to APPENDIX C.

4.5.8 Influence of state II stiffness in trilinear M(χ) without yielding

4.5.8.1 Orientation

In order to investigate the behaviour of the studied cantilever slab in Figure 4.52 with the trilinear moment curvature relationship without yielding input, a parametric study of state II stiffness, i.e. $E_{II} = E_I/2$ and $E_{II} = E_I/10$ was examined. The reader can refer to APPENDIX C for trilinear moment curvature relationsip without yielding input and for the moment distribution and shear forces distribution for these cases.

4.5.8.2 Load-displacement relation

In these cases, the cantilever slab studied was subjected to a load of $F = 200$ kN. The maximum vertical displacement u_z at the middle of the slab becomes larger when increasing the applied load F, see Figure 4.56. There is no formation of the collapse mechanism since there is no yield limit.

The vertical displacement u_z for these three cases are identical before the slab starts to crack. After the cracking, the stiffness of the studied slab adapted to the stiffness of each case. It is seen that after the cracking, the stiffer slab provides a smaller vertical displacement, i.e. $u_{z(EII=EI/2)} = 13$ mm < $u_{z(EII=EI/5)} = 25.3$ mm < $u_{z(EII=EI/10)} = 43.6$ mm.

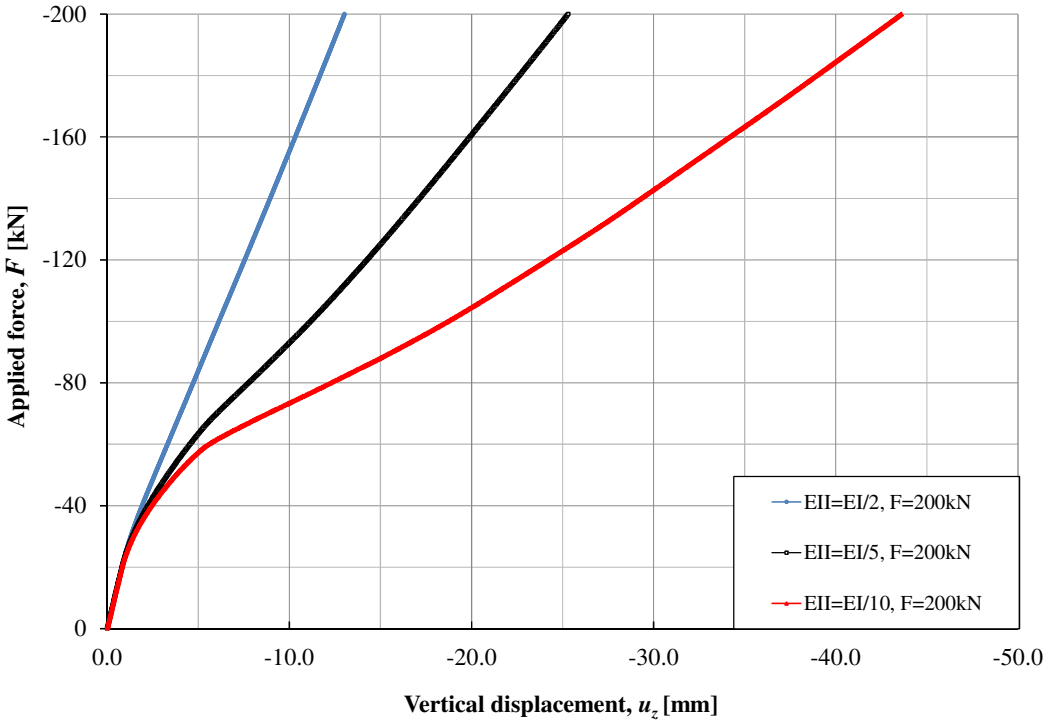

Figure 4.56. Vertical displacement u_z at different load level up to collapse load for $E_{II} = E_I/2$, $E_{II} = E_I/5$, $E_{II} = E_I/10$.

4.5.8.3 Moment

The moment distributions and the ratios of maximum moment $m_{y,max}$ to $m_{y,x}$ along fixed boundary for each case were plotted in Figure 4.57.

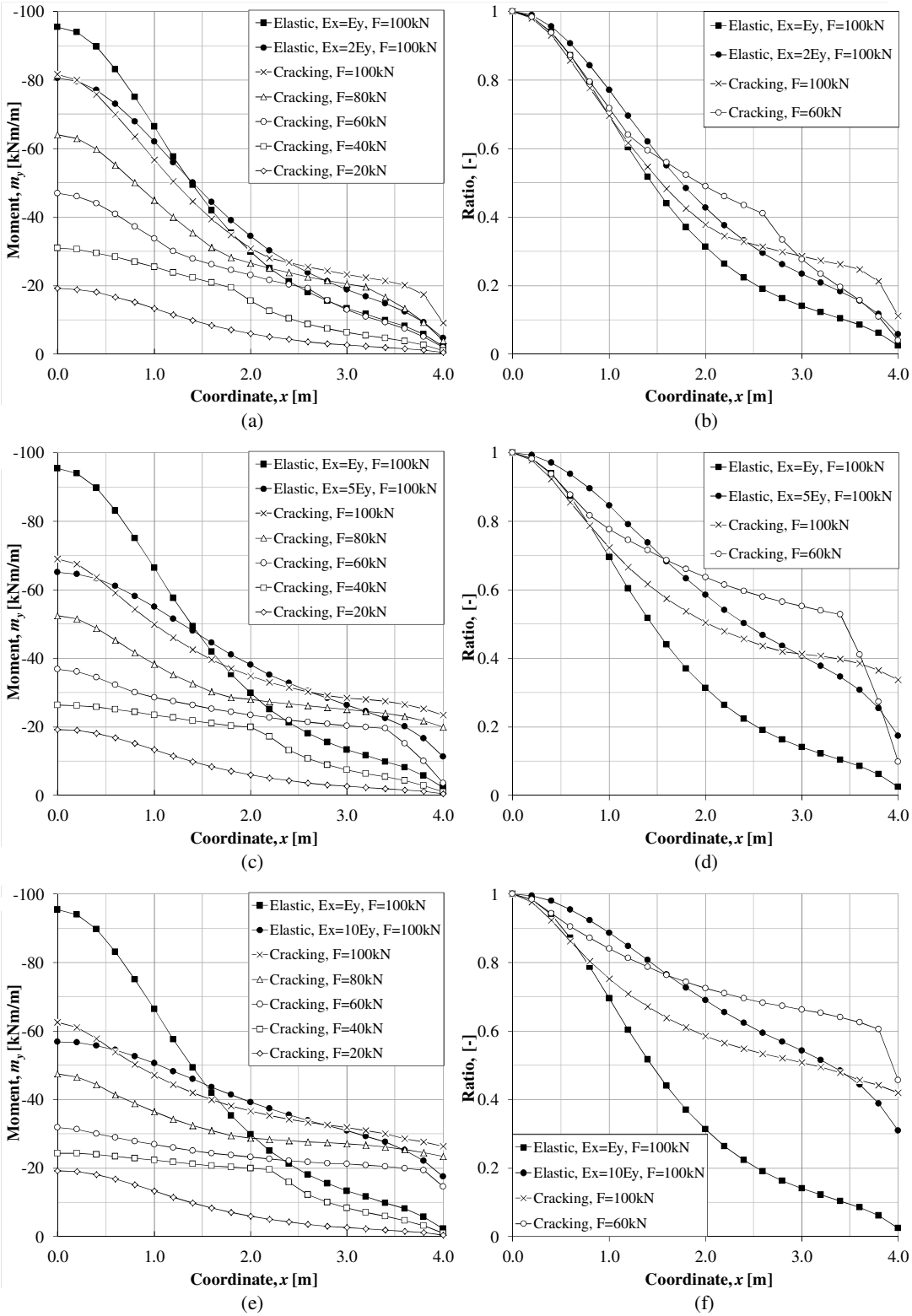

Figure 4.57. Comparisons of moment distribution for trilinear moment curvature relationship without yielding at different load level up to F = 100 kN for $E_{II} = E_I/2$, $E_{II} = E_I/5$, $E_{II} = E_I/10$.

The ratio of the maximum moment $m_{y,max}$ received from the FE analysis to moment distribution $m_{y,(x)}$ along x-direction is determined in equation (4-47).

$$\delta = \frac{m_{y,\max}}{m_{y,x}} \tag{4-47}$$

This δ corresponds to the distribution shape for the moment. Hence, $\delta_{y,m\text{-}k}$ defines a distribution shape for the moment obtained using trilinear moment curvature without yielding input while $\delta_{y,iso}$ defines a distribution shape for the moment received from the isotropic analysis.

The difference for the maximum moment received from the FE analysis with trilinear moment curvature without yielding input $m_{y,m\text{-}k,max}$ and maximum moment obtained from orthotropic FE analysis $m_{y,ortho,max}$ is calculated as:

$$\gamma = 100 \cdot \frac{\left|m_{y,m-k,\max}\right| - \left|m_{y,ortho,\max}\right|}{\left|m_{y,m-k,\max}\right|} \tag{4-48}$$

Where $m_{y,m\text{-}k,max}$ = maximum moment received from trilinear moment curvature without yielding input

$m_{y,ortho,max}$ = maximum moment obtained from orthotropic analysis

Table 4.5. Difference between trilinear moment curvature relationship without yielding input and orthotropic analysis.

Case	$m_{y,m\text{-}k,max}$ [kNm]	$m_{y,ortho,max}$ [kNm]	γ [%]
$E_{II} = E_{II}/2$	-81.6	-80.6	1.3
$E_{II} = E_{II}/5$	-69.0	-65.1	5.9
$E_{II} = E_{II}/10$	-62.5	-56.9	8.9

Figure 4.57a and Table 4.5 shows that when $F = 100$ kN, the difference γ between $m_{y,m\text{-}k}$ and $m_{y,ortho}$ for $E_{II} = E_I/2$ is $\gamma =$ 1.3 %. The distribution shape of moment from trilinear moment curvature relation without yieldin $\delta_{y,m\text{-}k}$ when $F = 100$ kN is close to that of elastic isotropic case $\delta_{y,iso}$ at about $0 < x < 1.4$ m, see Figure 4.57b. For $E_{II} = E_I/5$, Table 4.5 show that $\gamma = 5.9$ % and $\delta_{y,m\text{-}k}$ is close to $\delta_{y,iso}$ at around $0 < x < 1$ m, see Figure 4.57d. In case of $E_{II} = E_I/10$, $\gamma = 8.9$ % and $\delta_{y,m\text{-}k}$ is close to $\delta_{y,iso}$ at approximately $0 < x < 0.8$ m as illustrated in Figure 4.57f.

From the difference in percentage γ, it is seen that the orthotropic analysis provides a maximum moment which is close to the maximum moment obtained from the analysis of the studied cantilever slab with trilinear moment curvature without yielding input. Hence, it is concluded that an orthotropic analysis is a possible method to predict a design moment for the three cases mentioned in this Section. It is observed that the stiffer the studied slab is, the better the orthotropic FE analysis predicts the design moment.

Concerning the distribution shape for the moment, the distribution shape for moment from isotropic analysis can be used to predict the distribution shape for moment from

the trilinear moment curvature without yielding input. Consequently, $\delta_{y,iso}$ approaches $\delta_{y,m\text{-}k}$ when the studied cantilever become stiffer and stiffer as shown in Figure 4.57b, Figure 4.57d, Figure 4.57f.

5 Concluding remarks

5.1 Conclusions

This thesis studied the distribution of forces in a cantilever slab subjected to a single point load. A beam grillage model was analysed with different material models to capture the structural response of the cantilever slab.

In this Master Thesis project, a shell element model was used to validate the beam grillage element model for the cantilever slab studied in isotropic and orthotropic case. The result from the FE analysis shows that shell element is the most appropriate element when analysing the cantilever slab studied in elastic isotropic and orthotropic case. However, results received from the FE analysis also indicates that there is a good agreement between shell element and beam grillage element if appropriate mesh sizes for the beam elements are provided. Therefore, beam grillage models should be used with care, but can still be used to analyse the cantilever slab studied if correct mesh sizes are used.

Orthotropic analysis was used to simulate different stiffnesses of the slab in different directions. According to the comparisons made with nonlinear analysis it can be seen that an orthotropic analysis gives a good estimation of the maximum moment obtained before the effect of yielding takes place. Care has to be taken, though, of what different stiffnesses of the reinforced concrete structure that should be taken into account. Hence, such an orthotropic model taking this into account could successfully be used in service limit state (SLS) and is also as a conservative estimation in ultimate limit state (ULS).

In elasto-plastic analysis, the cantilever slab studied was examined using a beam grillage model with non-linear moment-curvature relationship. In this case, the element size affects the plastic moment capacity of the structure when using beam elements. The finer the mesh is, the closer the results obtained from the FE analysis converges to the expected solution. Based on the analysis of the cantilever slab studied in elasto-plastic case, the need for plastic rotation is small and hence the possibility of redistribution due to yielding is considerable. The FE analyses of the cantilever slab studied shows that in term of distribution width for moment, the recommendation given by Pacoste *et al.* (2012) is conservative. The effect of plastic redistribution, though, should be handled with care if there are moving load that might cause accumulated damage to the structure, which might lead to additional plastic rotation.

5.2 Further studies

Some simplifications related to the modelling of the slab studied have been made. In this report, in terms of distribution width for moment it is seen that the recommendation given by Pacoste *et al*. (2012) is conservative for the particular load case studied. In order to examine the recommendation for other cases, different combinations of loads and load positions are of interest. For the cantilever slab studied, it is proposed to also study the response for 2-4 point loads located in different positions of the slab. The study of the cantilever slab subjected to moving load is also worth being performed in order to study in what way such loading might affect the total need of plastic rotation.

Orthotropic analysis, used in this report to simulate different stiffness in two directions after cracking, can be developed by considering the actual ratio between the uncracked and cracked stiffnesses of a real reinforced concrete slab. The elasto-plastic moment-curvature model used to simulate the effect of cracking and yielding in this thesis gives an approximation of the structural response of the reinforced concrete cantilever slab. This type of modelling can be improved by giving actual input values for the elasto-plastic moment-curvature model determined from real reinforced concrete slabs.

This Master Thesis describes only the load distribution in a cantilever slab subjected to a single load. However the knowledge of load distribution for other types of slabs also needs to be expanded and developed. Therefore, analyses of one-way and two-way simply supported slabs, carried out with the same type of studies as in this thesis, is of interest. Moreover, the studies of load distribution of a more complicated slab, for example a slab in two spans supported by both line supports and columns would be of interest. When a load distribution in the longitudinal direction due to changed stiffness or yielding takes place, this will also affect the load distribution in the transverse direction, and therefore such an effect would be valuable to study.

Detail modelling of a slab with separate materials for concrete and reinforcement can be done in order to investigate the real structural response of the reinforced cantilever slab studied. With the modelling choice for the cantilever slab made in this report, it was seen that the slab always collapse due to the yielding in the elements along the fixed boundary and there is no sign of a more complex yield line failure. Therefore, a model with an increased length of the slab should be added to check that the more complex yield line failure can take place with this modelling technique.

6 References

ADINA, 2011. *Adina User Interface Command Reference Manual*. Vol 1: ADINA Solids & Structures Report ARD 11-2, ADINA R & D, Inc., Watertown, MA. USA.

ADINA, 2011. *Adina Primer*. Report ARD 11-7, ADINA R & D, Inc., Watertown, MA. USA.

ADINA, 2011. *Theory and Modelling Guide*. Vol 1: ADINA Solids & Structures Report ARD 11-8, ADINA R & D, Inc., Watertown, MA. USA.

Andersson S. och Karlsson H., 2012. *Structural response of reinforced concrete beams subjected to explosions*. Division of Structural Engineering, Concrete Structures, Chalmers University of Technology, Master Thesis 2012:103, Göteborg, Sweden.

Augustsson R. och Härenstam M., 2010. *Design of reinforced concrete slab with regard to explosions*. Division of Structural Engineering, Concrete Structures, Chalmers University of Technology, Master Thesis 2010:38, Göteborg, Sweden.

Bathe K.-J. (1996), Finite Element Procedures, Prentice Hall, Englewood Cliffs, New Jersey, 1996.

CEN, 2004. Eurocode 2: Design of concrete Structures – Part 1-1: General rules and rules for buildings. European Comittee for Standardization, Brussels, Belgium.

Engström B., 2011a. *Design and analysis of continuous beams and columns*, Report 2007:3, Edition 2011. Division of Structural Engineering, Concrete Structures, Chalmers University of Technology, Göteborg, Sweden.

Engström B., 2011b. *Design and analysis of slabs and flat slabs*. Division of Structural Engineering, Concrete Structures, Chalmers University of Technology, Göteborg, Sweden.

Ekström J., 2009. *Structural modelling with different finite element types*. Division of Structural Engineering, Concrete Structures, Chalmers University of Technology, Master Thesis 2012:103, Göteborg, Sweden.

G.A. Rombach (2004), Finite Element Design of Concrete Structures, Thomas Telford, 2004.

Mosley B., Bungey J., Hulse R. (2007), Reinforced concrete design to eurocode 2, Palgrave Macmillan, New York, N.Y. 10010, 2007.

Pacoste C., Plos M., Johansson M., (2012). *Recommendations for finite element analysis for the design of reinforced concrete slabs.* Royal Institute of Technology, Stockholm, Sweden.

Plos M., 2000. *Finite element analyses of reinforced concrete structures*, Compendium 96:14. Division of Structural Engineering, Concrete Structures, Chalmers University of Technology, Göteborg, Sweden.

Sustainable Bridges (2007) – Assessment for Future Traffic Demands and Longer Lives, Background Document D4.5, Non-Linear Analysis and Remaining fatigue Life of Reinforced Concrete Bridges.

APPENDIX A FE analysis-ADINA

A.1 Beam elements

In ADINA FE program, the beam element is a 2-node Hermitian beam with a constant cross-section. The element is initially straight and can be modelled by a 2D beam element or a 3D beam element. The material behaviour of the beam element used in ADINA can be described using either a cross-section shape and a material model, or a moment-curvature model.

A.1.1 Beam geometry

Figure A.1 shows the beam element along with its local coordinate system (*r,s,t*) and its global coordinate system (*X,Y,Z*). The *r*-direction always lies along the neutral line of the beam. The orientation of the *s* and *t* directions is defined using auxiliary point *K* as shown in Figure A.1. For the orientation of the *s* and *t* directions using orientation vector, reader can refer to *ADINA* (2011).

The beam element has 6 degrees of freedoms at each node including 3 translations and 3 rotations as illustrated in Figure A.1. These 3 translations and 3 rotations are denoted as:

u = local translation in *r*-direction
v = local translation in *s*-direction
w = local translation in *t*-direction
θ_r = local rotation around *r*-direction
θ_s = local rotation around *s*-direction
θ_t = local rotation around *t*-direction
K = auxiliary point used to define *s* and *t* directions

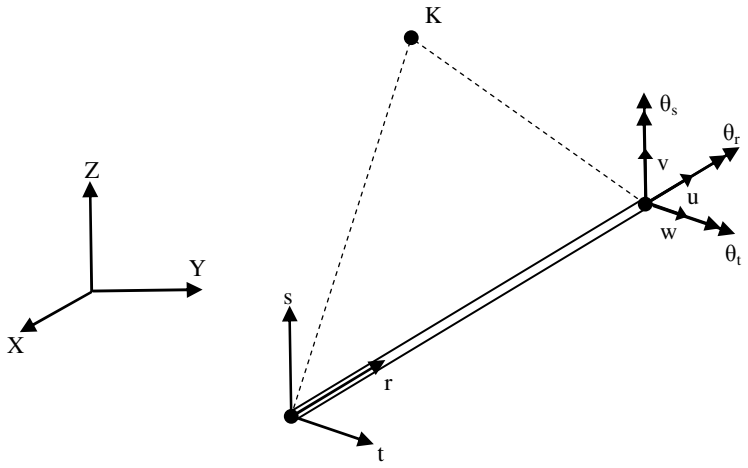

Figure A.1. Geometry definition using auxiliary node K including global and local coordinate system for beam element. From ADINA (2011).

A.1.2 Elastic-plastic beam element

The elastic-plastic beam elements can be modelled by a 2D beam or a 3D beam element. For 2D beam action, it assumes that the element deformations take place in the *r-s* plane (local axis of the element) as shown in Figure A.1. In this case, the

element has no stiffness corresponding to the deformation out of the *r-s* plane and therefore the element does not have any torsional stiffness. 2D beam elements need to be defined parallel to one of the *X-Y, Y-Z* plane, or *X-Z* global coordinate plane. Unlike 2D action, 3D action assumes that element deforms in any direction and 3D beam elements can be defined in any *X-Y-Z* global coordinate plane.

The elastic plastic beam element can be described using either a cross-section shape and a bilinear plastic material model, or an elastic-plastic moment-curvature model.

A.1.3 Bilinear plastic material model

For elasto-plastic material model, only bilinear plastic relation is available. In bilinear plastic material model, the ascending branch corresponds to the elastic part while the second part of the curve represents plastic response as shown in Figure A.2.

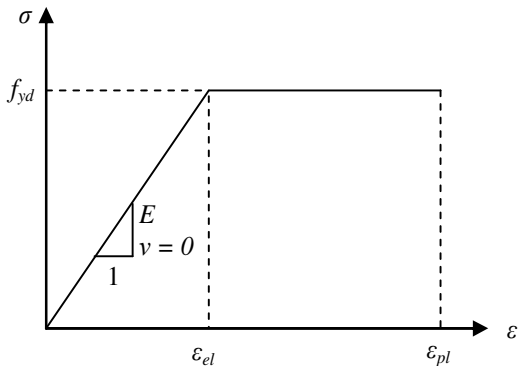

Figure A.2. Bilinear plastic material model used in ADINA.

With bilinear plastic material response shown in Figure A.2, ADINA does not recognize that the section is cracked as it assumes that the first part of the curve represent linear elastic response. Hence, it is difficult to choose a correct Young's modulus. For the analysis in state II, it is reasonable to model section as a fully cracked section without taking into account the tension stiffening effect. In order to perform state II analysis and model a fully cracked section it is necessary to find an equivalent Young's modulus. For how to determine the equivalent Young's modulus, the reader can refer to Chapter 3.

A.1.4 Elastic-plastic moment curvature model

The elastic-plastic moment curvature model in ADINA consists of uniaxial plasticity laws respectively applied to axial strain, each bending curvature and the twist angle per unit width.

The bending moment curvature relationship can either be symmetric or non-symmetric with respect to the sign of curvature and it depends on the axial force. The bending moment curvature relationship can be different between axial force in tension and axial force in compression. For the symmetry case as shown in Figure A.3, it is sufficient to enter only the positive value of the bending moment and corresponding curvature. In Figure A.3, the first data point always corresponds to yielding and the last data point always corresponds to rupture. In order to obtain a bilinear moment

curvature plasticity, it is only enter a multilinear plastic moment curvature with just two branches. For more details related to axial force and axial strain relationship, torsional moment and twist angle per unit length relationship, reader can refer to ADINA (2011).

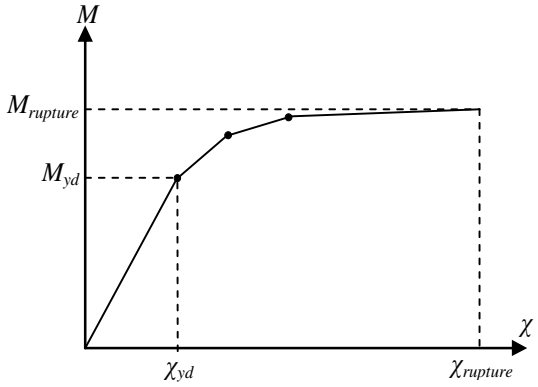

Figure A.3. Symmetric elasto-plastic moment-curvature beam input. From ADINA (2011).

A.2 Shell elements

In ADINA FE program, the shell element follows two assumptions used in the Timoshenko beam theory and the Reissner-Mindlin plate theory.

- First assumption: Material particles originally lying on a straight line normal to the midsurface remain on that straight during deformation.
- Second assumption: The stress perpendicular to the midsurface of the structure is zero.

For the analysis of the shell, these assumptions correspond to a very general shell element theory. 4-nodes shell element as shown in Figure A.4 is usually the most effective element to use when analysing the general shell element. Reader can refer to Bathe, K.J (1996) for more information about shell elements.

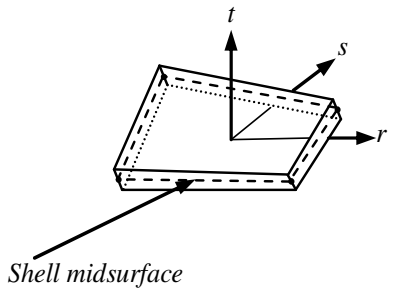

Figure A.4. 4-nodes shell element for thick and thin shells. Based on ADINA (2011).

In Figure A.4, coordinate system (*r,s,t*) and coordinate system (*X,Y,Z*) is local and global coordinate of the shell element defined in ADINA respectively.

ADINA (2011) recommends 4-nodes shell elements for the analysis of general shells. For more information about different types of shell elements, assumptions made, material models and formulations, and numerical integration, reader can refer to ADINA (2011).

APPENDIX B Modified alpha factor for the fictitious yield stress when using seven integration points

For elastic plastic beam elements used in ADINA finite element program, Newton-Cotes integration method is used in all coordinate directions. Seven integration points is used in s-and t- direction (local coordinate system for beam elements) for the rectangular Section in 3-D beam elements regardless of any number of integration input defined by the user in s- and t- direction. As seven integration points are used over the height of the cross-section, ADINA program replaces the actual stress distribution shown in Figure B.1a with a stress distribution determined by polynomial of order six depicted in Figure B.1b. In order to achieve the expected stress distribution in Figure B.1a, a factor α that can be used to transform ADINA's stress distribution to the expected stress distribution needs to be computed.

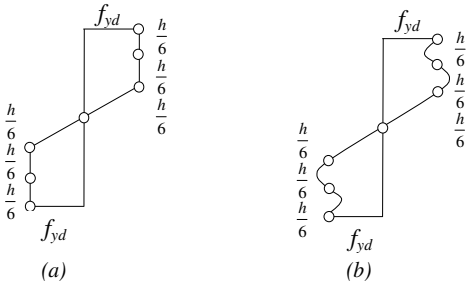

Figure B.1. Stress distribution over the cross-Section height (a) analytical expected stress distribution (b) stress distribution in ADINA.

From Figure B.1a, the ultimate moment capacity for the expected stress distribution can be determined using equation (B-3):

$$M_{rd} = \left(\left(f_y' \cdot \frac{h \cdot 2}{6} \right) \cdot 2 \cdot \frac{h}{6} + \left(f_y' \cdot \frac{h}{6} \cdot \frac{1}{2} \right) \cdot \frac{h}{6} \cdot \frac{2}{3} \right) \cdot w \cdot 2 \tag{B-1}$$

$$M_{rd} = f_y' \cdot w \cdot h^2 \cdot \left(\frac{2}{9} + \frac{1}{6} \cdot \frac{1}{6} \cdot \frac{1}{3} \cdot 2 \right) \tag{B-2}$$

$$M_{rd} = f_y' \cdot w \cdot h^2 \cdot \left(\frac{12}{54} + \frac{1}{54} \right) = \frac{13}{54} \cdot f_y' \cdot w \cdot h^2 \tag{B-3}$$

By normalizing the height of the cross-Section to 2 and yield stress to 1 of Figure B.1 as shown in Figure B.2 and choosing the polynomial of order six in excel, the stress distribution in ADINA can be determined by equation (B-4).

$$\sigma = 3.7x - 6.75x^3 + 4.05x^5 \qquad -1 < x < 1 \tag{B-4}$$

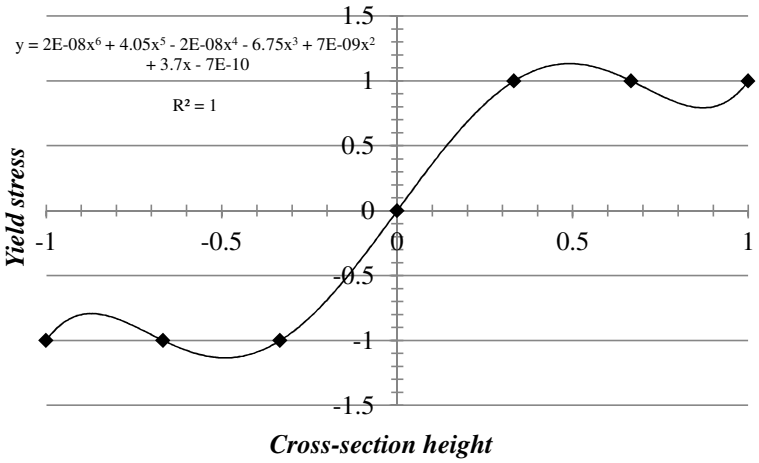

Figure B.2. Stress distribution in ADINA using polynomial of order six in excel.

The moment capacity of the stress distribution by normalizing the height to 2 and the yield stress to 1 in Figure B.2 can be computed by using equation (B-5).

$$M_{Adina} = \int_0^1 \left(\begin{matrix} 2\cdot 10^{-8}x^6 + 4.05x^5 - 2\cdot 10^{-8}x^4 - 6.75x^3 + 7\cdot 10^{-9}x^2 + 3.7x - \\ 7\cdot 10^{-10} \end{matrix} \right) x \cdot dx = 0.4619 \quad \text{(B-5)}$$

The moment capacity of the expected stress distribution by normalizing the height to 2 and the yield stress to 1 is determined by equation (B-6).

$$M_{\exp ected} = \int_0^{1/3} (3x)x \cdot dx + \int_{1/3}^{1} x \cdot dx = 0.4815 \quad \text{(B-6)}$$

The difference between ADINA's stress distribution and the expected stress distribution is:

$$\frac{0.4619}{0.4815} = 0.9593 \quad \text{(B-7)}$$

ADINA's stress distribution provides 4.07% smaller value compared to the expected stress distribution which means:

$$f_y{}' = 0.9593 \cdot f_y{}'_{\exp ected} \quad \text{(B-8)}$$

As a result, the expected moment capacity and α factor can be expressed in equation (B-9) and equation (B-10) respectively:

$$M_{rd} = \frac{13}{54} \cdot f_y{}' \cdot w \cdot h^2 = \left\{ f_y{}' = 0.9593 \cdot f_y{}'_{\exp ected} \right\} = \alpha \cdot f_y{}'_{actual} \cdot w \cdot h^2 \quad \text{(B-9)}$$

where α is

$$\alpha = \frac{13}{54} \cdot 0.9593 = 0.23094 \quad \text{(B-10)}$$

APPENDIX C Moment, shear force and deflection for cantilever slab

C.1 Isotropic case

C.1.1 Cantilever slab with shell elements

The geometry of the slab is shown in Figure 4.2.

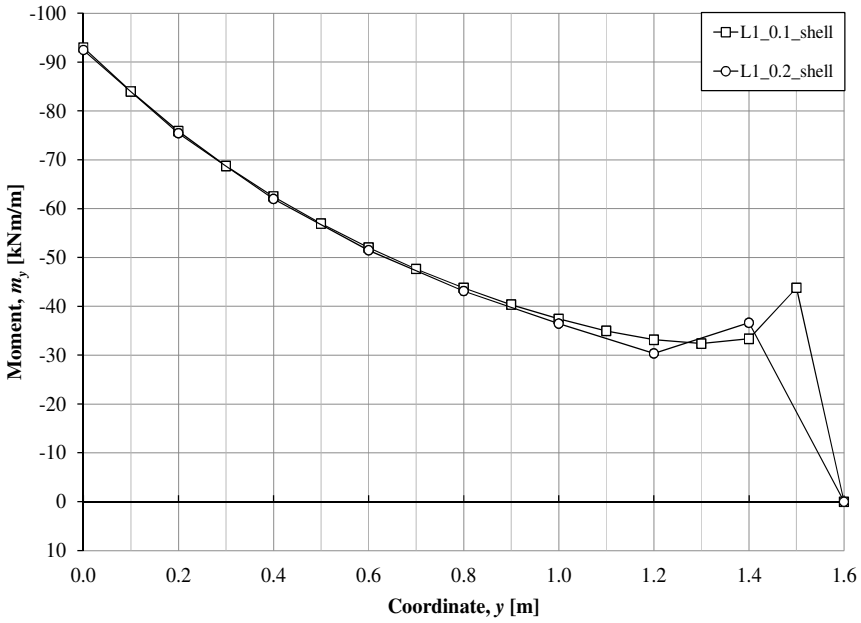

(a)

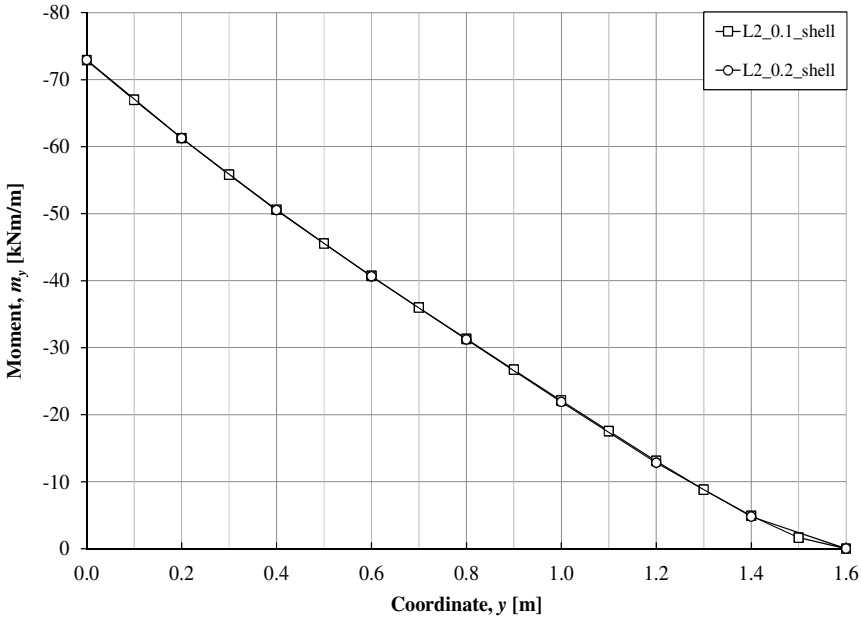

(b)

Figure C.1. Moment distribution m_y from FE-linear elastic analysis, 0.1 m shell elements and 0.2 m shell elements with Poisson's ratio ν = 0: (a) m_y along L_1 (b) m_y along L_2.

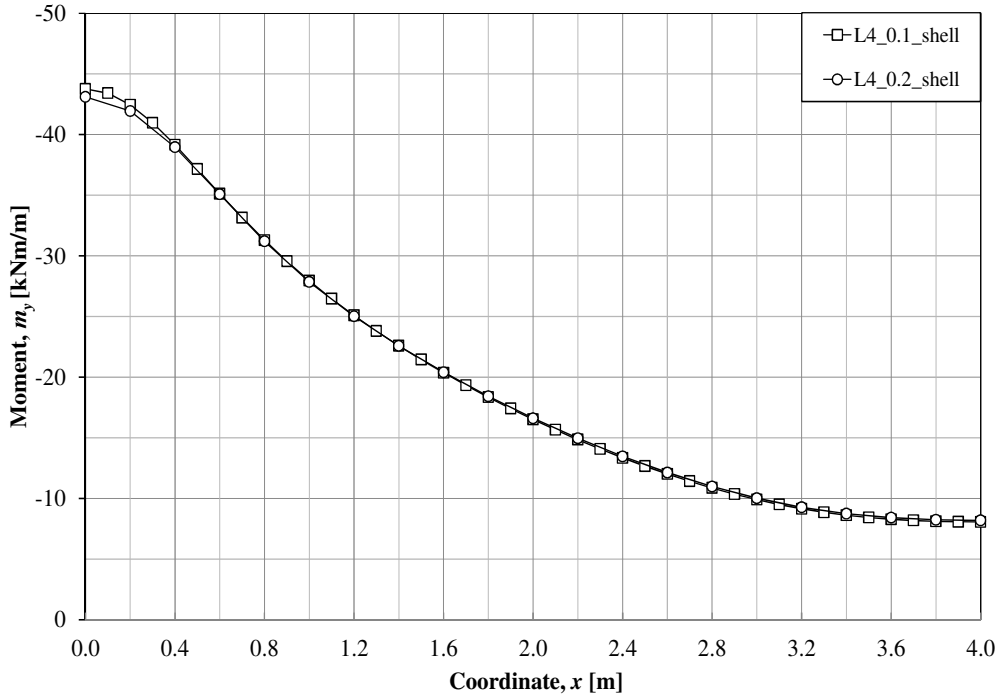

(a)

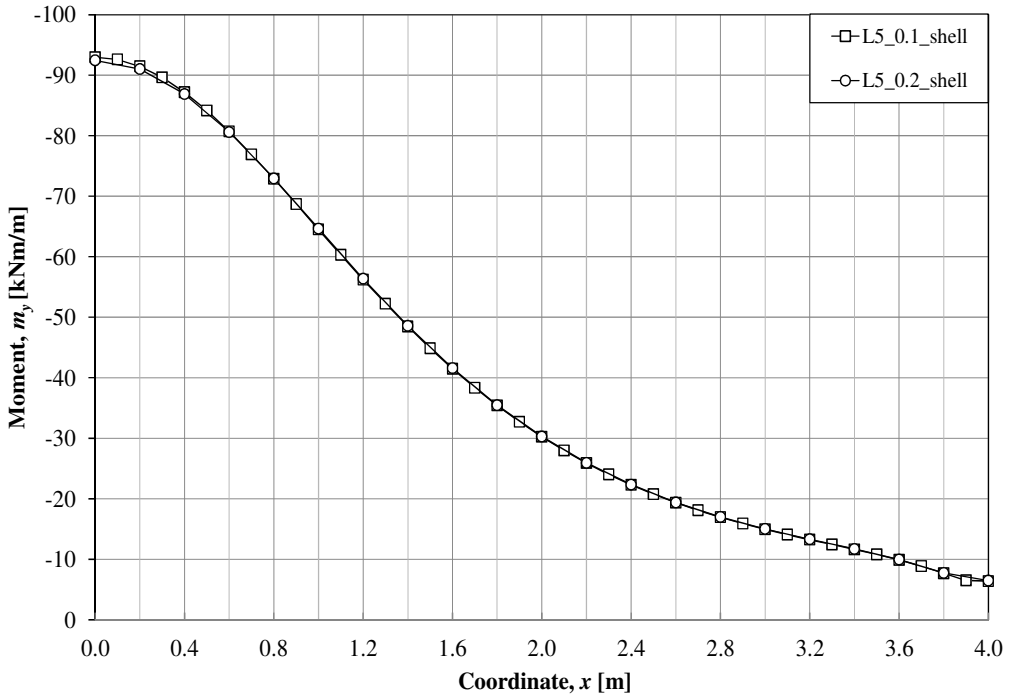

(b)

Figure C.2. Moment distribution m_y from FE-linear elastic analysis, 0.1 m shell elements and 0.2 m shell elements with Poisson's ratio ν = 0: (a) m_y along L_4 (b) m_y along L_5.

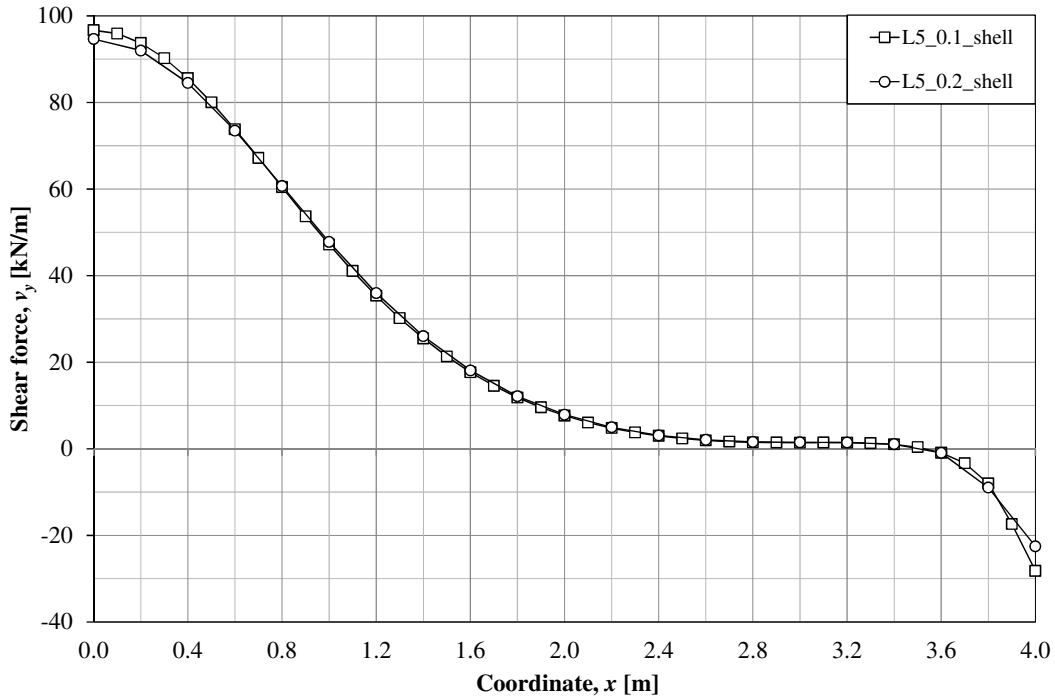

Figure C.3. Shear force distribution v_y along L_5 from FE-linear elastic analysis, 0.1 m shell elements and 0.2 m shell elements with Poisson's ratio ν = 0.

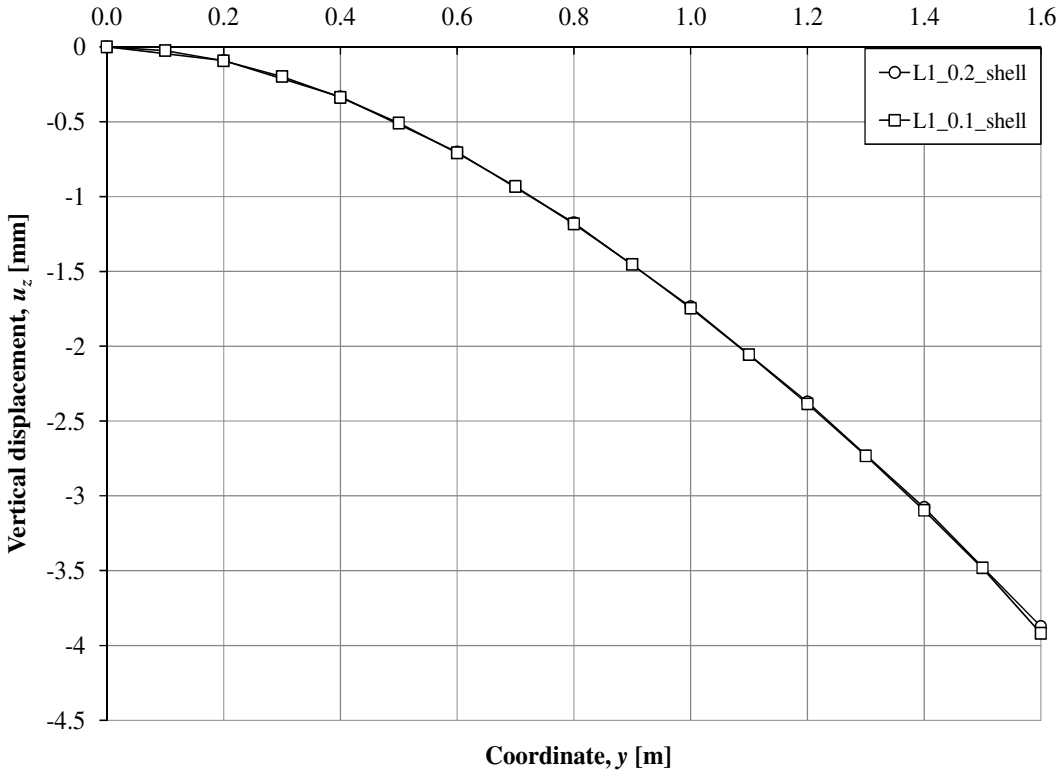

(a)

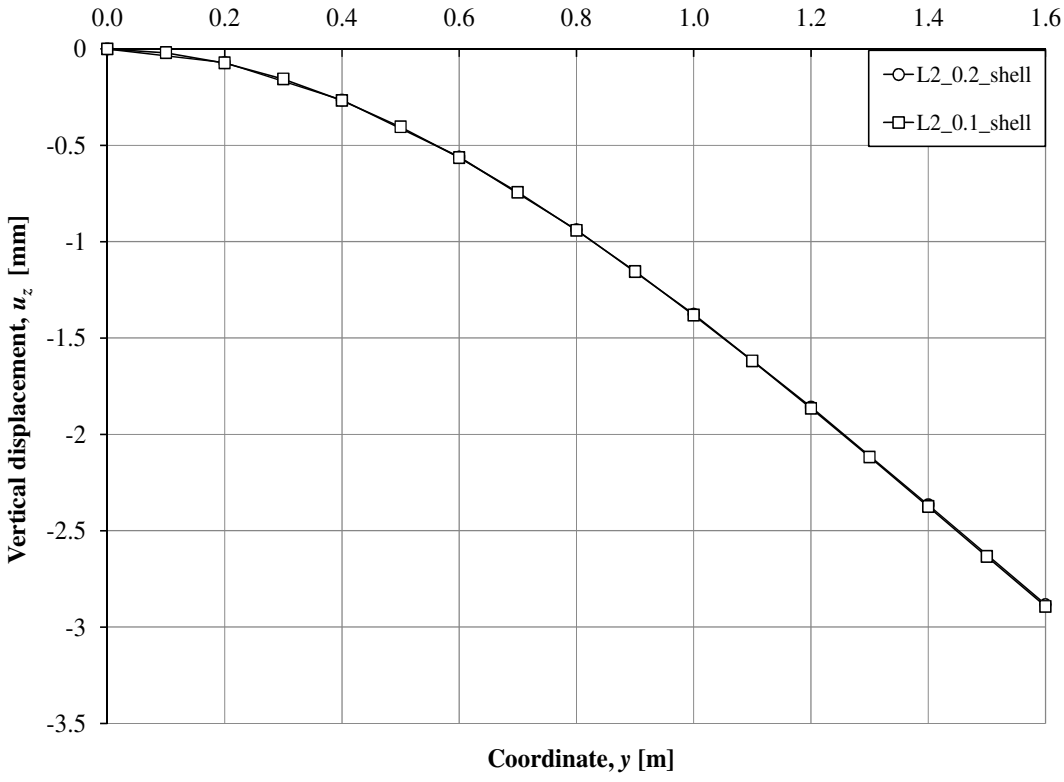

(b)

Figure C.4. Vertical displacement u_z from FE-linear elastic analysis, 0.1 m shell elements and 0.2 m shell elements with Poisson's ratio ν = 0: (a) vertical displacement-z along L_1 (b) vertical displacement-z along L_2.

C.1.2 Cantilever slab with beam elements

The geometry of the slab is shown in Figure 4.7.

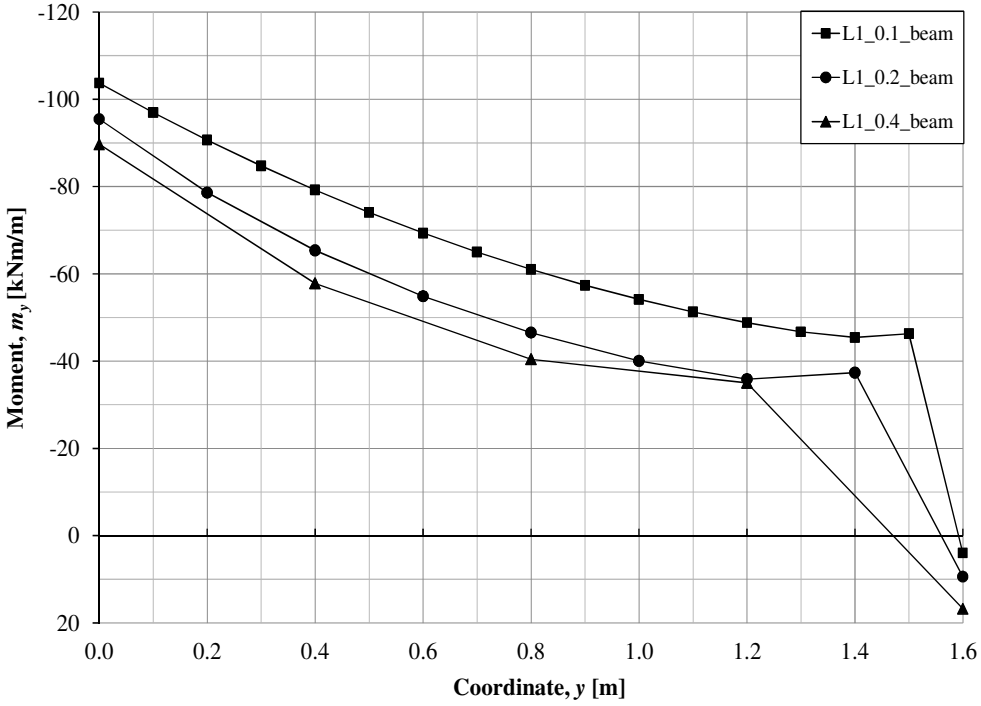

(a)

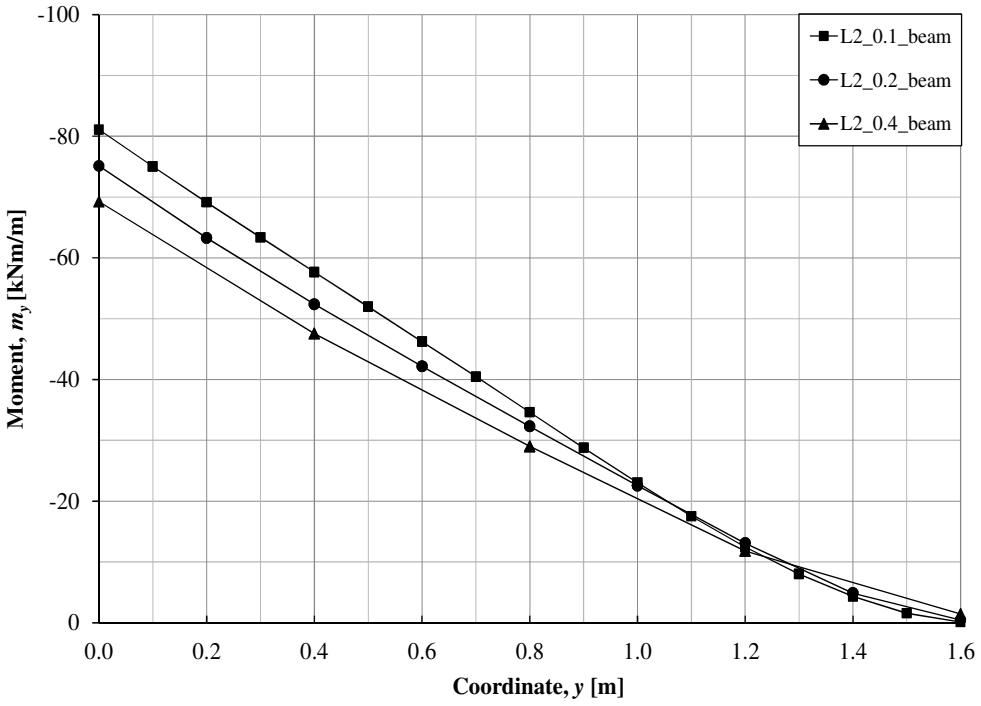

(b)

Figure C.5. Moment distribution m_y from FE-linear elastic analysis, 0.1 m beam elements, 0.2 m beam elements and 0.4 m beam elements with Poisson's ratio ν = 0: (a) m_y along L_1 (b) m_y along L_2.

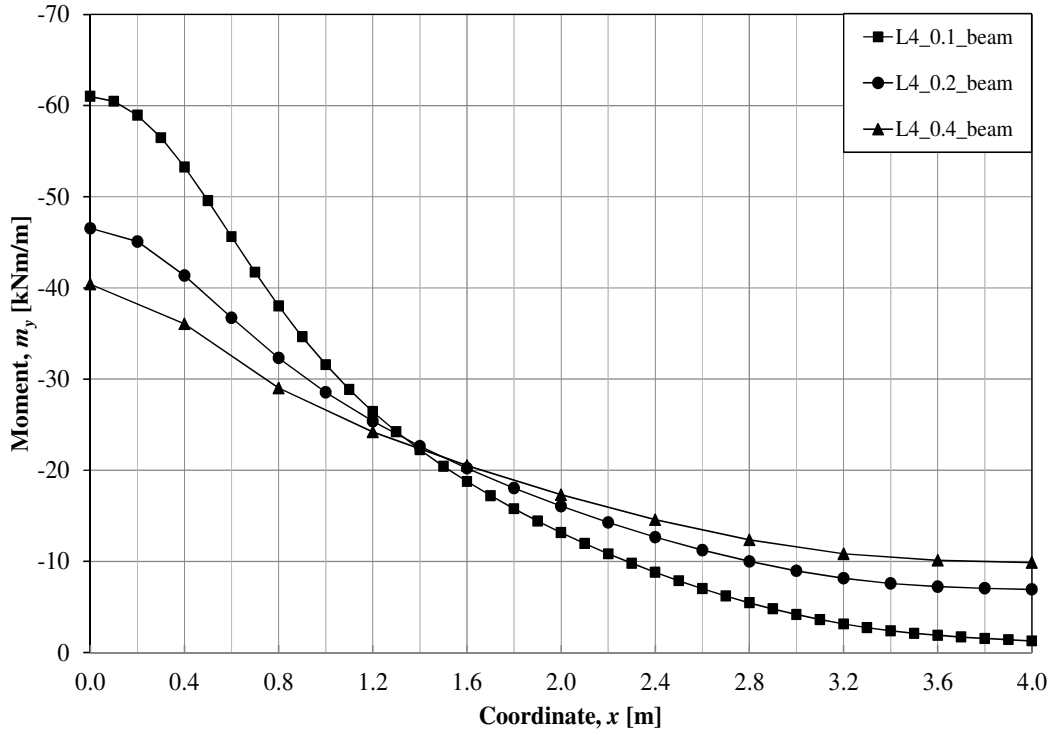

(a)

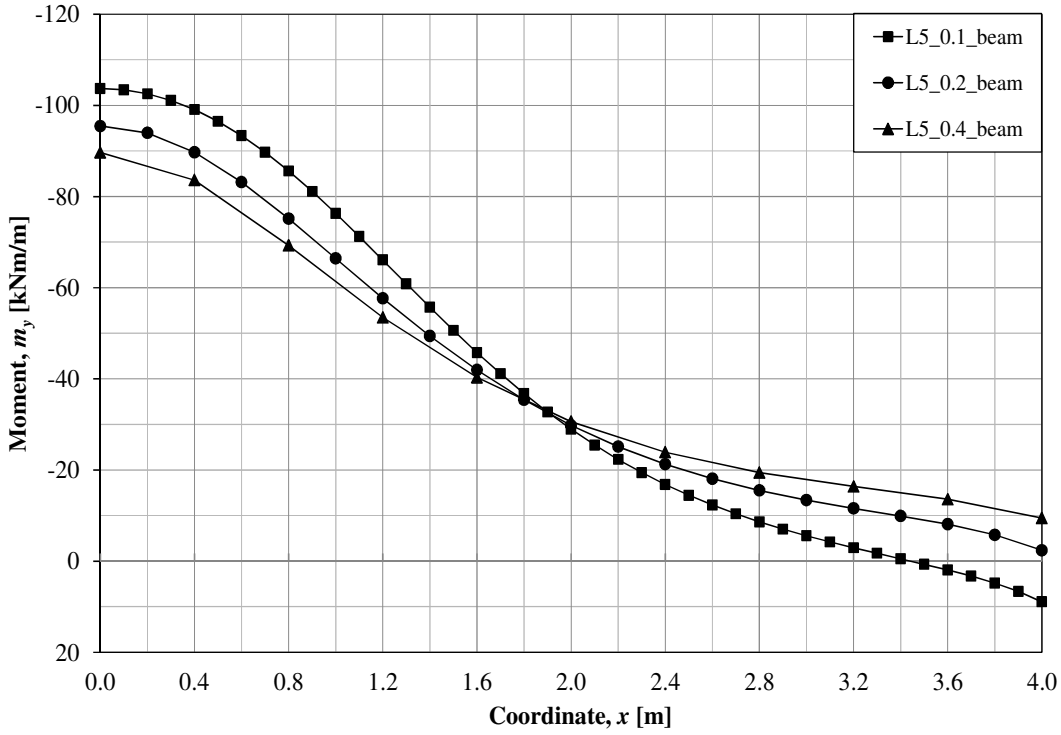

(b)

Figure C.6. Moment distribution m_y from FE-linear elastic analysis, 0.1 m beam elements, 0.2 m beam elements and 0.4 m beam elements with Poisson's ratio ν = 0: (a) m_y along L_4 (b) m_y along L_5.

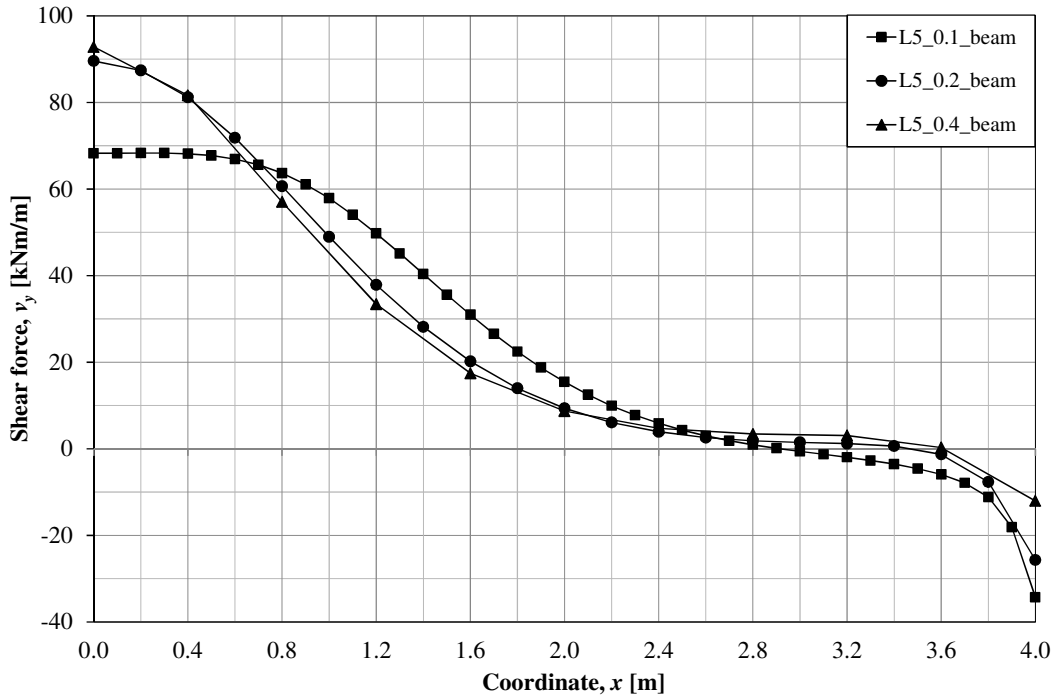

Figure C.7. Shear force distribution v_y along L_5 from FE-linear elastic analysis0.1 m beam elements, 0.2 m beam elements and 0.4 m beam elements with Poisson's ratio ν = 0.

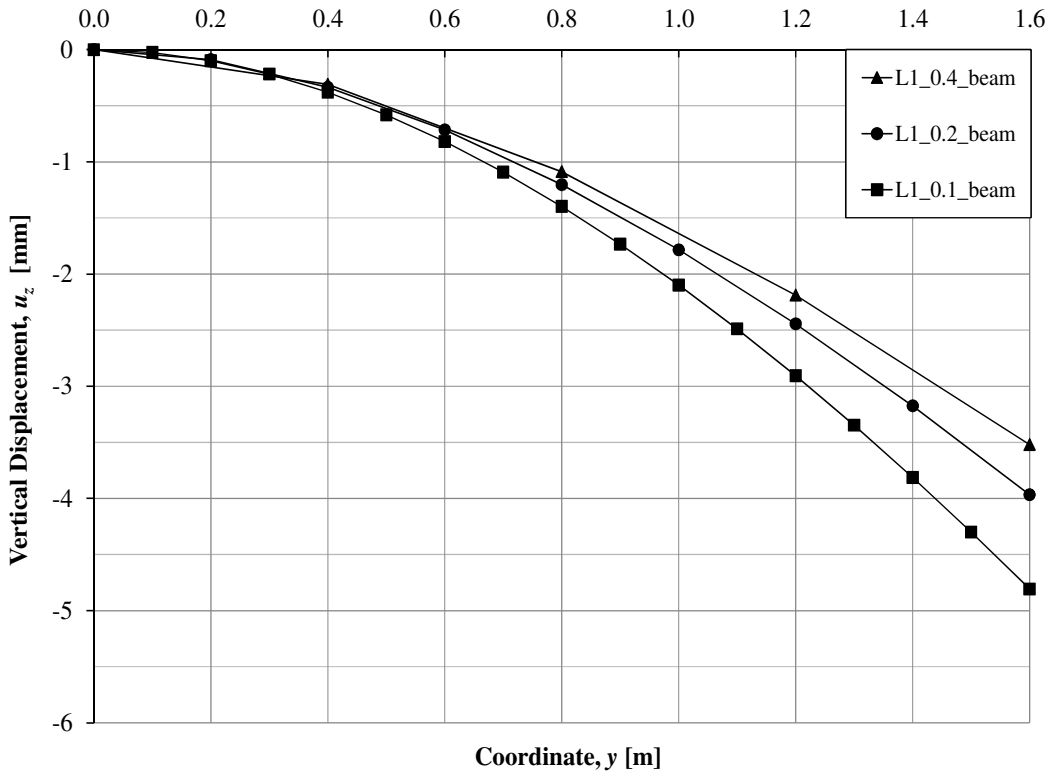

(a)

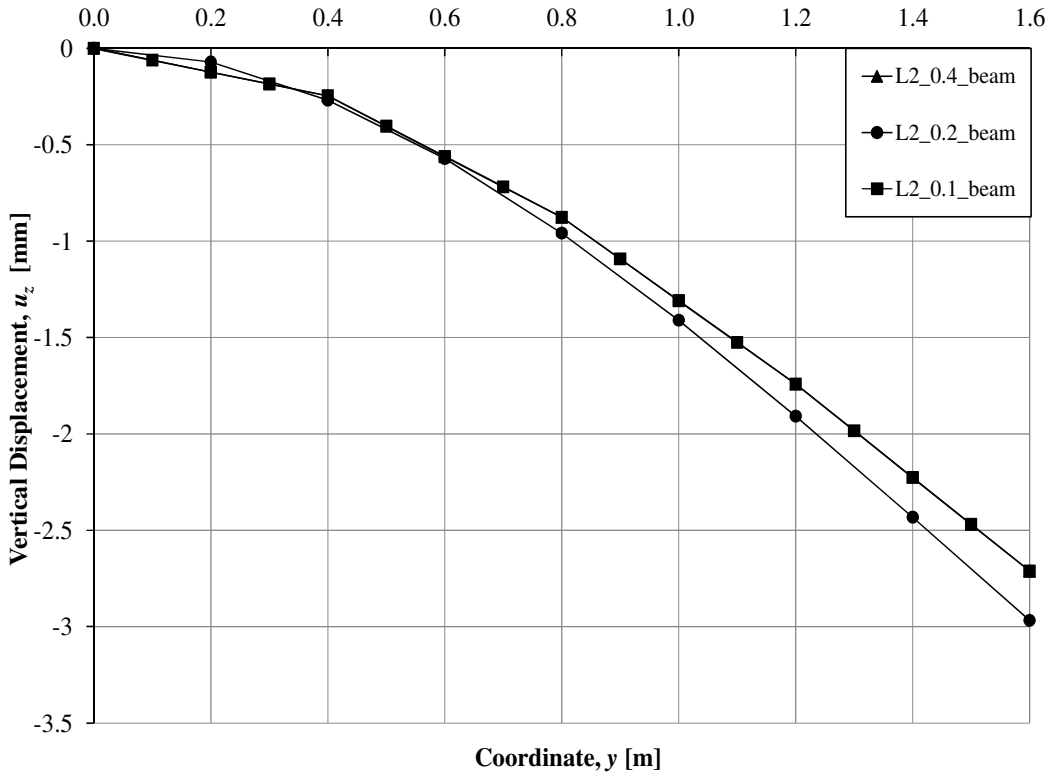

(b)

Figure C.8. Vertical displacement u_z from FE-linear elastic analysis, 0.1 m beam elements, 0.2 m beam elements and 0.4 m beam elements with Poisson's ratio ν = 0: (a) vertical displacement-z along L_1 (b) vertical displacement-z along L_2.

C.1.3 Comparisons between shell model and beam grids model

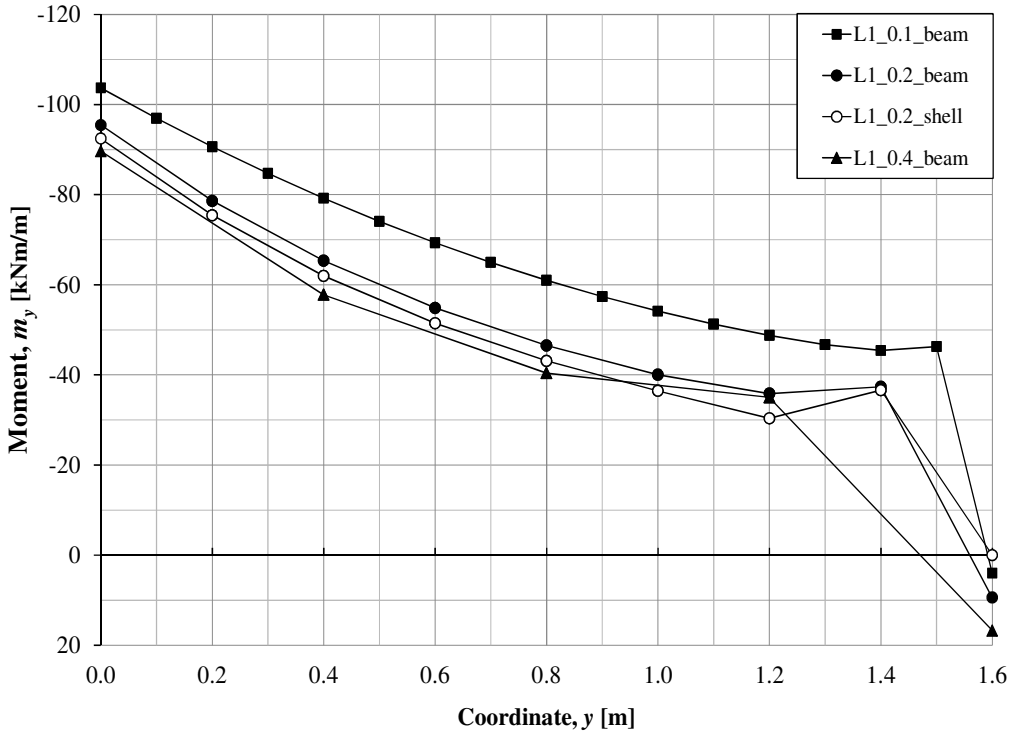

(a)

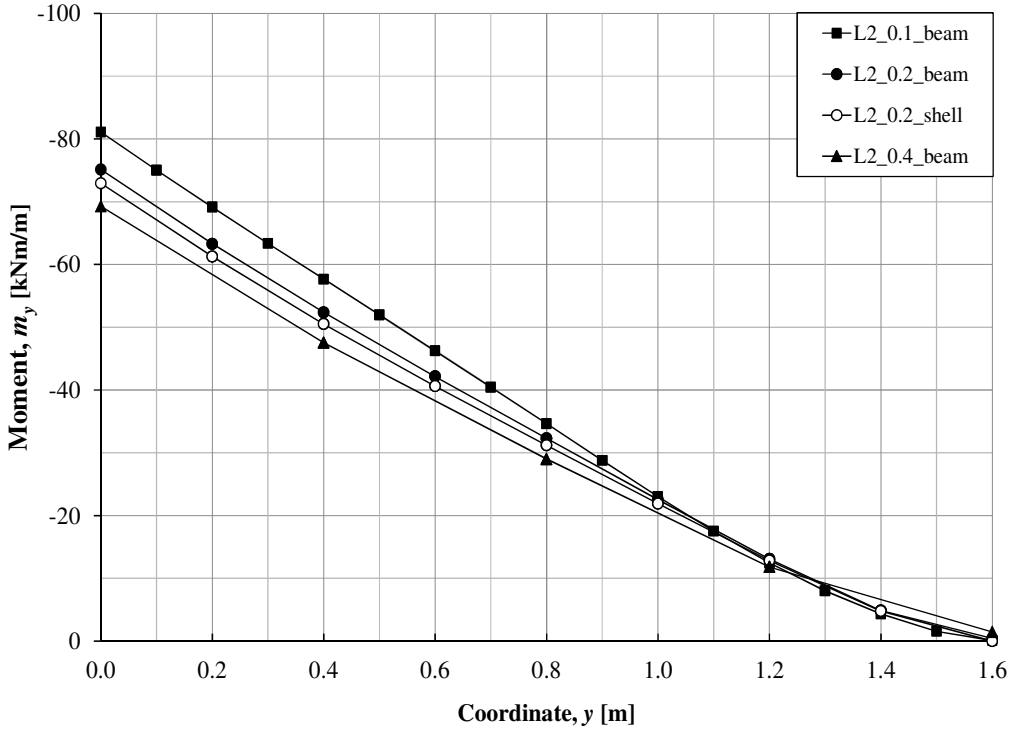

(b)

Figure C.9. Comparisons of moment distribution m_y from FE-linear elastic analysis between 0.1 m beam elements, 0.2 m beam elements, 0.4 m beam elements and 0.2 m shell elements with Poisson's ratio $\nu = 0$: (a) m_y along L_1 (b) m_y along L_2.

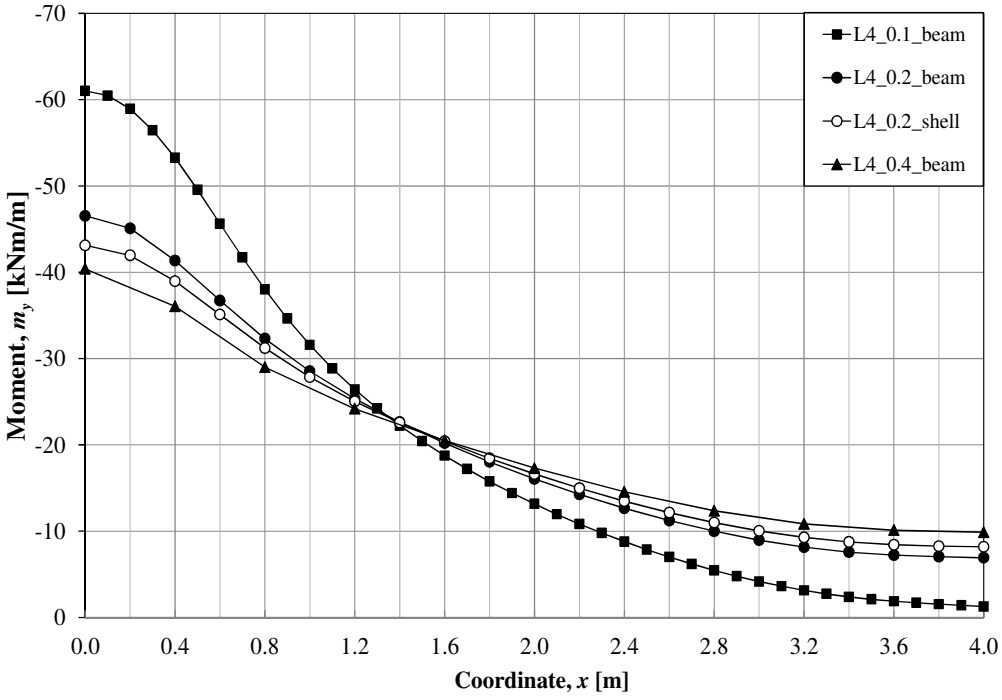

(a)

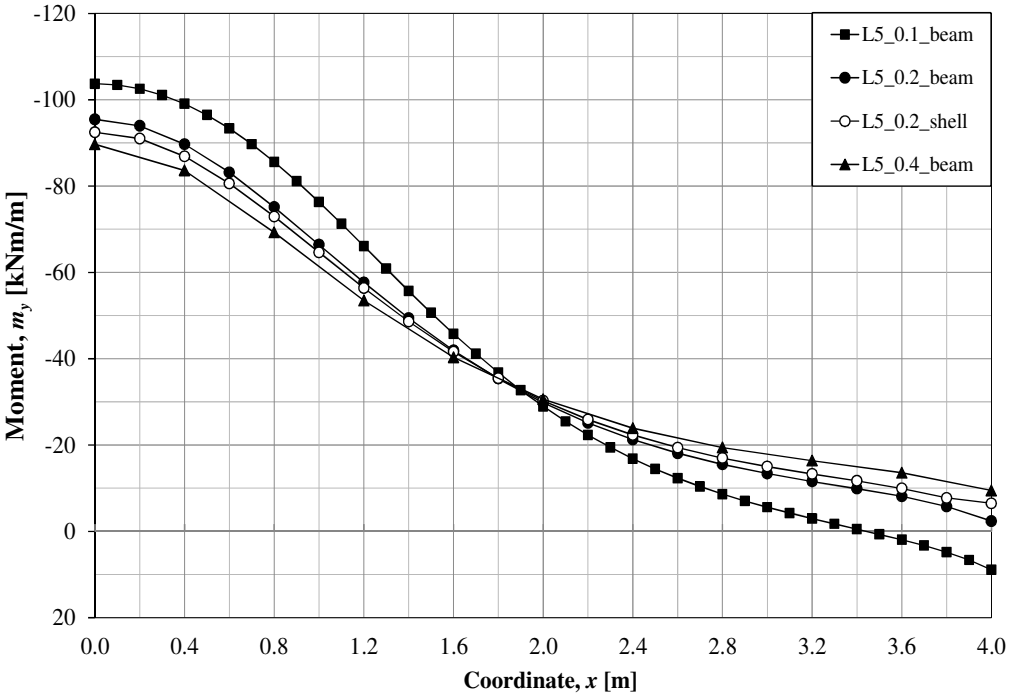

(b)

Figure C.10. Comparisons of moment distribution m_y from FE-linear elastic analysis between 0.1 m beam elements, 0.2 m beam elements, 0.4 m beam elements and 0.2 m shell elements with Poisson's ratio ν = 0: (a) m_y along L_4 (b) m_y along L_5.

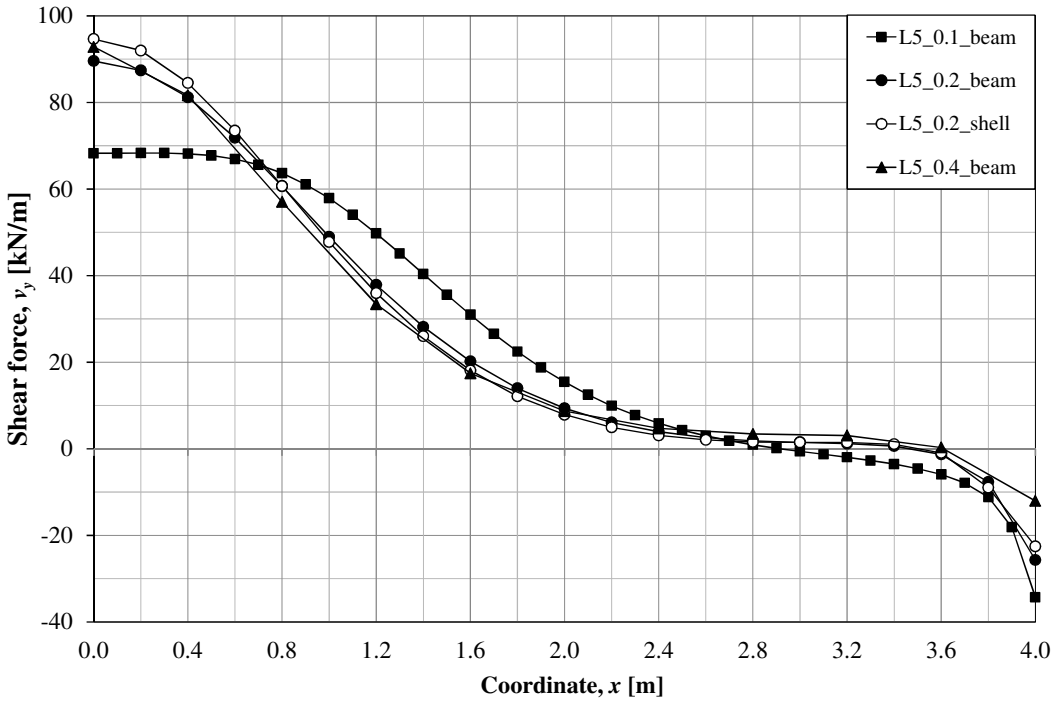

Figure C.11. Comparisons of shear force distribution v_y along L_5 from FE-linear elastic analysis between 0.1 m beam elements, 0.2 m beam elements, 0.4 m beam elements and 0.2 m shell elements with Poisson's ratio $\nu = 0$.

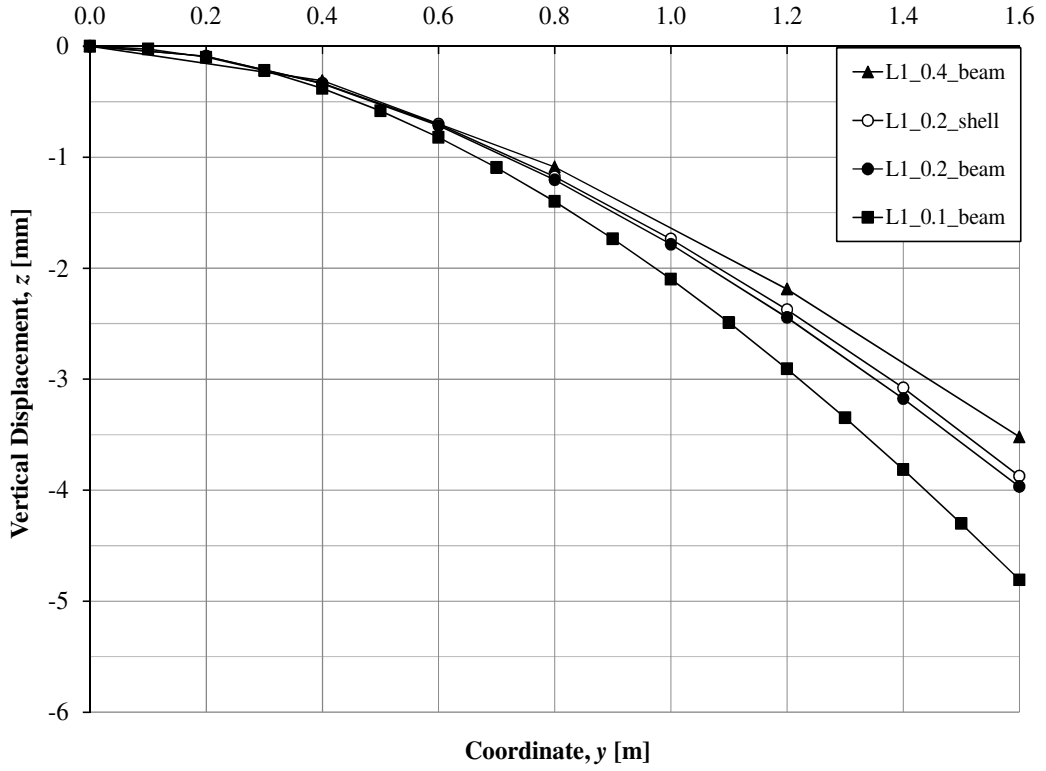

(a)

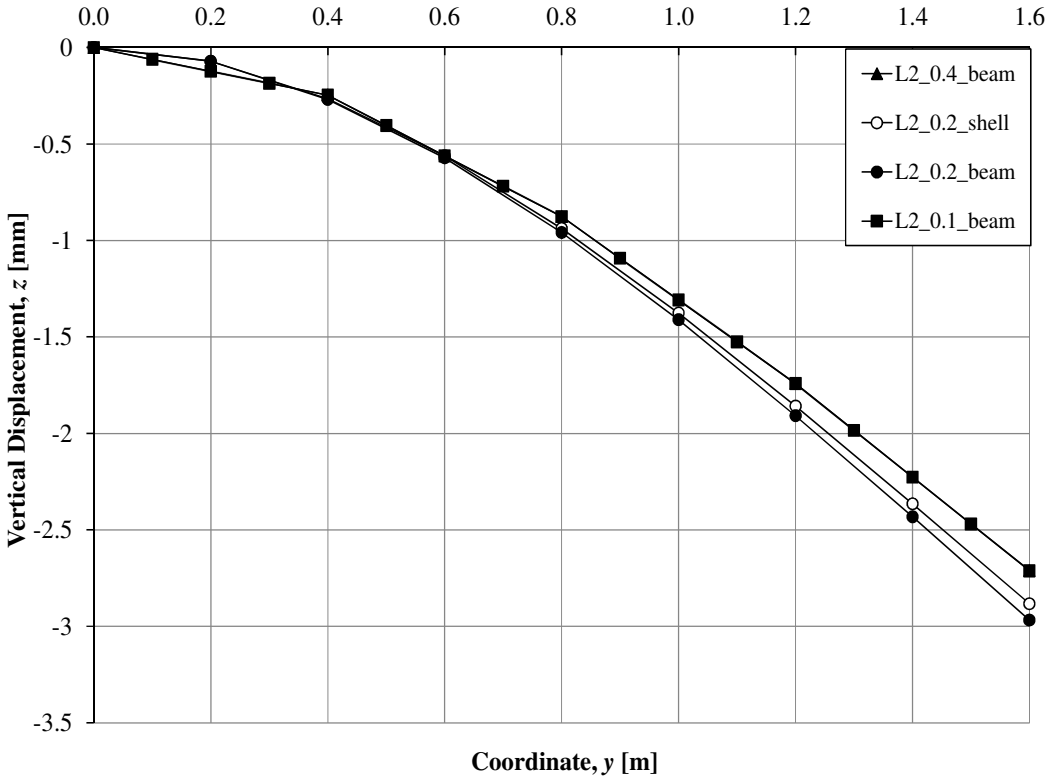

(b)

Figure C.12. Comparisons of vertical displacement u_z from FE-linear elastic analysis between 0.1 m beam elements, 0.2 m beam elements, 0.4 m beam elements and 0.2 m shell elements with Poisson's ratio ν = 0: (a) vertical displacement-z along L_1 (b) vertical displacement-z along L_2.

C.2 Orthotropic case

C.2.1 Cantilever slab with shell elements

The geometry of the slab is shown in Figure 4.2 with *Ex* = 0.1, 0.2, 0 5,1, 2, 5, 10*Ey*.

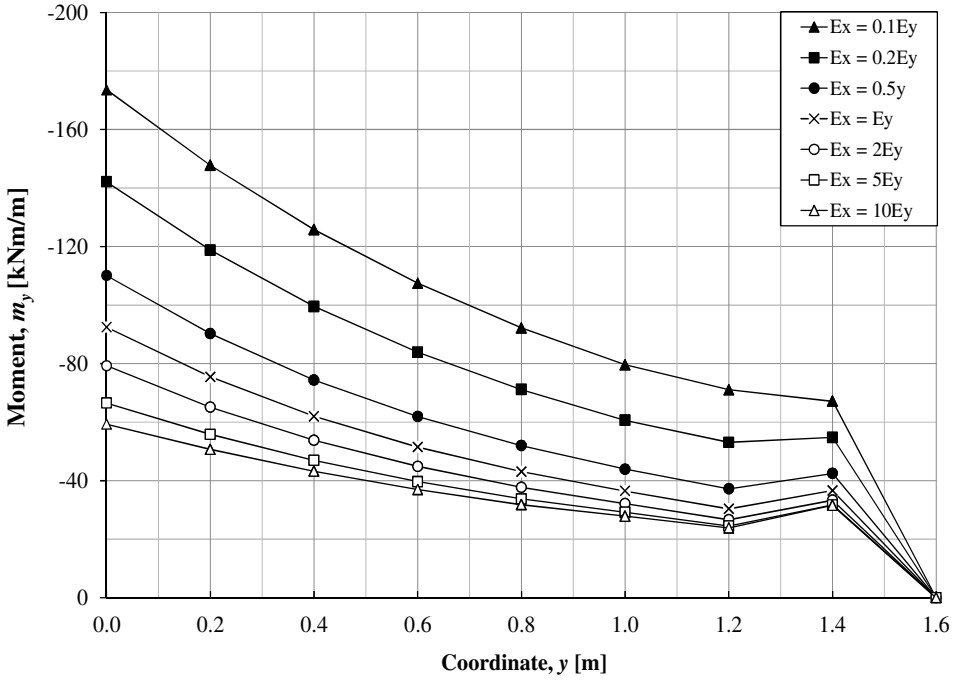

(a)

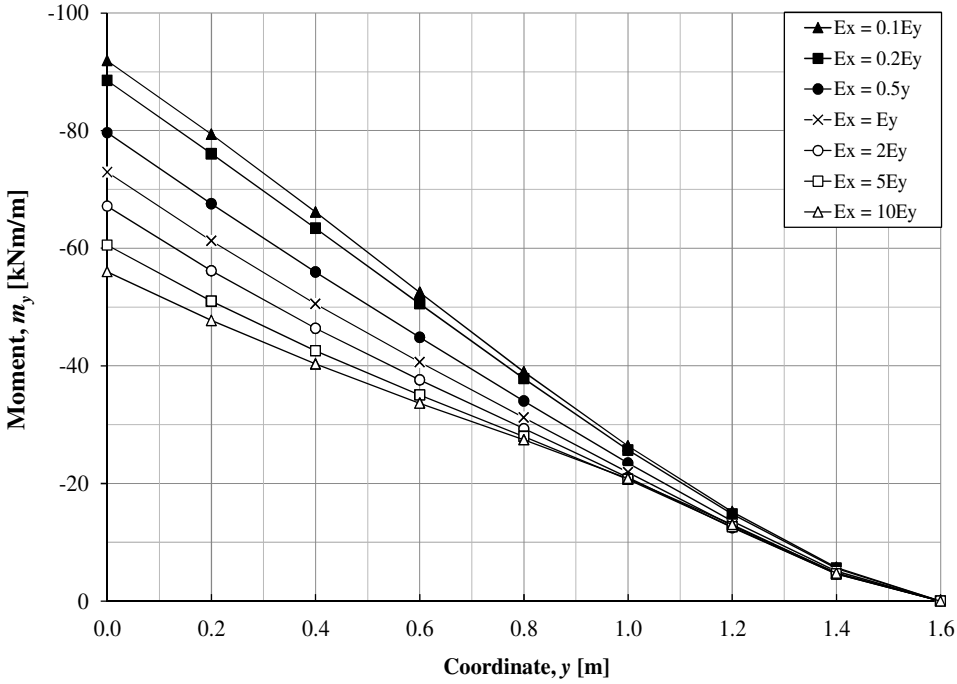

(b)

Figure C.13. Moment distribution m_y from FE-linear elastic orthotropic analysis using 0.2 m shell elements with Poisson's ratio ν = 0: (a) m_y along L_1 (b) m_y along L_2.

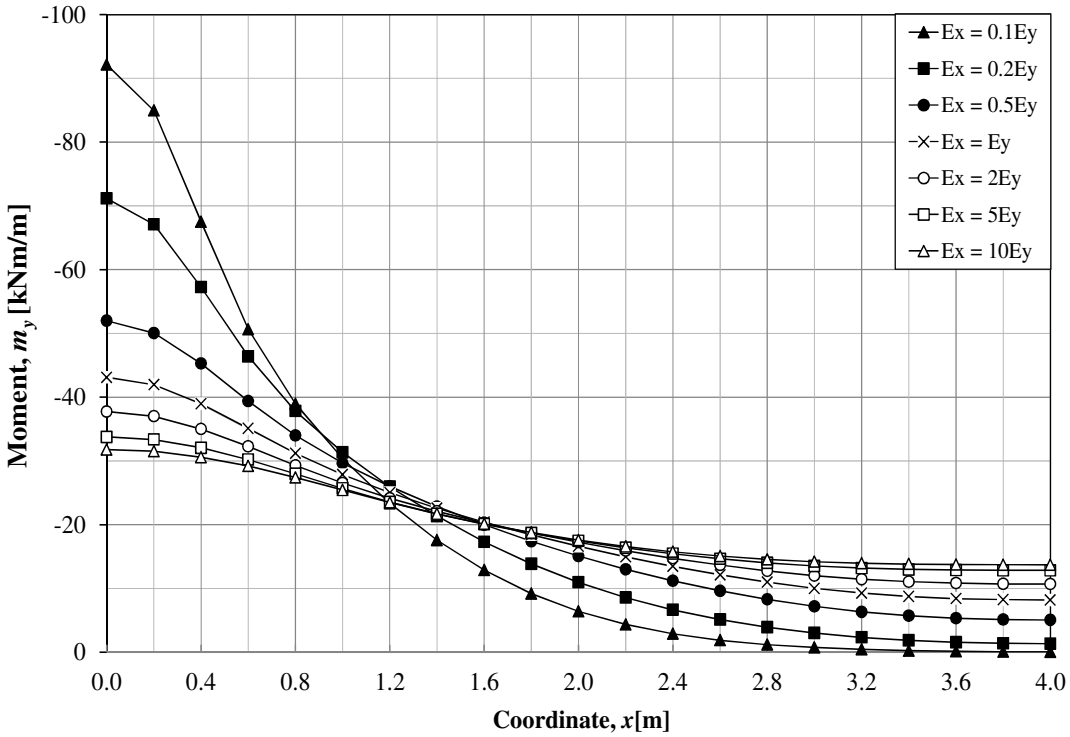

(a)

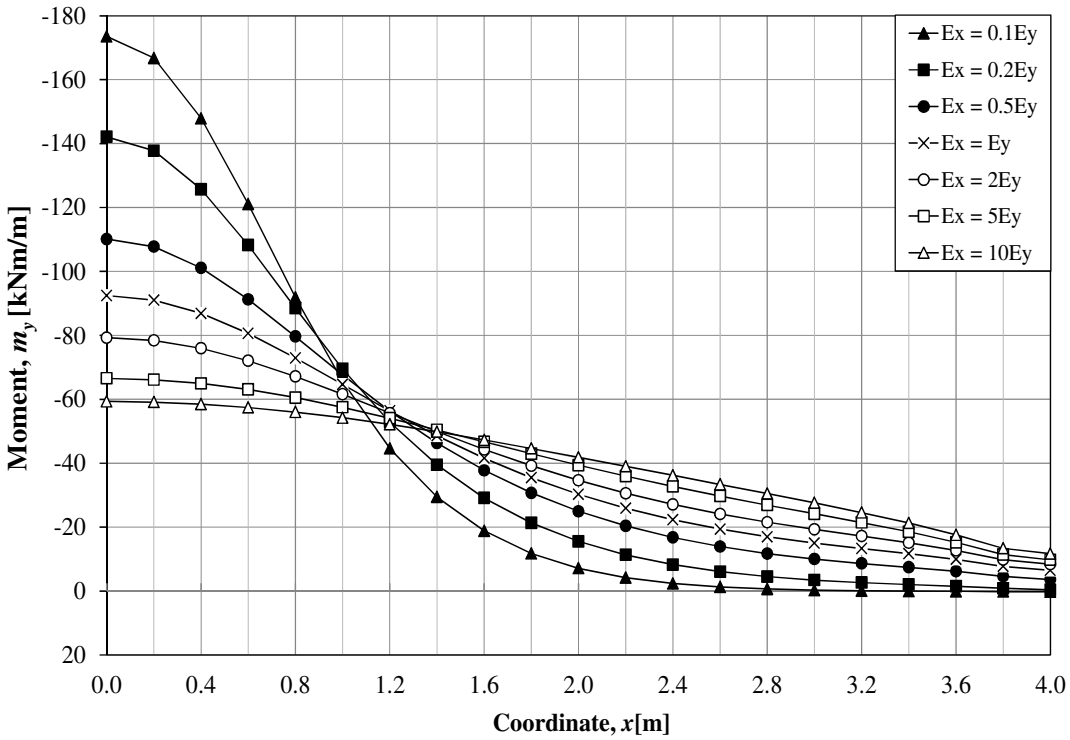

(b)

Figure C.14. Moment distribution m_y from FE-linear elastic orthotropic analysis using 0.2 m shell elements with Poisson's ratio v = 0: (a) m_y along L_4 (b) m_y along L_5.

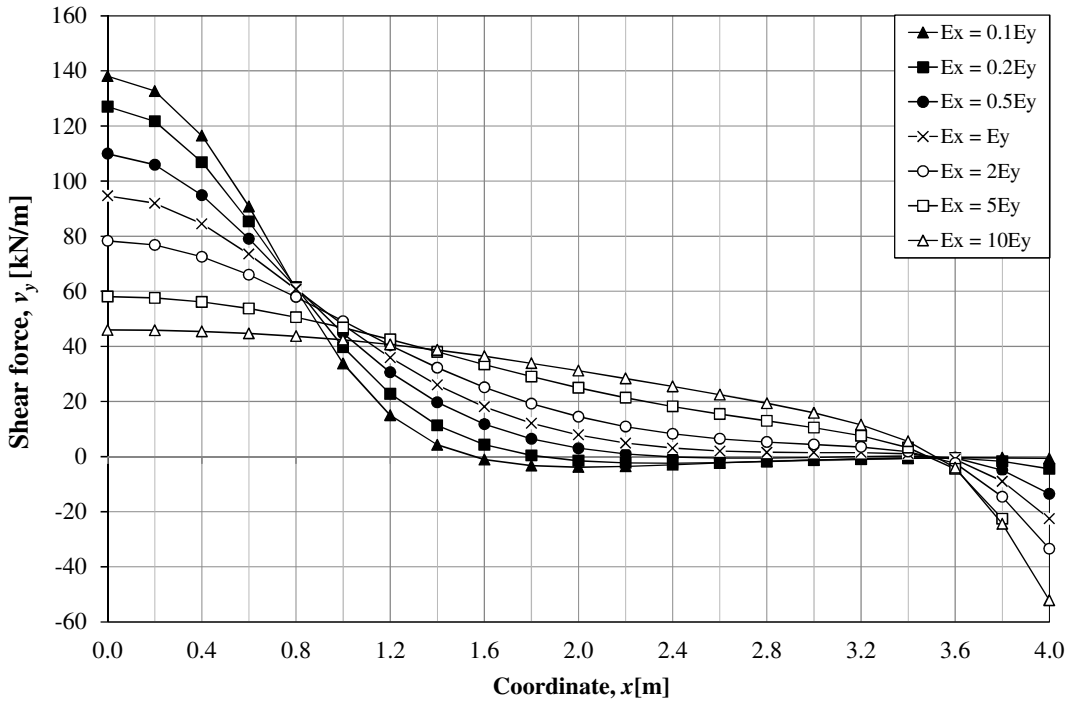

Figure C.15. Shear force distribution v_y along L_5 from FE-linear elastic orthotropic analysis using 0.2 m shell elements with Poisson's ratio ν = 0.

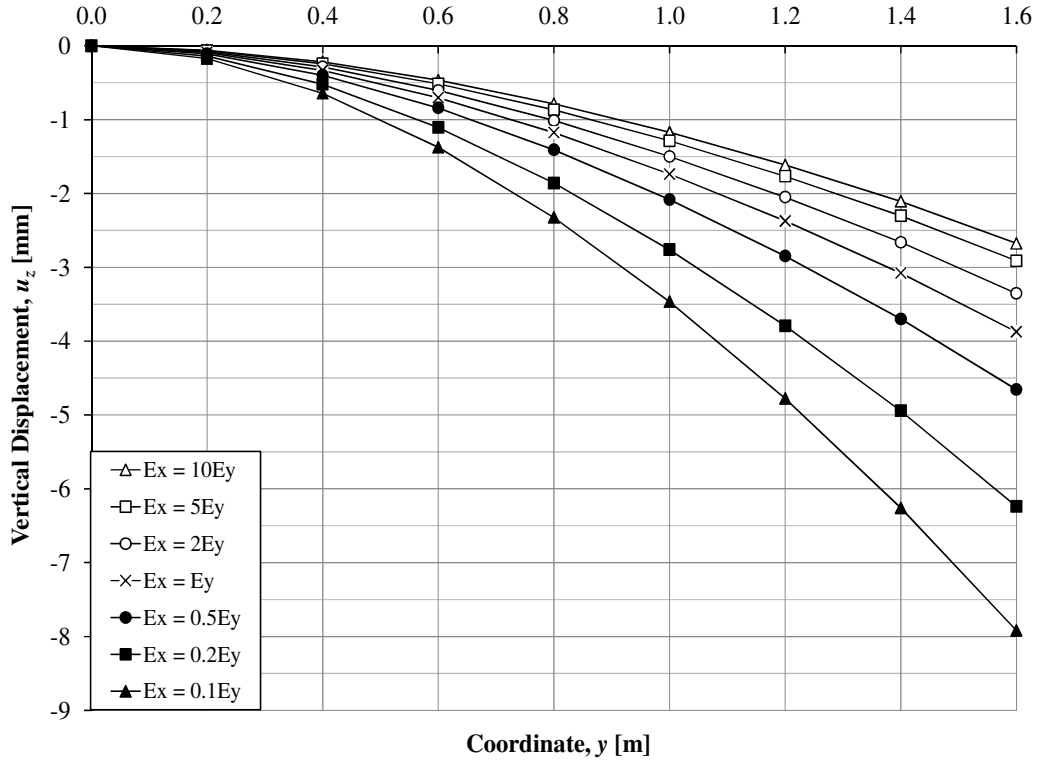

(a)

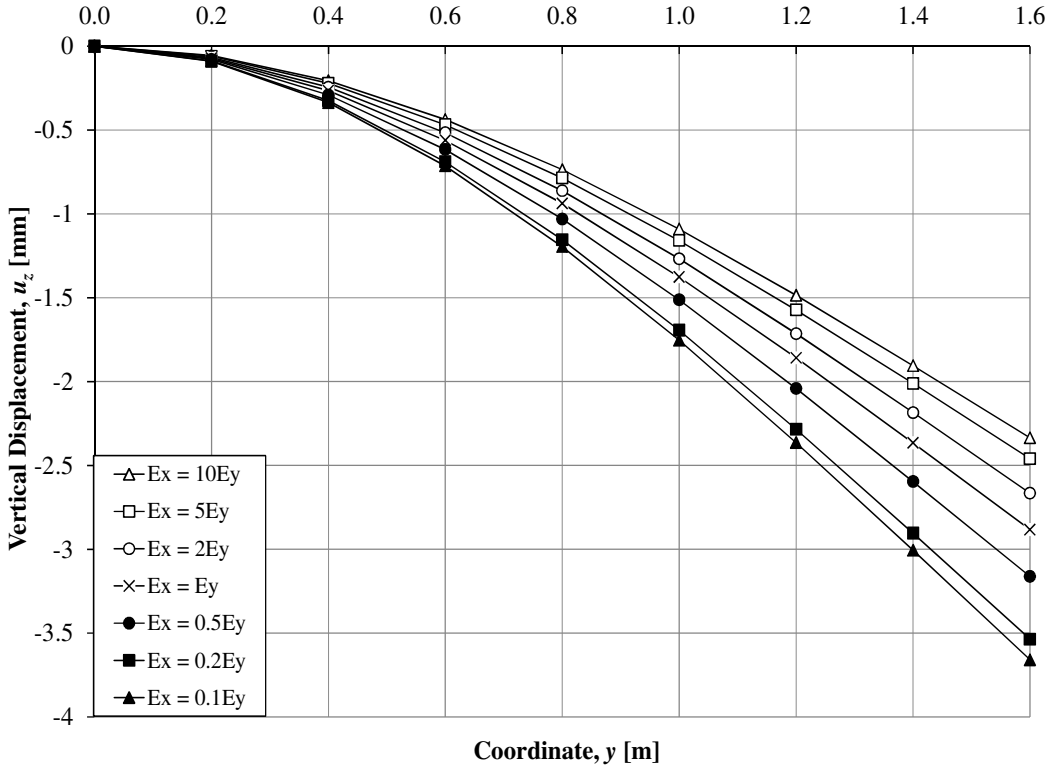

(b)

Figure C.16. Vertical displacement u_z from FE-linear elastic orthotropic analysis using 0.2 m shell elements with Poisson's ratio ν = 0: (a) vertical displacement-z along L_1 (b) vertical displacement-z along L_2.

C.2.2 Cantilever slab with beam elements

The geometry of the slab is shown in Figure 4.22 with *Ex* = 0.2, 0 5, 1, 5*Ey*.

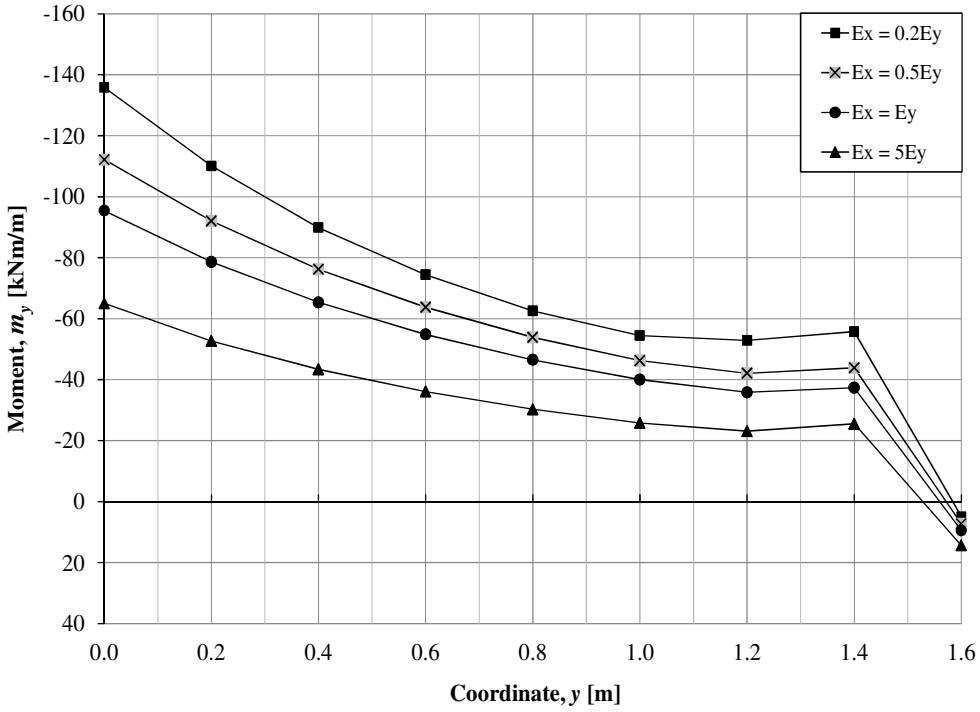

(a)

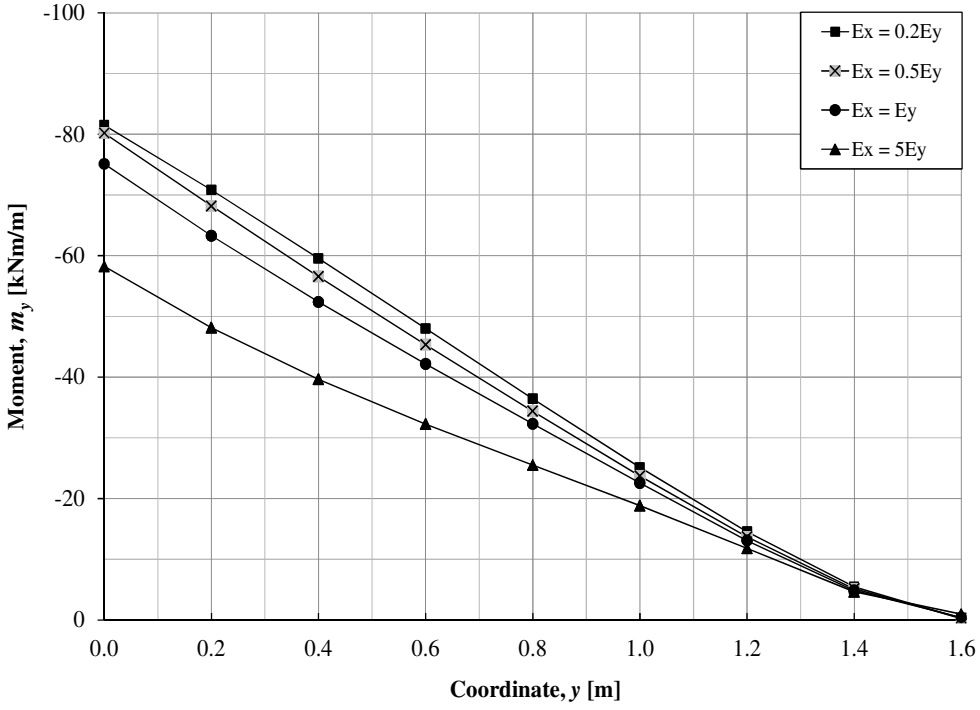

(b)

Figure C.17. Moment distribution m_y from FE-linear elastic orthotropic analysis using 0.2 m beam elements with Poisson's ratio ν = 0: (a) m_y along L_1 (b) m_y along L_2.

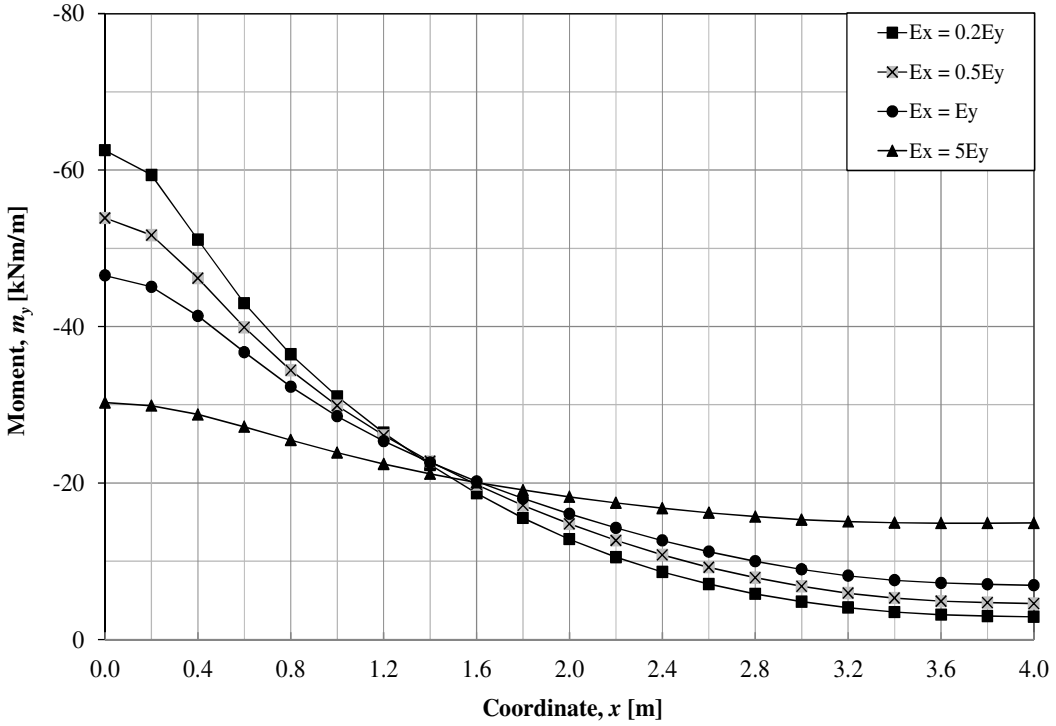

(a)

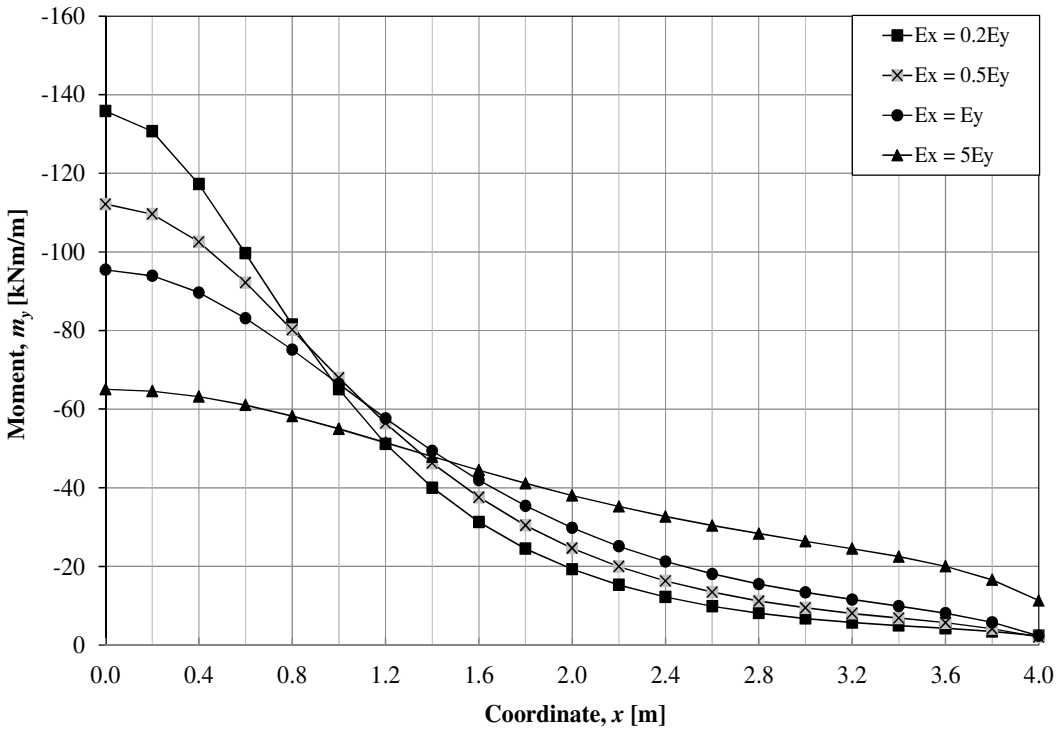

(b)

Figure C.18. Moment distribution m_y from FE-linear elastic orthotropic analysis using 0.2 m beam elements with Poisson's ratio ν = 0: (a) m_y along L_4 (b) m_y along L_5.

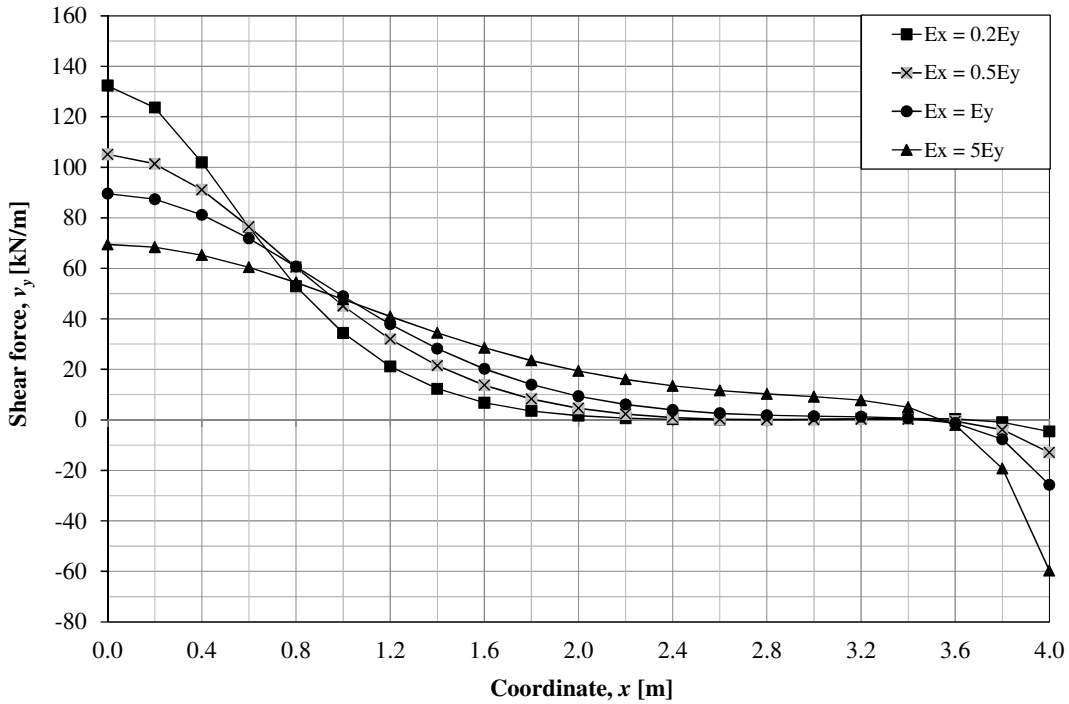

Figure C.19. Shear force distribution v_y along L_5 from FE-linear elastic orthotropic analysis using 0.2 m beam elements with Poisson's ratio $\nu = 0$.

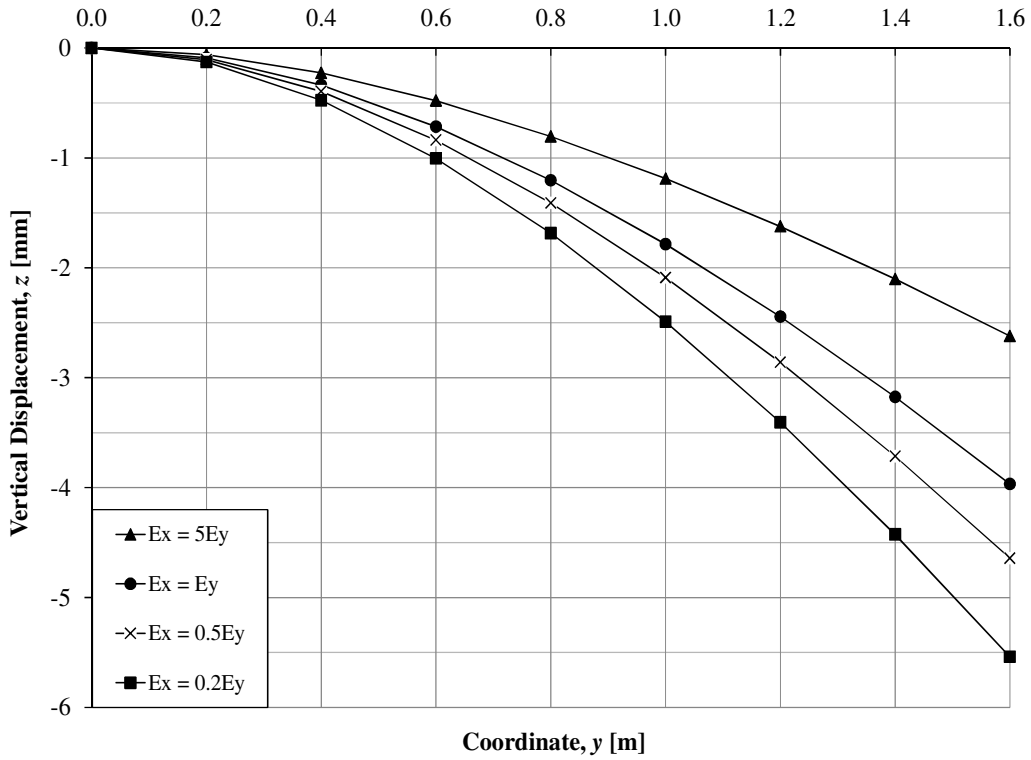

(a)

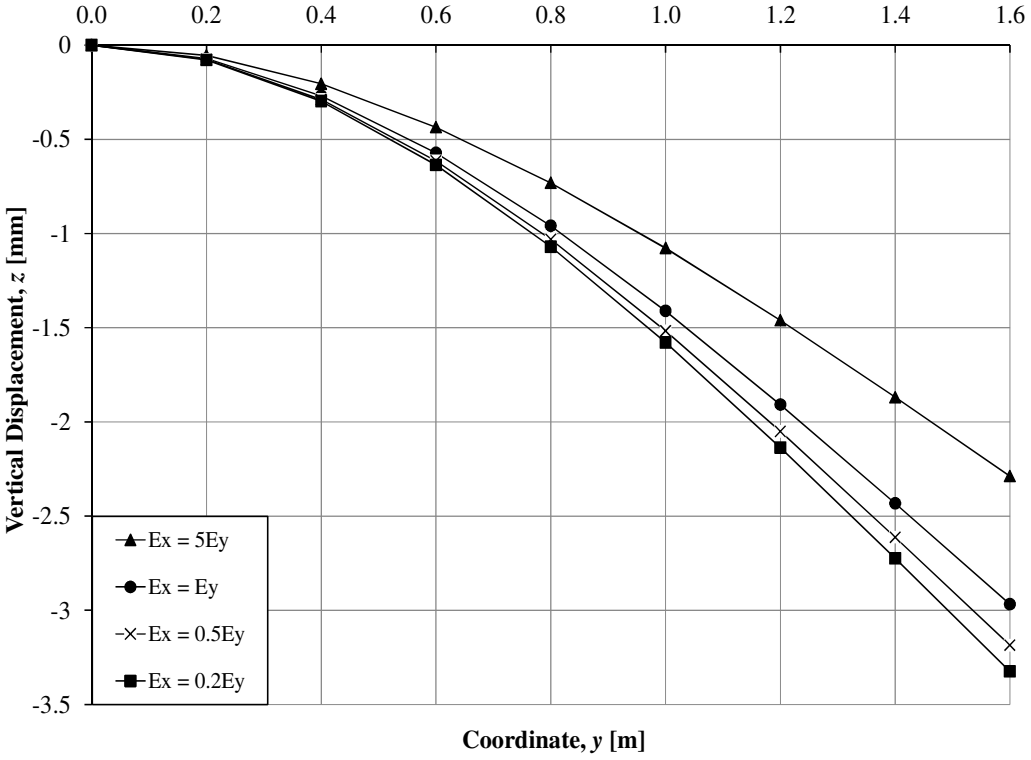

(b)

Figure C.20. Vertical displacement-z from FE-linear elastic orthotropic analysis using 0.2 m beam elements with Poisson's ratio ν = 0: (a) vertical displacement-z along L_1 (b) vertical displacement-z along L_2.

C.2.3 Comparisons between shell model and beam grids model

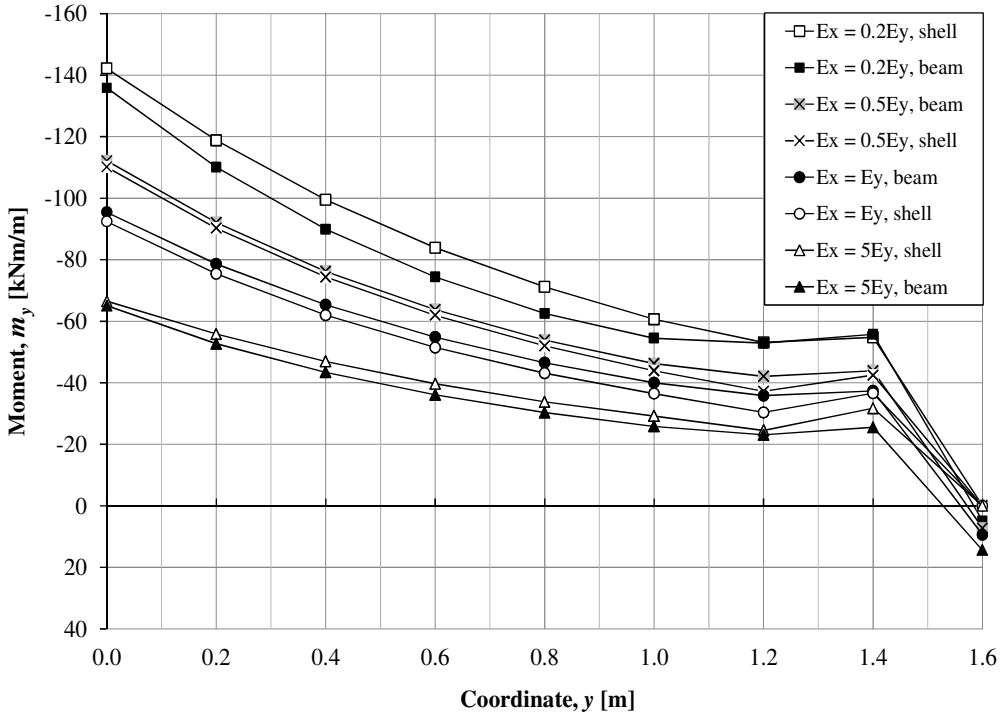

(a)

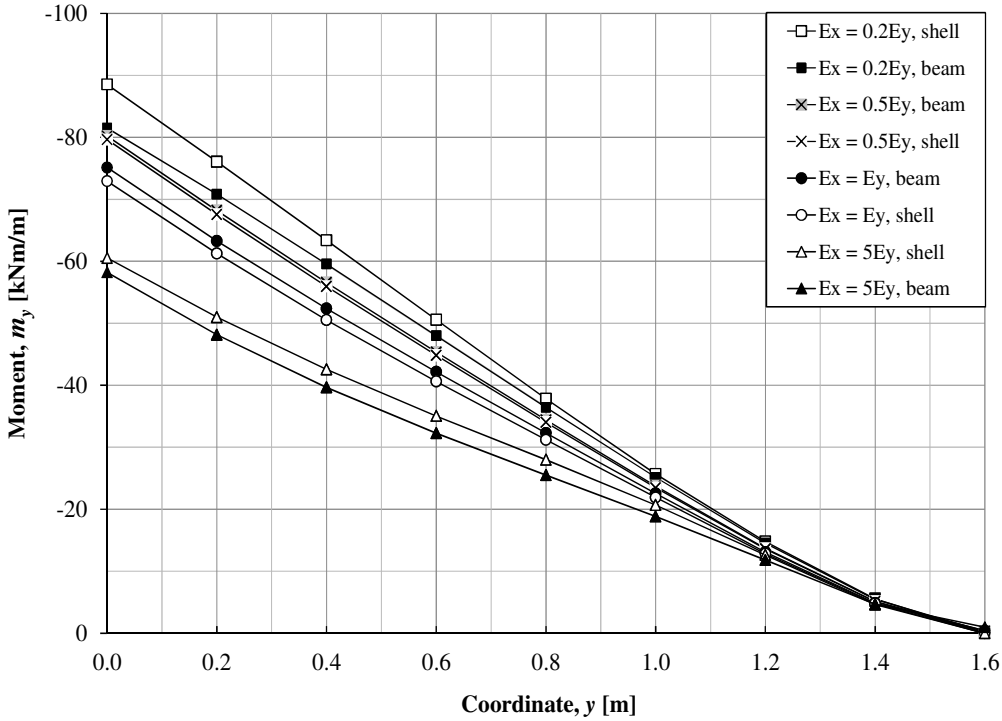

(b)

Figure C.21. Comparisons of moment distribution m_y from FE-linear elastic orthotropic analysis between 0.2 m beam elements and 0.2 m shell elements with Poisson's ratio ν = 0: (a) m_y along L_1 (b) m_y along L_2.

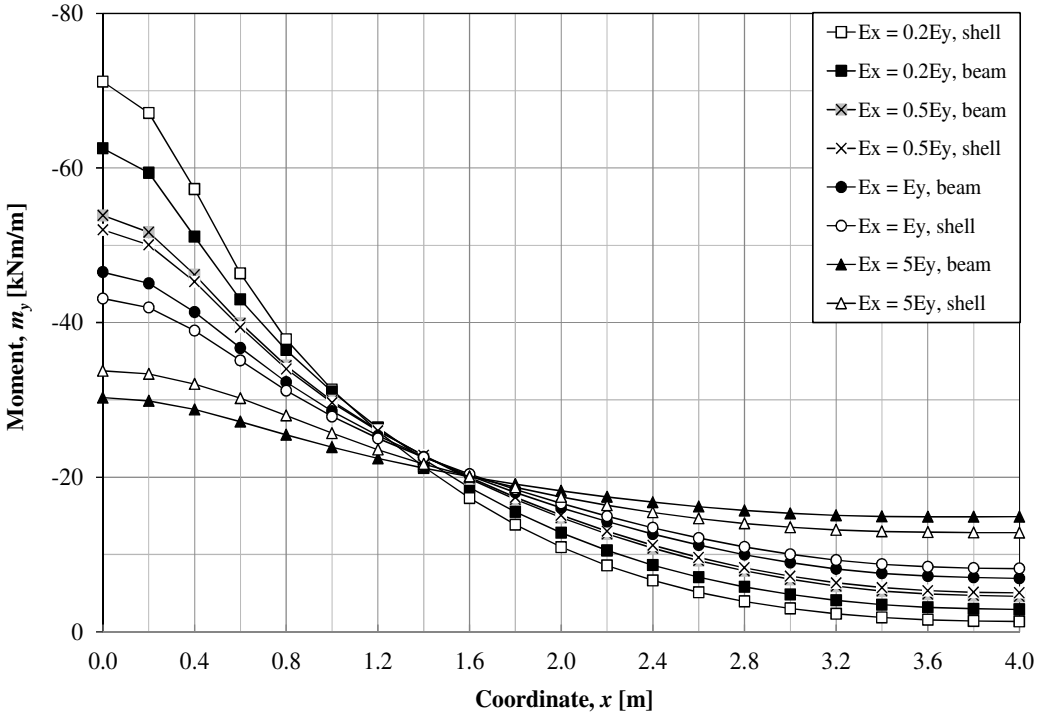

(a)

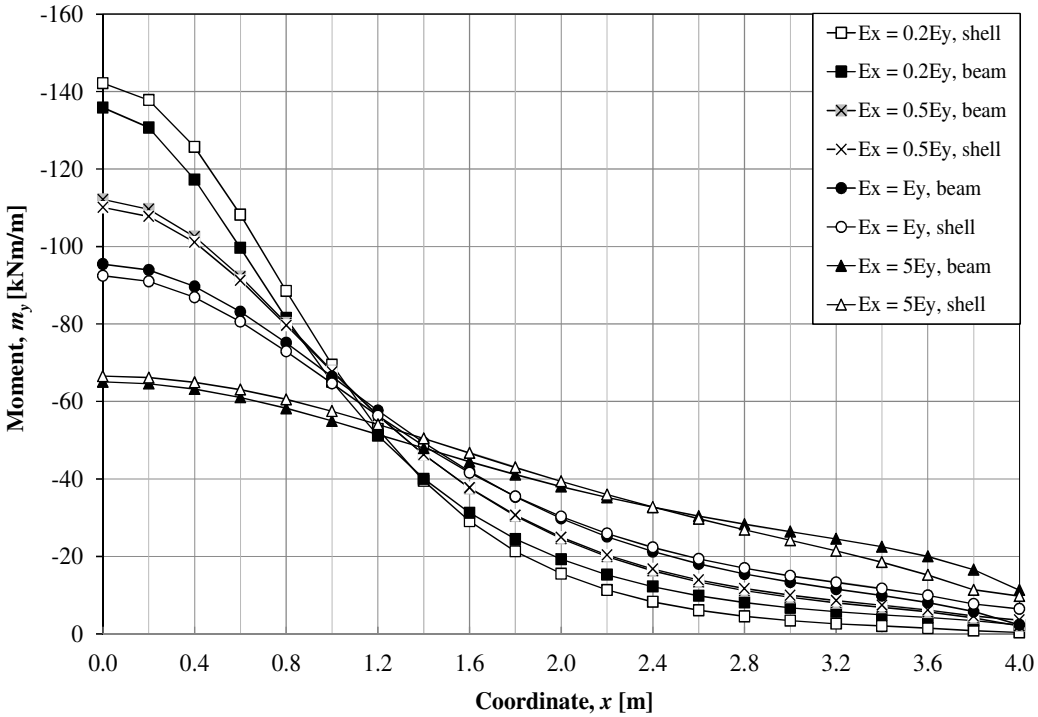

(b)

Figure C.22. Comparisons of moment distribution m_y from FE-linear elastic orthotropic analysis between 0.2 m beam elements and 0.2 m shell elements with Poisson's ratio ν = 0: (a) m_y along L_4 (b) m_y along L_5.

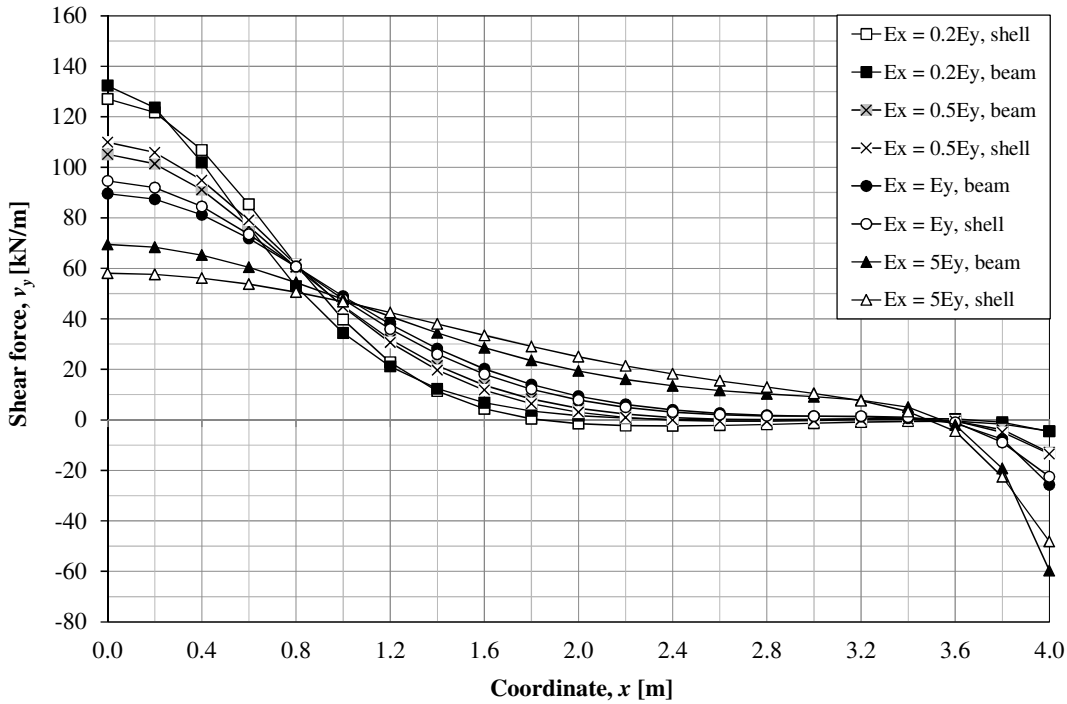

Figure C.23. Comparisons of shear force distribution v_y along L_5 from FE-linear elastic orthotropic analysis between 0.2 m beam elements and 0.2 m shell elements with Poisson's ratio ν = 0.

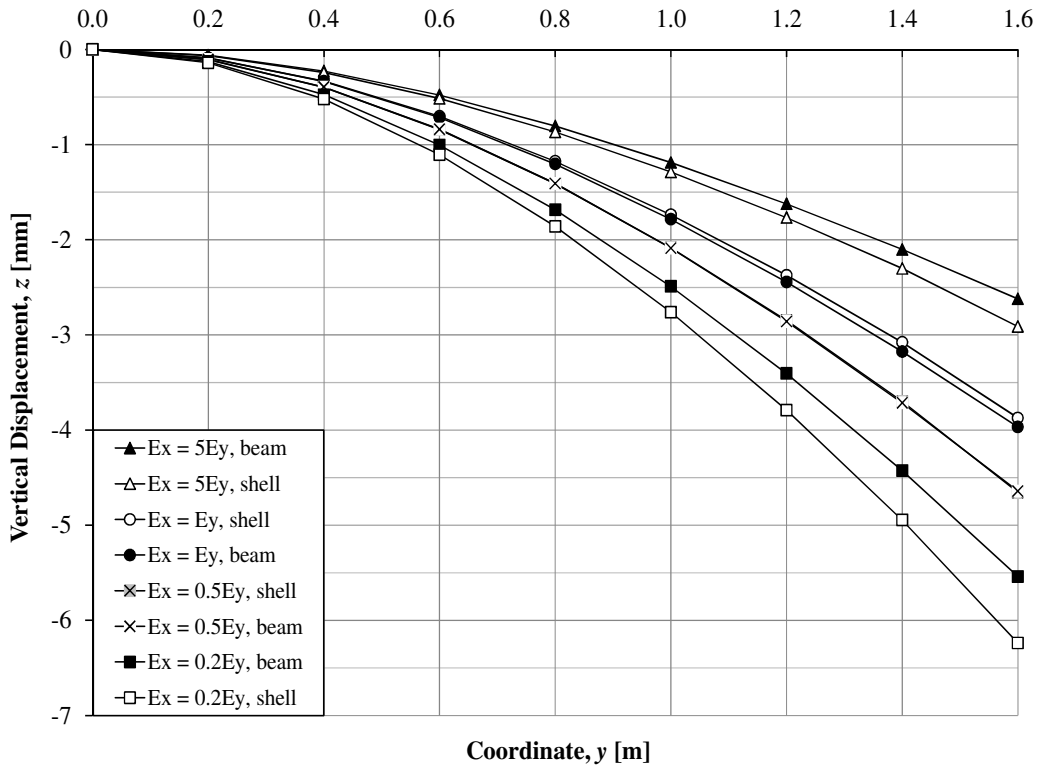

(a)

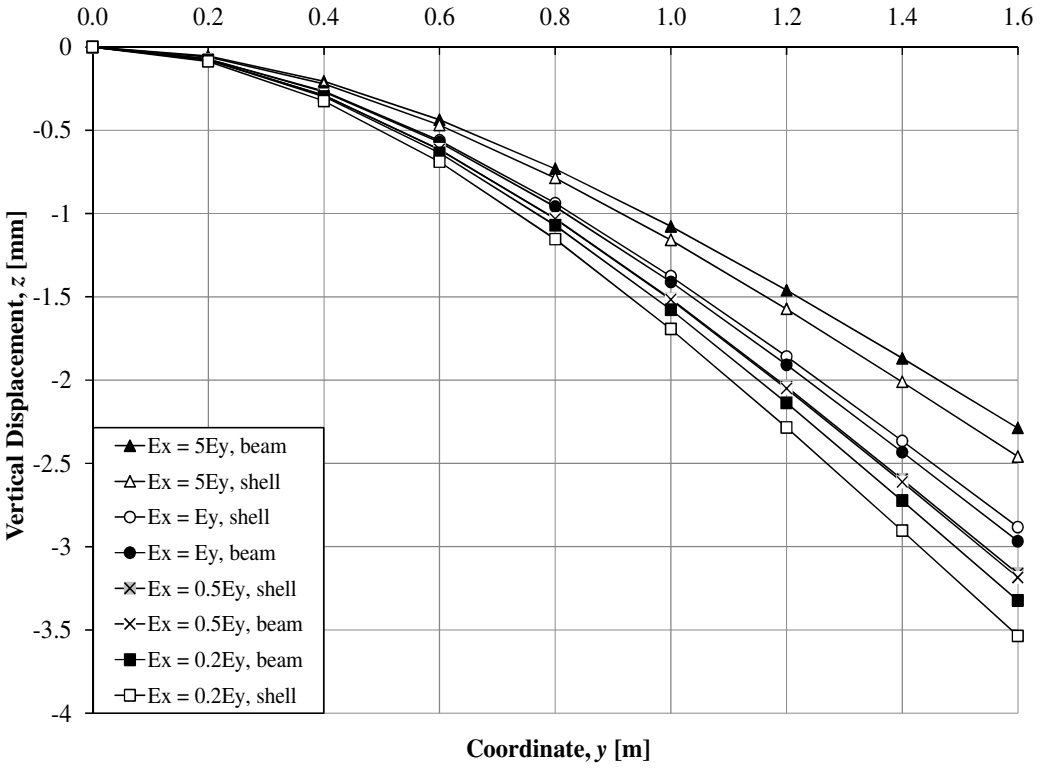

(b)

Figure C.24. Comparisons of vertical displacement u_z from FE-linear elastic orthotropic analysis between 0.2 m beam elements and 0.2 m shell elements with Poisson's ratio ν = 0: (a) vertical displacement-z along L_1 (b) vertical displacement-z along L_2.

C.3 Elasto-plastic case-cantilever slab with beam grillage model

C.3.1 Quadlinear M(χ) with $M_{pl} = 0.6\ M_{el}$

C.3.1.1 $E_{II} = E_I/5 = 6$ GPa

The geometry of the slab is shown in Figure 4.32 and moment curvature relationship input is given in Figure 4.33. The analysis is performed using 0.2 m beam elements with $v = 0$.

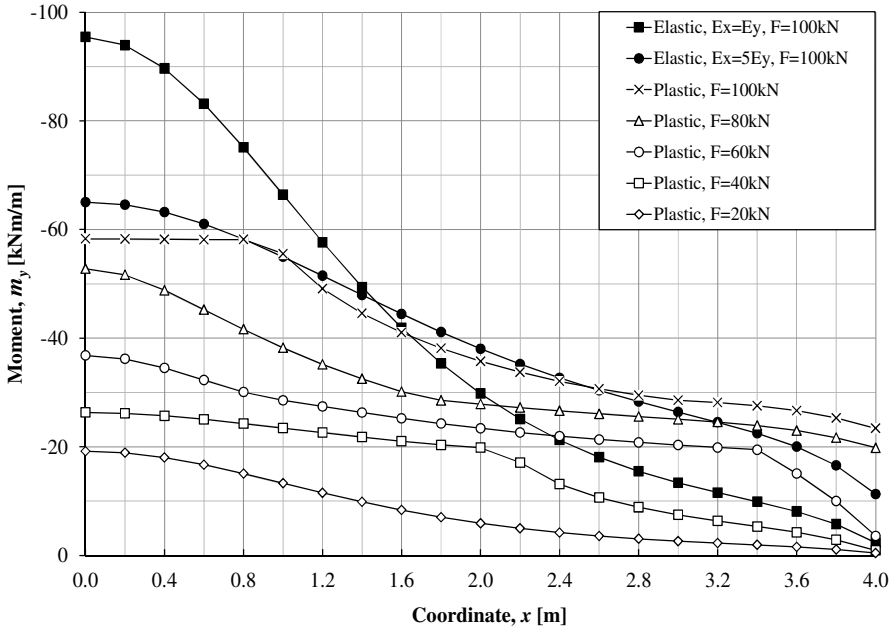

(a)

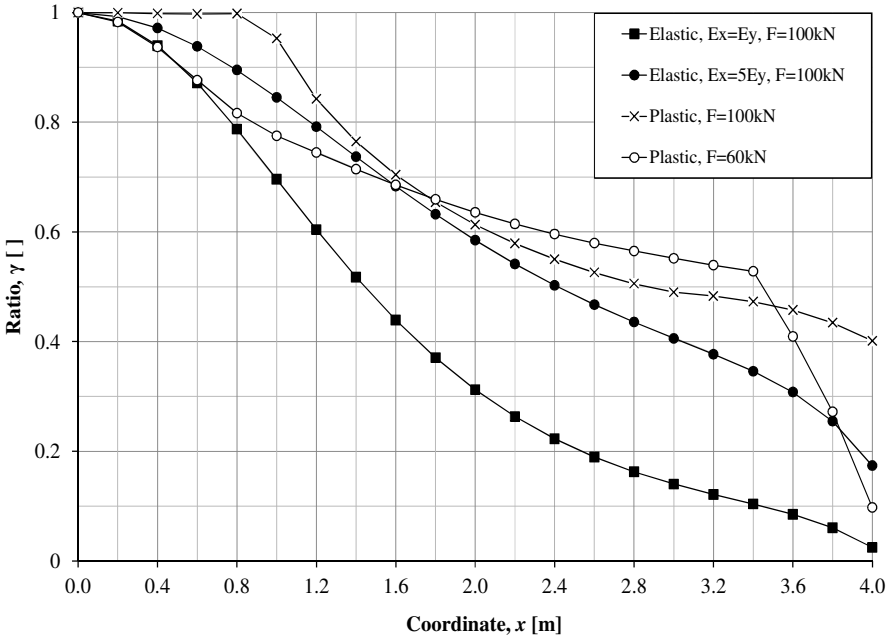

(b)

Figure C.25. Moment distribution m_y along L_5 at different load level up to 100 kN (a) moment distribution m_y (b) ratio of maximum moment $m_{y,max}$ to $m_{y,x}$ moment along L_5, $E_{II} = E_I/5$.

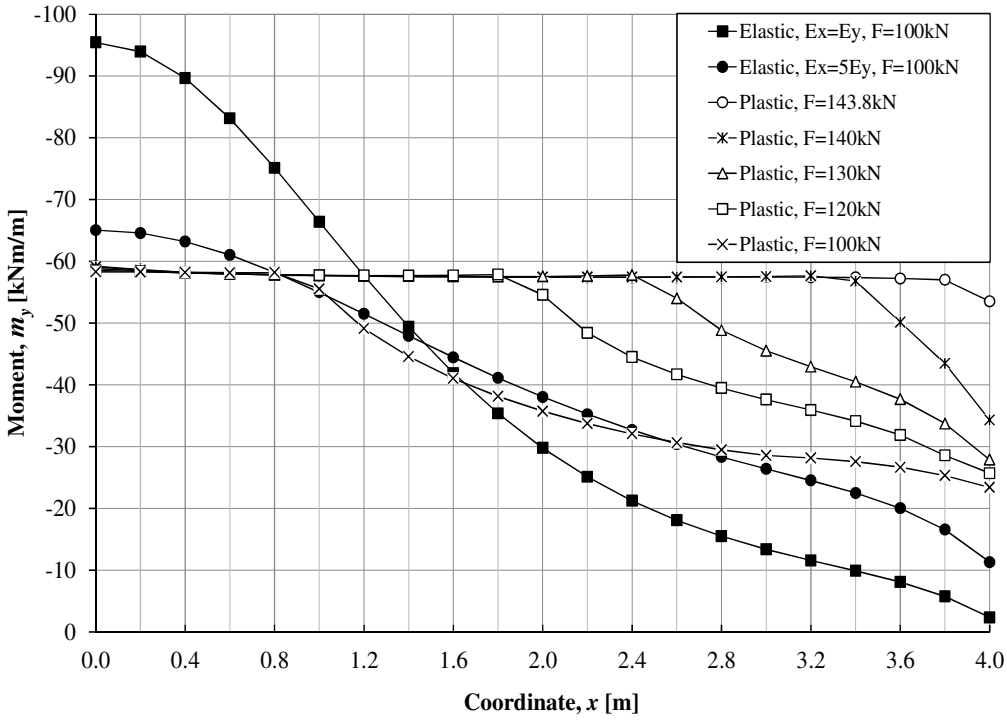

(a)

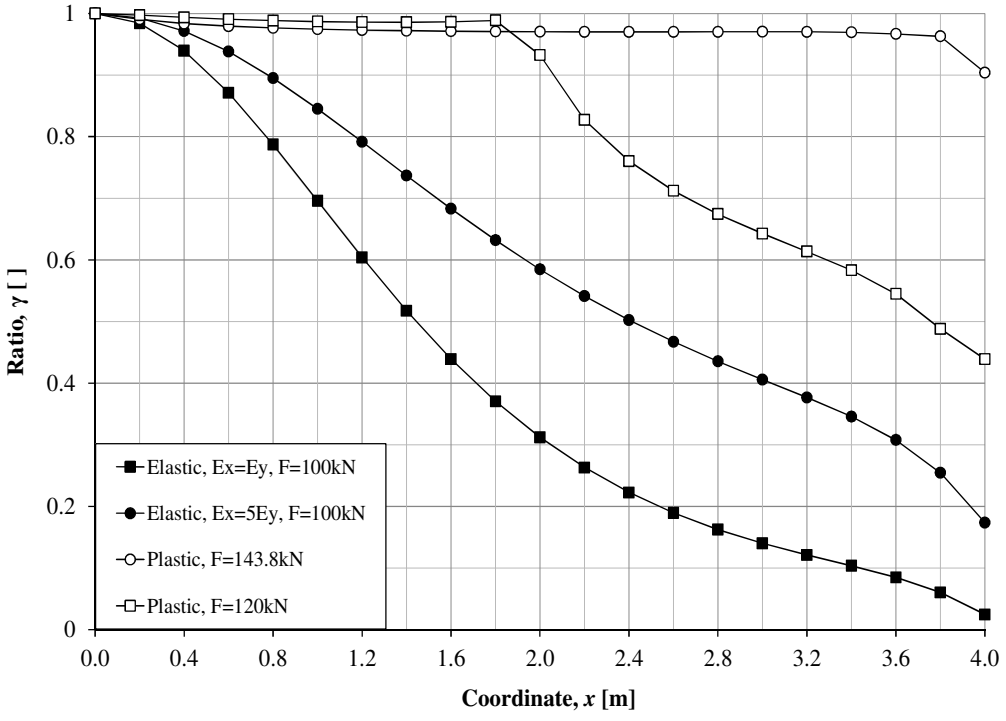

(b)

Figure C.26. Moment distribution m_y along L_5 at different load level up to 143.8 kN (a) moment distribution m_y (b) ratio of maximum moment $m_{y,max}$ to $m_{y,x}$ moment along L_5, $E_{II} = E_I/5$.

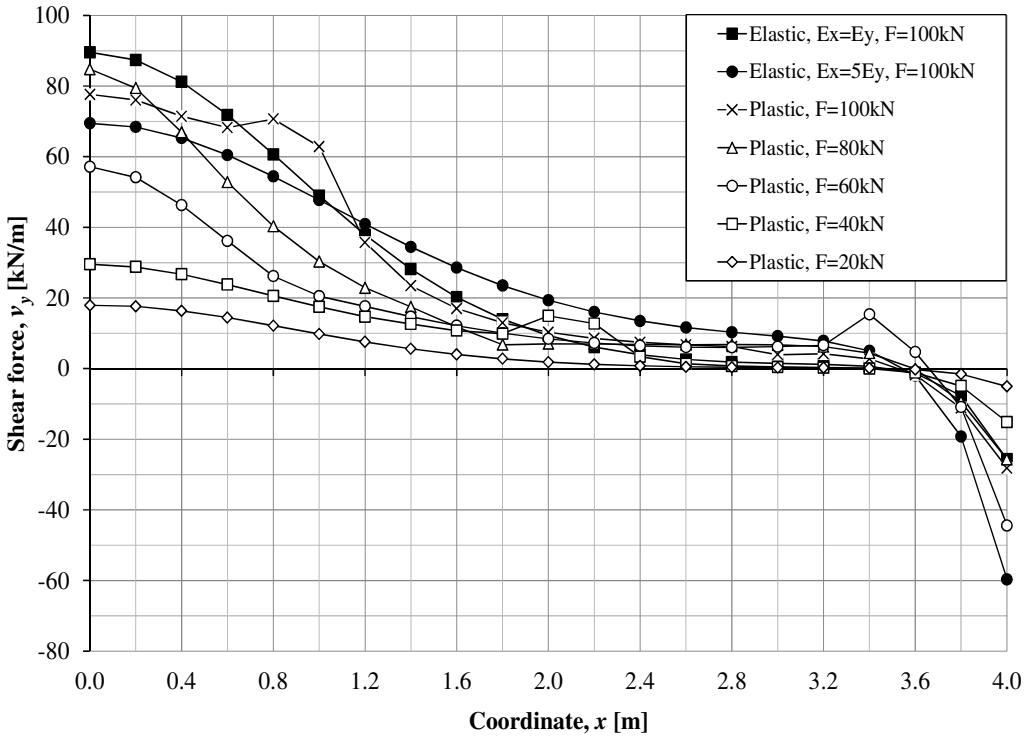

(a)

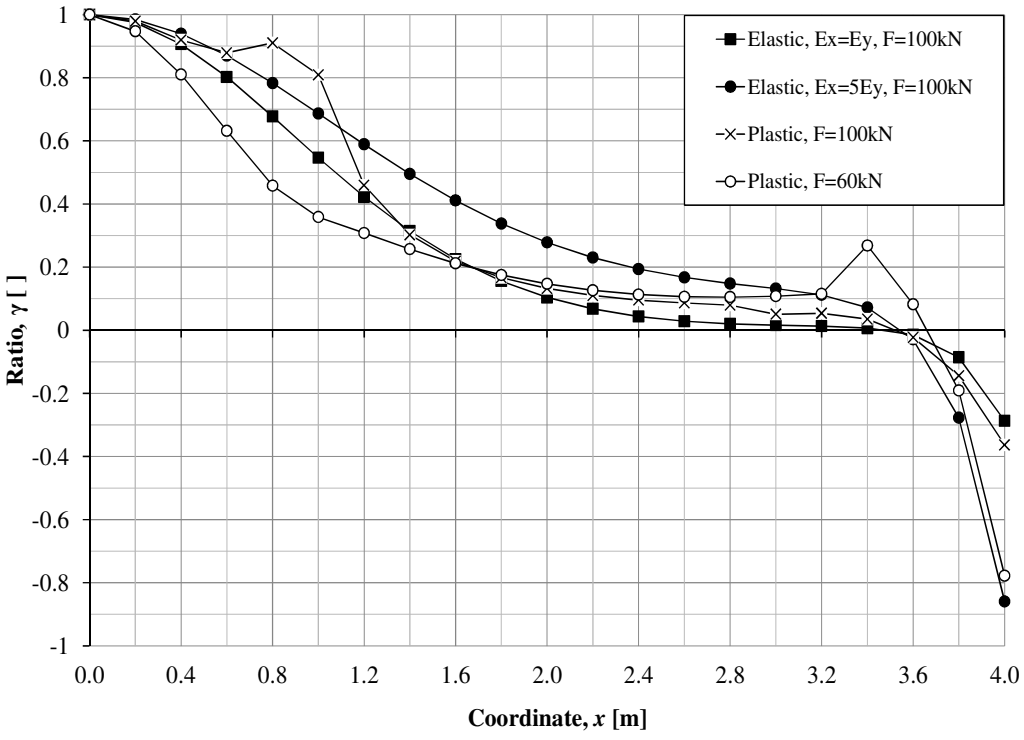

(b)

Figure C.27. Shear force distribution v_y along L_5 at different load level up to 100 kN (a) shear force distribution v_y (b) ratio of maximum shear force $v_{y,max}$ to $v_{y,x}$ moment along L_5, $E_{II} = E_I/5$.

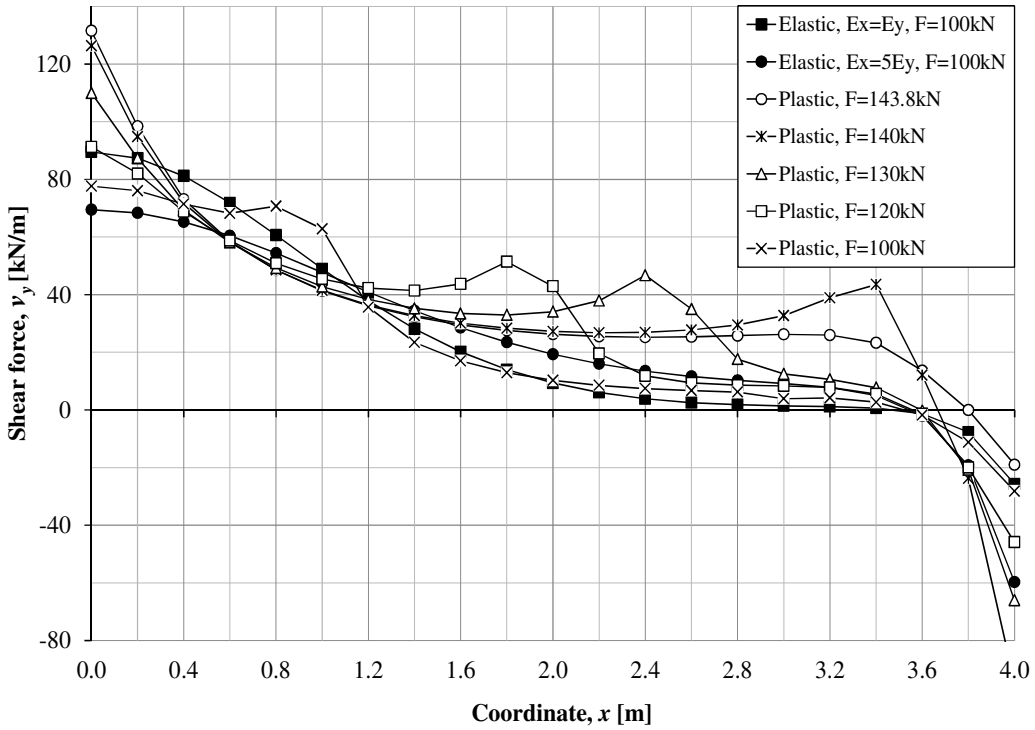

(a)

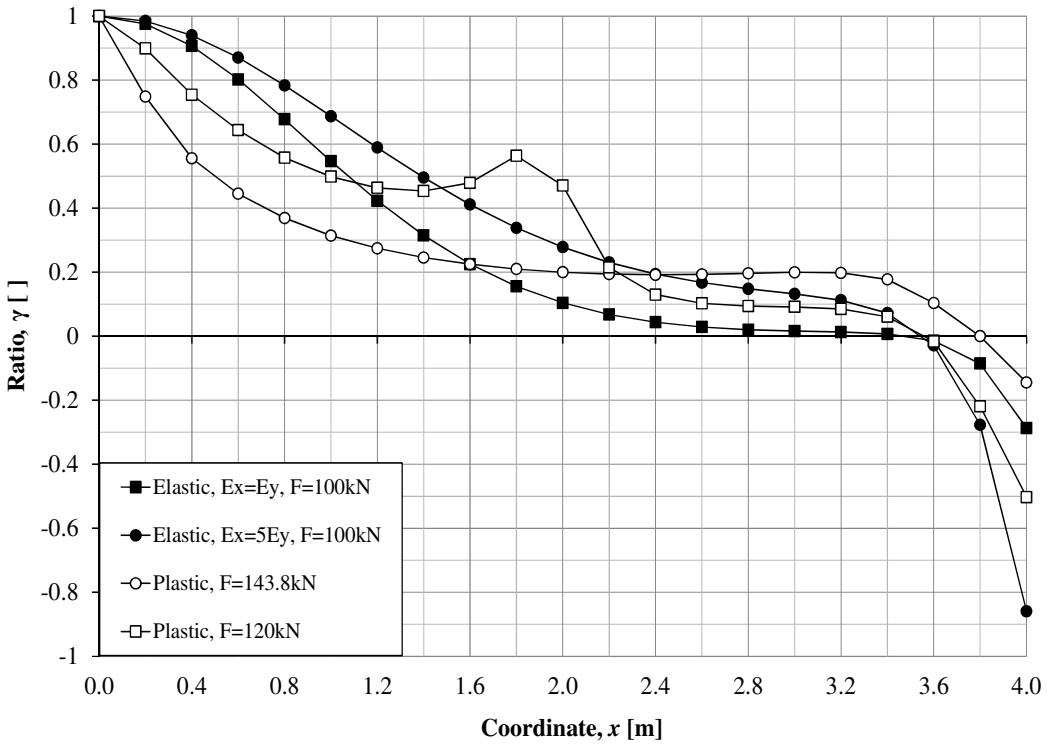

(b)

Figure C.28. Shear force distribution v_y along L_5 at different load level up to 143.8 kN (a) shear force distribution v_y (b) ratio of maximum shear force $v_{y,max}$ to $v_{y,x}$ moment along L_5, $E_{II} = E_I/5$.

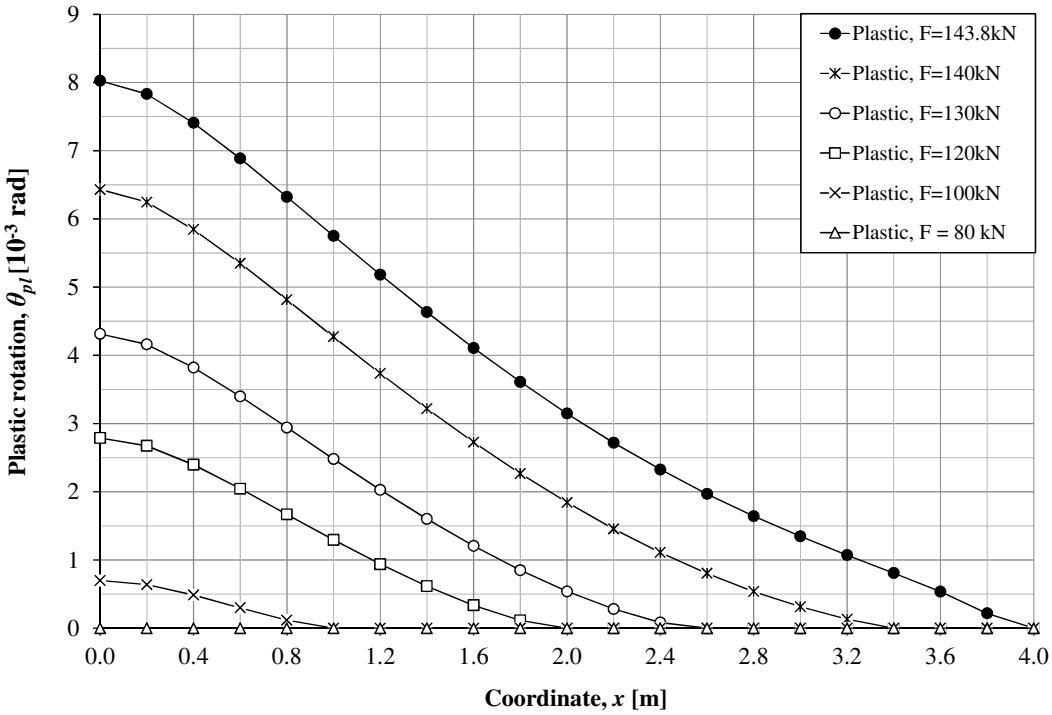

Figure C.29. Plastic rotation distribution θ_{pl} along L_5 at different load level up to 143.8 kN from FE-elsto-plastic using 0.2 m beam elements with Poisson's ratio $\nu = 0$, $E_{II} = E_I/5$.

C.3.1.2 $E_{II} = E_I/2 = 15$ GPa

The geometry of the slab is shown in Figure 4.32 and moment curvature relationship input is given in Figure C.30. The analysis is performed using 0.2 m beam elements with $v = 0$.

Here $M_{plastic} = 0.6M_{elastic,}$ $M_{cr2} = M_{plastic}/2$ and $M_{cr1} = M_{plastic}/3$ from equation (4-21) to equation (4-26) in Section 4.5.3.1 are kept unchanged.

The curvature χ_I , χ_{II} , χ_{III} and χ_{IV},of the moment-curvature diagram in Figure C.30 are determined from equation (C-1) to equation (C-4).

$$\chi_I = \frac{M_{cr1}}{E_I I} = \frac{3.8\times10^3}{30\cdot10^9\times\frac{0.2\times0.2^3}{12}} = 0.00095\ [1/\mathrm{m}] \tag{C-1}$$

$$\chi_{II} = \frac{M_{cr2}}{E_{II} I} = \frac{5.7\times10^3}{15\cdot10^9\times\frac{0.2\times0.2^3}{12}} = 0.00285\ [1/\mathrm{m}] \tag{C-2}$$

$$\chi_{III} = \frac{M_{plastic}}{E_{II} I} = \frac{11.4\times10^3}{15\cdot10^9\times\frac{0.2\times0.2^3}{12}} = 0.0057\ [1/\mathrm{m}] \tag{C-3}$$

$$\chi_{IV} = 10\ [1/\mathrm{m}] \tag{C-4}$$

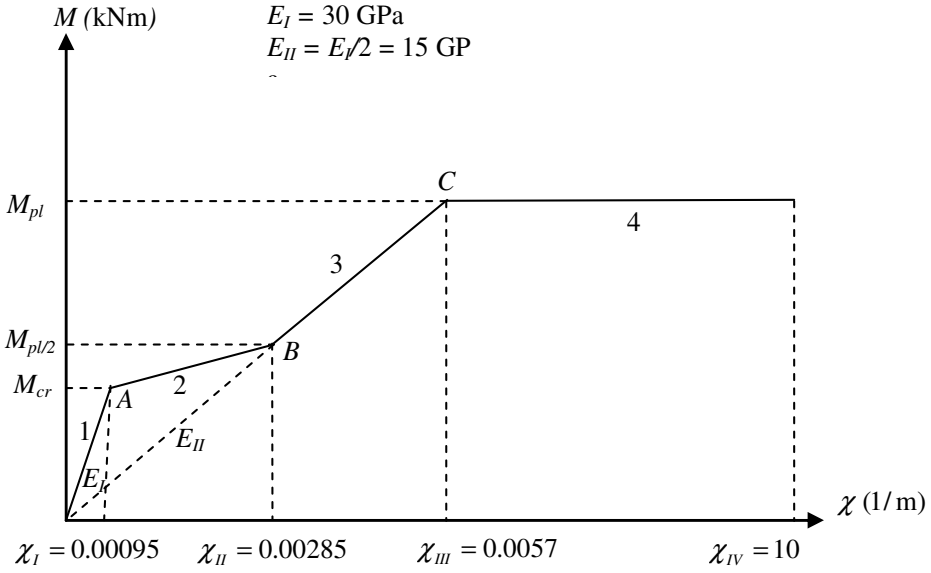

Figure C.30. Quadlinear moment-curvature relationship for the analysis of the studied cantilever slab in elasto-plastic case, $E_{II} = E_I/2$.

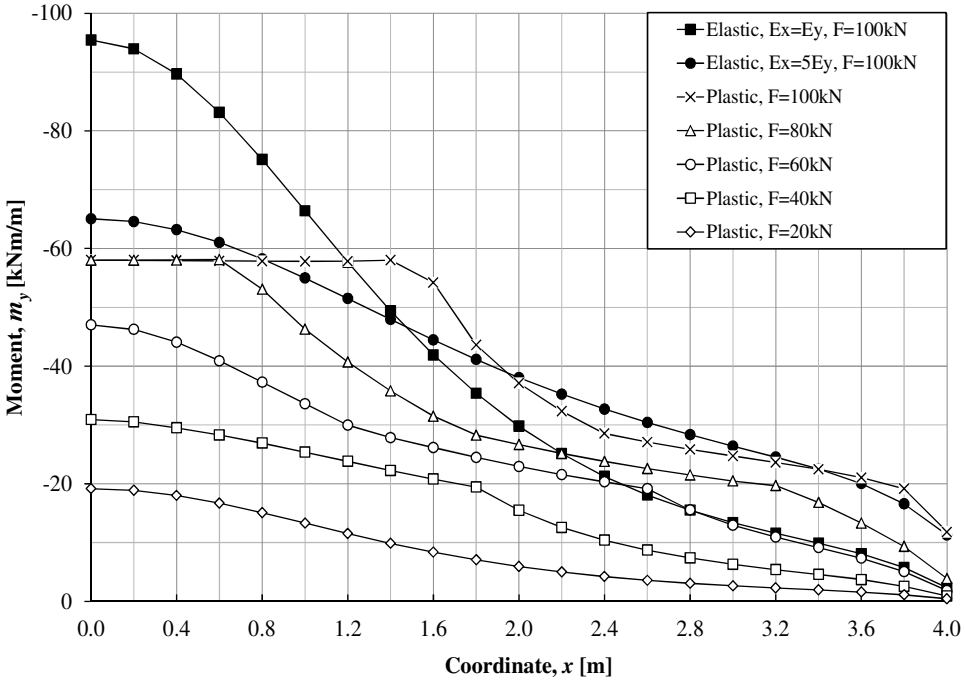

(a)

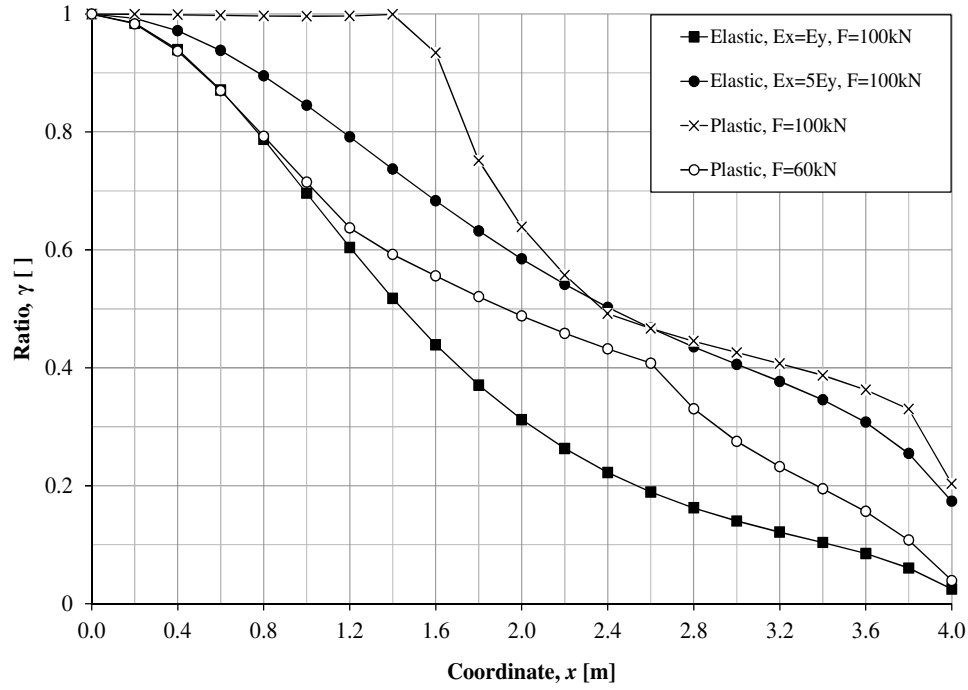

(b)

Figure C.31. Moment distribution m_y along L_5 at different load level up to 100 kN (a) moment distribution m_y (b) ratio of maximum moment $m_{y,max}$ to $m_{y,x}$ moment along L_5, $E_{II} = E_I/2$.

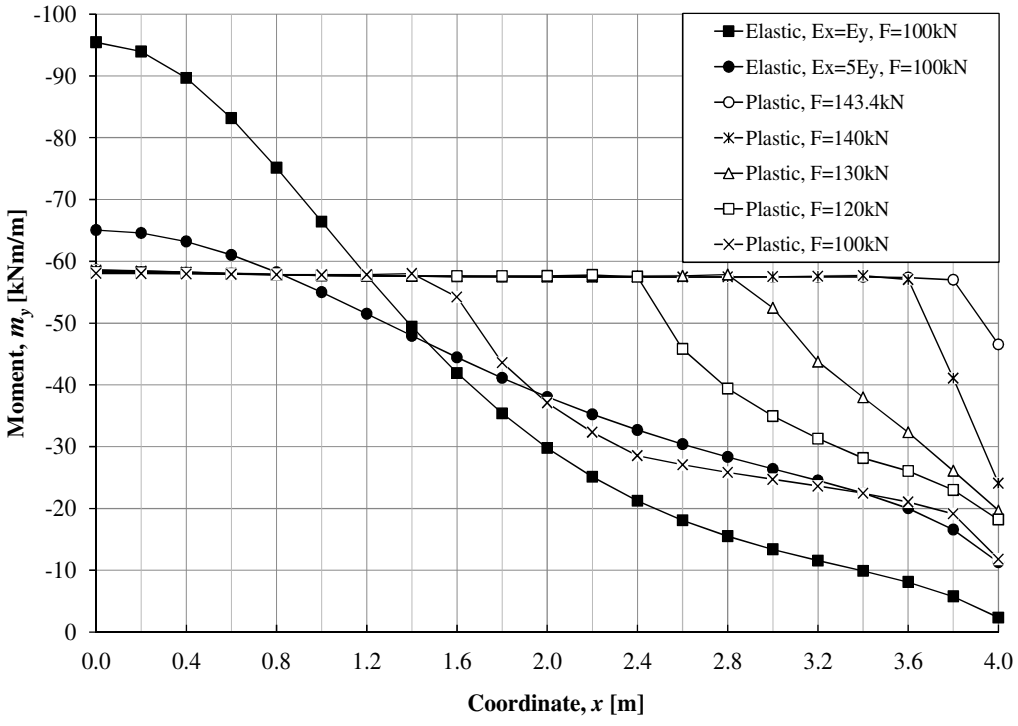

(a)

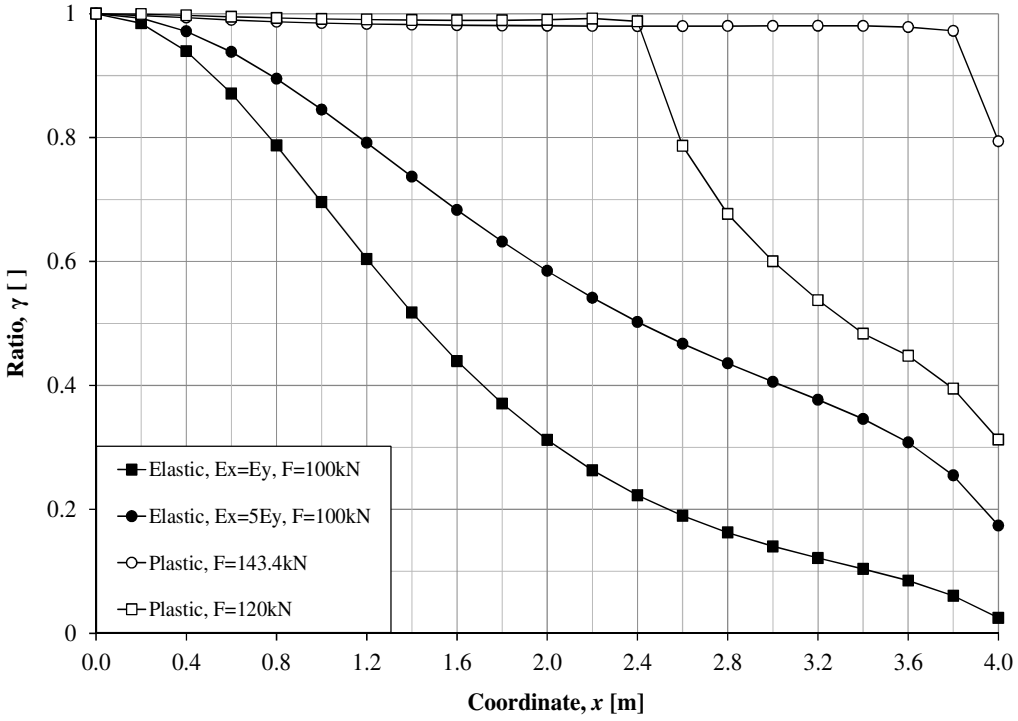

(b)

Figure C.32. Moment distribution m_y along L_5 at different load level up to 143.4 kN (a) moment distribution m_y (b) ratio of maximum moment $m_{y,max}$ to $m_{y,x}$ moment along L_5, $E_{II} = E_I/2$.

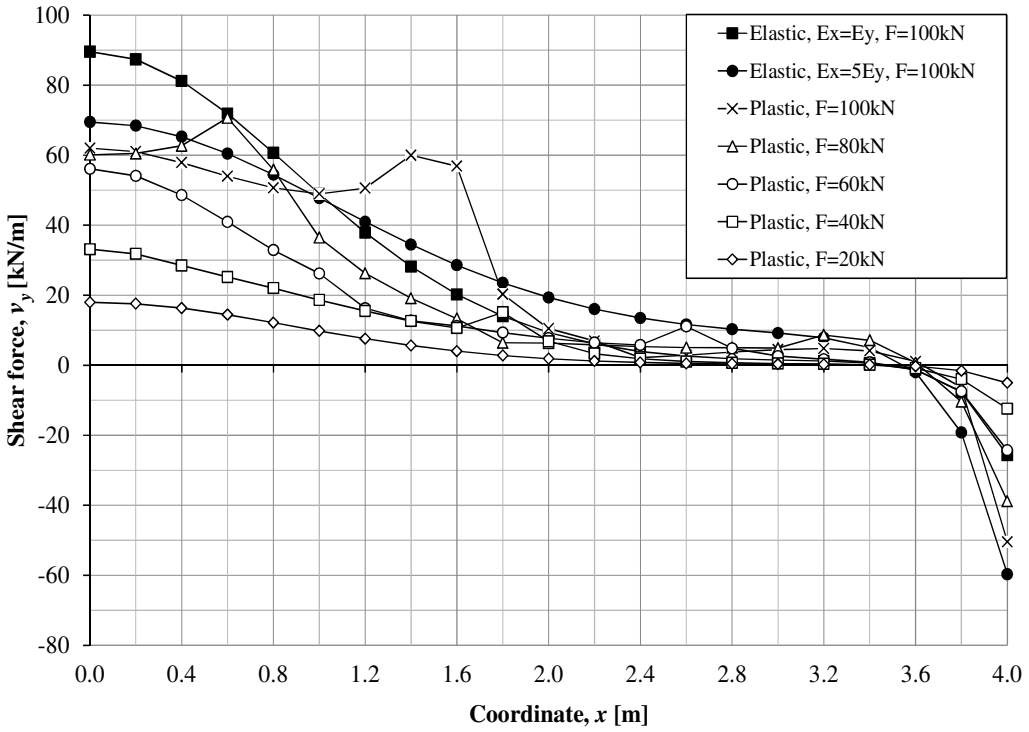

(a)

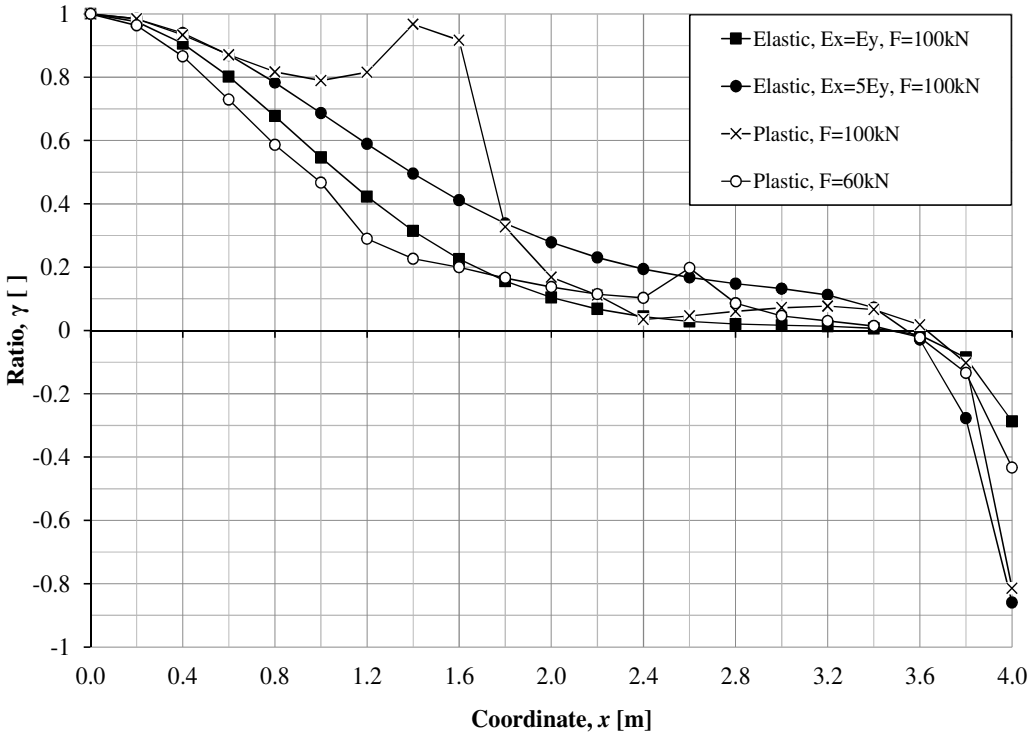

(b)

Figure C.33. Shear force distribution v_y along L_5 at different load level up to 100 kN (a) shear force distribution v_y (b) ratio of maximum shear force $v_{y,max}$ to $v_{y,x}$ moment along L_5, $E_{II} = E_I/2$.

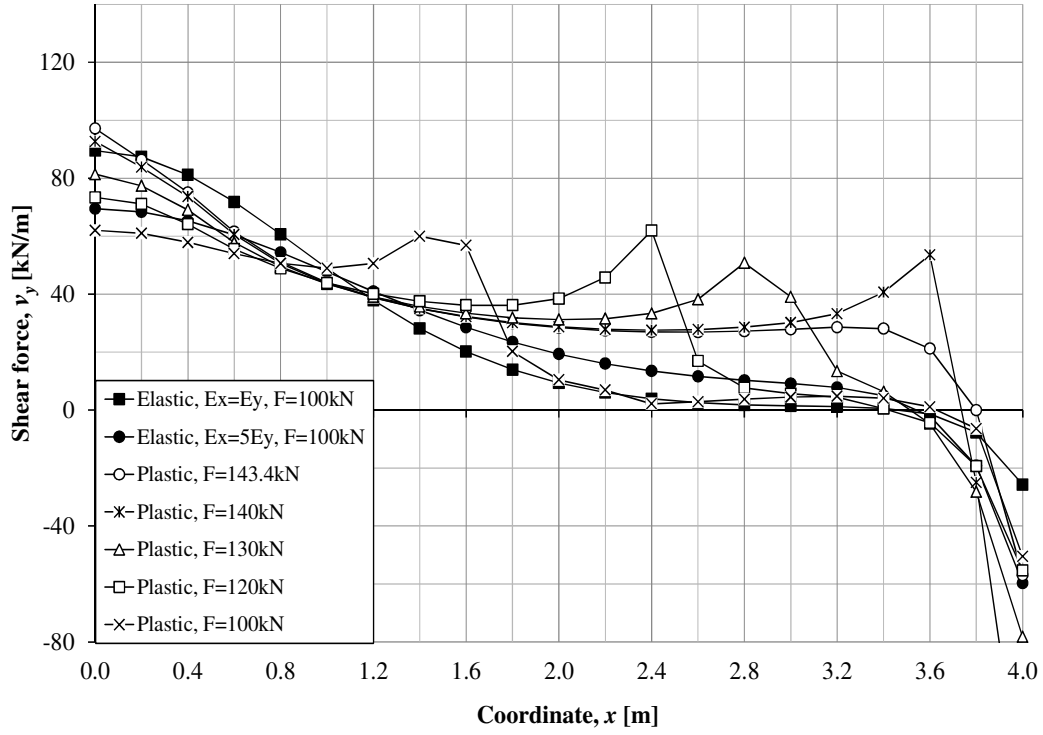

(a)

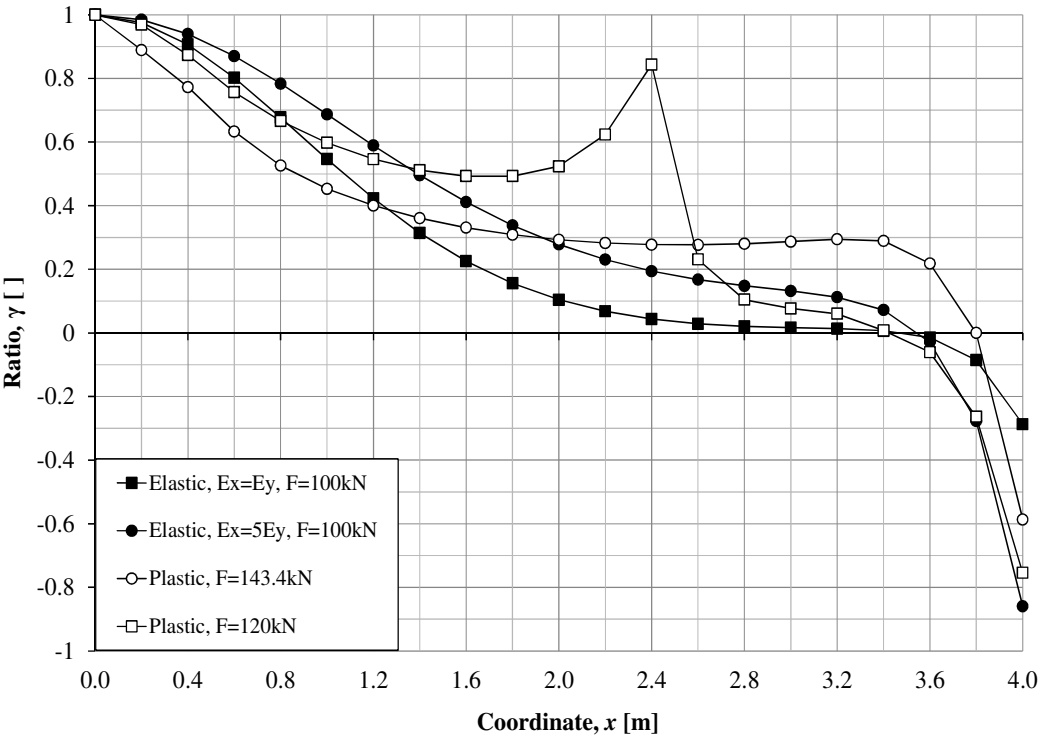

(b)

Figure C.34. Shear force distribution v_y along L_5 at different load level up to 143.4 kN (a) shear force distribution v_y (b) ratio of maximum shear force $v_{y,max}$ to $v_{y,x}$ moment along L_5, $E_{II} = E_I/2$.

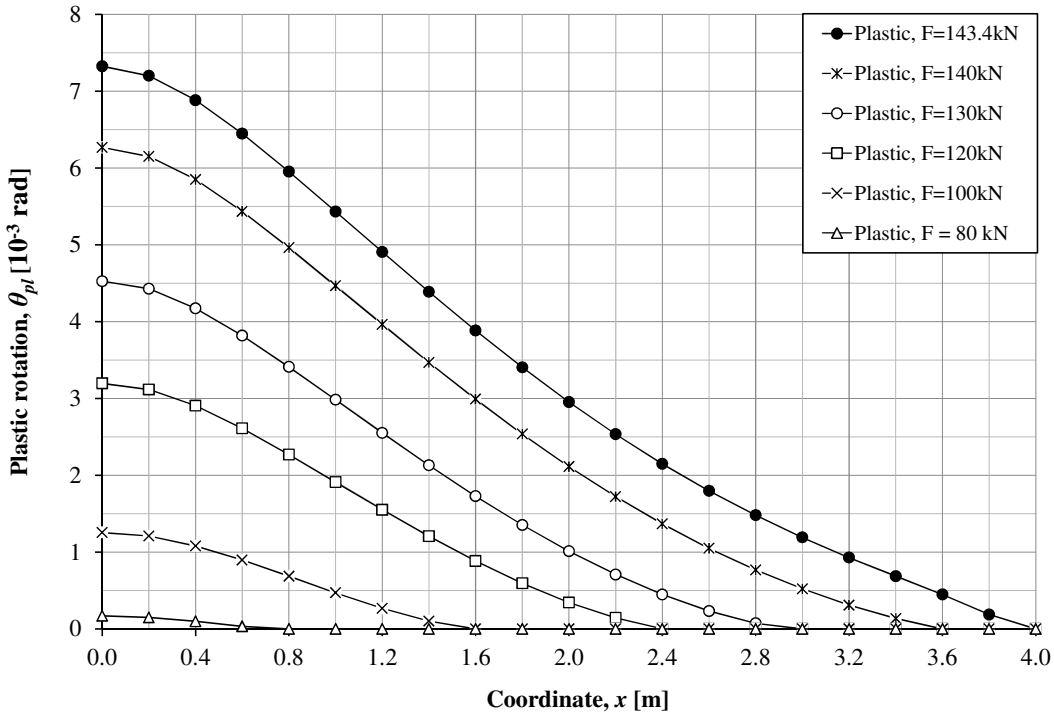

Figure C.35. Plastic rotation distribution θ_{pl} along L_5 at different load level up to 143.4 kN from FE-elsto-plastic using 0.2 m beam elements with Poisson's ratio $\nu = 0$, $E_{II} = E_I/2$.

C.3.1.3 $E_{II} = E_I/10 = 3$ GPa

The geometry of the slab is shown in Figure 4.32 and moment curvature relationship input is given in Figure C.36. The analysis is performed using 0.2 m beam elements with $v = 0$.

Like in case of $E_{II} = E_I/2 = 15$ GPa, $M_{plastic} = 0.6M_{elastic,}$ $M_{cr2} = M_{plastic}/2$ and $M_{cr1} = M_{plastic}/3$ from equation (4-21) to equation (4-26) in Section 4.5.3.1 are also kept unchanged for $E_{II} = E_I/10 = 3$ GPa.

The curvature χ_I , χ_{II} , χ_{III} , and χ_{IV} ,of the moment-curvature diagram in Figure C.36 are calculated as:

$$\chi_I = \frac{M_{cr1}}{E_I I} = \frac{3.8\times10^3}{30\cdot10^9\times\frac{0.2\times0.2^3}{12}} = 0.00095\left[1/\mathrm{m}\right] \tag{C-5}$$

$$\chi_{II} = \frac{M_{cr2}}{E_{II} I} = \frac{5.7\times10^3}{3\cdot10^9\times\frac{0.2\times0.2^3}{12}} = 0.01425\left[1/\mathrm{m}\right] \tag{C-6}$$

$$\chi_{III} = \frac{M_{plastic}}{E_{II} I} = \frac{11.4\times10^3}{3\cdot10^9\times\frac{0.2\times0.2^3}{12}} = 0.0285\left[1/\mathrm{m}\right] \tag{C-7}$$

$$\chi_{IV} = 10\ \left[1/\mathrm{m}\right] \tag{C-8}$$

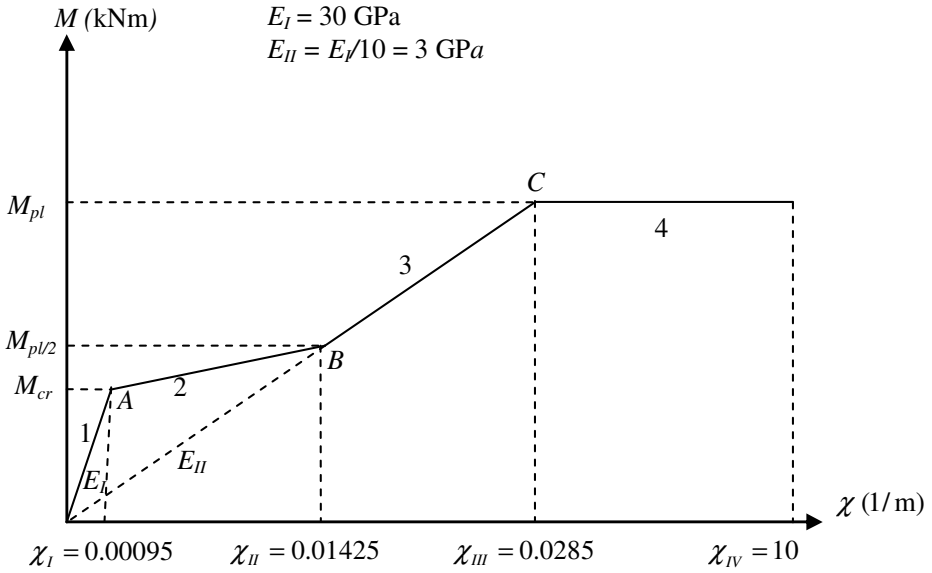

Figure C.36. Quadlinear moment-curvature relationship for the analysis of the studied cantilever slab in elasto-plastic case, $E_{II} = E_I/10$.

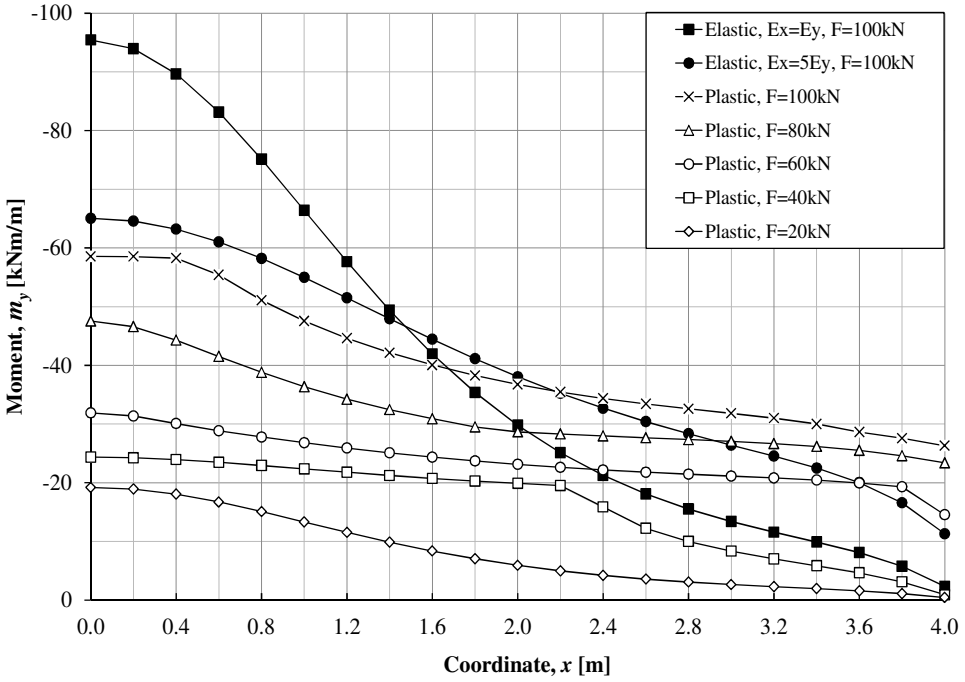

(a)

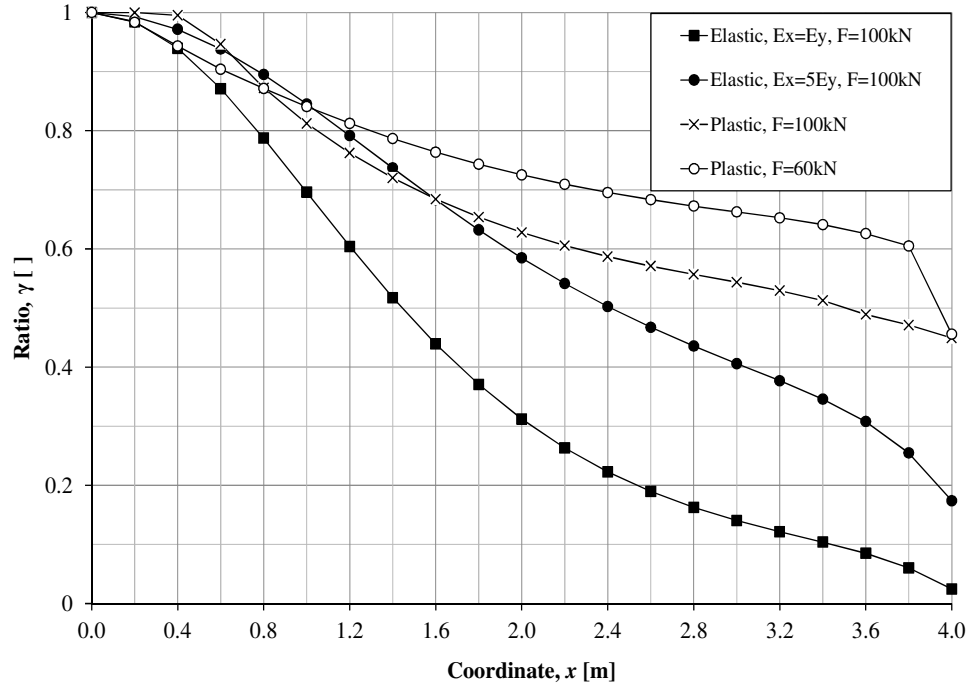

(b)

Figure C.37. Moment distribution m_y along L_5 at different load level up to 100 kN (a) moment distribution m_y (b) ratio of maximum moment $m_{y,max}$ to $m_{y,x}$ moment along L_5, $E_{II} = E_I/10$.

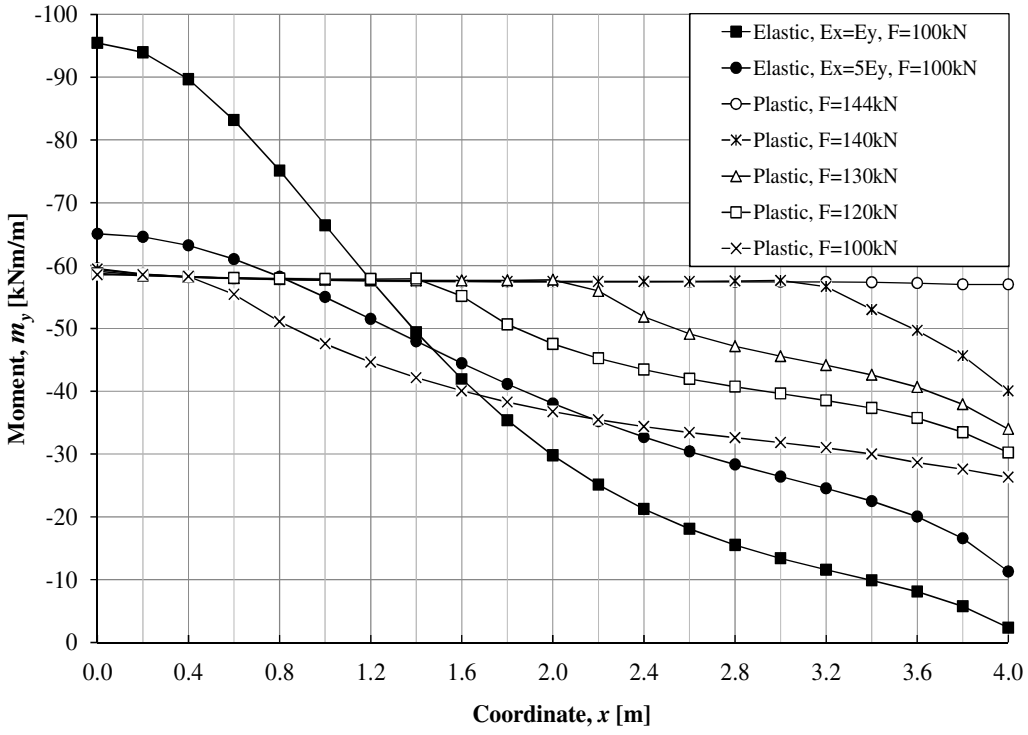

(a)

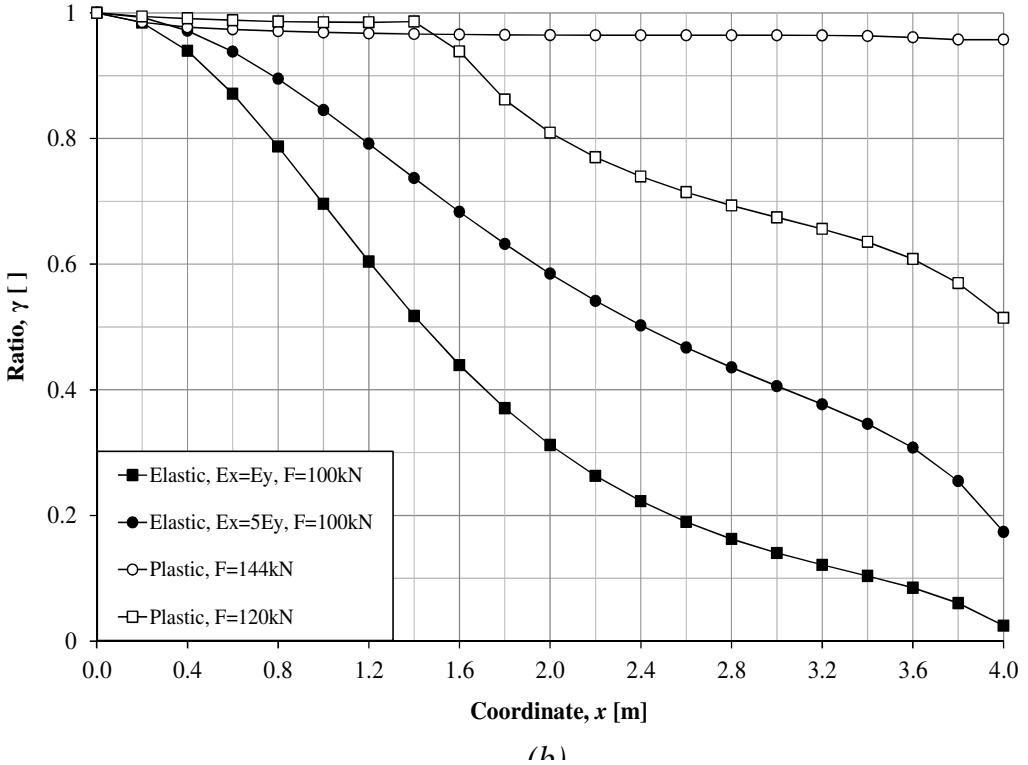

(b)

Figure C.38. Moment distribution m_y along L_5 at different load level up to 144 kN (a) moment distribution m_y (b) ratio of maximum moment $m_{y,max}$ to $m_{y,x}$ moment along L_5, $E_{II} = E_I/10$.

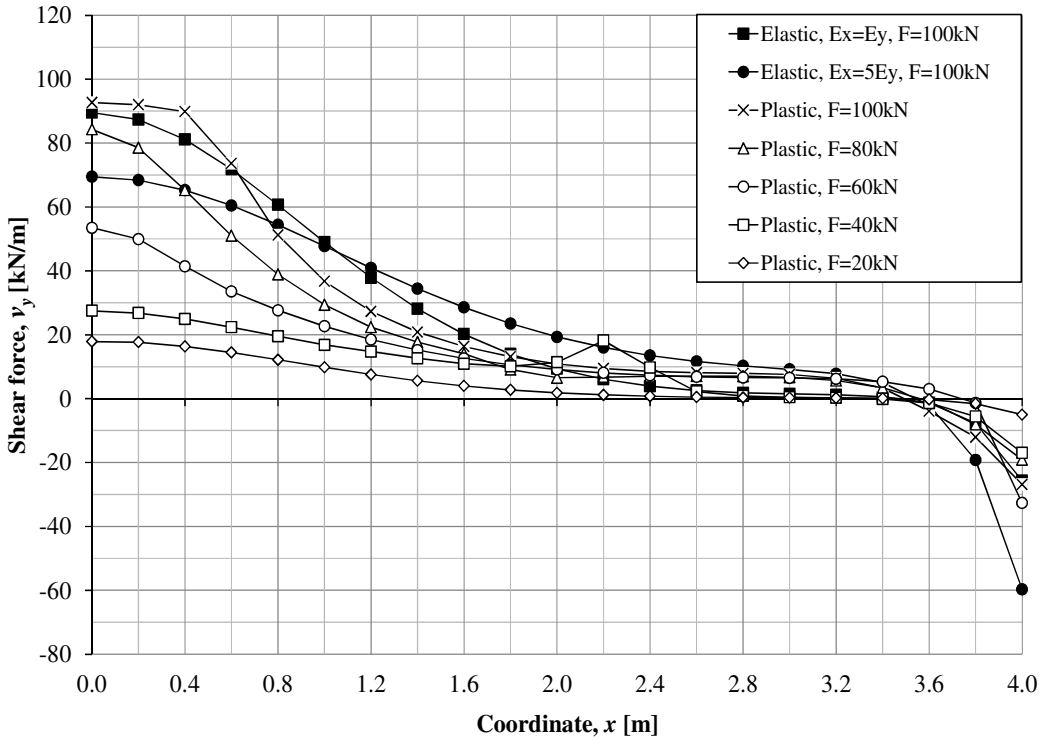

(a)

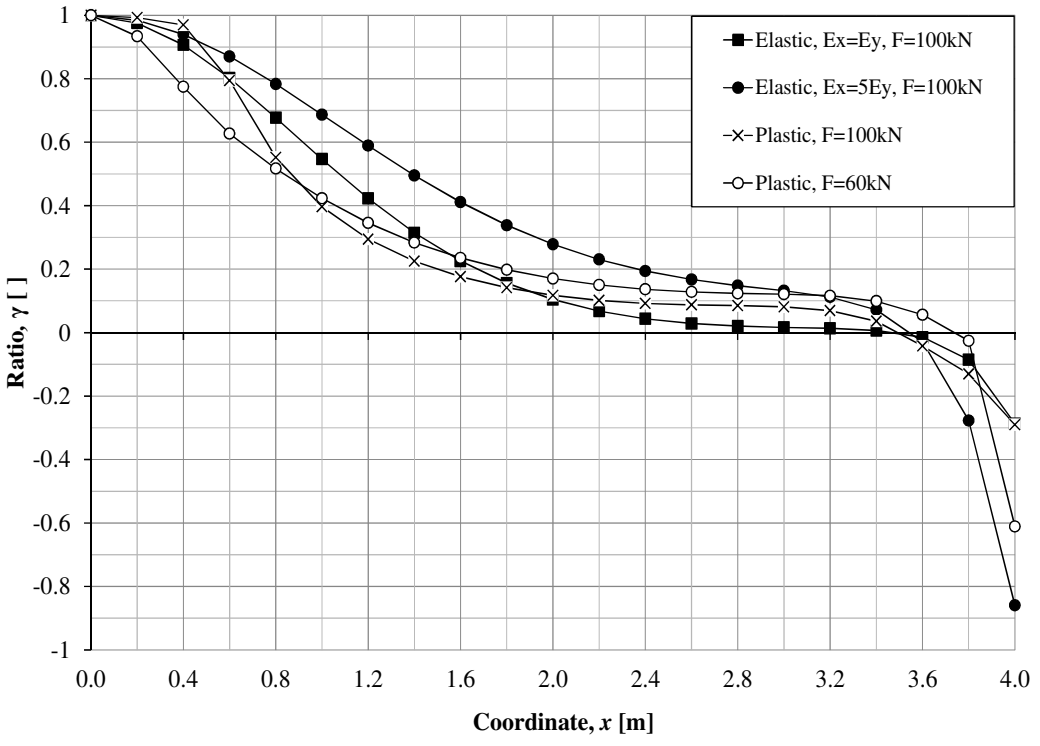

(b)

Figure C.39. Shear force distribution v_y along L_5 at different load level up to 100 kN (a) shear force distribution v_y (b) ratio of maximum shear force $v_{y,max}$ to $v_{y,x}$ moment along L_5, $E_{II} = E_I/10$.

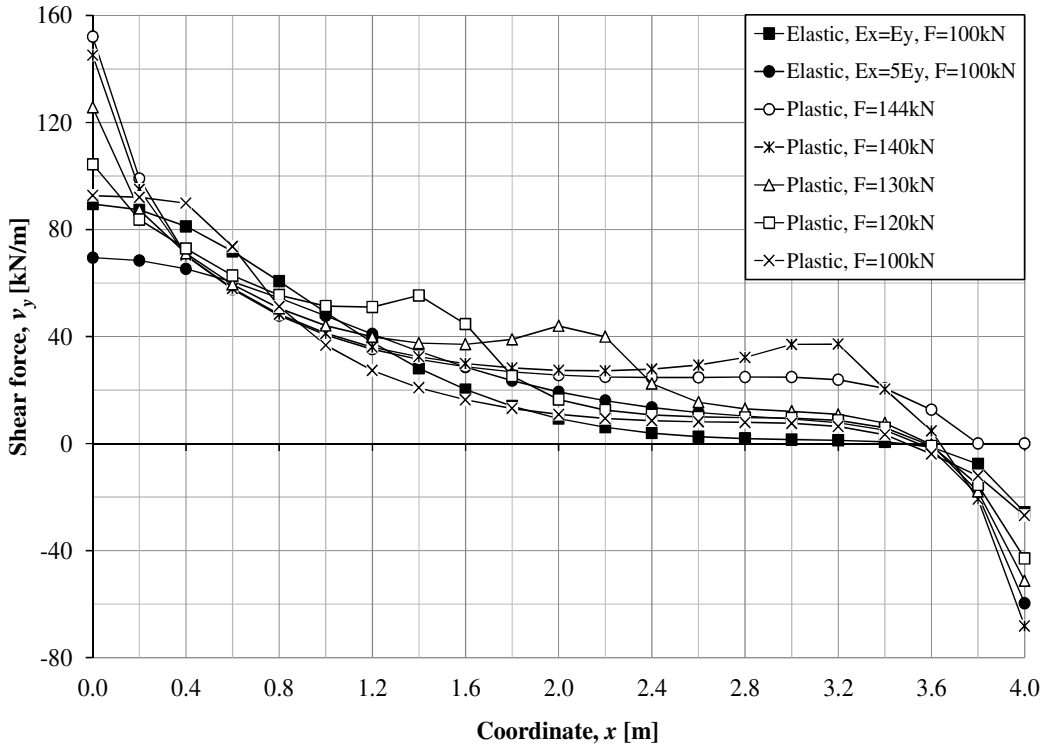

(a)

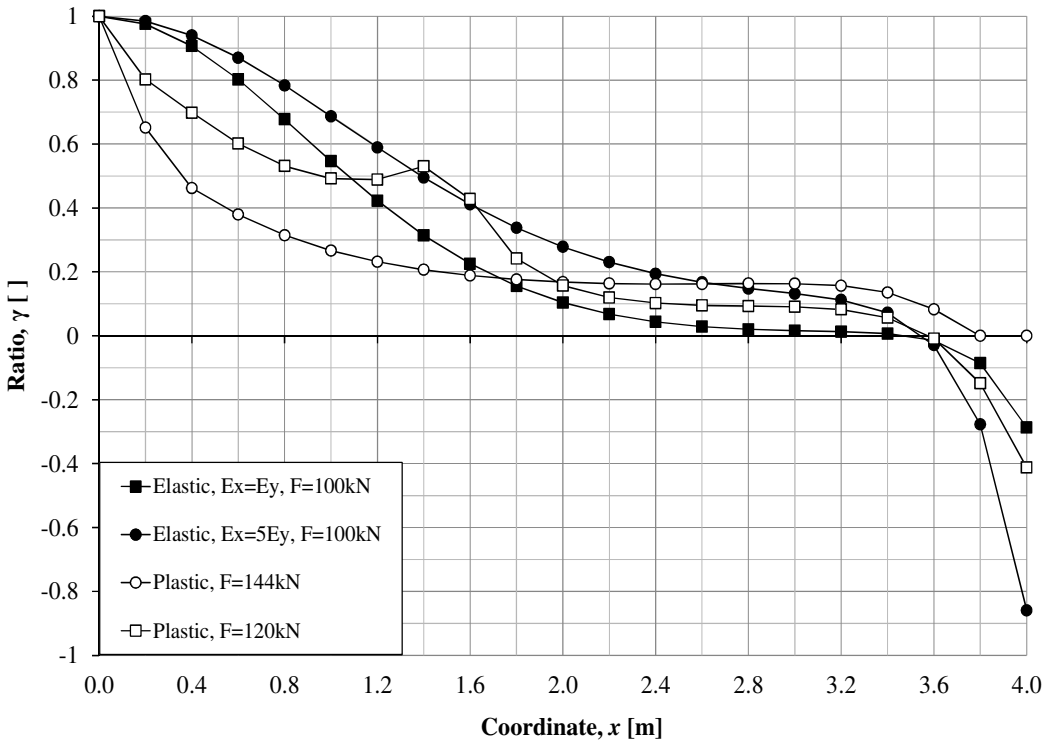

(b)

Figure C.40. Shear force distribution v_y along L_5 at different load level up to 144 kN (a) shear force distribution v_y (b) ratio of maximum shear force $v_{y,max}$ to $v_{y,x}$ moment along L_5, $E_{II} = E_I/10$.

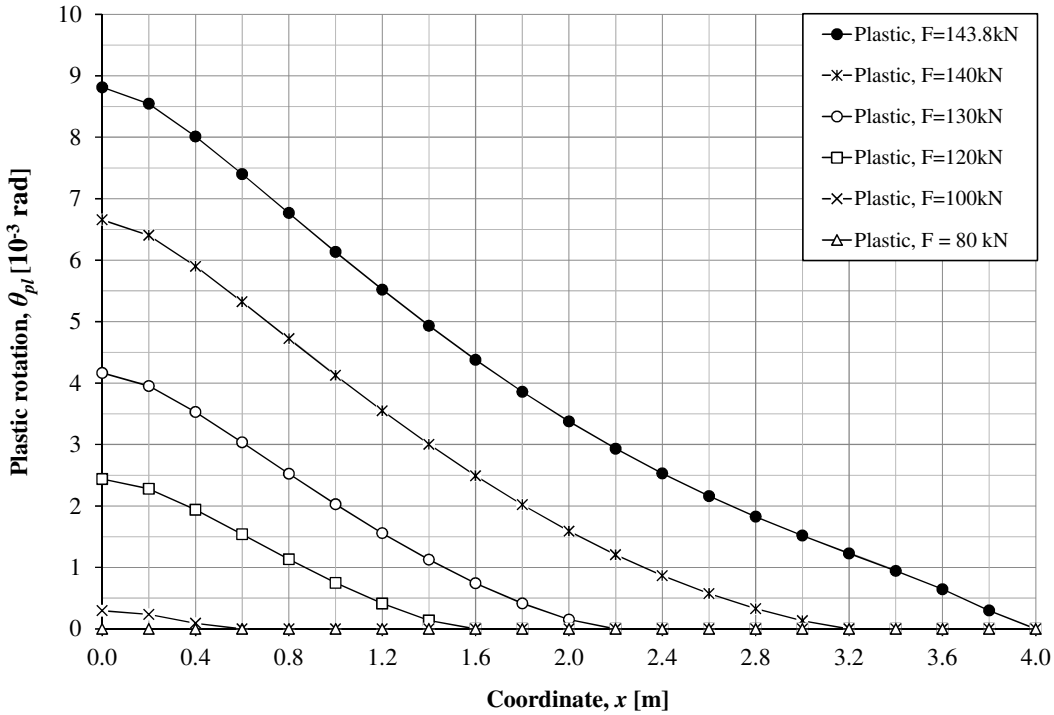

Figure C.41. Plastic rotation distribution θ_{pl} along L_5 at different load level up to 144 kN from FE-elsto-plastic using 0.2 m beam elements with Poisson's ratio $\nu = 0$, $E_{II} = E_I/10$.

C.3.2 Trilinear M(χ) with $M_{pl} = 0.6\ M_{el}$ and $E_{II} = E_I/5 = 6$ GPa

The geometry of the slab is shown in Figure 4.32 and moment curvature relationship input is given in Figure 4.44. The analysis is performed using 0.2 m beam elements with $v = 0$.

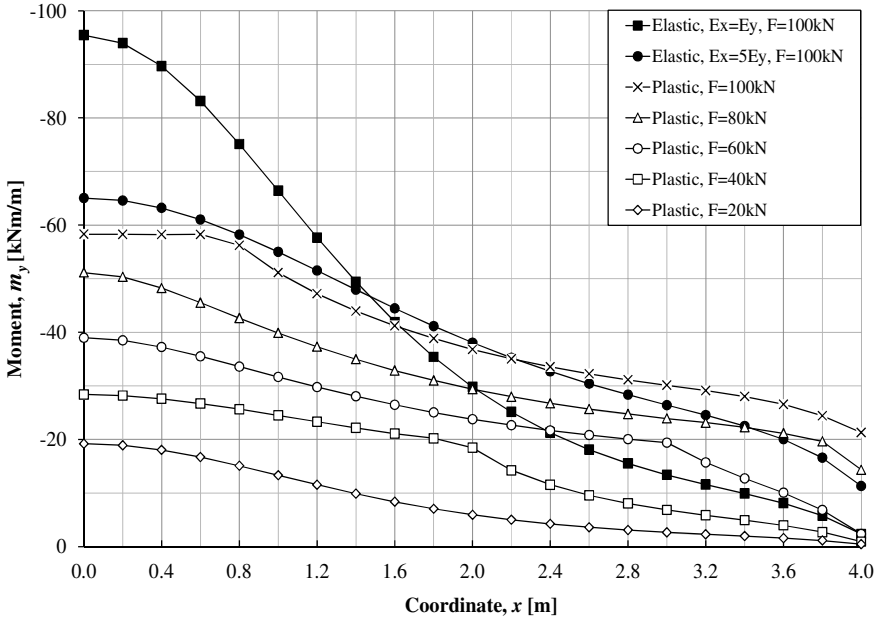

(a)

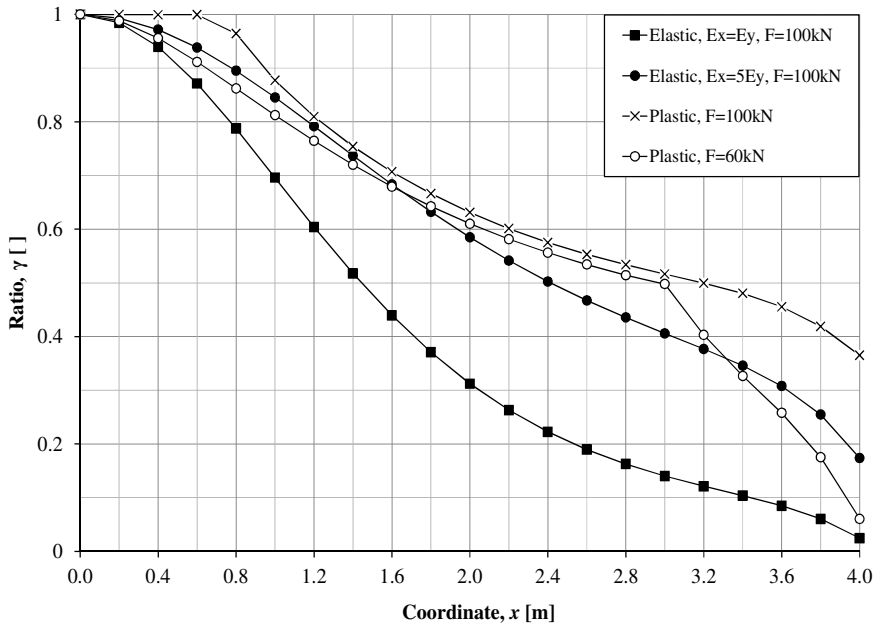

(b)

Figure C.42. Moment distribution m_y along L_5 at different load level up to 100 kN (a) moment distribution m_y (b) ratio of maximum moment $m_{y,max}$ to $m_{y,x}$ moment along L_5, $E_{II} = E_I/5$.

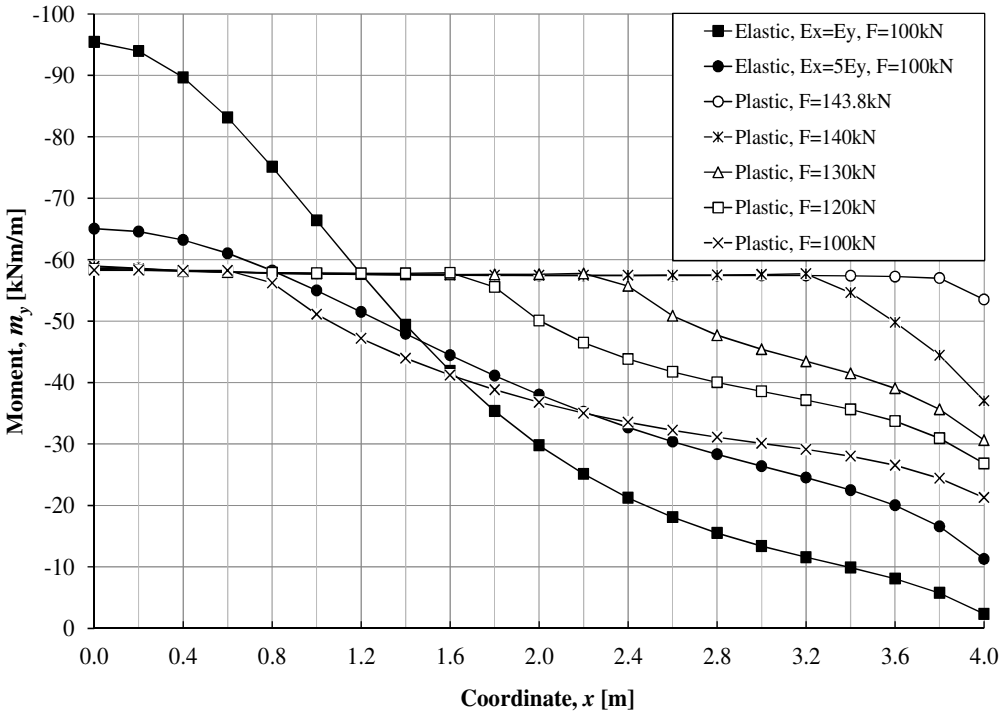

(a)

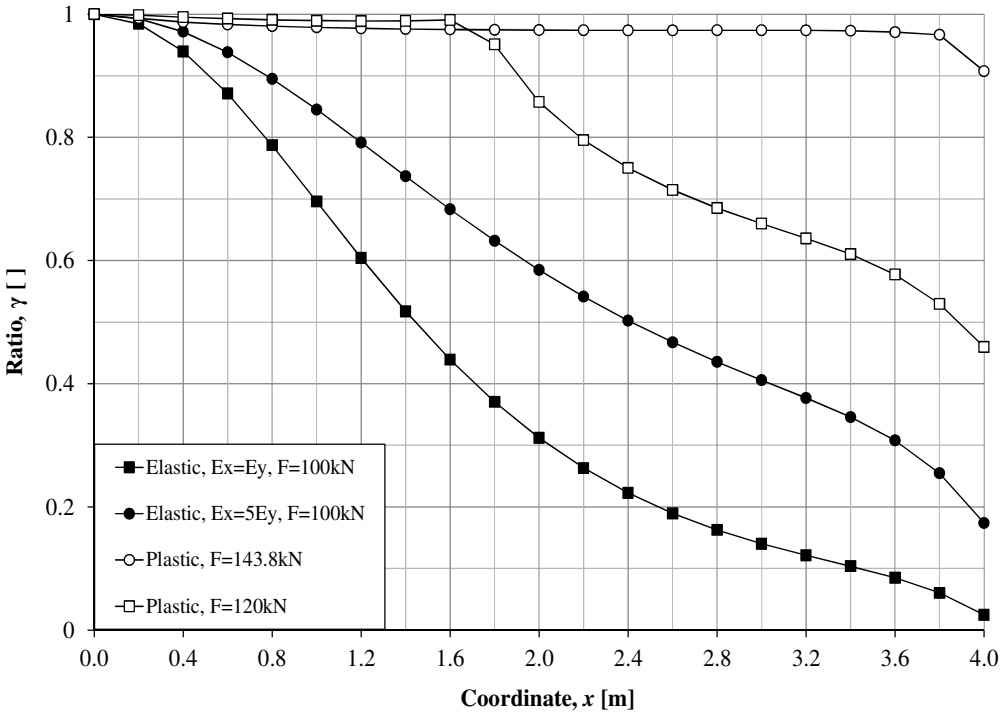

(b)

Figure C.43. Moment distribution m_y along L_5 at different load level up to 143.8 kN (a) moment distribution m_y (b) ratio of maximum moment $m_{y,max}$ to $m_{y,x}$ moment along L_5, $E_{II} = E_I/5$.

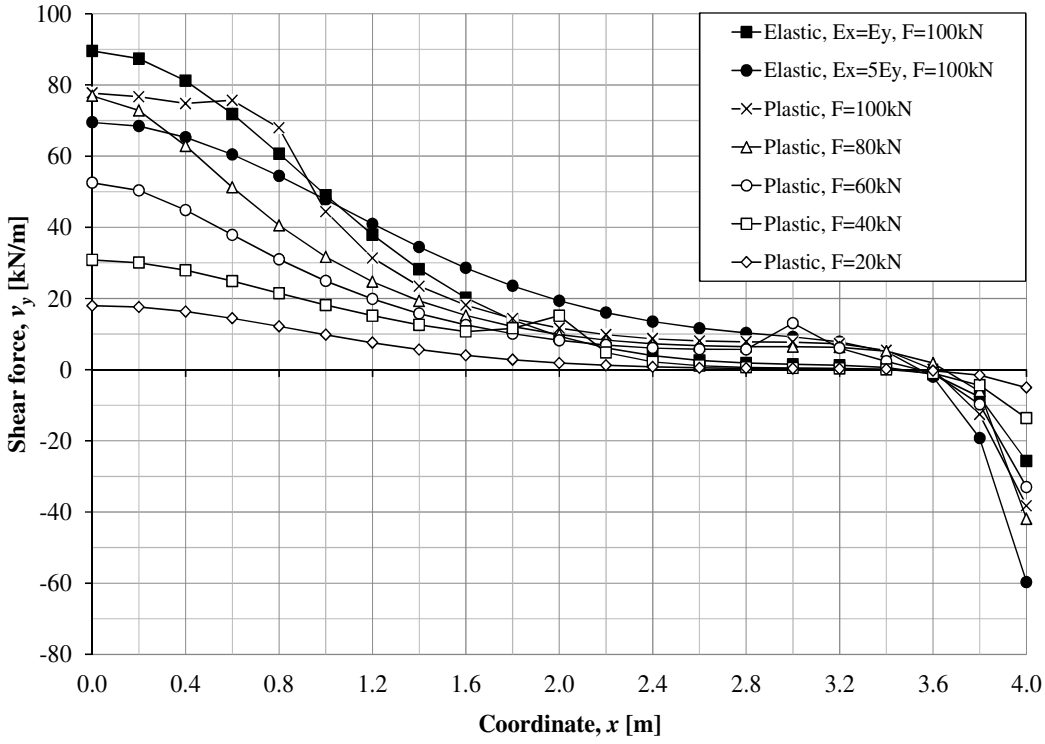

(a)

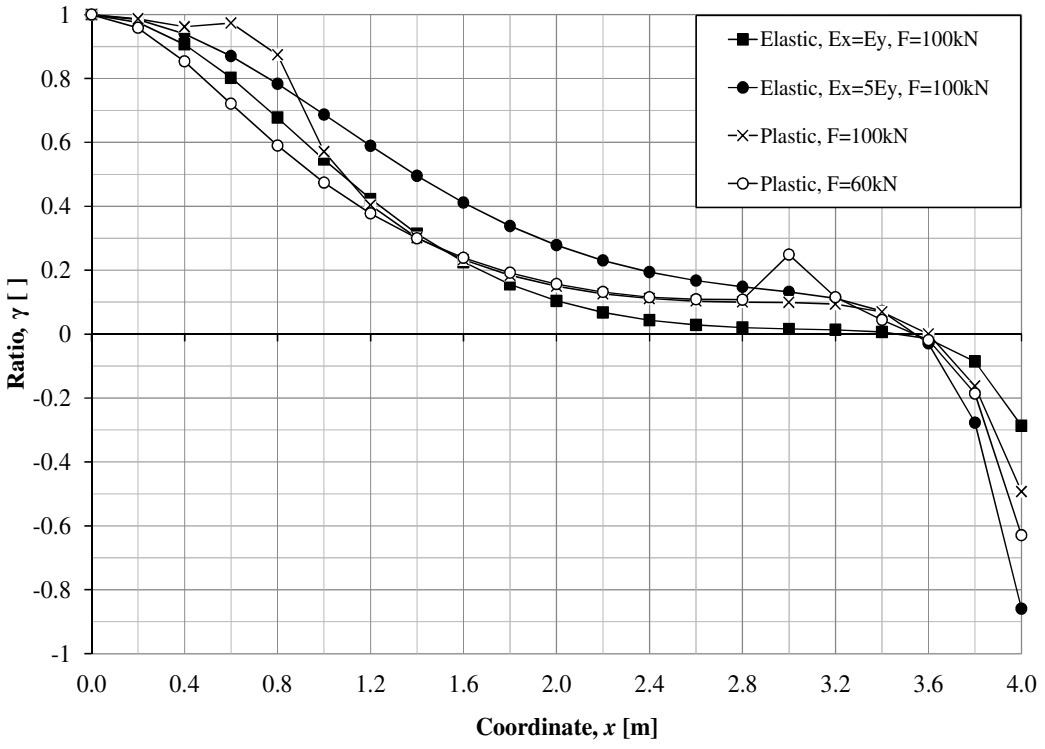

(b)

Figure C.44. Shear force distribution v_y along L_5 at different load level up to 100 kN (a) shear force distribution v_y (b) ratio of maximum shear force $v_{y,max}$ to $v_{y,x}$ moment along L_5, $E_{II} = E_I/5$.

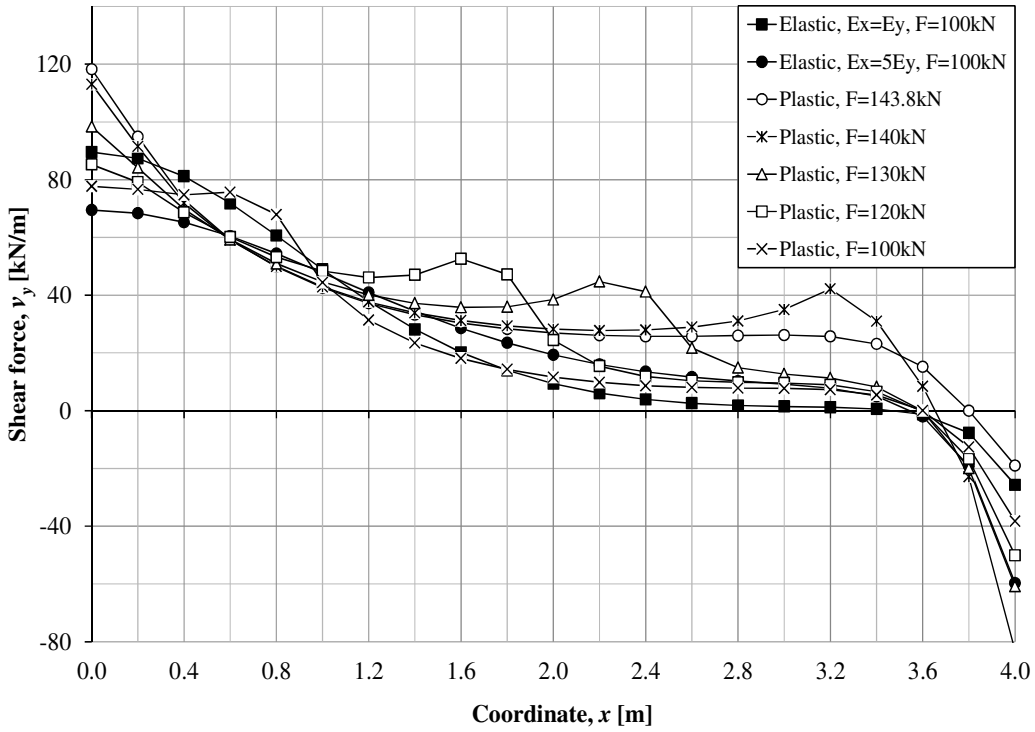

(a)

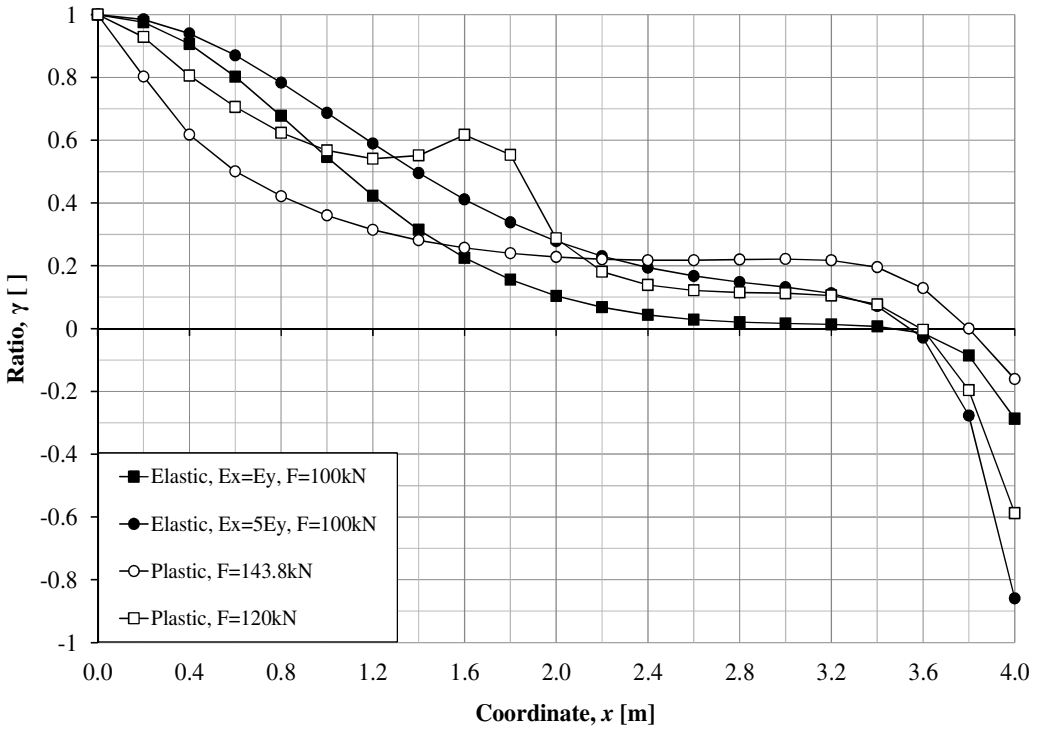

(b)

Figure C.45. Shear force distribution v_y along L_5 at different load level up to 143.8 kN (a) shear force distribution v_y (b) ratio of maximum shear force $v_{y,max}$ to $v_{y,x}$ moment along L_5, $E_{II} = E_I/5$.

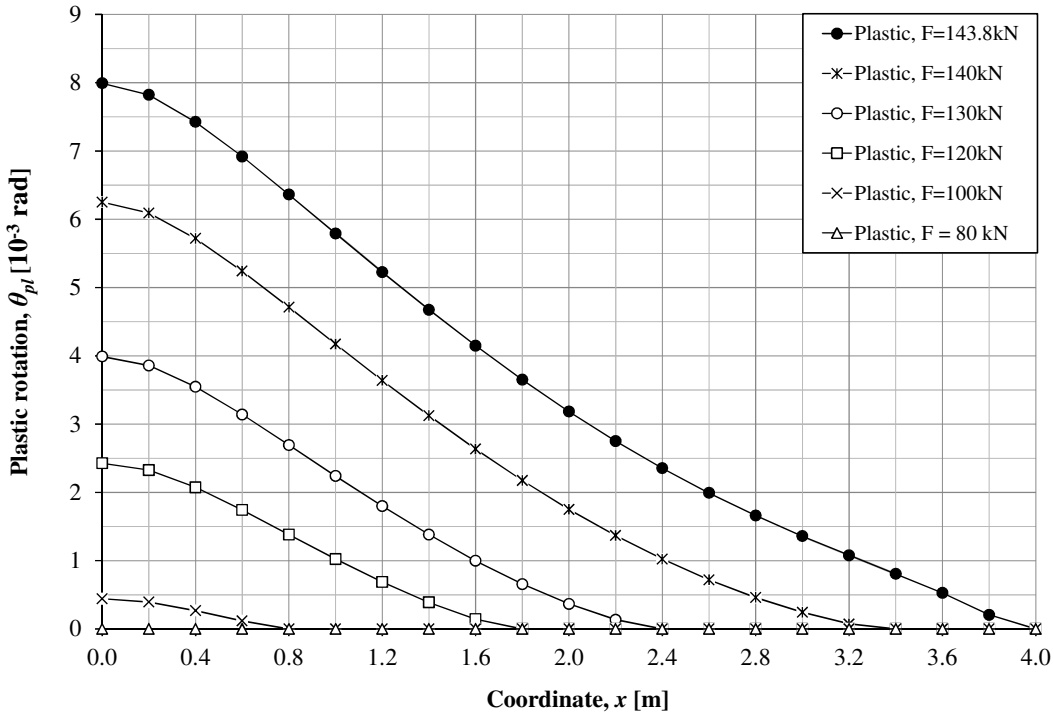

Figure C.46. Plastic rotation distribution θ_{pl} along L_5 at different load level up to 143.8 kN from FE-elsto-plastic using 0.2 m beam elements with Poisson's ratio $\nu = 0$, $E_{II} = E_I/5$.

C.3.3 Quadlinear M(χ) with M_{pl} = 0.4 M_{el} and E_{II} = E_I/5 = 6 GPa

The geometry of the slab is shown in Figure 4.32 and moment curvature relationship input is given in Figure 4.48. The analysis is performed using 0.2 m beam elements with $\nu = 0$.

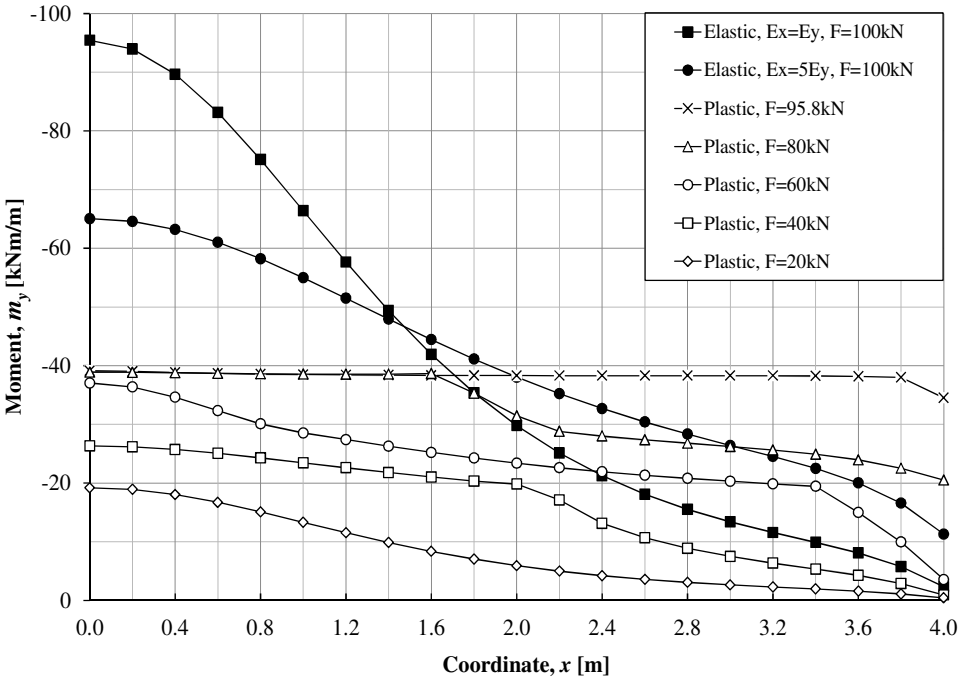

(a)

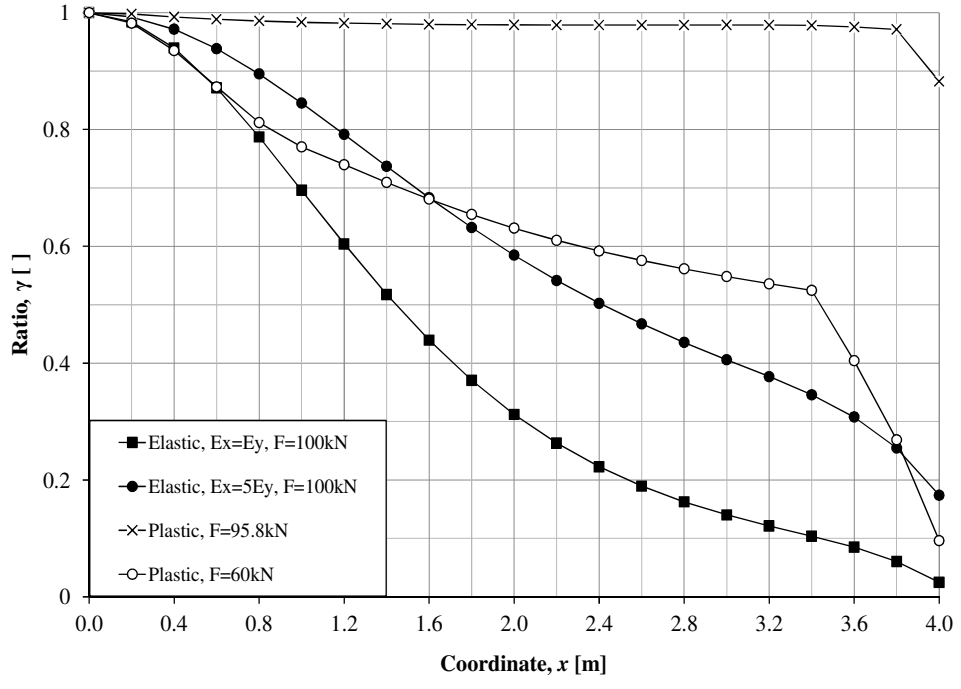

(b)

Figure C.47. Moment distribution m_y along L_5 at different load level up to 95.8 kN (a) moment distribution m_y (b) ratio of maximum moment $m_{y,max}$ to $m_{y,x}$ moment along L_5, M_{pl} = 0.4 M_{el}, E_{II} = E_I/5.

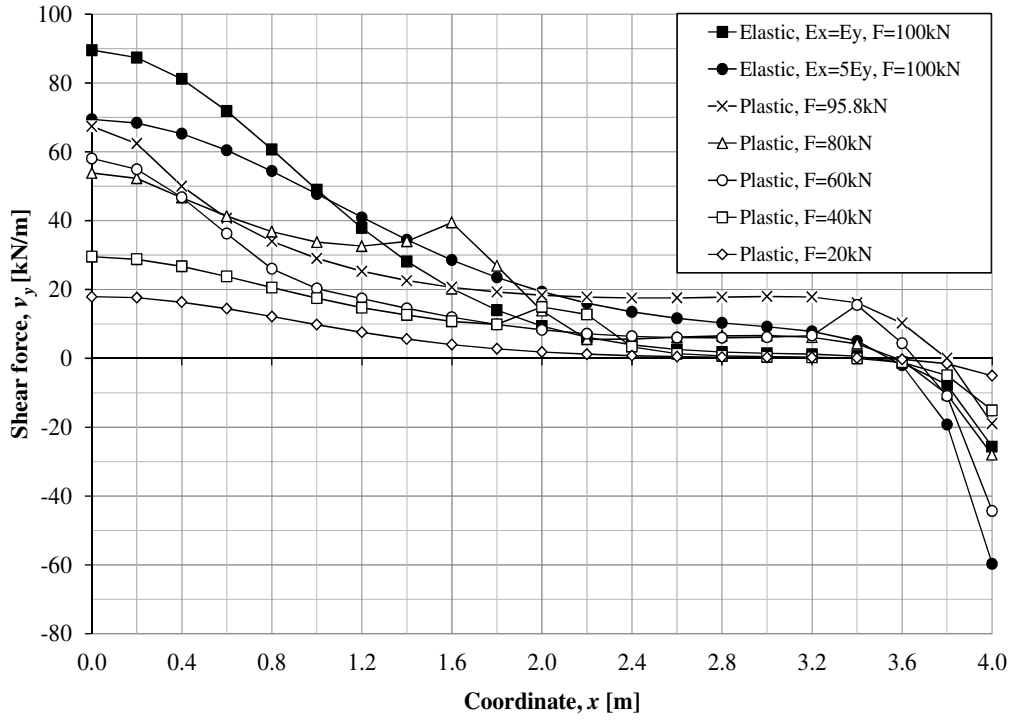

(a)

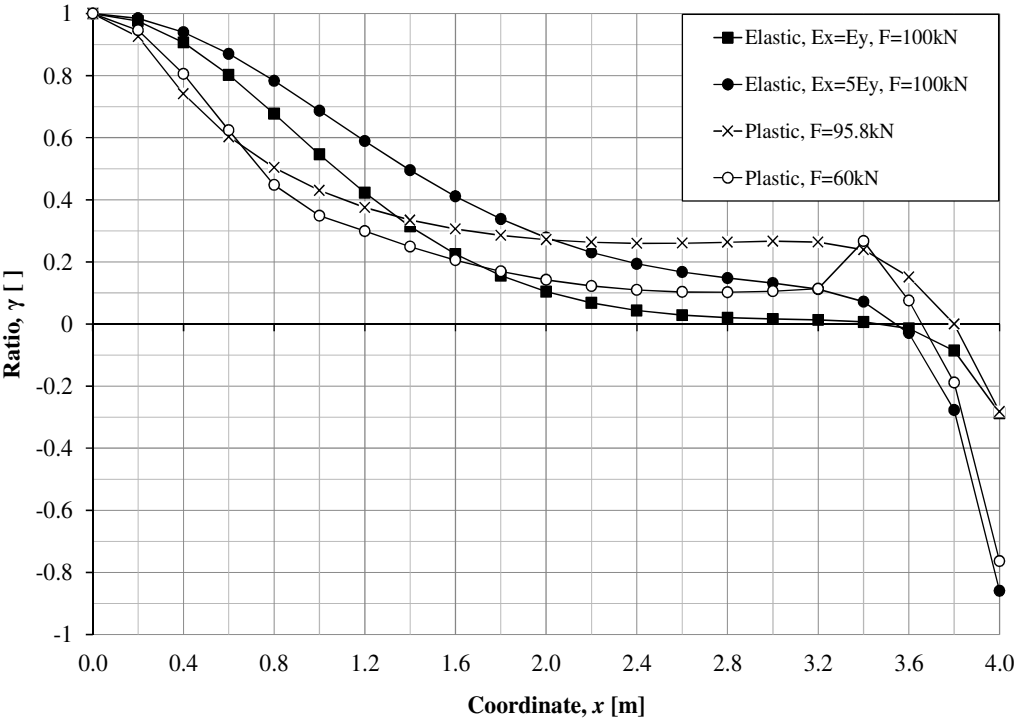

(b)

Figure C.48. Shear force distribution v_y along L_5 at different load level up to 95.8 kN (a) shear force distribution v_y (b) ratio of maximum shear force $v_{y,max}$ to $v_{y,x}$ moment along L_5, $M_{pl} = 0.4\ M_{el}$, $E_{II} = E_I/5$.

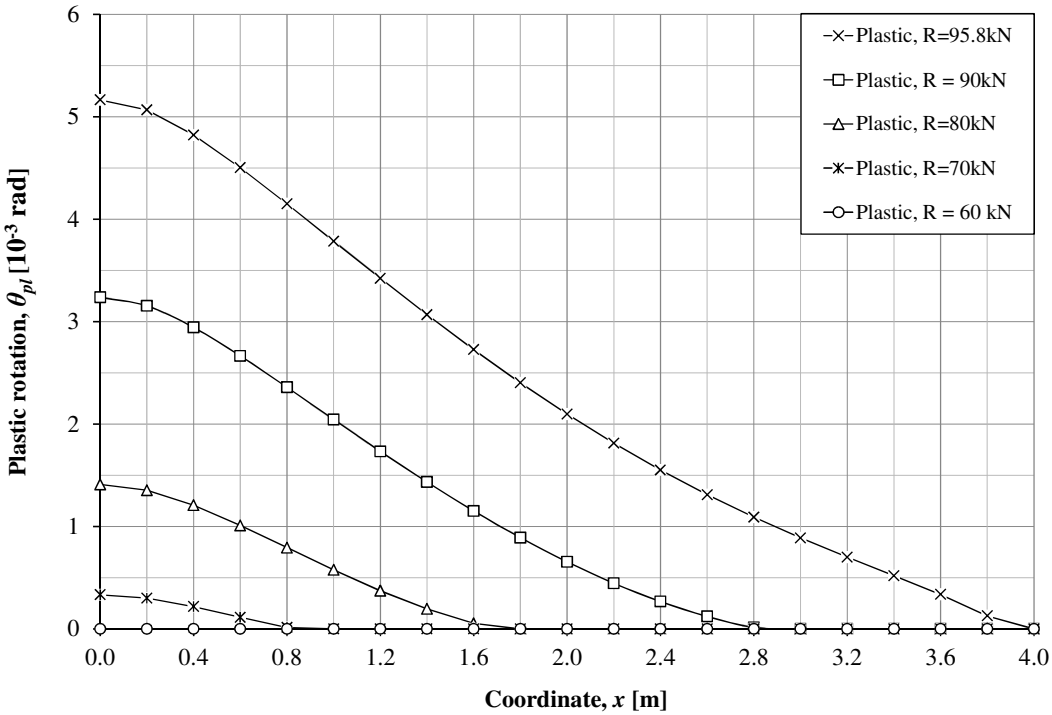

Figure C.49. Plastic rotation distribution θ_{pl} along L_5 at different load level up to 95.8 kN from FE-elsto-plastic using 0.2 m beam elements with Poisson's ratio $\nu = 0$, $M_{pl} = 0.4\ M_{el}$, $E_{II} = E_I/5$.

C.3.4 Trilinear M(χ) without yielding

C.3.4.1 $E_{II} = E_I/5 = 6$ GPa

The geometry of the slab is shown in Figure 4.32 and moment curvature relationship input is given in Figure 4.53. The analysis is performed using 0.2 m beam elements with $v = 0$.

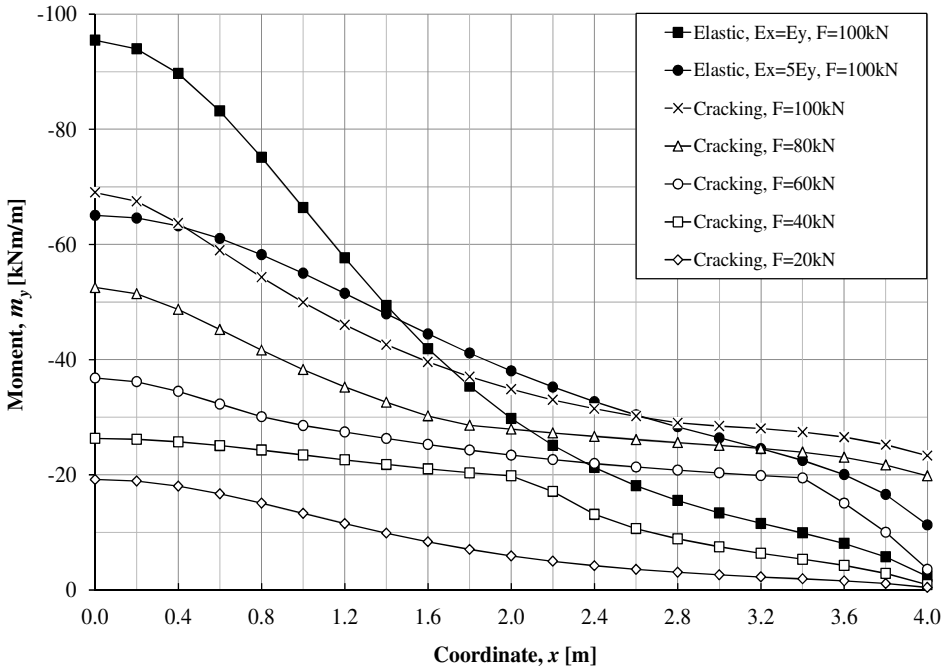

(a)

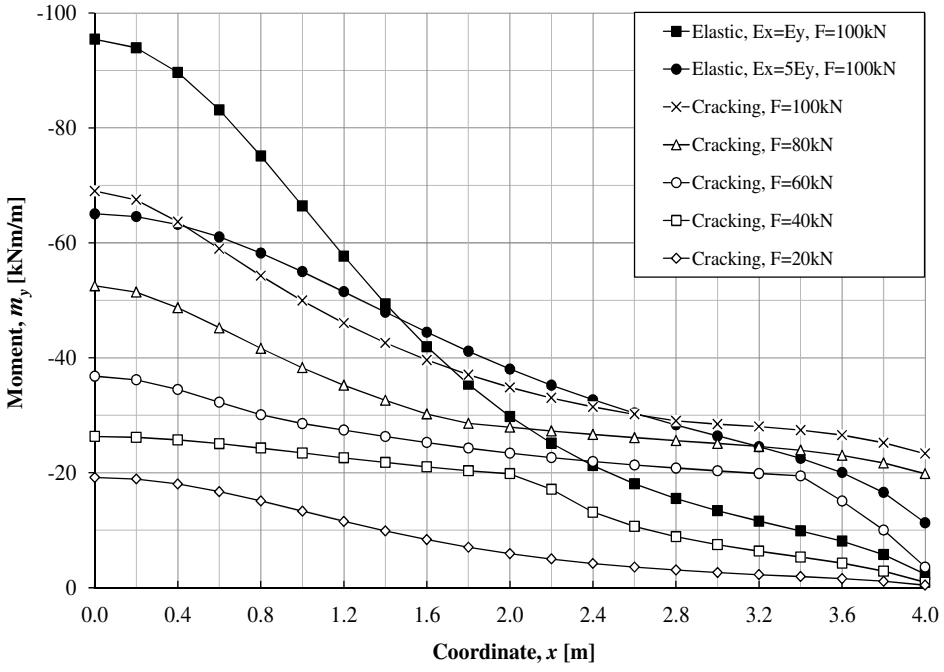

(b)

Figure C.50. Moment distribution m_y along L_5 at different load level up to 100 kN (a) moment distribution m_y (b) ratio of maximum moment $m_{y,max}$ to $m_{y,x}$ moment along L_5, $E_{II} = E_I/5$.

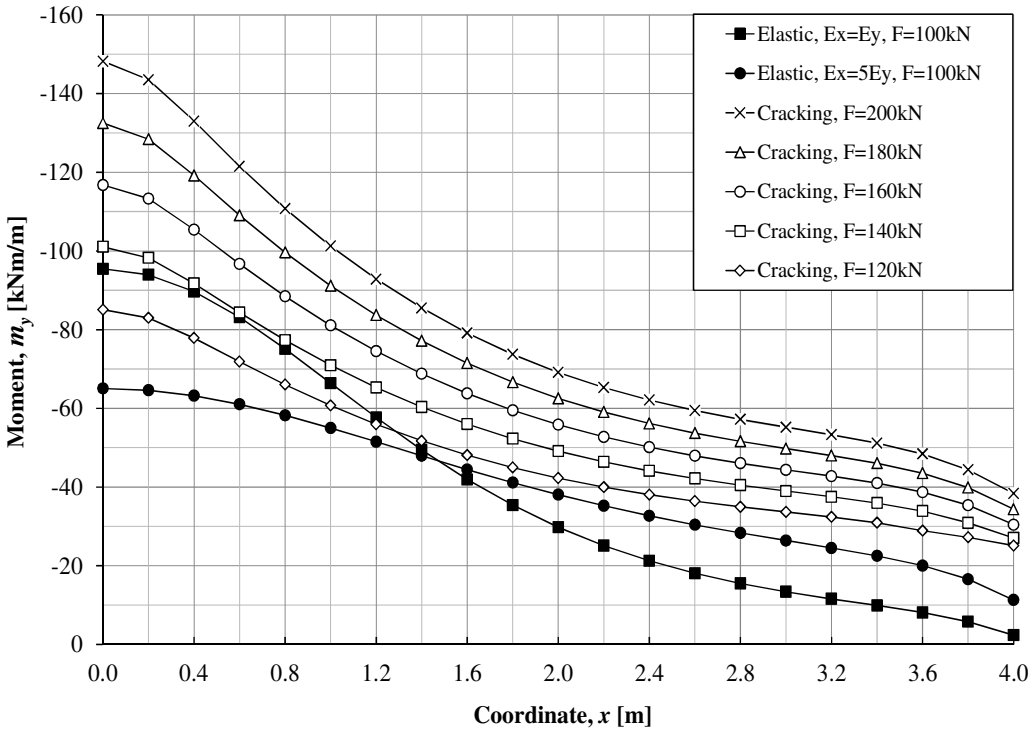

(a)

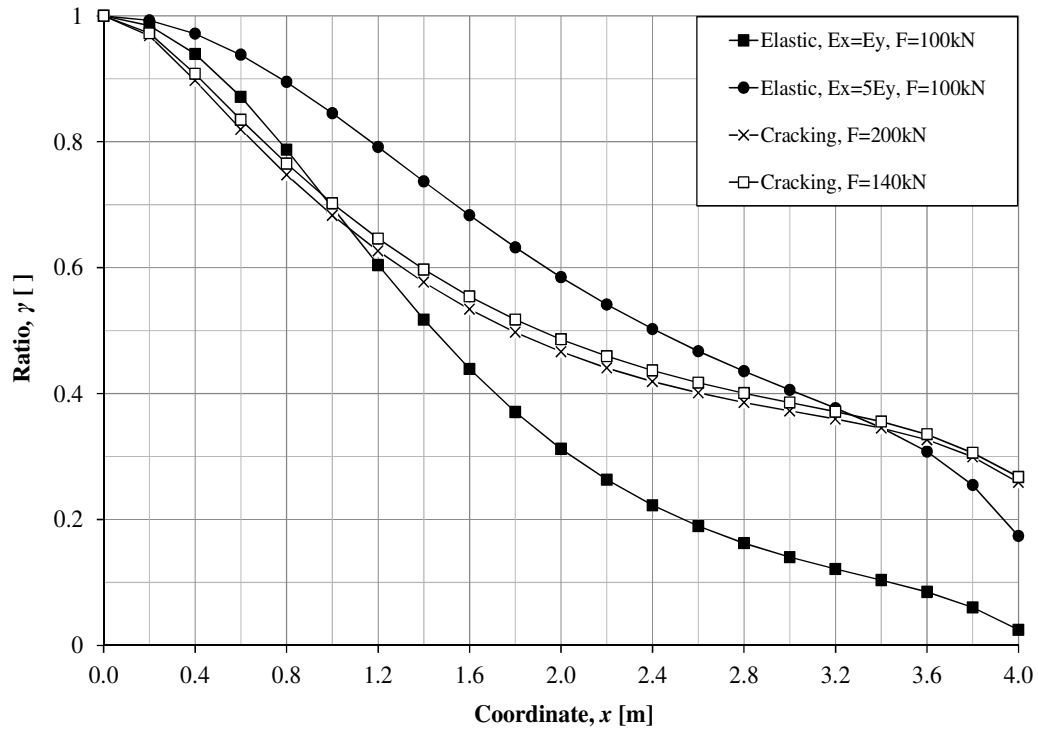

(b)

Figure C.51. Moment distribution m_y along L_5 at different load level up to 200 kN (a) moment distribution m_y (b) ratio of maximum moment $m_{y,max}$ to $m_{y,x}$ moment along L_5, $E_{II} = E_I/5$.

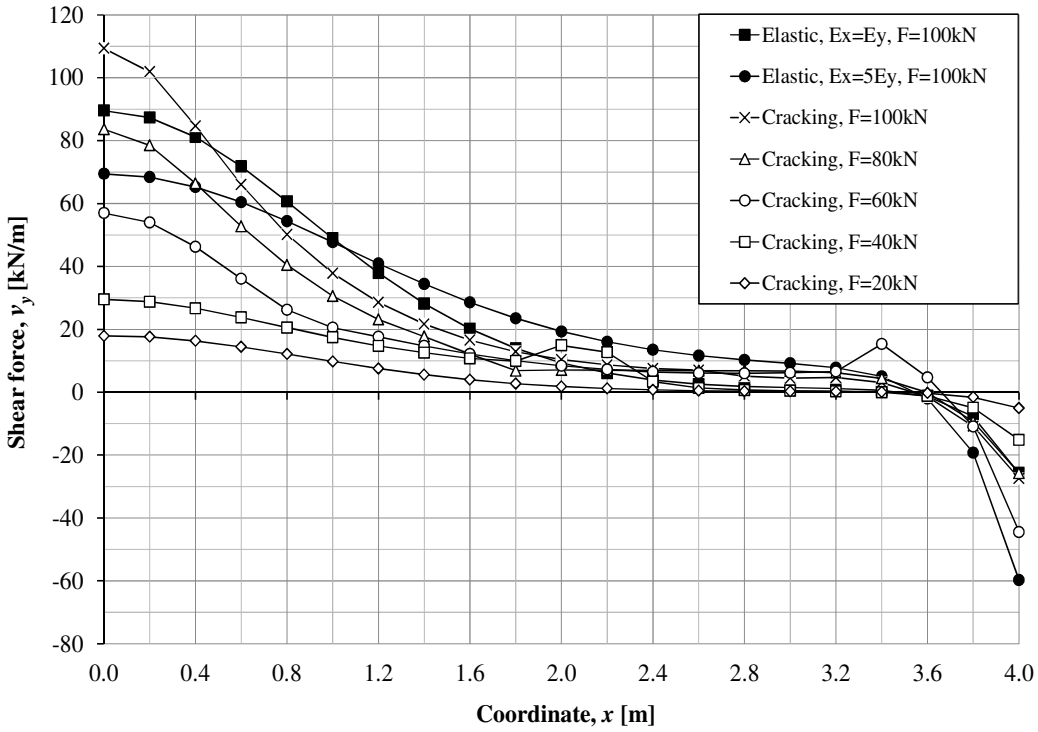

(a)

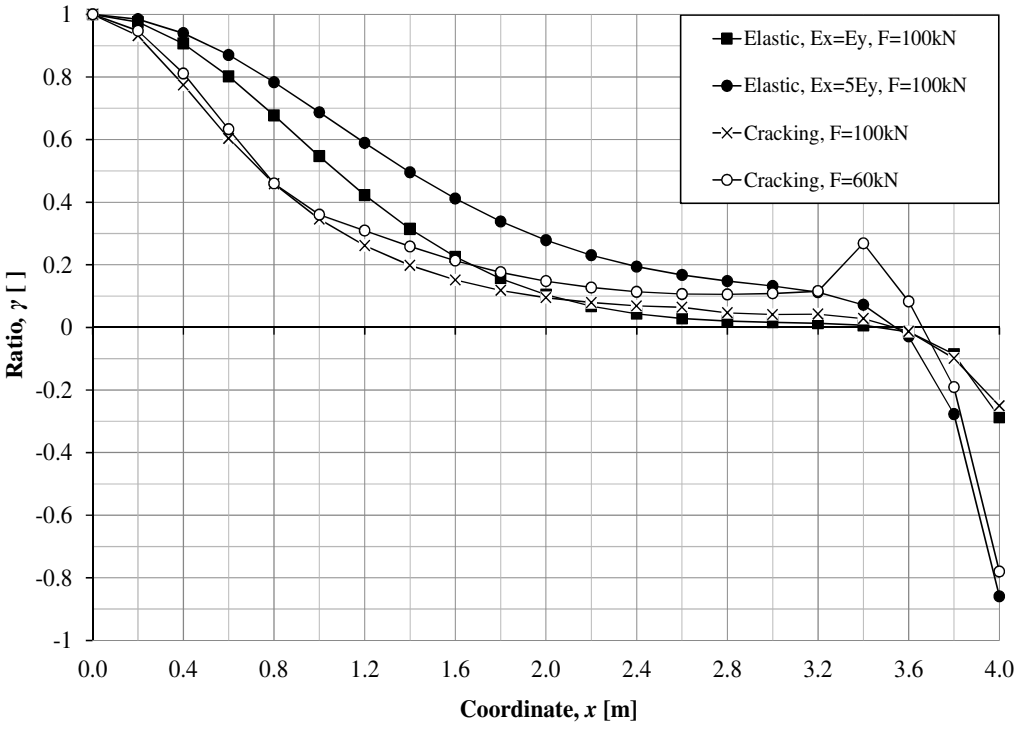

(b)

Figure C.52. Shear force distribution v_y along L_5 at different load level up to 100 kN (a) shear force distribution v_y (b) ratio of maximum shear force $v_{y,max}$ to $v_{y,x}$ moment along L_5, $E_{II} = E_I/5$.

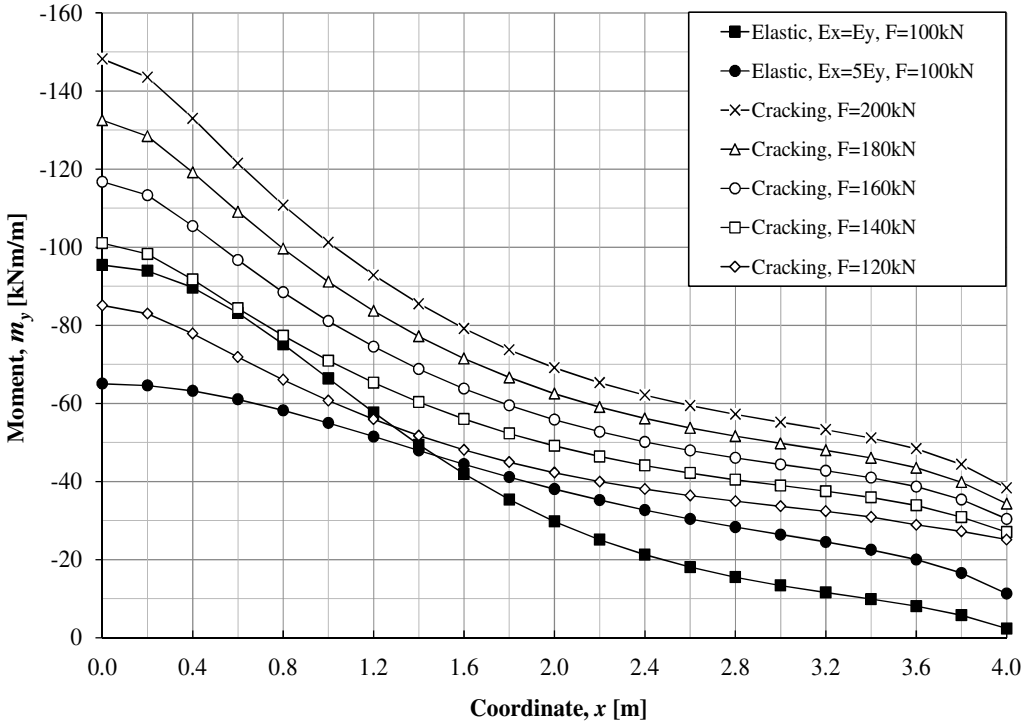

(a)

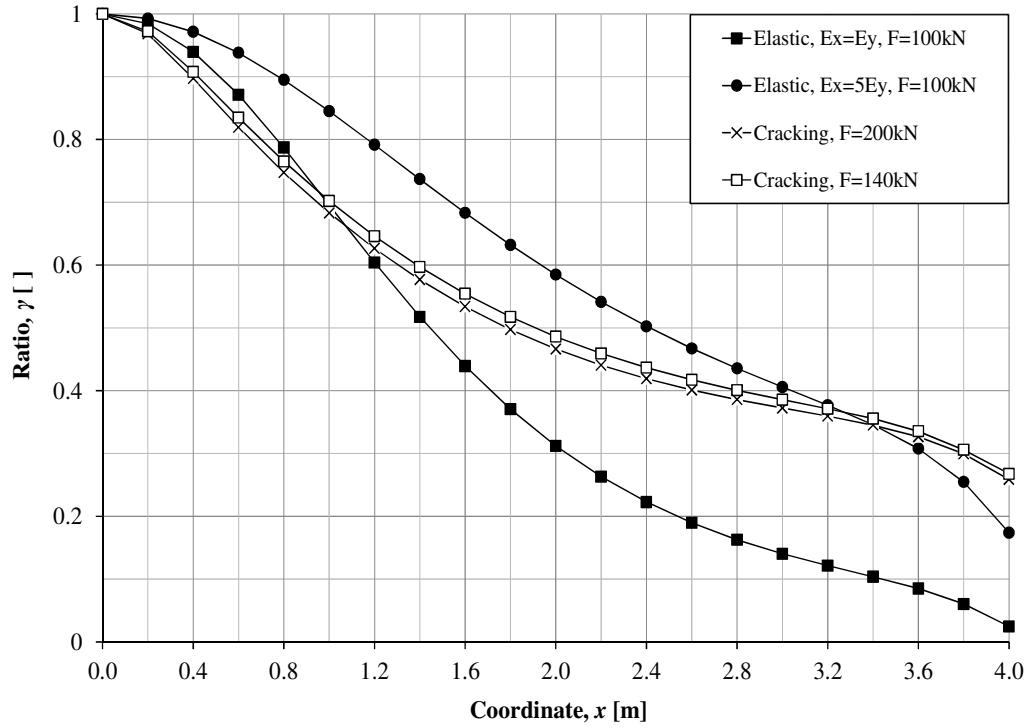

(b)

Figure C.53. Shear force distribution v_y along L_5 at different load level up to 200 kN (a) shear force distribution v_y (b) ratio of maximum shear force $v_{y,max}$ to $v_{y,x}$ moment along L_5, $E_{II} = E_I/5$.

C.3.4.2 $E_{II} = E_I/2 = 15$ GPa

The geometry of the slab is shown in Figure 4.32 and moment curvature relationship input is given in Figure C.54. The analysis is performed using 0.2 m beam elements with $v = 0$.

$M_{cr1} = 19$ kNm/m, $M_{cr2} = 28.5$ kNm/m, $M_{pl} = 5$ kNm/m in Section 4.5.7 were kept constant and the corresponding curvature were determined based on the principle in Section 4.5.3.1.

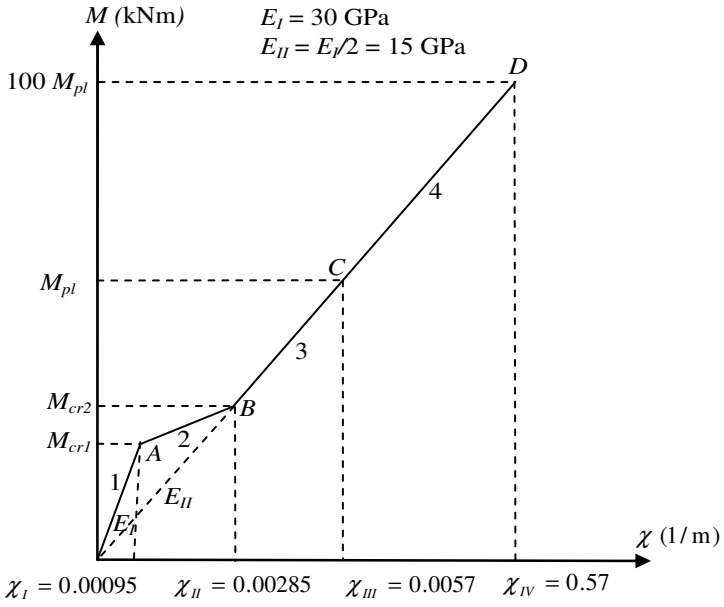

Figure C.54. Trilinear moment-curvature without yielding relationship for the analysis of the studied cantilever slab, $E_{II} = E_I/2$.

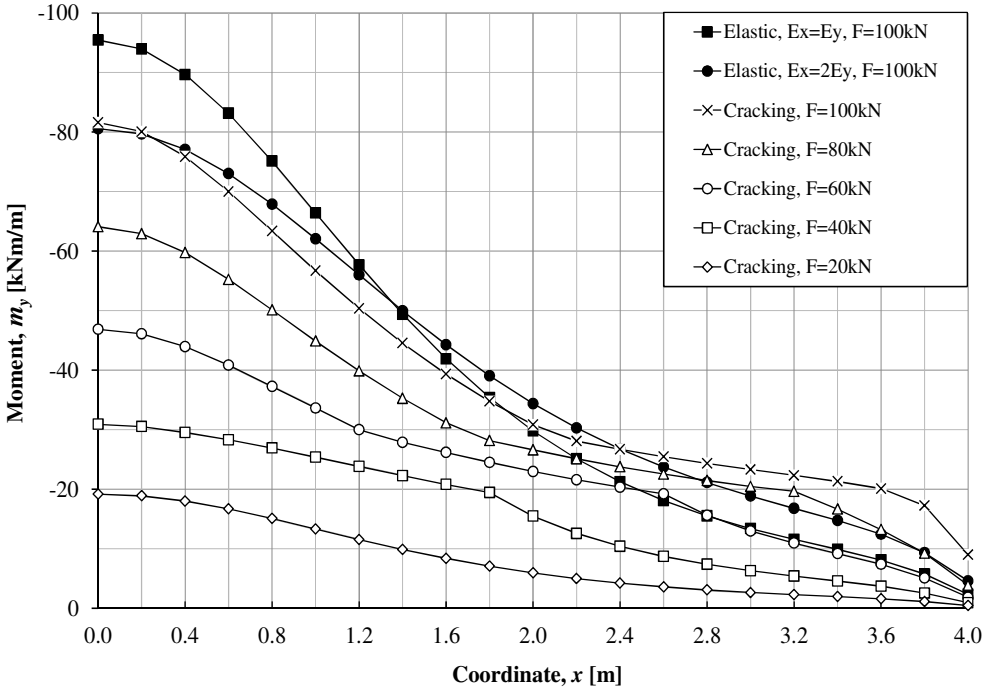

(a)

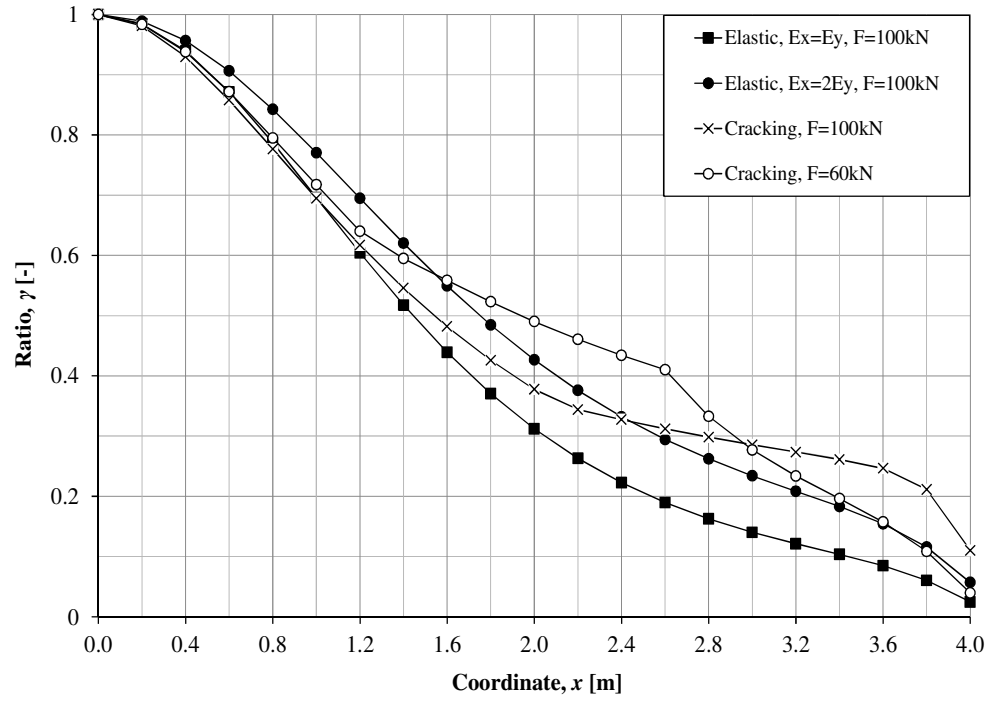

(b)

Figure C.55. Moment distribution m_y along L_5 at different load level up to 100 kN (a) moment distribution m_y (b) ratio of maximum moment $m_{y,max}$ to $m_{y,x}$ moment along L_5, $E_{II} = E_I/2$.

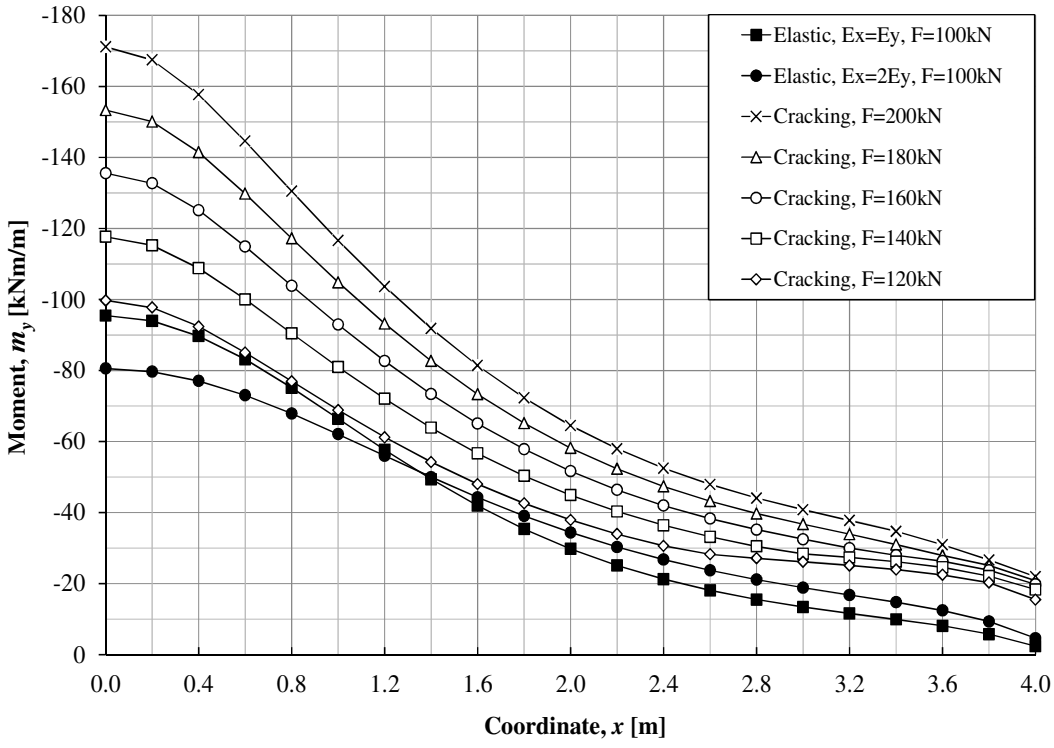

(a)

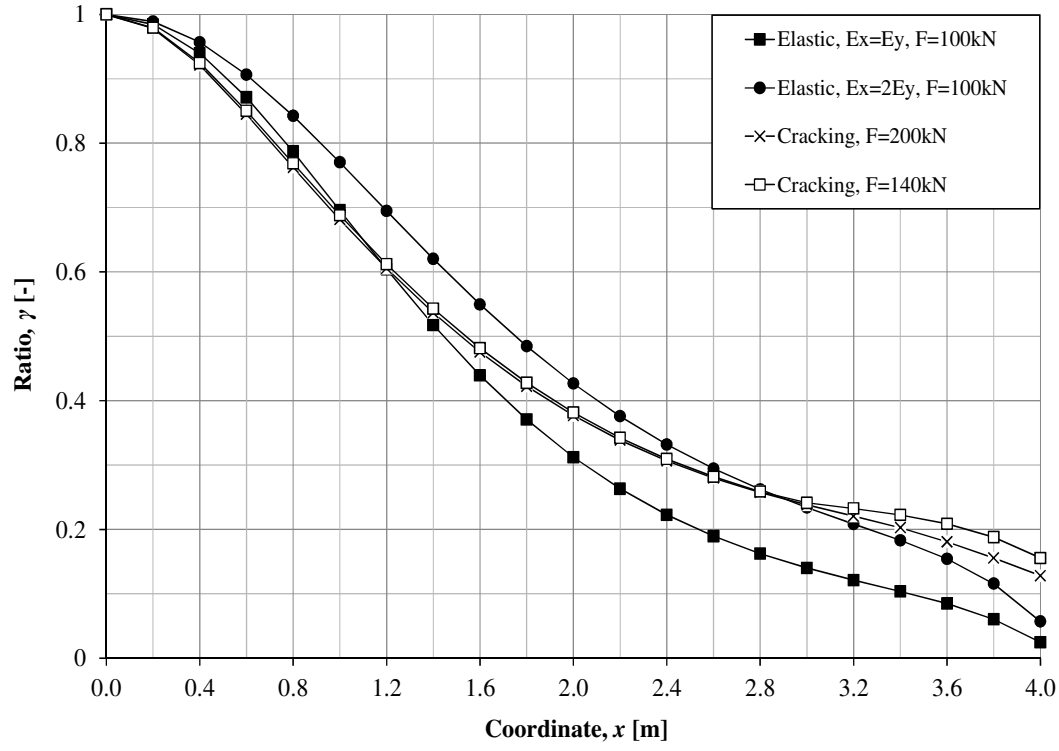

(b)

Figure C.56. Moment distribution m_y along L_5 at different load level up to 200 kN (a) moment distribution m_y (b) ratio of maximum moment $m_{y,max}$ to $m_{y,x}$ moment along L_5, $E_{II} = E_I/2$.

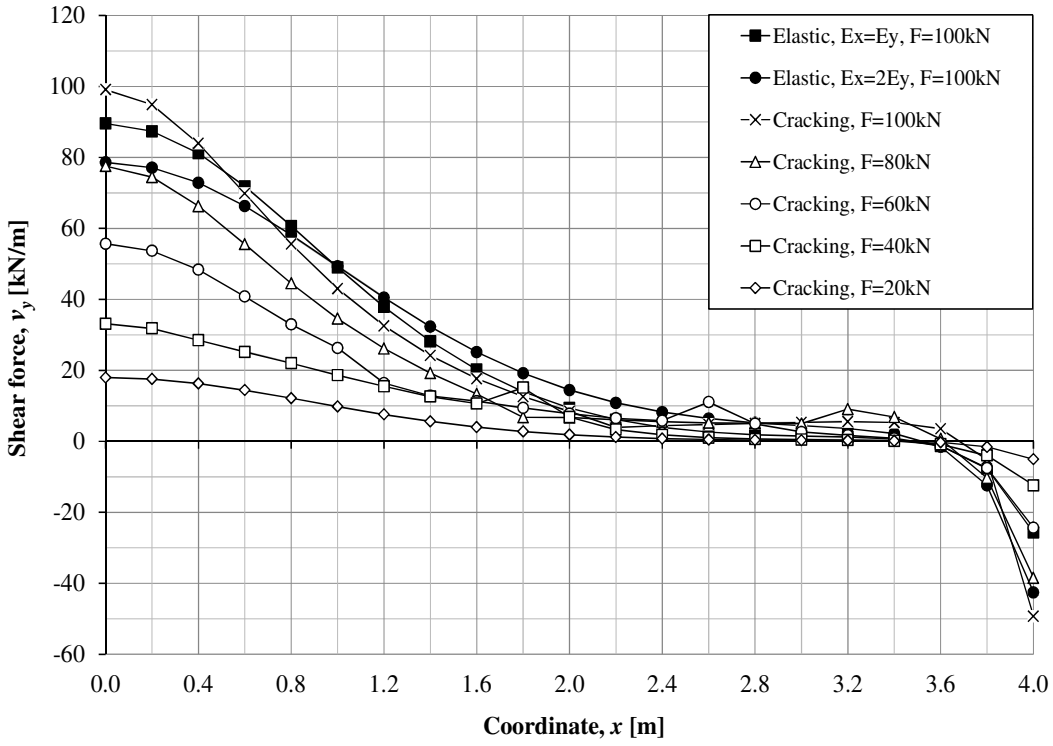

(a)

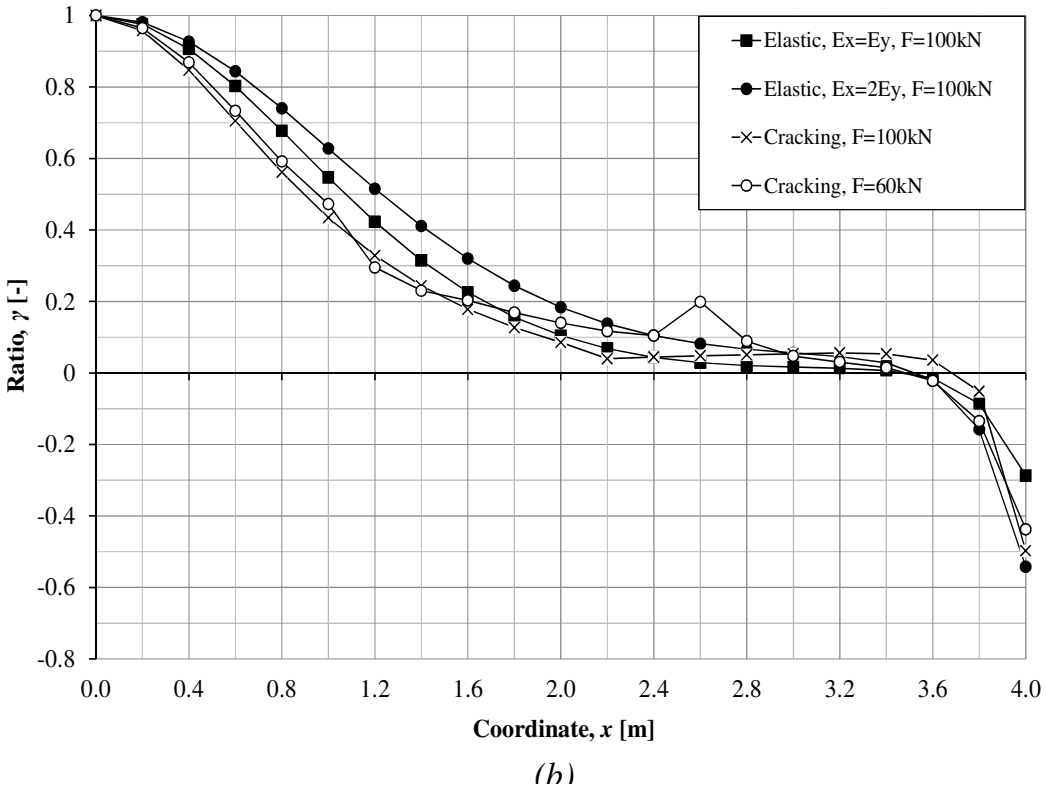

(b)

Figure C.57. Shear force distribution v_y along L_5 at different load level up to 100 kN (a) shear force distribution v_y (b) ratio of maximum shear force $v_{y,max}$ to $v_{y,x}$ moment along L_5, $E_{II} = E_I/2$.

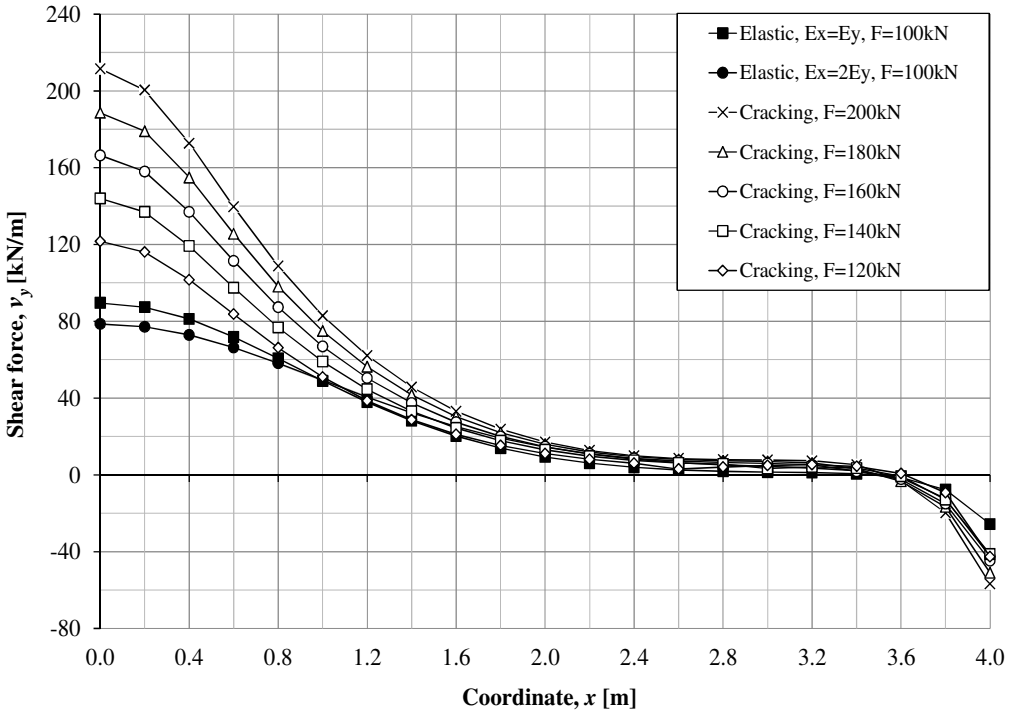

(a)

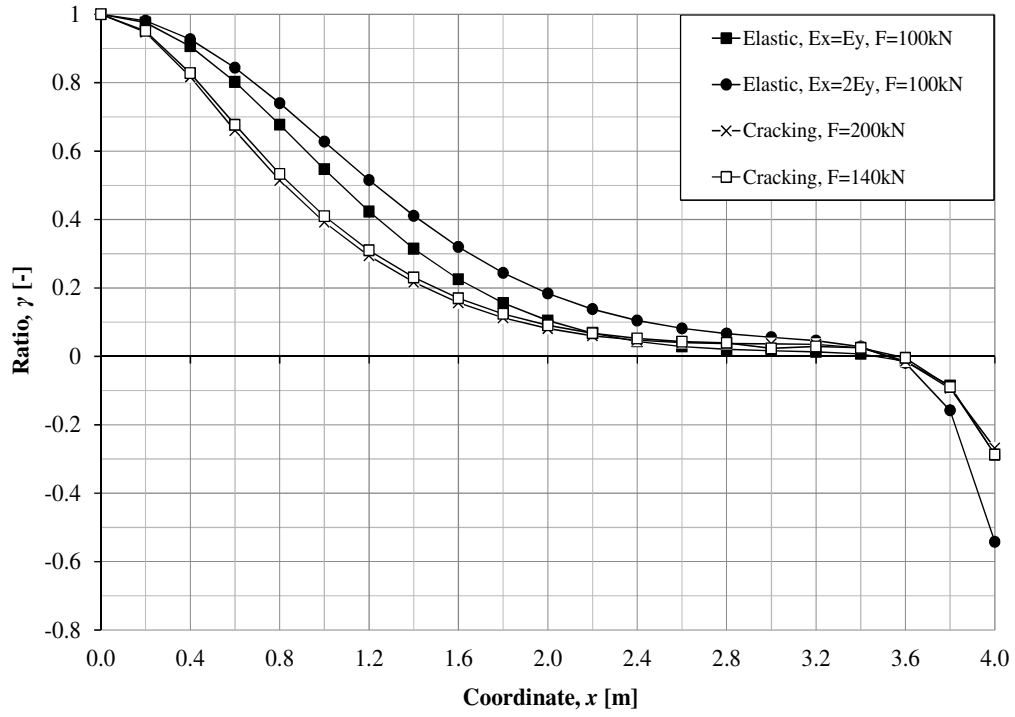

(b)

Figure C.58. Shear force distribution v_y along L_5 at different load level up to 200 kN (a) shear force distribution v_y (b) ratio of maximum shear force $v_{y,max}$ to $v_{y,x}$ moment along L_5, $E_{II} = E_I/2$.

C.3.4.3 $E_{II} = E_I/10 = 3$ GPa

The geometry of the slab is shown in Figure 4.32 and moment curvature relationship input is given in Figure C.59. The analysis is performed using 0.2 m beam elements with $v = 0$.

$M_{cr1} = 19$ kNm/m, $M_{cr2} = 28.5$ kNm/m, $M_{pl} = 5$ kNm/m in Section 4.5.7 were kept constant and the corresponding curvature were determined based on the principle in Section 4.5.3.1.

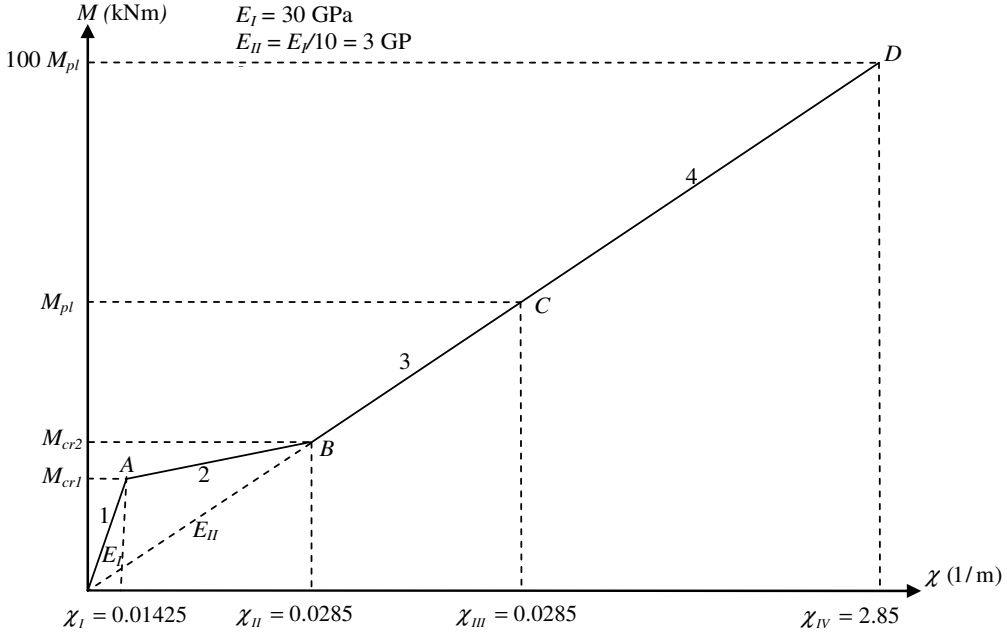

Figure C.59. Trilinear moment-curvature without yielding relationship for the analysis of the studied cantilever slab, $E_{II} = E_I/10$.

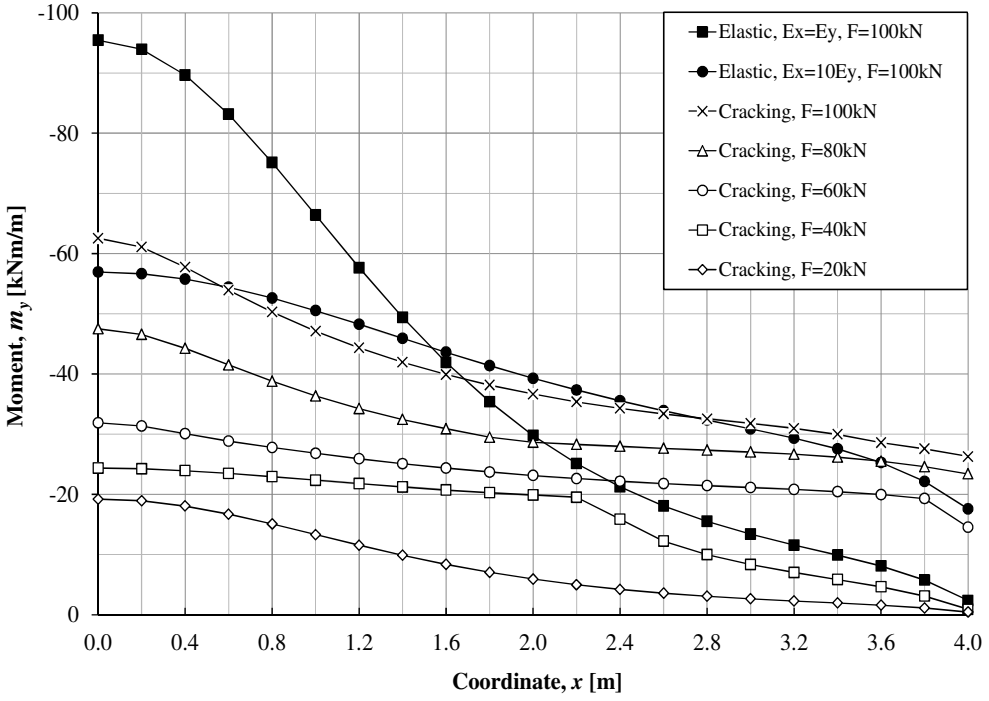

(a)

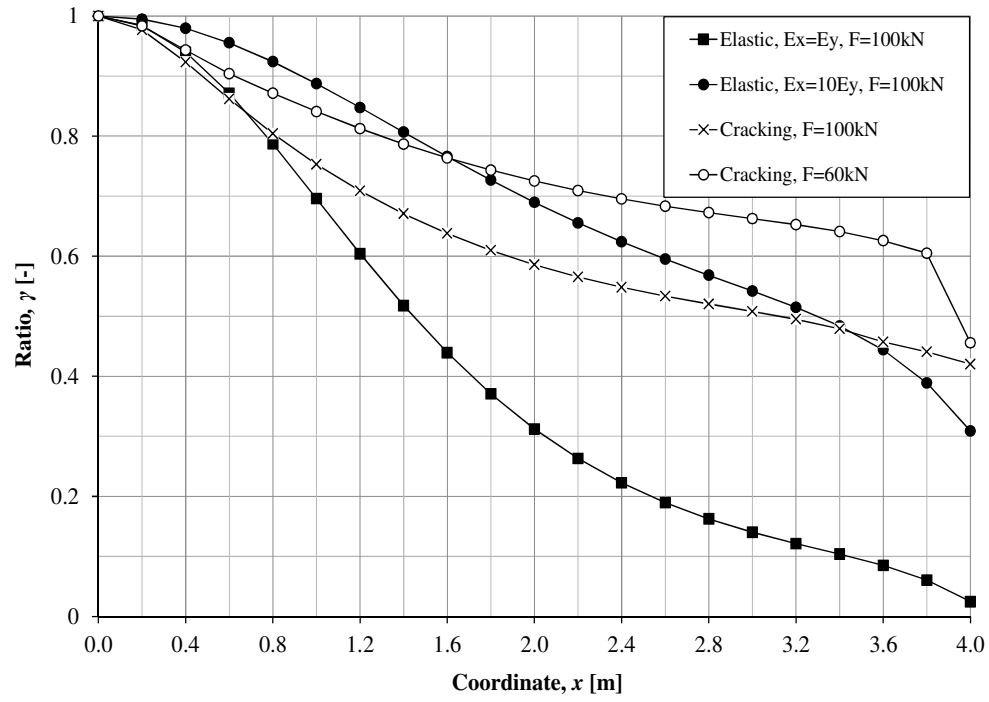

(b)

Figure C.60. Moment distribution m_y along L_5 at different load level up to 100 kN (a) moment distribution m_y (b) ratio of maximum moment $m_{y,max}$ to $m_{y,x}$ moment along L_5, $E_{II} = E_I/10$.

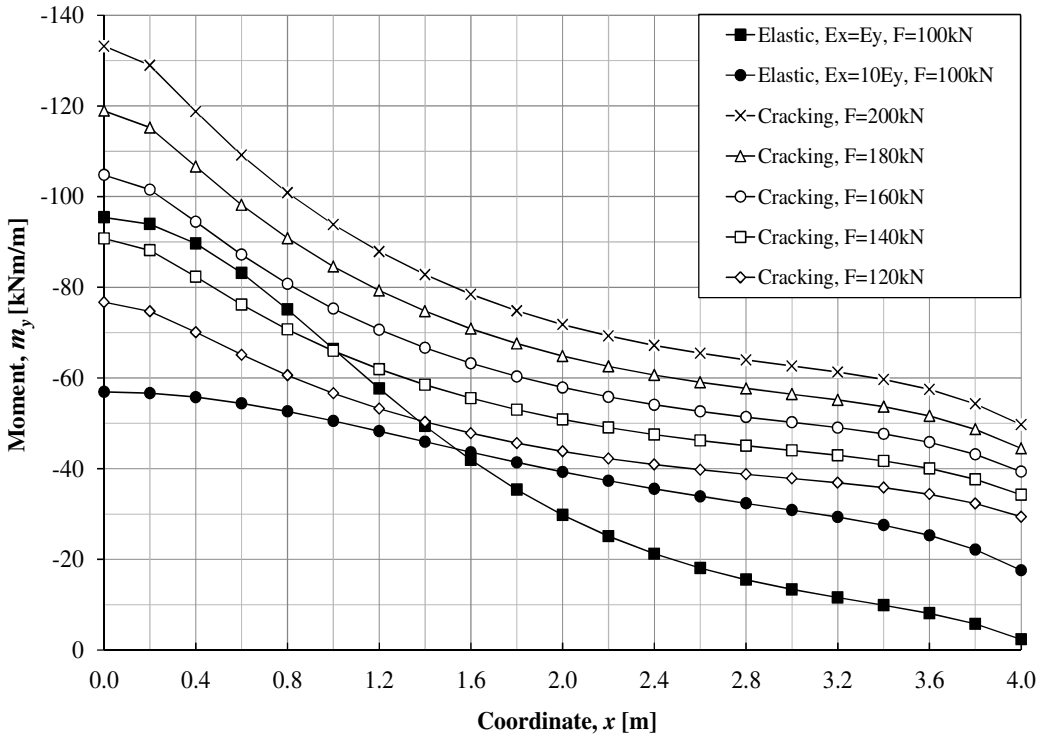

(a)

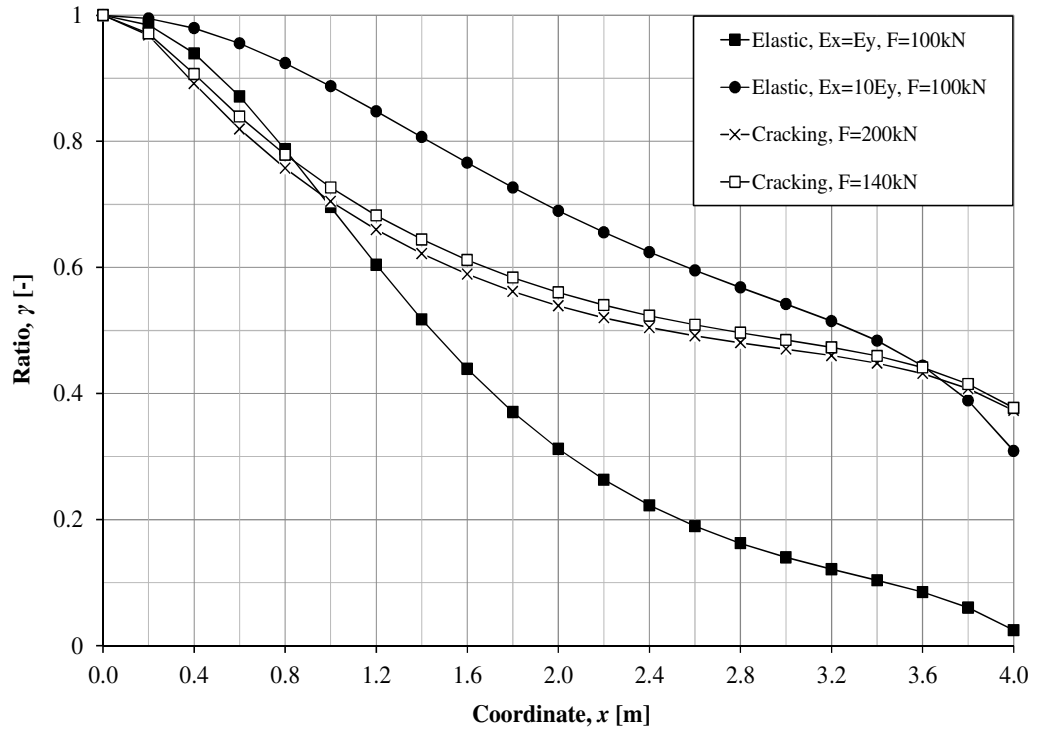

(b)

Figure C.61. Moment distribution m_y along L_5 at different load level up to 200 kN (a) moment distribution m_y (b) ratio of maximum moment $m_{y,max}$ to $m_{y,x}$ moment along L_5, $E_{II} = E_I/10$.

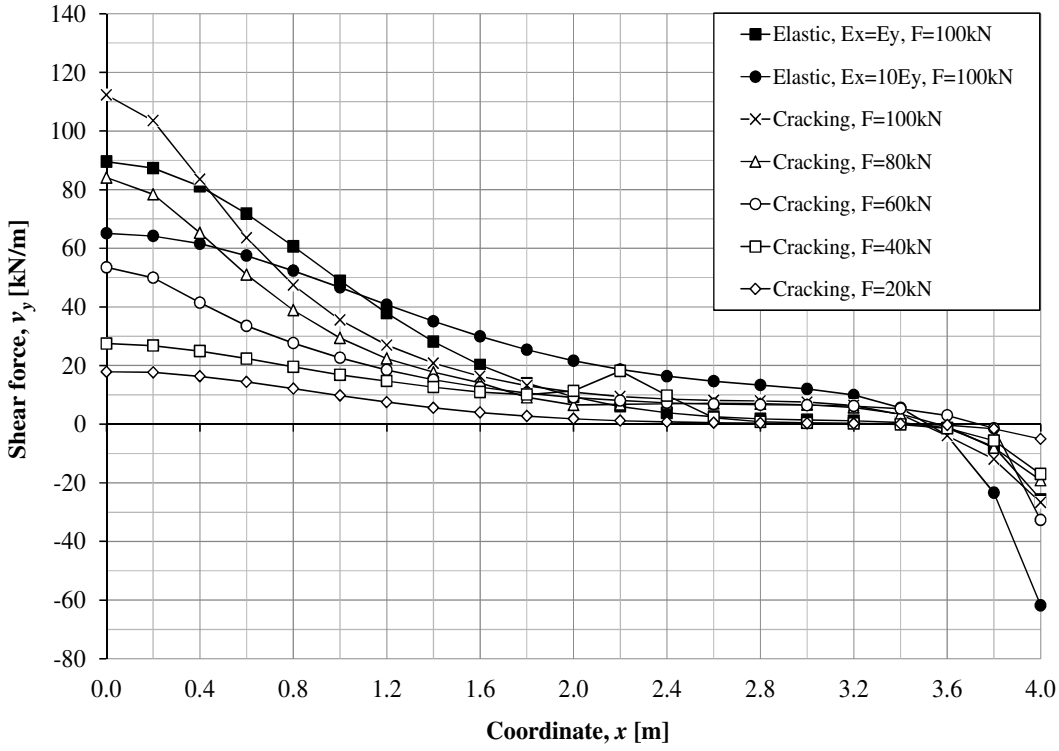

(a)

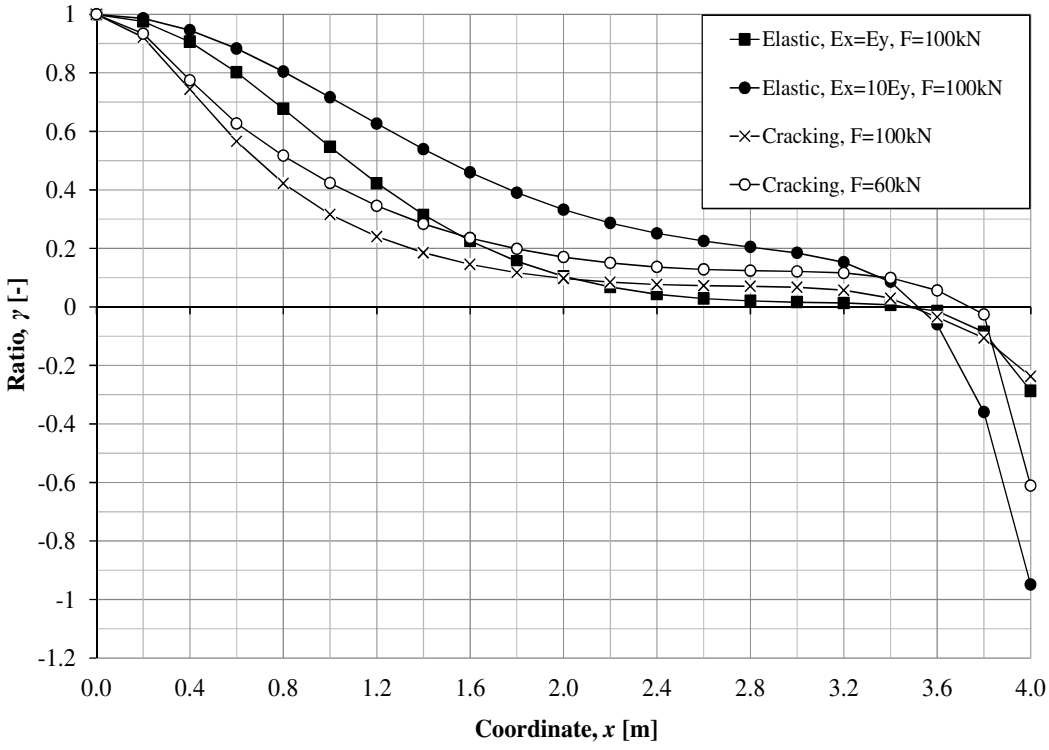

(b)

Figure C.62. Shear force distribution v_y along L_5 at different load level up to 100 kN (a) shear force distribution v_y (b) ratio of maximum shear force $v_{y,max}$ to $v_{y,x}$ moment along L_5, $E_{II} = E_I/10$.

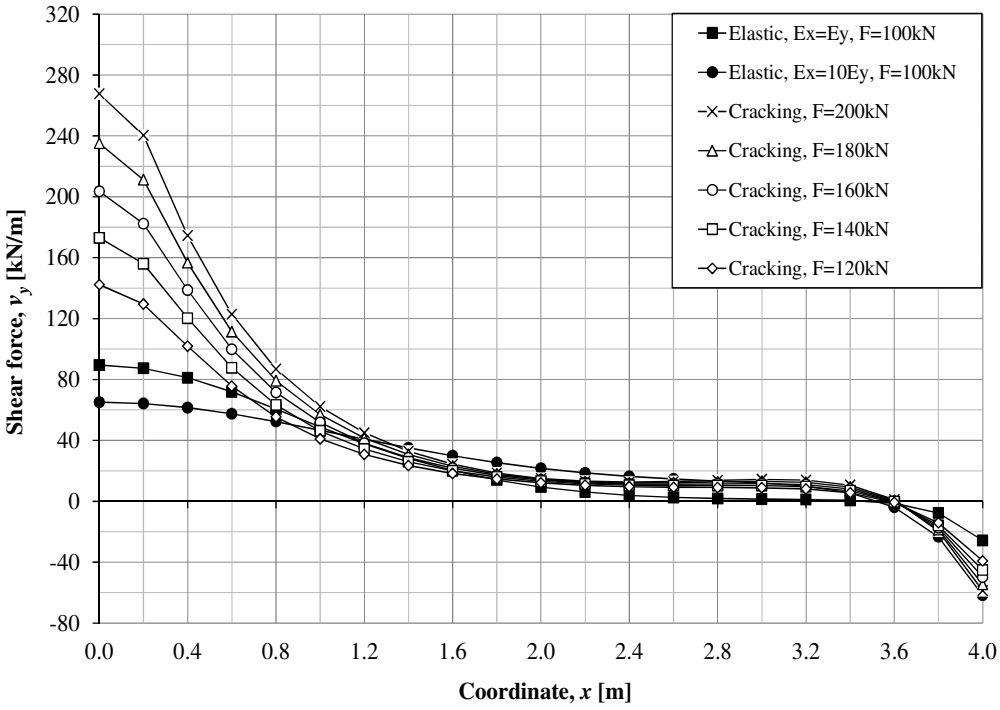

(a)

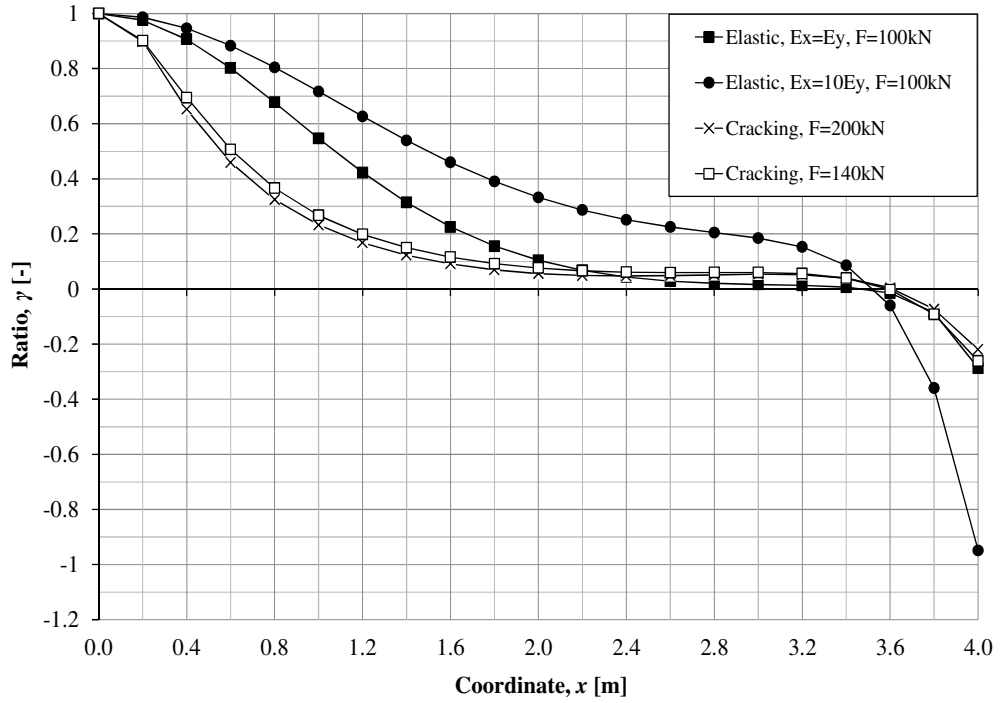

(b)

Figure C.63. Shear force distribution v_y along L_5 at different load level up to 200 kN (a) shear force distribution v_y (b) ratio of maximum shear force $v_{y,max}$ to $v_{y,x}$ moment along L_5, $E_{II} = E_I/10$.

APPENDIX D Shear forces distribution

D.1 Isotropic 0.2 m shell element L = 3 m

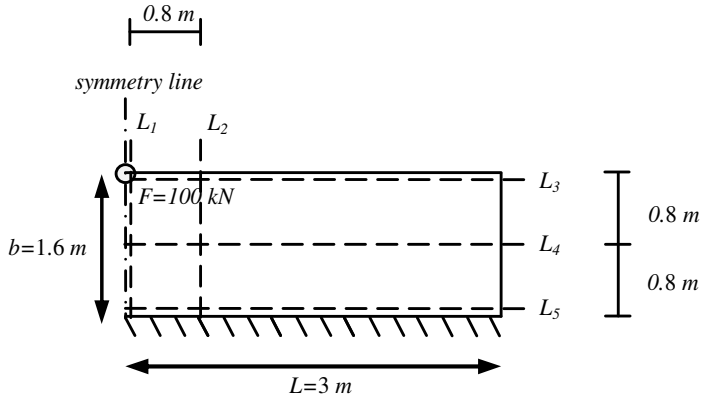

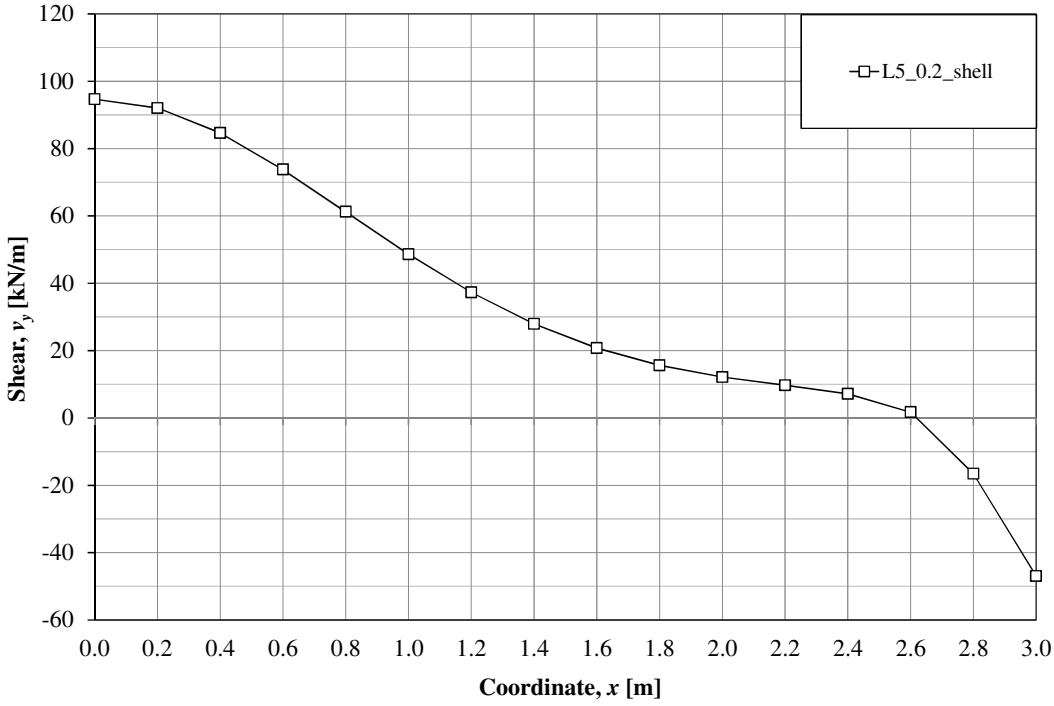

Figure D. 1. Shear force distribution v_y along L_5 from FE-linear elastic analysis isotropic with Poisson's ratio v = 0 using 0.2 m shell elements.

D.2 Isotropic 0.2 m shell element L = 6 m

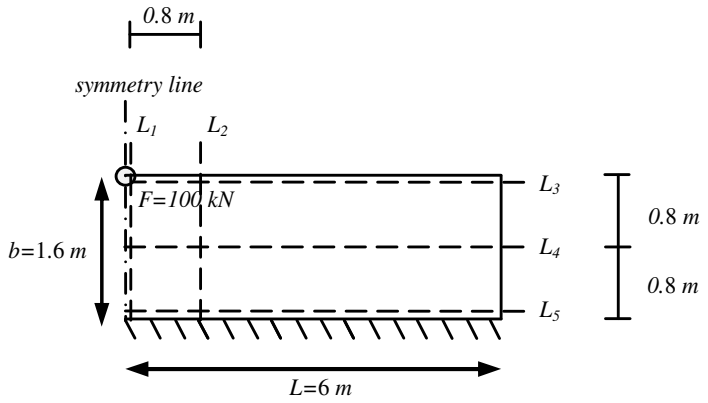

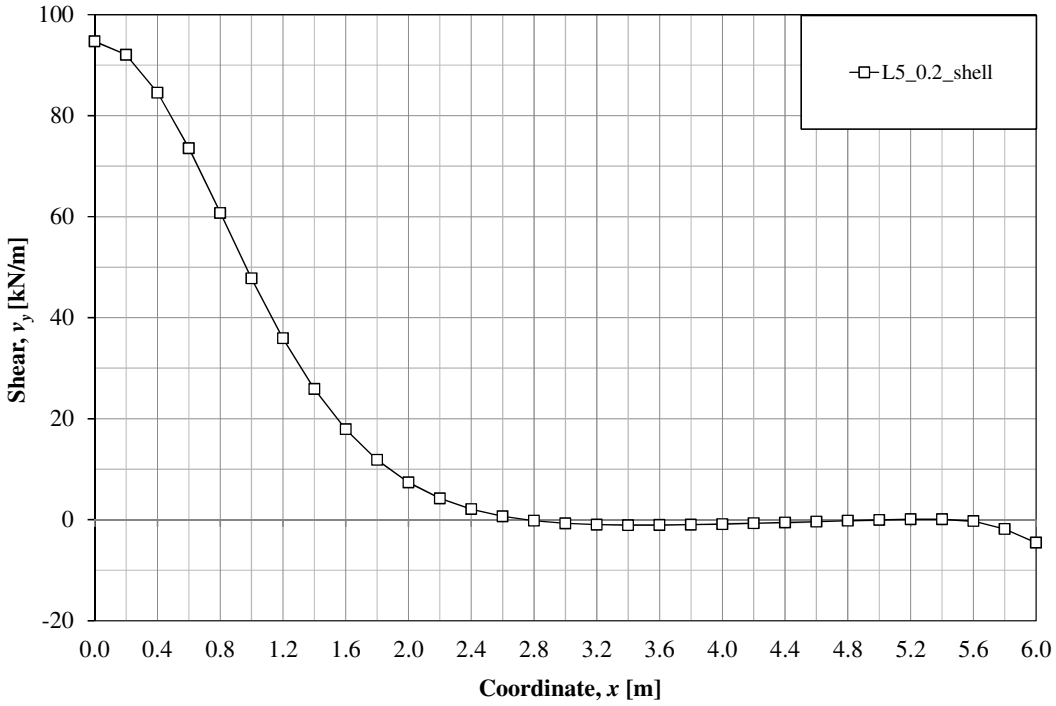

Figure D. 2. Shear force distribution v_y along L_5 from FE-linear elastic analysis isotropic with Poisson's ratio ν = 0 using 0.2 m shell elements.

APPENDIX E Plastic rotation of a cantilever beam

E.1 Geometry and loading

In order to determine a plastic rotation of a cantilever beam, a 1.6 metre long, 0.2 metre width and 0.2 metre thickness cantilever beam subjected to a prescribed displacement of $u_z = 3$ m shown in Figure E.1 and Figure E.2 were examined. The plastic rotation of this beam is calculated using both bilinear moment-curvature input and tri-linear moment curvature input.

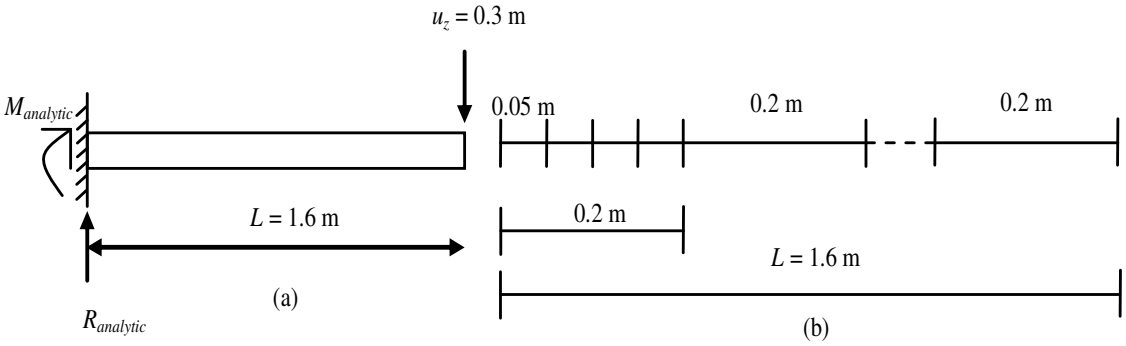

Figure E.1 (a) Geometry of the beam (b) 2 different meshes.

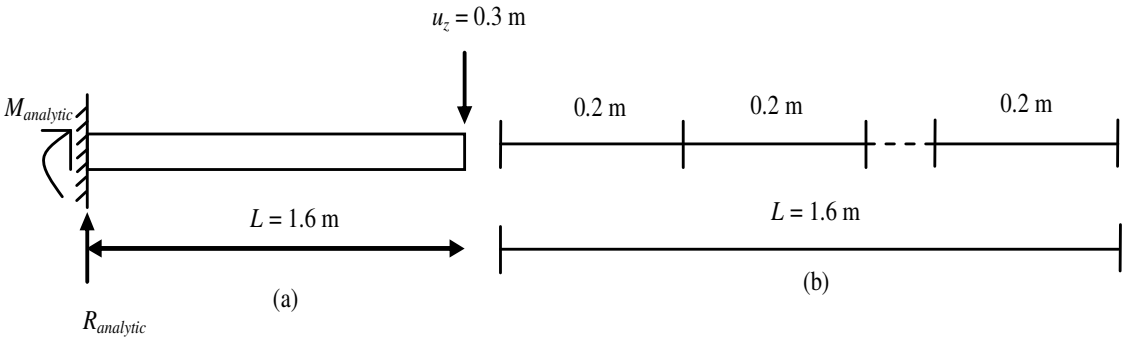

Figure E.2 (a) Geometry of the beam (b) single mesh.

E.2 Alternative methods for plastic rotation of a cantilever beam

The cantilever beam in Figure E.1 was examined. This cantilever beam has a certain plastic rotation under certain prescribed displacement magnitude-u_z. There are three alternative methods to determine the plastic rotation capacity of this cantilever beam. The first and the second method are based on plastic curvature while the third method depends on displacement and rotation relationship. As mentioned in Section 2.2.4, plastic rotation is the area under plastic curvature over a plastic region. It is known that only the first element of this beam yields. Therefore, it is possible to determine the plastic rotation using only the plastic curvature of the first element of the beam. This plastic rotation can be computed by using equation (E-1).

$$\theta_{pl} = \int_0^{l_{el}} \chi_{pl} dx = \sum_0^i \chi_{pl,i} \cdot \Delta x_i \tag{E-1}$$

$$\Delta x_i = \left| x_2 - x_1 \right| \tag{E-2}$$

$$\chi_{pl,i} = \chi_i - \chi_y \tag{E-3}$$

Where θ_{pl} = plastic rotation

$\chi_{pl,i}$ = plastic curvature at point i

χ_i = total curvature at point i

χ_y = yield curvature

x_1 = section x_1

x_2 = section x_2

Δx_i = distance between section x_1 and section x_2

If the first four integration points of the first element yield and are linear while the fifth integration point does not yield as shown in Figure E.3, the plastic rotation capacity can be determined using equation (E-4) instead.

$$\theta_{pl} = \frac{\chi_{pl,1} \cdot l_{el,1}}{2} \tag{E-4}$$

Where $\chi_{pl,i}$ = plastic curvature at integration point 1

$l_{el,1}$ = length of the first element

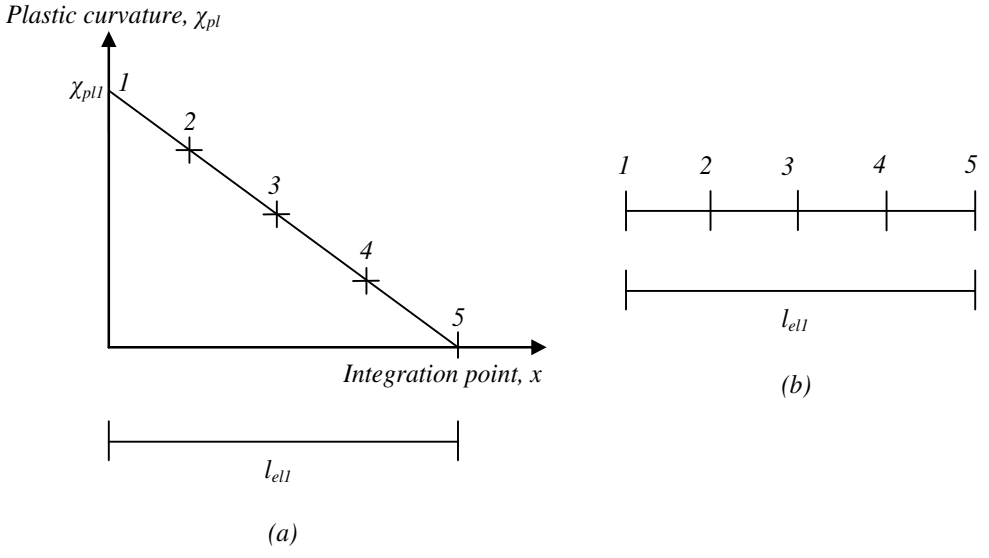

Figure E.3. (a) Plastic curvature and integration point relationship (b) integration point along axial direction of an element.

This plastic rotation θ_{pl} is the area under plastic curvature. The plastic rotation of the above cantilever beam can also be determined by using displacement and rotation

relationship as illustrated in Figure E.4. This plastic rotation θ_{pl} can be derived in equation (E-11).

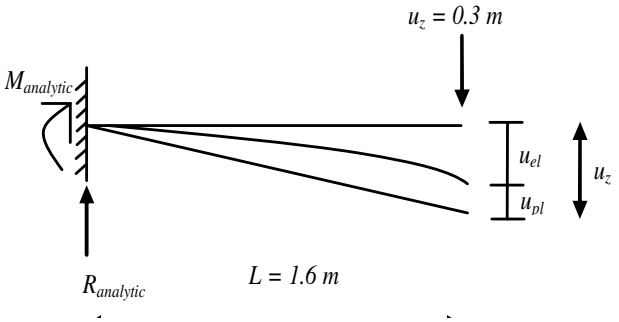

Figure E.4. Rotation and displacement relationship

The moment and curvature relationship is determined from equation (E-5). The elastic curvature χ_{el} and plastic curvature χ_{pl} can be seen in Figure 2.12a.

$$\chi_{ela} = \frac{M}{EI} \tag{E-5}$$

The displacement of a cantilever beam under point load in case of linear elastic response is calculated using equation (E-6).

$$u_{ela} = \frac{PL^3}{3EI} \tag{E-6}$$

The bending moment due to point is determined in equation (E-7).

$$M = PL \tag{E-7}$$

Combine equation (E-5), equation (E-6) and equation (E-7), equation (E-8) is obtained.

$$u_{ela} = \frac{\chi_{ela} \cdot L^2}{3} \tag{E-8}$$

Then a plastic displacement can be computed in equation (E-9) and equation (E-10).

$$u_{pl} = u_{tot} - u_{ela} \tag{E-9}$$

$$u_{pl} = u_{tot} - \frac{\chi_{ela} \cdot L^2}{3} \tag{E-10}$$

Finally, the plastic rotation can be calculated using equation (E-11).

$$\theta_{pl} = \frac{u_{pl}}{L} = \frac{u_{tot}}{L} - \frac{\chi_{ela} \cdot L}{3} \tag{E-11}$$

Where θ_{pl} = plastic rotation
P = point load applied at the edge of the beam
L = length of the beam
u_{tot} = total displacement
u_{ela} = elastic displacement

u_{pl} = plastic displacement

χ_{ela} = elastic curvature

The difference in percentage between method 1, method 2 and method 3 are calculated from equation (E-12), equation (E-13) and equation (E-14) respectively.

$$\gamma_{12} = 100 \cdot \frac{\left|\theta_{pl,method1}\right| - \left|\theta_{pl,method2}\right|}{\left|\theta_{pl,method1}\right|} \tag{E-12}$$

$$\gamma_{13} = 100 \cdot \frac{\left|\theta_{pl,method1}\right| - \left|\theta_{pl,method3}\right|}{\left|\theta_{pl,method1}\right|} \tag{E-13}$$

$$\gamma_{23} = 100 \cdot \frac{\left|\theta_{pl,method2}\right| - \left|\theta_{pl,method3}\right|}{\left|\theta_{pl,method2}\right|} \tag{E-14}$$

E.3 Bilinear moment-curvature input-2 different meshes

The material data input for the analysis of 3D beam with the geometry shown in Figure E.1 using bilinear moment-curvature illustrated in Figure E.5 was studied.

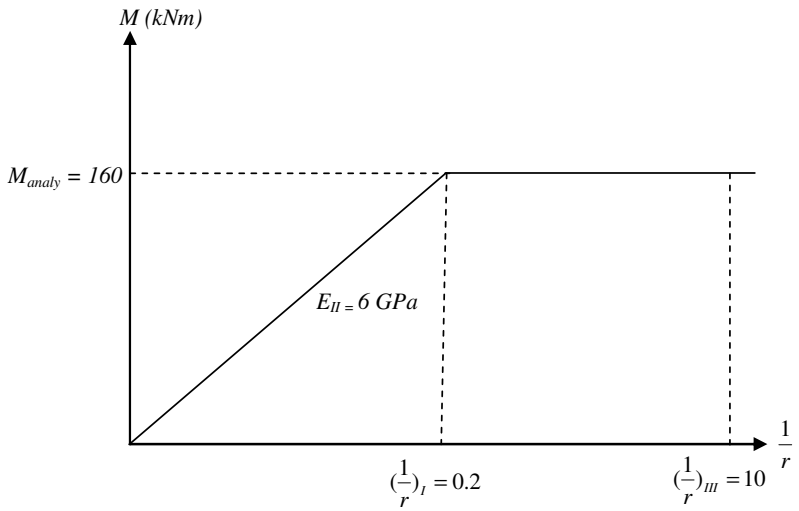

Figure E.5 Bilinear moment curvature relationship input for 3-D beam in elasto-plastic case.

From Figure E.6, it is seen that the reason for the difference between method 1 and method 2 of plastic rotation is that the value of the plastic curvature of the corresponding integration points is non-linear. Figure E.6 also shows that method 2 is not accurate when the plastic curvature value is non-linear. Method 2 provides the value larger than expected as the area below the non-linear plastic curvature curve is larger than the area of triangle.

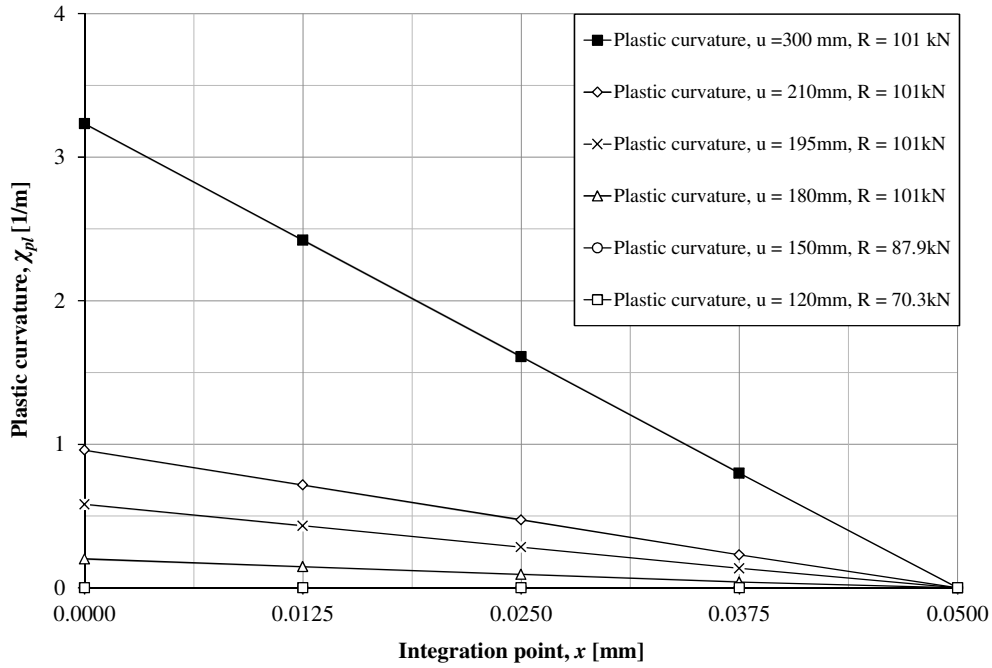

Figure E.6 Plastic curvature and integration relation with regard to increased prescribed displacement, two different meshes.

The plastic rotation of the cantilever beam in Figure E.1 using method 1, method 2 and method 3 expressed in equation (E-1), equation (E-4) and equation (E-11) respectively are summarized in Table E.1.

Table E.1. Comparisons of plastic rotation of a cantilever beam between the three methods using bilinear moment curvature relationship model-two different meshes.

Prescribed displacement u_{pre} (mm)	120	150	180	195	210	300
Reaction force R (kN)	70.3	87.9	101	101	101	101
$\theta_{pl,1} = \sum_{0}^{i} \chi_{pl,i} \cdot \Delta x_i$ (10^{-3} rad)	0	0	4.8	14.3	23.7	80.6
$\theta_{pl,2} = \frac{\chi_{pl,1} \cdot l_{el,1}}{2}$ (10^{-3} rad)	0	0	5.1	14.5	24	80.8
$\theta_{pl,3} = \frac{u}{L} - \frac{\chi_{ela} \cdot L}{3}$ (10^{-3} rad)	0	0	5.8	15.2	24.6	80.8
γ_{12} [%]	-	-	-5.3	-1.8	-1.1	-0.3
γ_{13} [%]	-	-	-21.8	-6.7	-3.6	-0.3
γ_{23} [%]	-	-	-15.7	-4.8	-2.5	0

From Table E.1, it is seen that difference between method 1 and method 2 for plastic rotation of the cantilever beam is converged when the prescribed displacement-u_z becomes larger and larger. The larger the displacement is, the plastic curvature curve will to tend to be linear. From Figure E.6 and Table E.1, it is concluded that method 2 is a safe-side method, but it is unconservative and it can estimate an approximation plastic rotation of the studied cantilever in Figure E.1. When the prescribed displacement u_{pre} = 195 mm and R = 101 kN, the plastic rotation due to method 1 is $\theta_{pl,1} = 14.3 \cdot 10^{-3}$ rad and the plastic rotation due to method 2 is $\theta_{pl,2} = 14.5 \cdot 10^{-3}$ and $\gamma_{12} =$ 1.8 %. The difference between method 1 and method 2 when the plastic rotation $\theta_{pl,2} > 14 \cdot 10^{-3}$ is considered acceptable. Therefore method 2 will be used to determine a plastic rotation of the cantilever slab in Chapter 5.

E.4 Bilinear moment-curvature input-single mesh

In order to be sure that the three methods for plastic rotation of the cantilever beam is accurate; the cantilever bean in Figure E.2 was examined with bilinear moment-curvature illustrated in Figure E.5.

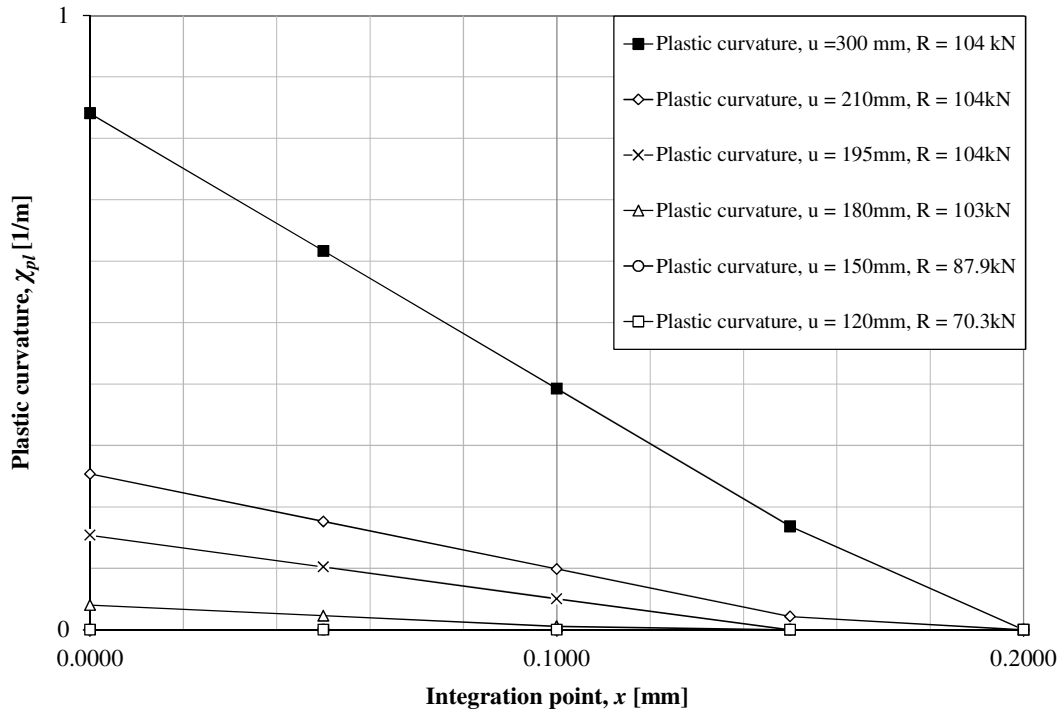

Figure E.7 Plastic curvature and integration relation with regard to increased prescribed displacement, single mesh.

From Figure E.7, method 2 is accurate when the plastic curvature at each integration point is linear. Method 2 is on safe-side and can be used to estimate the plastic rotation of the cantilever beam.

The plastic rotation of the cantilever beam with single mesh in Figure E.2 using method 1, method 2 and method 3 expressed in equation (E-1), equation (E-4) and equation (E-11) respectively are summarized in Table E.2.

Table E.2. Comparisons of plastic rotation of a cantilever beam between the three methods using bilinear moment curvature relationship model-single mehs.

Prescribed displacement u_{pre} (mm)	120	150	180	195	210	300
Reaction force R (kN)	70.3	87.9	104	104	104	104
$\theta_{pl,1} = \sum_{0}^{i} \chi_{pl,i} \cdot \Delta x_i$ (10^{-3} rad)	0	0	2.4	11.5	21.2	79.9
$\theta_{pl,2} = \frac{\chi_{pl,1} \cdot l_{el,1}}{2}$ (10^{-3} rad)	0	0	4.0	15.4	25.4	84.1
$\theta_{pl,3} = \frac{u}{L} - \frac{\chi_{ela} \cdot L}{3}$ (10^{-3} rad)	0	0	5.8	15.2	24.6	80.8
γ_{12} [%]	-	-	-65.1	-34.1	-19.8	-5.2
γ_{13} [%]	-	-	-140.0	-32.5	-16.1	-1.2
γ_{23} [%]	-	-	-45.3	-1.2	-3.1	3.8

From Table E.2, it is seen that difference between method 1, method 2 and method 3 converged for a very large prescribed displacement u_z. Since the error between method 1 and method 2 when using single mesh is larger than those when using two different meshes, two different meshes is recommended for the the analysis of the cantilever beam in elasto-plastic case.

E.5 trilinear moment-curvature input

The material data input for the analysis of 3-D beam with the geometry shown in Figure E.1 using trilinear moment-curvature illustrated in Figure E.5 is studied.

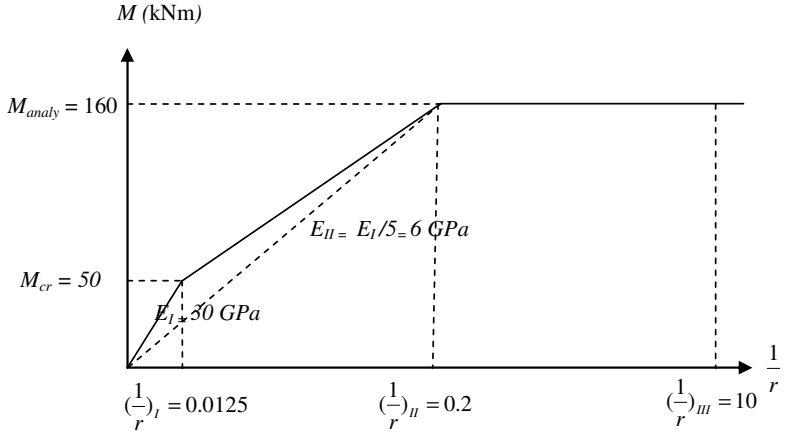

Figure E.8 Trilinear moment curvature relationship input for 3-D beam in elasto-plastic case.

The moment and curvature input value in Figure E.8 can be found in equation (3-17), equation (3-18) and from Figure 3.8. Like bilinear moment-curvature input, the difference between method 1 and method 2 of plastic rotation is due to the non-linearity of the value of the plastic curvature of the corresponding integration points.

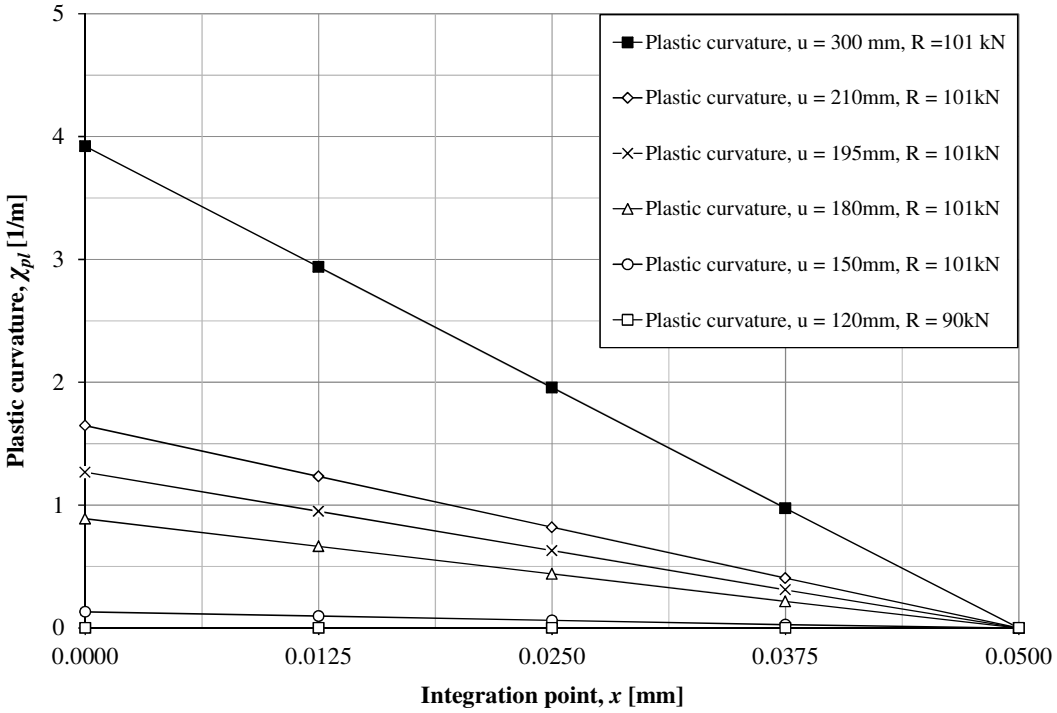

Figure E.9 Plastic curvature and integration relation with regard to increased prescribed displacement.

Table E.3. Comparisons of plastic rotation of a cantilever beam between the three methods using trilinear moment curvature relationship model.

Prescribed displacement u_{pre} (mm)	120	150	180	195	210	300
Reaction force R (kN)	90	101	101	101	101	101
$\theta_{pl,1} = \sum_{0}^{i} \chi_{pl,i} \cdot \Delta x_i$ (10^{-3} rad)	0	3.12	22.1	31.5	41	97.9
$\theta_{pl,2} = \frac{\chi_{pl,1} \cdot l_{el,1}}{2}$ (10^{-3} rad)	0	3.29	22.2	31.7	41.2	98
$\theta_{pl,3} = \frac{u}{L} - \frac{\chi_{ela} \cdot L}{3}$ (10^{-3} rad)	0	0	5.83	15.2	24.6	80.8
γ_{12} [%]	-	-5.38	-0.8	-0.5	-0.4	-0.2
γ_{13} [%]	-	100	73.6	-51.8	40.0	17.4
γ_{23} [%]	-	100	73.8	-52.0	40.3	17.5

Like bilinear moment-curvature input case, from Table E.3, it is seen that difference between method 1 and method 2 for plastic rotation of the cantilever beam is converged when the prescribed displacement becomes larger and larger. When the prescribed displacement u_{pre} = 165 mm and R = 101 kN, the plastic rotation due to method 1 is $\theta_{pl,1} = 12.6 \cdot 10^{-3}$ rad and the plastic rotation due to method 2 is $\theta_{pl,2} = 12.8 \cdot 10^{-3}$ and γ_{12} = 1.3 %. The difference between method 1 and method 2 when the plastic rotation $\theta_{pl,2} > 12 \cdot 10^{-3}$ is considered acceptable. Therefore method 2 will be used to determine a plastic rotation of the cantilever slab in Chapter 5.

It is note that method 3 is only valid for bilinear moment-curvature input and it is not valid when using multi-linear moment curvature input for elasto-plastic case. The reason is that for elasto-plastic moment-curvature input in ADINA, the first data point always corresponds to yielding and the last data point always corresponds to rupture. Therefore, when using multi-linear moment curvature relationship, equation (E-5), equation (E-6) and equation (E-8) are not valid from M_{cr} to M_{analy} in Figure E.8.

APPENDIX F Modelled slab versus real slab

F.1 Geometry

As a real reinforced concrete slab is not modelled in this report, a slab with certain dimension and material properties is chosen. What does the studied cantilever slab in Figure 4.32 with input data in Figure 4.33 mean in reality?

Let's assume a slab with dimension shown in Figure F.1. The concrete slab is C30/37 and reinforcement B500 are chosen.

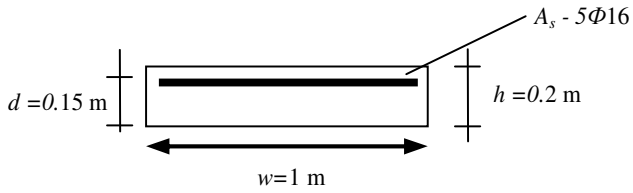

Figure F.1 Cross-section of a real concrete slab.

F.2 Stiffness

Concerning cracking moment of concrete, one might argue about which tensile properties of concrete, i.e. characteristic value or mean value should be used. In this case, the mean value of the concrete tensile strength is assumed.

The total amount of reinforcement:

$$A_s = \frac{A_{\phi 16}}{s} = \frac{201}{0.2} = 1005 \cdot 10^{-6} \text{ m}^4 \tag{F-1}$$

The moment of inertia for uncracked state (state I) ignoring reinforcement is determined in equation (F-2).

$$I_I = \frac{wh^3}{12} = \frac{1 \cdot 0.2^3}{12} = 6.67 \cdot 10^{-4} \text{ m}^4 \tag{F-2}$$

α is the ratio between the Young's modulus for reinforcement and concrete and determine as:

$$\alpha = \frac{E_{sm}}{E_{cm}} = \frac{200}{33} = 6.06 \tag{F-3}$$

A_I total area of the cross section determined as:

$$A_I = wh + (\alpha - 1) \cdot A_s = 1 \cdot 0.2 + (6.06 - 1) \cdot 1005 \cdot 10^{-6} = 0.205 \text{ m}^2 \tag{F-4}$$

The effective depth d is:

$$d = h - c = 0.2 - 0.05 = 0.15 \text{ m} \tag{F-5}$$

x_{bar} centre of gravity of the section determined as:

$$\bar{x} = \frac{wh \cdot \frac{h}{2} + (\alpha - 1) \cdot A_s \cdot d}{A_I} = \frac{1 \cdot 0.2 \cdot \frac{0.2}{2} + (6.06 - 1) \cdot 1005 \cdot 10^{-6} \cdot 0.15}{0.205} = 0.101 \text{ m} \quad \text{(F-6)}$$

The moment of inertia for uncracked state (state) taking into account reinforcement is determined in equation (F-7).

$$I_{I,reinforcement} = \frac{wh^3}{12} + wh(\frac{h}{2} - \bar{x})^2 + (\alpha - 1) \cdot A_s \cdot (d - \bar{x})^2$$
$$= \frac{1 \cdot 0.2^3}{12} + 1 \cdot 0.2(\frac{0.2}{2} - 0.101)^2 + (6.06 - 1) \cdot 1005 \cdot 10^{-6} \cdot (0.15 - 0.101)^2 \quad \text{(F-7)}$$
$$= 6.79 \cdot 10^{-4} \text{ m}^4$$

In state II, the moment of inertia must be calculated from the cracked cross-section. By assuming negligible normal forces, the height of the compressed zone x can be determined by equilibrium as:

$$x = \frac{w\frac{x^2}{2} + \alpha A_s d}{bx + \alpha A_s} \quad \text{(F-8)}$$

and can be rearranged as:

$$x^2 + \frac{2\alpha A_s}{w}(x - d) = 0 \quad \text{(F-9)}$$

Then x can be determined as:

$$x = -\frac{\alpha A_s}{w} + \sqrt{\left(\frac{\alpha A_s}{w}\right)^2 + \frac{2\alpha A_s d}{w}} = -\frac{6.06 \cdot 1005 \cdot 10^{-6}}{1} + \sqrt{\left(\frac{6.06 \cdot 1005 \cdot 10^{-6}}{1}\right)^2 + \frac{2 \cdot 6.06 \cdot 1005 \cdot 10^{-6} \cdot 0.15}{1}} = 0.037 \text{ m} \quad \text{(F-10)}$$

The moment of inertia in state II can then be calculated as

$$I_{II} = \frac{wx^3}{3} + \alpha A_s (d - x)^2 = \frac{1 \cdot 0.037^3}{3} + 6.06 \cdot 1005 \cdot 10^{-6} \cdot (0.15 - 0.037)^2 \quad \text{(F-11)}$$
$$= 9.46 \cdot 10^{-5} \text{ m}^4$$

The ratio between uncracked and cracked moment inertia is:

$$\gamma = \frac{EI_I}{EI_{II}} = \frac{6.67 \cdot 10^{-4}}{9.46 \cdot 10^{-5}} = 7.05 \tag{F-12}$$

F.3 Cracking moment

It is possible to determine the cracking moment using moment of inertia of uncracked section with and without taking into account the reinforcement, i.e. I_I or $I_{I,reinforcement}$

In this case, cracking moment is computed using moment of inertia of state I ignoring reinforcement as:

$$m_{cr} = f_{ctm} \cdot \frac{wh^2}{6} = 2.9 \cdot 10^6 \cdot \frac{1 \cdot 0.2^2}{6} = 19.33 \text{ kNm/m} \tag{F-13}$$

F.4 Maximum internal resistance

When the plastic case is considered, the deformation of the slab does no longer follow the elastic deformation shape and the stiffness is no importance. In this case, the internal resistance is important. The partial coefficients used for steel and concrete are equal to 1.15 and 1.5 respectively. Factors $\alpha_R = 0.81$ and $\beta_R = 0.416$ are stress block factors when the section has reached its ultimate capacity according to Eurocode 2, CEN (2004).

The height of compression zone x is determined as:

$$x = \frac{f_{yd} A_s}{\alpha_R f_{cd} w} = \frac{\frac{500 \cdot 10^6}{1.15} \cdot 1005 \cdot 10^{-6}}{0.81 \cdot \frac{30 \cdot 10^6}{1.5} \cdot 1} = 0.027 \text{ m} \tag{F-14}$$

The moment capacity for rectangular cross Section is:

$$\begin{aligned} m_{rd} &= f_{yd} \cdot A_s (d - \beta \cdot x) \\ &= \frac{500 \cdot 10^6}{1.15} \cdot 1005 \cdot 10^{-6} (0.15 - 0.416 \cdot 0.027) = 60.64 \text{ kNm/m} \end{aligned} \tag{F-15}$$

F.5 Plastic rotation capacity

Reader can refer to Section 2.2.4 for plastic rotation capacity.

The ratio between the height of compression zone and effective depth is:

$$\frac{x_u}{d} = \frac{0.027}{0.15} = 0.179 \tag{F-16}$$

From Figure 2.13 with x_u/d = 0.179 , ClassB steel and concrete C30/37 are used, $\theta_{pl,d}$ is obtained as:

$$\theta_{pl,d} = 13 \cdot 10^{-3} \text{ rad} \tag{F-17}$$

The shear slenderness λ determined as:

$$\lambda = \frac{l_o}{d} = \frac{1.6}{0.15} = 10.67 \tag{F-18}$$

$$k_\lambda = \sqrt{\frac{\lambda}{3}} = \sqrt{\frac{10.67}{3}} = 1.88 \tag{F-19}$$

Therefore, the plastic rotation capacity of the section is determined in equation (F-20).

$$\theta_{rd} = k_\lambda \theta_{pl,d} = 1.88 \cdot 13 \cdot 10^{-3} = 24.5 \cdot 10^{-3} \text{ rad} \tag{F-20}$$

From Figure 2.13 with ClassB steel and concrete C30/37 are used, $\theta_{pl,d,min}$ is obtained as:

$$\theta_{pl,d,\min} = 5.6 \cdot 10^{-3} \text{ rad} \tag{F-21}$$

$$\theta_{rd,\min} = k_\lambda \theta_{pl,d,\min} = 1.88 \cdot 5.6 \cdot 10^{-3} = 10.53 \cdot 10^{-3} \text{ rad} \tag{F-22}$$

F.6 Comparison between modelled slab and real reinforced concrete slab

When the plastic rotation capacity of the cantilever slab in Figure F.1 is determined, it is possible to estimate the plastic rotation capacity of the studied cantilever slab in Figure 4.32 with input data in Figure 4.33 in Section 4.5.3 by comparing m_{cr}, stiffness ratio γ, and moment capacity m_{rd}. The comparison between the real reinforced concrete slab in Figure F.1 and the studied chosen in Figure 4.32 with input data in Figure 4.33 in Section 4.5.3 is summarized in

Table F.1 Comparison between real reinforced concrete slab and modelled slab.

Parameters	Real RC slab	Modelled slab
L_0 (m)	1.6	1.6
h (m)	0.2	0.2
w (m)	1	1
d (m)	0.15	0.15
Concrete	C30/37	?

Reinforcem ent	5ϕ16, B500	?
$\gamma = \frac{E_c I_I}{E_c I_{II}}$	7.05	5
m_{cr} (kNm/m)	19.33	19
m_{rd} (kNm/m)	60.64	57
$\theta_{rd} = k_\lambda \theta_{pl,d}$ (10^{-3} rad)	24.5	*?*
$\theta_{rd,\min} = k_\lambda \theta_{pl,d,\min}$ (10^{-3} rad)	10.53	10.53

As can be seen in Table F.1, the properties of studied cantilever slab in Figure 4.32 are close to real concrete slab in Figure F.1.Therefore, it is concluded that it is a reasonable slab that is close to reality. Since the geometry of these two slabs are the same and m_{rd} are close to each other, the plastic rotation capacity of the studied cantilever slab in in Figure 4.32 with input data in Figure 4.33 should be around the region of $\theta_{rd} = 24.5 \cdot 10^{-3}$ rad. The minimum plastic rotation of these two slabs is $\theta_{rd,min} = 10.6 \cdot 10^{-3}$ rad.